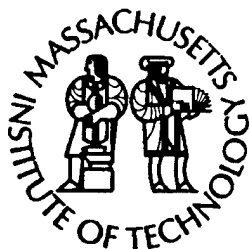
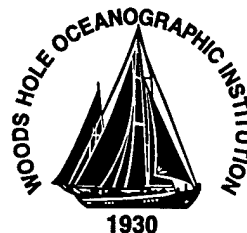


MIT/WHOI 97-09

**Massachusetts Institute of Technology
Woods Hole Oceanographic Institution**



**Joint Program
in Oceanography/
Applied Ocean Science
and Engineering**



DOCTORAL DISSERTATION

*The Geological Record of Oceanic Crustal Accretion and
Tectonism at Slow-Spreading Ridges*

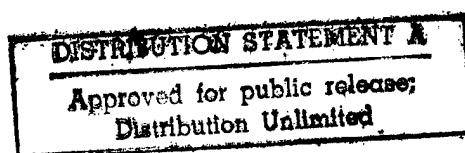
by

Gary Edward Jaroslow

December 1996

19971014 056

DTIC QUALITY INSPECTED 8



MIT/WHOI

97-09

The Geological Record of Oceanic Crustal Accretion and Tectonism at
Slow-Spreading Ridges

by

Gary Edward Jaroslow

Massachusetts Institute of Technology
Cambridge, Massachusetts 02139

and

Woods Hole Oceanographic Institution
Woods Hole, Massachusetts 02543

December 1996

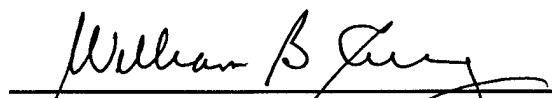
DOCTORAL DISSERTATION

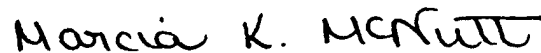
Funding was provided by the Office of Naval Research through Contract No. N00014-90-J-1621
and ASSERT Grant No. N00014-93-1-1153.

Reproduction in whole or in part is permitted for any purpose of the United States Government.
This thesis should be cited as: Gary Edward Jaroslow, 1996. The Geological Record of Oceanic
Crustal Accretion and Tectonism at Slow-Spreading Ridges. Ph.D. Thesis. MIT/WHOI, 97-09.

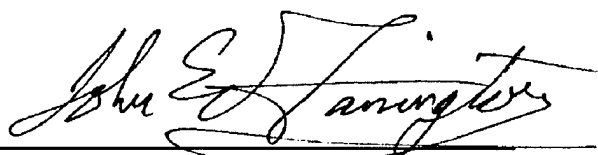
Approved for publication; distribution unlimited.

Approved for Distribution:


William B. Curry, Chair
Department of Geology and Geophysics



Marcia K. McNutt
MIT Director of Joint Program



John W. Farrington
WHOI Dean of Graduate
Studies

DTIC QUALITY INSPECTED 3

The Geological Record of Oceanic Crustal Accretion and Tectonism at Slow-Spreading Ridges

by

Gary Edward Jaroslow

B. S., University of Massachusetts, 1990.

SUBMITTED IN PARTIAL FULFILLMENT OF THE REQUIREMENTS FOR THE
DEGREE OF DOCTOR OF PHILOSOPHY

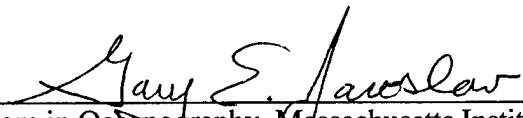
at the
MASSACHUSETTS INSTITUTE OF TECHNOLOGY
and the
WOODS HOLE OCEANOGRAPHIC INSTITUTION

December, 1996

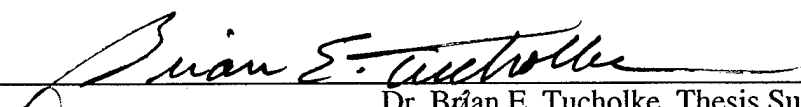
© Gary E. Jaroslow, 1996. All rights reserved

The author hereby grants to MIT and WHOI permission to reproduce and distribute copies of this thesis document in whole or in part.

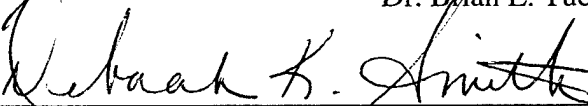
Signature of Author


Joint Program in Oceanography, Massachusetts Institute of Technology and
Woods Hole Oceanographic Institution, December 1996

Certified by


Dr. Brian E. Tucholke, Thesis Supervisor

Accepted by


Deborah K. Smith, Chair, Joint Committee for Marine Geology and Geophysics,
Massachusetts Institute of Technology and Woods Hole Oceanographic Institution

THE GEOLOGICAL RECORD OF OCEANIC CRUSTAL ACCRETION AND TECTONISM AT SLOW-SPREADING RIDGES

by

Gary Edward Jaroslow

Submitted to the Department of Earth, Atmospheric, and Planetary Sciences
Massachusetts Institute of Technology
and
Department of Geology and Geophysics
Woods Hole Oceanographic Institution

December, 1996

in partial fulfillment of the requirements
for the degree of Doctor of Philosophy

Abstract

Studies of the morphology of slow-spreading ridges have contributed enormously to our understanding of the generation of oceanic crust. However, such work has largely been confined to the ridge axis, and therefore is limited in its application. The objective of this Thesis was to interpret the structural development of slow-spreading ridge segments by: 1) delineating the nature, magnitude, and relative importance of primary tectonic and volcanic processes that control crustal morphology, 2) investigating the spatial and temporal variability of these processes, and 3) examining how rheological variations in the lithosphere constrain its structural configuration. To that end, this Thesis provides detailed documentation of faults and volcanoes (seamounts) at the Mid-Atlantic Ridge from 25°25'N to 27°10'N and extending from zero-age crust at the ridge axis to ~29 Ma crust on the ridge flank. This information is used to analyze the evolution of ocean crust from initial formation on the rift-valley floor to degradation by aging processes on the ridge flank. In addition, deformation conditions in the lithosphere are examined from study of naturally deformed mantle rocks recovered from fault zones at slow-spreading ridges.

Accumulation of sediments affects the seafloor morphological expression of ocean crustal structure. Therefore, to study the morphological record of crustal accretion and tectonism at the Mid-Atlantic Ridge, sediment thicknesses were mapped over the same region where the faults and seamounts were analyzed. All available seismic-reflection data were interpreted, and conversions from reflection time to thickness in meters were made based on compressional-wave velocity data. Areal patterns of sediment distribution were constrained by using seafloor shape determined from Hydrosweep multibeam bathymetry, and by interpretation of backscatter patterns in Hawaii MR1 sidescan-sonar data. The maps show that accumulation of thick sediments along the western flank of the Mid-Atlantic Ridge occurs mainly in sediment ponds within crustal depressions. The largest ponds (up to 800 m sediment thickness) are located over relatively deep crust within non-transform discontinuities and within ridge-parallel valleys between abyssal hills. The ridge-parallel

valleys both accumulate sediment and serve as pathways for sediment transport towards the larger ponds within non-transform discontinuities. Draping of thick sediments (>10 m) across abyssal hills between ponds is uncommon. Initial sediment deposition began as a pelagic veneer, and it subsequently was removed to the sediment ponds by gravity-driven flows and bottom currents. Sediment thickness averaged along isochrons shows a trend of increasing sediment cover with increasing crustal age up to ~17 Ma crust, and sediment thickness decreases on 17 - 28 Ma crust. This sediment-thickness pattern is best explained by depression of the calcite compensation depth to below ridge-crest level about 17 m.y. ago.

A detailed analysis of faulting on the western flank of the Mid-Atlantic Ridge provides new constraints on the role of faulting in the formation of topography at slow-spreading ridges. Faults and fault geometries were documented by application of image analysis techniques to an extensive multibeam bathymetry dataset and by interpretation of sidescan-sonar imagery. It is found that creation of rift-valley and abyssal-hill topography is controlled by faulting on both inward- and outward-facing normal faults. Uplift of crust to the crest of the rift mountains is accommodated by extension on normal faults that dip toward the ridge axis, with slip being concentrated on faults near the base of the rift-valley walls. Reduction of rift-valley relief toward the crest of the rift mountains is accomplished by slip on outward-facing normal faults that are active in the upper rift-valley walls. Outward-facing faults account for 40% of the faults observed on the ridge flank. The generation of pairs of inward- and outward-facing faults results in common horst and graben terrain that forms most abyssal hills. There is no significant faulting beyond the crest of the rift mountains. Short-term (~3 m.y.) temporal variations in brittle strain observed off-axis on the ridge flank most likely reflect changes in magmatic versus relatively amagmatic extension at the ridge axis. Regionally, high fault density and high fault strain correlate with increased residual mantle Bouguer anomaly, i.e., thin crust formed by relatively amagmatic extension; low fault densities and low strains correlate with reduced residual gravity anomaly or thicker crust formed by more magmatic extension. Fault populations also show strong differences in geometry, density and strain with intrasegment tectonic setting. Observations at inside-corner crust are consistent with faulting of relatively thick, cold lithosphere with limited magmatic extension: strains are large and fault spacings tend to be greater than those at segment centers. At segment centers, faults are longer, more linear, more closely spaced, and have smaller offsets and lower total strains; this pattern suggests a thinner brittle lid and more magmatic extension.

Approximately 85 axial seamounts and 1290 off-axis seamounts were identified on the western flank of the Mid-Atlantic Ridge in Hydrosweep bathymetry. There is no evidence for off-axis volcanism, indicating that the seamounts were constructed on the inner rift-valley floor of the Mid-Atlantic Ridge and then transported off-axis. The abundance of off-axis seamounts shows that large sections of oceanic crust are transported intact through the rift-valley wall to the ridge flank. Seamount population density, size distribution, and shape were determined to quantitatively investigate spatial and temporal variations in the seamount population and to examine how seamounts are modified during tectonic transport away from the ridge axis. During initial transport of seamounts up the rift-valley walls (0.6 - 2 m.y.), few seamounts are destroyed by the predominant inward-facing faults, but seamount height on average is decreased. In the upper portions of the rift-valley walls, on 2 - 4 Ma crust, newly formed outward-facing faults destroy and degrade a significant number of seamounts. Beyond the crest of the rift mountains, faults no longer affect seamounts, and changes in the off-axis seamount population reflect temporal variations in crustal aging processes and/or long-period changes in seamount production at the ridge axis. Seamount population density estimated for the entire off-axis seamount population has a positive relationship with crustal thickness as inferred from

gravity data, suggesting that more seamounts are produced when increased magma supply produces thicker crust. We observe no temporal correlation of seamount populations between adjacent ridge segments, indicating that the magmatic cycles of ridge segments operate independently of one another. There are no observed changes in measured seamount density with along-axis position in individual ridge segments. This may reflect real invariance in seamount population, or it may reflect the inadequacy of our acoustic systems to detect important but geologically subtle variations in style of volcanism along-axis.

Microstructures preserved in abyssal peridotites dredged from slow-spreading ridges record several different physical regimes of deformation. Two major classes of abyssal peridotites are identified based on detailed microstructural analysis. 1) Medium- to coarse-grained tectonites are associated with mantle upwelling and emplacement to the base of the lithosphere. These tectonites give geothermometric temperatures of $\sim 755^{\circ}\text{C}$ or higher, interpreted here to represent lower temperature limits for diffusive exchange during cooling. 2) Fine-grained mylonites are associated with faults and shear zones that develop during extension of the oceanic lithosphere. Geothermometry and flow laws for olivine suggest that deformation in some fine-grained mylonites occurred by diffusion creep down to $\sim 600^{\circ}\text{C}$. Rheological data indicate that dislocation creep is not likely to occur at this temperature. Therefore, reduction in grain size by cataclasis, or possibly dynamic recrystallization, resulted in a transition in deformation mechanism from dislocation- to diffusion-creep during uplift (and/or cooling). Characteristics of these fine-grained mylonites indicate that shear zones that extend into the upper mantle will be weaker than expected if deformation was accommodated by brittle processes or dislocation creep.

Thesis Supervisor: Brian E. Tucholke
 Senior Scientist
 Woods Hole Oceanographic Institution

Acknowledgements

First of all, I am particularly grateful for the help, guidance, and opportunities that Brian Tucholke has given me from my first summer in Woods Hole as a Summer Fellow to my final weeks scrambling to finish this thesis. Brian's patience, respect, and availability go well beyond his job description of Thesis Advisor, and I thank him. I have learned a great deal about scientific analysis by having him as my mentor.

I also owe a great deal of gratitude to Henry Dick, Debra Smith, and Greg Hirth. Each has a unique way of approaching scientific problems, and I have benefited tremendously from their knowledge and geological insight. Not only do I thank Henry for introducing and guiding me through his wonderful world of peridotites, but he deserves special kudos for bringing Geodynamics to the students at WHOI. It was an invaluable seminar, and through its fieldtrips I have learned alot (and eaten some of my most memorable meals). Debbie is responsible for rekindling my boyhood fascination with volcanoes, and she has helped me see the light of statistics. Greg's advice, friendship and encouragement have helped me a great deal. I can only hope that some of his knowledge of structural geology has rubbed off on me.

Much of my graduate school education is grounded in the informal interactions with scientists and students at WHOI and MIT. Among the many people whom I thank for stimulating and helpful conversations, I am particularly grateful to Javier Escartín, Elazar Uchupi, Jian Lin, John Goff, Peter Shaw, Kathy Gillis, Debbie Kelley, Marty Kleinrock, Kip Hodges, Dan Lizarralde, and Bob Grieses.

Much of my thesis is based on extensive datasets acquired at sea using the equipment and data processing techniques of WHOI's Deep Submergence Laboratory. It has been my privilege and benefit to work closely with Ken Stewart, Jon Howland, Marty Marrah, Xiaou Tang, and Helen Huang of DSL. Their efforts have added substantially to several projects I have worked on and form the basis of the image-processing fault-detection algorithm used in Chapter 3.

My acknowledgements would be incomplete without thanking the many staff members who facilitate daily life at WHOI. These include: the folks in Education, (especially Jake Pierson, Abbie Alvin, and Julia Westwater, who from day one treated me more as a friend than a student), Peter Lemmond, Dolores Chausse, and Lori Dolby (without whose assistance I would probably still be in graduate school), Roy Smith, Pam Foster, Janet Johnson, and Anita Palm (who have made my life easier in innumerable ways), and the incomparable librarians, Colleen Hurter, and Alora Paul. These are all first-rate people who make WHOI a great work environment.

I came to graduate school for an education, and I'm leaving having made some of the best friends a person can wish for in life. Each of the following have not only supported me through the trials and tribulations of graduate school, but have enriched my life in untold ways: Gorka Sancho, Chris Weidman, Javier Escartín, Joe Lacasce, Cecile Mauritzen, Dan Lizarralde, Deana Erdner, Emilie Hooft, Christopher Bradlee, Melissa Weidman, Rafi Katzman, Helen Webb, Garrett Ito, Cecily Wolfe, Hega Lizarralde, David Mann, Amy Donner, Gaspar Taroncher, Ee Lin Lim and Sheri White. With each name I smile.

Special warm-hearted thanks go to Bob Krasner and Debra Trebitz, whose countless phone calls, visits, care packages, photos and musical treats have carried me through more than one trying chapter in my life.

I also wish to acknowledge and remember my sweet Meaghan. For she gave me happiness every day of the tough first years of my graduate career.

To Nancy, who put sparkle in the last year and a half of my life, I say simply, "Shut the door."

My life force is my family. Their support and generosity have given me the strength to endure the wild ride of a major career and lifestyle change. The few accomplishments I have achieved during my lifetime, including this thesis, is a projection of their love and confidence in me. I can honestly say that I couldn't have done it without them...especially my parents. I dedicate this thesis to my mother and father.

TABLE OF CONTENTS

ABSTRACT	2
ACKNOWLEDGEMENTS	5
Chapter 1	
INTRODUCTION	11
References	15
Chapter 2	
DISTRIBUTION OF SEDIMENTS ON 0 - 29 MA CRUST, 25°25' - 27°10'N, WESTERN NORTH ATLANTIC OCEAN	
Introduction	18
Methods	20
Sediment distribution with respect to topography	21
Sediment accumulation over time	23
Effects on basement morphology studies	24
Summary	25
References	28
Table	30
Figure Captions	31
Figures	33
Chapter 3	
TECTONIC EXTENSION AT A SLOW-SPREADING MID-OCEAN RIDGE IN SPACE AND TIME: A QUANTITATIVE FAULT STUDY ON THE MID-ATLANTIC RIDGE BETWEEN 25°30' AND 27°10'N	
Introduction	43
Tectonic setting	47
Data and methods	48
<i>Limitations</i>	52

Regional fault patterns	53
<i>Orientation and geometry of faults</i>	53
<i>Inward- versus outward-facing faults</i>	54
<i>Fault parameters</i>	55
<i>Regional strain estimates</i>	56
Spatial variations in faulting patterns	57
<i>Correlation with residual mantle Bouguer anomaly</i>	57
<i>Correlation with intrasegment position</i>	58
Temporal record of faulting	59
Discussion	61
<i>Effects of scarp degradation and sedimentation</i>	
<i>on fault parameters</i>	61
<i>Intrasegment variations in faulting</i>	62
<i>Intersegment comparison</i>	63
<i>Faulting in the rift valley</i>	64
<i>Ridge-flank faults</i>	64
Conclusions	70
References	73
Tables	80
Figure Captions	85
Figures	89

Chapter 4 RECORD OF SEAMOUNT PRODUCTION AND OFF-AXIS EVOLUTION IN THE WESTERN NORTH ATLANTIC OCEAN, 25°25' - 27°10'N

Introduction	108
Geological Background	109

Study area	112
Data and methods	113
Seamount population comparisons	116
<i>Axial versus off-axis seamount populations</i>	117
<i>Temporal variations in seamount population</i>	118
<i>Intersegment variations in seamount population</i>	120
<i>Seamount population variations correlated with gravity signature</i>	121
<i>Intrasegment variations in seamount population</i>	123
Discussion	124
<i>Modification of seamounts during transport off-axis</i>	125
<i>Seamount populations in relation to ridge segmentation</i>	130
Summary	132
References	135
Tables	139
Figure Captions	143
Figures	146

Chapter 5

ABYSSAL PERIDOTITE MYLONITES: IMPLICATIONS FOR GRAIN-SIZE SENSITIVE FLOW AND STRAIN LOCALIZATION IN THE OCEANIC LITHOSPHERE

	161
Abstract	162
Introduction	162
Geologic setting	163
Sample selection	165
Analytical techniques	165
Primary mineralogy and high-temperature alteration	167

Microstructure	168
Geothermometry	172
<i>Equilibrium temperatures</i>	174
Discussion	176
<i>Effects of grain-size reduction on strain localization in peridotite mylonites</i>	176
<i>Interpretation of geothermometry</i>	177
Implications for tectonics of slow-spreading mid-ocean ridges	178
Conclusions	179
References	179
 Chapter 6 CONCLUSIONS	 183
APPENDIX	187

Chapter 1

INTRODUCTION

Ocean crust is generated at diverging plate boundaries through an interplay of magmatic construction and tectonic extension. A major focus of this Thesis is the spatial and temporal variation in oceanic crustal structure resulting from changes in the balance between these processes. Spreading rate fundamentally controls magmatism and lithospheric strain at mid-ocean spreading centers. At fast (90 - 180 mm/yr full rate) spreading centers the ridge crest is characterized by an axial high (200 - 400 m) underlain by magma chambers that may be continuous for tens of kilometers (e.g., Detrick, 1987; Burnett et al., 1989; Toomey et al., 1990). Crust produced at fast-spreading centers has relatively smooth topography. In comparison, slow (10 - 50 mm/yr full rate) spreading centers, such as the Mid-Atlantic Ridge (MAR), have a 1.5 - 3.0 km deep rift valley. To date, the only geophysical evidence to indicate that crustal magma chambers or bodies exist at slow-spreading ridges is at a magmatically active segment of the Reykjanes Ridge (Constable et al., 1996), but results of seismic studies so far preclude the existence of any steady-state magma chambers (Toomey et al., 1985; Huang et al., 1986; Huang and Solomon, 1988). The topography of slow-spreading ridges is characterized by rough, faulted terrain. These observations suggest that magmatism plays the dominant role in crustal formation and morphology at fast-spreading ridges, whereas at slow-spreading ridges these are controlled in large part by mechanical extension.

Recent studies of axial morphology at both fast- and slow-spreading ridges have shown that all mid-ocean ridges are segmented (Schouten et al., 1985). Mid-ocean ridges are segmented at scales of 20 to 100 km by both large transform offsets (> 30 km or 2 m.y. offset) and smaller non-transform discontinuities (Macdonald et al., 1988). Fundamental

structural and lithological changes occur along the length of individual segments (e.g., Rona et al., 1976; Macdonald and Luyendyk, 1977; Kuo and Forsyth, 1988; Sempéré et al., 1990; Carbotte et al., 1991; Grindlay et al., 1991; Blackman and Forsyth, 1991). Based on along-axis data, it has been hypothesized that segmentation is controlled by the dynamics of mantle upwelling, by melt distribution, and by mechanical extension (e.g., Whitehead et al., 1984; Lin et al., 1990; Macdonald et al., 1991; Mutter and Karson, 1992).

Resolution of the temporal and spatial interplay of volcanism and tectonism requires knowledge of off-axis crustal structure. Information on time-varying characteristics of crustal structure at slow-spreading ridges has in large part been limited to investigations along major fracture zones (e.g., Pockalny et al., 1988; Tucholke and Schouten, 1988; Dick et al., 1991). However, recent off-axis investigations have provided new perspectives and constraints on the spatial and temporal evolution of ridge segmentation. French American Ridge Atlantic (FARA) research programs in the MARK area south of the Kane Fracture Zone (SEADMA I survey; Gente et al., 1995) and at 28°-29°N (SARA survey; Sloan and Patriat, 1992) have acquired across-axis data out to 10 Ma crust, and Tucholke et al. (1992) recently acquired geological and geophysical data on 0 - 29 Ma crust over the west flank of the MAR at 25°25'N - 27°10'N. A fundamental observation of these off-axis studies is that ridge segments bounded by non-transform discontinuities have consistent internal geological and geophysical structure, and they exhibit intra- and inter-segment variations that appear to relate to melt supply (Tucholke et al., *in press*).

The objective of this Thesis was to interpret the structural development of slow-spreading ridge segments by: 1) delineating the nature, magnitude, and relative importance of primary tectonic and volcanic processes that control crustal morphology, 2) investigating the spatial and temporal variability of these processes, and 3) examining how rheological variations in the lithosphere constrain its structural configuration. To that end, this Thesis

provides detailed documentation of faults and volcanoes (seamounts) on the Mid-Atlantic Ridge at 25°25' to 27°10'N and from the ridge axis to 29 Ma crust, and it analyzes the evolution of these features from their formation in the rift valley to their degradation by aging processes on the ridge flank. In addition, deformation conditions in the lithosphere are examined from study of naturally deformed mantle rocks recovered from fault zones at slow-spreading ridges.

Accumulation of sediments strongly affects the seafloor morphological expression of ocean crustal structure. Therefore, to study the morphological record of crustal accretion and tectonism, it is necessary to know the sediment distribution in the area studied. Sediment thicknesses were mapped over the west flank of the Mid-Atlantic Ridge at 25°25' - 27°10'N (Chapter 2) to document the distribution of sediments, and these data allow us to better analyze seafloor morphology and interpret basement structure in subsequent chapters.

In Chapter 3, a method is developed to identify faults in multibeam bathymetry, and the distribution of brittle strain is quantitatively assessed and related to ridge segmentation. Previous studies have examined the character of faulting from the inner-floor of the rift valley to the crest of the rift mountains (e.g., Macdonald and Luyendyk, 1977; Searle and Laughton, 1977; Shaw, 1992); Chapter 3 quantitatively examines the spatial and temporal record of brittle strain taken up by faults not only within the rift valley but also on the ridge flank. It is the aim of Chapter 3 to further our understanding of the role of normal faulting in the formation and segmentation of ridge topography.

Seamount volcanism plays a large role in crustal construction at the slow-spreading MAR. Hundreds (> 450) of seamounts have recently been identified on the inner-valley floor of the MAR rift valley between 24° - 30°N alone (Smith and Cann, 1990; 1992). Chapter 4 documents the existence of abundant seamounts on the flank of the MAR and provides evidence for their construction within the rift valley. The effects of normal

faulting documented in Chapter 3 are used to explain significant changes in seamount population abundance, size distribution, and shape that occur as seamounts are transported from the inner-valley floor to the crest of the rift mountains and onto the ridge flank. In addition, intra- and inter-segment variations in seamount populations are examined and related to segmentation patterns.

Brittle extension taken up by normal faults (Chapter 3) is controlled in part by the rheology of the oceanic lithosphere (e.g., Chen and Morgan, 1990; Shaw, 1992). Current mechanical models of lithosphere deformation at mid-ocean ridges are based on experimental and geophysical observations and assumptions that do not necessarily reflect realistic geological conditions. Chapter 5 provides constraints on the rheology of the oceanic lithosphere from analysis of abyssal peridotite mylonites formed at slow-spreading ridges. Textures, geothermometry, and metamorphic assemblages of these rocks are examined to better understand the mechanisms of deformation that were active during their emplacement in the seafloor.

The research presented in Chapters 2 and 3 were done in collaboration with Brian E. Tucholke, and that of Chapter 4 was conducted with both Deborah K. Smith and Brian E. Tucholke. These chapters have not yet been published. Chapter 5 was published with co-authors Greg Hirth and Henry J. B. Dick in a 1996 special issue of *Tectonophysics* dedicated to Neville Carter.

References

- Blackman, D. K., and D. W. Forsyth, Isostatic compensation of tectonic features of the Mid-Atlantic Ridge: 25°-27°30'S, *J. Geophys. Res.*, 96, 11741-11758, 1991.
- Burnett, M. S., D. W. Caress, and J. A. Orcutt, Tomographic image of the magma chamber at 12°50'N on the East Pacific Rise, *Nature*, 339, 206-208, 1989.
- Carbotte, S. M., S. M. Welch, and K. C. Macdonald, Spreading rates, rift propagation, and fracture zone offset histories during the past 5 my on the Mid-Atlantic Ridge; 25°-27°30'S and 31°-34°30'S, *Mar. Geophys. Res.*, 13, 51-80, 1991.
- Chen, Y., and W. J. Morgan, A nonlinear rheology model for mid-ocean ridge axis topography, *J. Geophys. Res.*, 95, 17583-17604, 1990.
- Constable, S., L. MacGregor, C. Peirce, D. Navin, M. Inglis, G. Heinson, and A. White, Multi-component geophysical survey finds a slow-spreading ridge magma chamber, *EOS, Trans. Am. Geophys. Union*, 77, 700, 1996.
- Detrick, R. S., P. Buhl, E. Vera, J. Mutter, J. Orcutt, J. Madsen, and T. Brocher, Multichannel seismic imaging of a crustal magma chamber along the East Pacific Rise, *Nature*, 326, 35-41, 1987.
- Dick, H. J. B., H. Schouten, P. S. Meyer, D. G. Gallo, H. Bergh, R. Tyce, P. Patriat, K. T. M. Johnson, J. Snow, and A. Fischer, Tectonic evolution of the Atlantis II Fracture Zone, in *Proceedings of the Ocean Drilling Program, Scientific Results, 118*, edited by R. P. Von Herzen, P. T. Robinson, et al., 359-358, U.S. Government Printing Office, Washington, D.C., 1991.
- Gente, P., R. A. Pockalny, C. Durand, C. Deplus, M. Maia, G. Ceuleneer, C. Mével, M. Cannat, and C. Laverne, Characteristics and evolution of the segmentation of the Mid-Atlantic ridge between 20°N and 24°N during the last 10 Myr., *Earth Planet. Sci. Lett.*, 129, 55-71, 1995.
- Grindlay, N. R., P. J. Fox, and K. C. Macdonald, Second-order ridge axis discontinuities in the South Atlantic: Morphology, structure, evolution, and significance, *Mar. Geophys. Res.*, 13, 21-49, 1991.
- Huang, P. Y., and S. C. Solomon, Centroid depths of mid-ocean ridge earthquakes: Dependence on spreading rate, *J. Geophys. Res.*, 93, 13,445-13,477, 1988.
- Huang, P. Y., S. C. Solomon, E. A. Bergman, and J. L. Nabelek, Focal depths and mechanisms of Mid-Atlantic Ridge earthquakes from body waveform inversion, *J. Geophys. Res.*, 91, 579-598, 1986.

- Kuo, B. Y., and D. W. Forsyth, Gravity anomalies of the ridge-transform system in the South Atlantic between 31° and 34.5°S: Upwelling centers and variations in crustal thickness, *Mar. Geophys. Res.*, 10, 205-232, 1988.
- Lin, J., G. M. Purdy, H. Schouten, J.-C. Sempéré and C. Zervas, Evidence from gravity data for focused magmatic accretion along the Mid-Atlantic Ridge, *Nature*, 344, 627-632, 1990.
- Macdonald, K. C., P. J. Fox, L. J. Perram, M. F. Eisen, R. M. Haymon, S. P. Miller, S.M. Carbotte, M.-H. Cormier, and A.N. Shor, A new view of the mid-ocean ridge from the behavior of ridge-axis discontinuities, *Nature*, 335, 217-225, 1988.
- Macdonald, K. C., and B. P. Luyendyk, Deep-tow studies of the structure of the Mid-Atlantic Ridge crest near lat 37°N, *Geol. Soc. Am. Bull.*, 88, 621-636, 1977.
- Macdonald, K. C., D. S. Scheirer, and S. M. Carbotte, Mid-ocean ridges: discontinuities, segments and giant cracks, *Science*, 253, 986-994, 1991.
- Mutter, J. C., and J. A. Karson, Structural processes at slow-spreading ridges, *Science*, 257, 627-634, 1992.
- Pockalny, R. A., R. S. Detrick, P. J. Fox, Morphology and tectonics of the Kane Transform from Sea Beam bathymetry data, *J. Geophys. Res.*, 93, 3179-3193, 1988.
- Rona, P. A., R. N. Harbison, B. G. Bassinger, R. B. Scott, and A. J. Nalwalk, Tectonic fabric and hydrothermal activity of Mid-Atlantic Ridge Crest (Lat. 26°N), *Geol. Soc. Am. Bull.*, 87, 661-674, 1976.
- Schouten, H., K. D. Klitgord, and J. A. Whitehead, Segmentation of mid-ocean ridges, *Nature*, 317, 225-229, 1985.
- Searle, R. C., and A. S. Laughton, Sonar studies of the Mid-Atlantic Ridge and Kurchatov Fracture Zone, *J. Geophys. Res.*, 82, 5313-5328, 1977.
- Sempéré, J.-C., G. M. Purdy, and H. Schouten, Segmentation of the Mid-Atlantic Ridge between 24°N and 30°40'N, *Nature*, 344, 427-431, 1990.
- Shaw, P., Ridge segmentation, faulting and crustal thickness in the Atlantic Ocean, *Nature*, 358, 490-493, 1992.
- Sloan, H., and P. Patriat, Kinematics of the North American - African plate boundary between 28° and 29°N during the last 10 Ma: Evolution of the axial geometry and spreading rate and direction, *Earth Planet. Sci. Lett.*, 113, 323-341, 1992.
- Smith, D. K., and J. R. Cann, Hundreds of small volcanoes on the median valley floor of the Mid-Atlantic Ridge at 24-30°N, *Nature*, 344, 427-431, 1990.

- Smith, D. K., and J. R. Cann, The role of seamount volcanism in crustal construction at the Mid-Atlantic Ridge (24°-30°N), *J. Geophys. Res.*, 97, 1645-1658, 1992.
- Toomey, D. R., G. M. Purdy, S. C. Solomon, and W. S. D. Wilcock, The three-dimensional seismic velocity structure of the East Pacific Rise near latitude 9°30' N, *Nature*, 347, 639-645, 1990.
- Toomey, D. R., S. C. Solomon, G. M. Purdy, and M. H. Murray, Microearthquakes beneath the median valley of the Mid-Atlantic Ridge near 23°N: Hypocenters and focal mechanisms, *J. Geophys. Res.*, 90, 5443-5458, 1985.
- Tucholke, B. E., J. Lin, and M. C. Kleinrock, Crustal structure of spreading segments on the western flank of the Mid-Atlantic ridge at 25°25'N to 27°10'N, *EOS, Trans. Am. Geophys. Union*, 73, 537-538, 1992.
- Tucholke, B. E., J. Lin, M. C. Kleinrock, M. A. Tivey, T. B. Reed, J. Goff, and G.E. Jaroslow, Segmentation and crustal structure of the western Mid-Atlantic Ridge flank, 25°25' - 27°10'N and 0 - 29 m.y., *J. Geophys. Res.* (in press).
- Tucholke, B. E., and H. Schouten, Kane Fracture Zone, *Mar. Geophys. Res.*, 10, 1-39, 1988.
- Whitehead, J. A., H. J. B. Dick, and H. Schouten, A mechanism for magmatic accretion under spreading centers, *Nature*, 312, 146-148, 1984.

Chapter 2

DISTRIBUTION OF SEDIMENTS ON 0 - 29 MA CRUST, 25°25' - 27°10'N, WESTERN NORTH ATLANTIC OCEAN

Introduction

Study of sediment distribution over mid-ocean ridges is important for understanding sedimentation processes on relatively new oceanic crust and to provide sediment-thickness information for morphological analysis of mid-ocean-ridge basement structure. In this study, sediment distribution patterns on the western flank of the Mid-Atlantic Ridge (MAR) are examined for relationships between sediment accumulation and crustal aging. The objective of this study is to define where sediment accumulations may completely or partially mask basement structure (e.g., faults and seamounts) important in the evolution of the MAR.

Past studies of sediment accumulation on the northern MAR were based on widely spaced data and provided good general descriptions of both regional sedimentation and, in some areas, local patterns (e.g., van Andel and Komar, 1969; van Andel and Bowin, 1968; Ewing et al., 1973; Tucholke et al., 1982). Tucholke et al. (1982) showed that average sediment thickness over the rift valley and ridge flank of the MAR in the central North Atlantic is thin (averaging less than 100 m) owing to youth of the crust, isolation from terrigenous sediment sources, and position beneath the unproductive, mid-gyre surface waters of the central Sargasso Sea. Sediment accumulation in the MAR rift valley and on the upper western MAR flank was found by van Andel and Komar (1969) to be patchy, with sediments tending to accumulate as ponds in closed basement depressions. Ewing et al. (1964) also noted that away from the ridge axis a thin but fairly continuous blanket of pelagic sediments covers topographic highs along the ridge flank, with thicker deposits

occurring in most of the intervening valleys. It also has been suggested that average sediment thickness increases roughly monotonically with distance from the ridge axis due to relatively constant accumulation rate on the aging crust (Ewing and Ewing, 1967; Ewing et al., 1973).

Recent collection of seismic-reflection profiles, multibeam bathymetry, and sidescan-sonar images of the Mid-Atlantic Ridge rift valley and western ridge flank between 25°25' and 27°10'N (Figure 1) provides a high-density dataset which allows us to map sediment distribution in detail. The present study provides the first detailed mapping (scale 1:200,000) of sediment distribution on young (0 - 29 Ma) ocean crust of the Mid-Atlantic Ridge. The analysis extends ~400 km from the ridge axis to 29 Ma crust on the ridge flank. We describe the distribution of sediments in relation to the morphology of the crust, and we examine how long-term temporal variations in sediment accumulation are related to crustal age and to paleoceanographic conditions. Finally, we assess the effects of sediment cover on quantitative characterization of faults and seamounts, as described in Chapters 3 and 4.

The rift valley and ridge flank of the MAR are characterized by rugged topography with relief of a few hundred to a few thousand meters (Chapter 3, Figure 2). An outstanding topographic feature of the ridge flank is regular, isochron-parallel, ridge-and-valley terrain formed by long, narrow abyssal hills and intervening valleys. The abyssal hills range in height from 125 - 450 m with characteristic widths of 3 - 17 km (Goff et al., 1995) and lengths often reaching nearly the full along-isochron length of spreading segments (~30 - 100 km). Valley floors between abyssal hills are typically wide (2-10 km) with little relief because of sediment cover.

Abyssal hills are interrupted along isochrons by deep fracture valleys, which are the fossil traces of non-transform, ridge-axis discontinuities that offset the ridge axis and separate spreading segments (Tucholke et al., *in press*). These valleys have deep,

intermittent basins and are variable in orientation, although their trends generally crosscut the ridge-parallel abyssal hill topography. The valleys typically are ~400 - 500 m deeper than the isochron-parallel valleys between abyssal hills.

Methods

Sediment thickness was mapped from a combination of seismic-profiler data, multibeam bathymetry, and sidescan-sonar imagery. The primary seismic (watergun) data were obtained during Ewing Cruise 9208 (Figure 2, Table 1). These data were supplemented by other, earlier Lamont-Doherty Earth Observatory seismic profiles (airgun), and by a single near-bottom profile obtained by the Naval Research Laboratory (NRL) across a large sediment pond located at 26°10'N, 46°15'W. Picks of sediment thickness in reflection time were made 2 minutes (~0.5 km) apart along ship tracks, and the spacing between ship track lines was 4 to 9 km. In order to contour sediment thickness, trends were interpolated between track lines from structure observed in Hydrosweep multibeam bathymetric maps. We used the Hydrosweep bathymetry of Tucholke et al. (*in press*), which has ~90 -100% regional coverage (Chapter 3, Figure 2).

We also used HMR1 long-range sidescan-sonar data (20-km swath) to map areas of high backscatter that we infer to represent thinly sedimented crust. Many of these areas probably are sediment-free. Video and still-camera imagery were obtained during Jason Remotely Operated Vehicle (ROV) dives (Tucholke et al., 1993) on two off-axis scarps that coincide with areas of high backscatter in side-scan sonar data (~26°34'N, 48°05'W, and ~26°08'N, 46°12'W); these images confirm that the scarps mostly are devoid of sediments. In general, thin sediment cover may be largely transparent to the 11/12 kHz signal of the HMR1 sidescan sonar (de Moustier and Matsumoto, 1993); thus, strong backscatter probably also originates from basement that has sediment cover of less than a few meters.

We interpret all high-backscatter areas to have less than 10 m of sediment cover, although actual thicknesses may be a few meters or less.

Conversion of picked reflection times to sediment thickness in meters was made based on compressional-wave velocity (V_p) data derived from an NRL Deep Towed Acoustic-Geophysics System (DTAGS) experiment located over a large sediment pond at 26°10'N, 46°15'W (J. Gettrust, written communication 1995). Figure 3 shows a plot of V_p versus depth. We constructed a best-fit polynomial and integrated over travel time to derive the relationship $H = 1520 t (1.038 t^{1/2} + 1)$, where H = sediment thickness in meters, and t = one-way travel time from seafloor to basement in seconds. The curve of V_p versus depth was constrained to a seafloor intercept of 1520 m/s, which is the mean V_p of the upper ~10 m of sediment; this value is nearly the same as local bottom-water velocity, and it is within 10 - 20 m/s of velocities typically measured in surficial sediments cored from the western North Atlantic (e.g., Tucholke and Shirley, 1979). Sound velocity increases rapidly with depth below seafloor to about 0.02 sec, then levels off to a lower gradient.

The sediment-thickness maps are shown in Figure 4 (cover pocket). They are contoured at 50-m intervals; black area have thicknesses approximately ≤ 10 m and correspond to areas of high backscatter in HMR1 sidescan-sonar data.

Sediment Distribution with Respect to Topography

The most striking features of the sediment distribution are that sediments are ponded in topographic depressions, and that there is no detectable blanket of continuous pelagic sediment (Figure 4). High HMR1 backscatter and 3.5-kHz profiles show that crust on the inner rift-valley floor (from zero-age crust of the neovolcanic zone to the first major valley-bounding faults at ~0.5 - 0.7 Ma) has no detectable sediment cover, i.e., total sediment accumulation does not exceed a few meters. On the upper rift-valley walls and on

the ridge flank, nearly all structural lows have ponded sediments. Intervening structural highs such as abyssal hills and fault scarps have <10 m of sediment cover, and bare-rock outcrops appear to be common even on crust as old as 29 m.y.

The thickest sediments occur in ponds within the ridge-parallel valleys between abyssal hills and particularly within the fracture valleys of non-transform discontinuities in the ridge flank. The ponded sediments in the ridge-parallel valleys are (exceptionally) up to 600 m thick, but they more typically range from ~50 m to 350 m thick. The ponds are very elongate, with widths < 1 km to ~6 km and lengths up to 42 km. Where abyssal hills are discontinuous along strike, sediment ponds may spread across isochrons to widths several times those found in individual, isolated valleys. Pond surfaces in the ridge-parallel valleys generally deepen gradually toward discontinuities, so the valley floors serve as passageways for sediment transport towards segment ends. The cross-isochron valleys of non-transform discontinuities contain the thickest sediments, typically up to 500 m and locally up to 800 m. The ponds vary greatly in plan shape but usually are ~15 km to 65 km long (across isochrons) and ~15 km wide (along isochrons).

The shallow MAR is inaccessible to terrigenous sediment sources (Tucholke et al., 1982), and pelagic rain provides the only significant sediment supply. Sediments cored from the rift valley or ridge flank of the MAR typically contain foraminiferal-nannofossil ooze and calcareous clays (van Andel and Komar, 1969; Melson et al., 1979). This pelagic rain should form uniform drape, but thin sediments on bathymetric highs show that the pelagic sediment is removed and redeposited in the valleys. Redeposition probably occurs by the action of continuous slope creep and small-scale "flow," slides and debris flows, turbidity currents, and bottom currents. All these processes act to redistribute sediments from topographic highs to lows. There is evidence that all four processes are operative. 1) Small-scale movement: As shown in Figure 5, photographs taken along Jason transects in the study area show that small sediment cascades commonly fill slope irregularities and

create sediment-filled pockets and terraces in steep basement slopes above the level of deeper ponds. These small pockets indicate that nearly continuous small-scale sediment movement redistributes unstable deposits downslope. 2) Slides and debris flows: Disturbed stratal sequences and chaotic seismic facies with weak reflections are diagnostic of sediments emplaced by slides or debris flows (e.g., Mitchum et al., 1977). An example of such facies is evident in the DTAGS seismic profile across the large sediment pond at 26°10'N, 46°10'W (Figure 6). 3) Turbidity currents: van Andel and Komar (1969) examined piston cores from sediment ponds on the MAR flank between 22° and 23°N and found them all to have laminated, fining-upward turbidite beds. Turbidites also were cored at DSDP Site 395, located in an ~300 m thick sediment pond in the same area (Melson et al., 1979). Flat-lying, well laminated sediments that were deposited by turbidity currents are observed in seismic profiles of most large ponds on the ridge flank (e.g., Figure 6). 4) Current-controlled deposition: Bedload sediment transport by bottom currents is indicated by ripple marks on the surface of some ponds (Figure 7). Also, visual observation using ROV Jason on ~24 Ma crust shows that level crests of ridges have sediment cover only in local basement depressions (Tucholke et al., 1993), indicating that currents sweep sediment from exposed basement elevations to protected, lower-energy locations. Finally, although most sediment ponds are relatively flat and seismically well laminated (i.e., typical of turbidite deposits, Figure 6), many smaller ponds (< 150 m sediment thickness) are "tilted" or have irregular surfaces (Figure 8). Tilted ponds could indicate deposition from the slopes on only one side of a pond, or it could represent asymmetric deposition from bottom currents.

Sediment Accumulation over Time

To examine changes in total sediment accumulation versus crustal age, sediment thicknesses (Figure 4) were picked along a series of regularly spaced cross-isochron lines

subparallel to flow lines (Figure 9). The large sediment ponds along non-transform discontinuities were not included because they clearly include turbidites transported over long distances from large areas of surrounding crust. Picks were spaced at 0.5 km and were averaged in 1-m.y. age bins. Crustal ages were determined from magnetic anomaly identifications (Tucholke et al., *in press*).

Total average sediment accumulation versus age is plotted in the bar chart of Figure 10. A relatively steady increase in sediment accumulation with increasing crustal age up to ~17 Ma crust is observed. Farther off-axis, average sediment accumulation slowly decreases to 20 - 25 m at the western edge of the survey (~29 Ma crust). We expect sediment accumulation to increase uniformly with distance from the ridge axis if pelagic sediments accumulate at a constant rate on ocean crust that is also spreading at a relatively constant rate (Ewing and Ewing, 1967; Ewing et al., 1973). The apparently contradictory observation that older seafloor has less sediment probably can be best explained by changes in paleoceanographic conditions during the early Miocene. If, prior to the early Miocene, the MAR crest was below a relatively shallow calcite compensation depth (CCD), it would have accumulated only a thin veneer of slowly deposited pelagic clays. A depression of the CCD to a depth below the MAR rift mountains (~2700 m) at about 17 Ma would have caused thick, carbonate-rich sediments to be deposited on younger crust. This is consistent with available data; a marked depression of the CCD to ridge-flank depths about this time is documented from DSDP borehole data (Tucholke and Vogt, 1979), but borehole control on specific depths of the CCD currently is inadequate to determine detailed effects on sediment thickness patterns.

Effects on Basement Morphology Studies

Because only thin, patchily distributed sediments occur in the rift valley and on the crest of the rift mountains and western flank of the northern MAR, it is possible to study

the structure of ocean crust based largely on seafloor morphology. Sediment cover throughout the region is < 50 m, except in the scattered sediment ponds marked by closed contours in Figure 4. Young crust in the rift valley has little ($< 2 - 3$ meters) or no sediment cover. High-standing features such as ridges and seamounts, and steep-sloped basement structures such as fault scarps, are largely kept free of sediment by gravity-driven sediment redistribution and by the activity of bottom currents.

Sediment accumulation on the ocean crust can affect fault analyses in two ways (Chapter 3): 1) buildup of sediment at the base of fault scarps can reduce fault throws measured from multibeam bathymetric data, and 2) burial of low-amplitude fault scarps can reduce regional fault density. Both of these effects act to reduce estimates of regional strain derived from these fault parameters.

Sediment accumulation has similar effects on seamount analyses. Burial of seamounts reduces the number of seamounts detected in bathymetry and therefore reduces seamount population density. It does not, however, reduce the distribution of seamount heights as modeled by characteristic height (Chapter 4).

Based on the results of this study, the strongest regional effects of sediment cover on fault and seamount analyses will be off-axis, along fracture valleys of non-transform discontinuities and in ridge-parallel abyssal hill valleys. Young crust within the MAR rift valley and at the crest of the rift mountains will not be affected significantly. Specific effects of sedimentation on fault and seamount analyses are given in Chapters 3 and 4.

Summary

Sediments in the rift valley and on the western flank of the northern Mid-Atlantic Ridge are regionally thin and patchily distributed in local, thick ponds. The thickest ponds are within crustal depressions along non-transform discontinuities in the ridge flank (up to 800 m thick) and in valleys between abyssal hills (up to 100's m thick). The ridge-parallel

valleys between abyssal hills serve as passageways for sediment transport towards the large ponds along discontinuities, but they also accumulate sediments with typical thicknesses of ~50 - 350 m (exceptionally ~600 m). Abyssal hills between ponds rarely have sediment cover >10 m thick. Sediments were initially deposited as a pelagic drape, but they subsequently were redistributed downslope by small-scale flows, mass wasting, and bottom currents to form isolated or interconnected ponds.

Sediment thickness averaged along crustal isochrons shows a trend of increasing sediment cover with increasing crustal age up to ~17 Ma crust. Farther off-axis, average accumulation slowly decreases out to 29 Ma crust. This unusual observation is best explained by a depression of the CCD to a depth below the crest of the rift mountains (~2700 m) but above the deeper ridge flank (~4000 m) about 17 m.y. ago. For at least ~11 m.y. prior to this depression of the CCD, the Mid-Atlantic Ridge probably was below the CCD and thus accumulated only a thin veneer of slowly deposited pelagic clays. Younger crust (<17 Ma) is interpreted to have acquired more rapidly deposited carbonates, which thin with decreasing crustal age toward the ridge axis.

Acknowledgments

This study is a part of the ONR Acoustic Reverberation Special Research Program, and we thank M. Orr, M. Badiey, and J. Kravitz for their support in making the Mid-Atlantic Ridge field studies possible. We also thank the scientific and technical staffs, officers, and crew of R/V Ewing Cruise 92-08 for their assistance in data collection and processing. Additional thanks are extended to J. Gettrust for providing DTAGS compressional-wave velocities, to L. Dolby for compiling sediment-thickness data, to P. Lemmond for technical assistance, and to P. Oberlander and E. Souweijn for drafting the maps. Finally, we are indebted to T. Osychny for volunteer cartographic assistance. This

research was also supported by Office of Naval Research Grant N00014-90-J-1621.

G.E.J. was also supported by ONR AASERT Grant N00014-93-1-1153.

References

- de Moustier, C. and H. Matsumoto, Seafloor acoustic remote sensing with Multibeam echo-sounders and bathymetric sidescan sonar systems, *Mar. Geophys. Res.*, 15, 27-42, 1993.
- Ewing, M., J. Ewing, and M. Talwani, Sediment distribution in the oceans: the Mid-Atlantic Ridge, *Geol. Soc. Am. Bull.*, 75, 17-36, 1964.
- Ewing, J., and M. Ewing, Sediment distribution on the mid-ocean ridges with respect to spreading of the sea floor, *Science*, 156, 1590-1592, 1967.
- Ewing, M., G. Carpenter, C. Windisch, and J. Ewing, Sediment distribution in the oceans: The Atlantic, *Geol. Soc. Am. Bull.*, 84, 71-88, 1973.
- Goff, J. A., B. E. Tucholke, J. Lin, G. E. Jaroslow, and M. C. Kleinrock, Quantitative analysis of abyssal hills in the Atlantic Ocean: A correlation between inferred crustal thickness and extensional faulting, *J. Geophys. Res.*, 100, 22509-22522, 1995.
- Kalra, A. K., and J. A. Showalter, Acoustic mapping of subsurface structures within the sediment pond with towed vertical array for ARSRP reverberation studies, *EOS, Trans. Am. Geophys. Union*, 74, 1993.
- Melson, W. G., P. D. Rabinowitz, et al. *Initial Reports of the Deep Sea Drilling Project* 45, 717 pp., U. S. Government Printing Office, Washington, D.C., 1979.
- Mitchum, R. M., Jr., P. R. Vail, and J. B. Sangree, Seismic stratigraphy and global changes of sea level, Part 6: Stratigraphic interpretation of seismic reflection patterns in depositional sequences, in *Seismic Stratigraphy--Applications to Hydrocarbon Exploration*, edited by C. E. Payton, 117-133, Amer. Assoc. Petr. Geol., 1977.
- Smith, W. H. F., and D. T. Sandwell, Marine gravity field from declassified Geosat and ERS-1 altimetry, *EOS, Trans. Am. Geophys. Union*, 76, 1995.
- Tucholke, B. E., R. E. Houtz, and W. J. Ludwig, Sediment thickness and depth to basement in western North Atlantic basin, *Am. Assoc. Petrol. Geol. Bull.*, 66, 1384-1395, 1982.
- Tucholke, B. E., J. Lin, M. C. Kleinrock, M. A. Tivey, T. B. Reed, J. Goff, and G. E. Jaroslow, Segmentation and crustal structure of the western Mid-Atlantic Ridge flank, 25°25' - 27°10'N and 0 -29 m.y., *J. Geophys. Res.* (in press).
- Tucholke, B. E., and D. J. Shirley, Comparison of laboratory and in situ compressional-wave velocity measurements on sediment cores from the western North Atlantic, *J. Geophys. Res.*, 84, 687-695, 1979.

- Tucholke, B. E., and P. R. Vogt, Western North Atlantic: Sedimentary evolution and aspects of tectonic history, in *Initial Reports of the Deep Sea Drilling Project, 43*, edited by B. E. Tucholke and P. R. Vogt, U. S. Govt. Printing Office, Washington, D. C., 791-825, 1979.
- van Andel, T. H., and C. O. Bowin, Mid-Atlantic Ridge between 22° and 23° North latitude and the tectonics of mid-ocean rises, *J. Geophys. Res.*, 73, 1279-1298, 1968.
- van Andel, T. H., and P. D. Komar, Ponded sediments of the Mid-Atlantic Ridge between 22° and 23° North latitude, *Geol. Soc. Am. Bull.*, 80, 1163-1190, 1969.

Table 1: Sources of data

Institution	Data Records	Cruise #
Woods Hole Oceanographic Institution	MB, SCS (watergun), 3.5 kHz, SSS	EW9208
Lamont-Doherty Earth Observatory	SCS (airgun)	V2012, V2501, V2602, V2603, V2806, V3107
Naval Research Laboratory	DTAGS	KN138-15

MB=Multibeam bathymetry; SCS=Single-channel seismic profiles; 3.5-kHz profiles;
DTAGS=Deep Towed Acoustics-Geophysics System; SSS=Hawaii MR1 long-range sidescan sonar.

Figure Captions

- Figure 1. Location of study area (inset box outlined in white) over the rift valley and ridge flank of the MAR. Plate boundaries (thin lines) are indicated in lower-right map. Base map is satellite-derived free-air gravity anomaly (Smith and Sandwell, 1995), which shows intermediate-scale (10's km) MAR structure.
- Figure 2. Ship track lines in study area, locating single-channel seismic reflection and 3.5-kHz profiles used to map sediment distribution. R/V Ewing Cruise 9208 shown by solid lines; other cruises shown by dotted lines.
- Figure 3. Compressional-wave velocity determinations plotted against one-way travel time subbottom, derived from DTAGS data over a large sediment pond at $\sim 26^{\circ}10' \text{ N}$, $46^{\circ}10' \text{ W}$. Conversion equation represents best fit polynomial to the data (solid line) integrated over travel time, where H =sediment thickness in meters, t =one-way travel time in seconds.
- Figure 4. (Cover pocket) Maps of sediment thickness on the western flank of the Mid-Atlantic Ridge from the ridge axis to 29 Ma crust. Contour interval is 50 m. Black areas have high backscatter in HMR1 sidescan-sonar data and are interpreted to have sediment cover 0 - 10 m thick.
- Figure 5. Video image of sediment pockets filling depressions in manganese-coated pillow basalts on a ~ 24 Ma scarp, 3553 m below sea level, located at $26^{\circ}35.2' \text{ N}$, $48^{\circ}05.9' \text{ W}$. Field of view is $\sim 1.5 \times 2$ m. Site B, Jason Lowering 152, Image 20:16:53.18 (R/V Knorr Cruise 138, Leg 14).
- Figure 6. DTAGS seismic profile of sediment pond at $26^{\circ}10' \text{ N}$, $46^{\circ}10' \text{ W}$ showing well laminated turbidite fill. Beds created by sediment slides or debris flows (chaotic, weak-reflection patterns) are evident at about 90 - 130 m and 160 - 215 m subbottom. Profile from Kalra and Showalter (1993).

Figure 7. Video image of ripples in sediment pond on ~24 Ma crust 3643 m below sea level, located at 26°04.2' N, 45°15.3'W. Field of view is ~4 x 5 m. Site B, Jason Lowering 152, Image 20:25:10.14 (R/V Knorr Cruise 138, Leg 14).

Figure 8. 3.5-kHz echo-sounding profiles showing examples of small sediment ponds with tilted or uneven surfaces. Vertical scale is approximate sediment thickness in meters. All profiles from R/V Ewing Cruise 9208. a) Profile JD210, 1215Z at 25°58'N, 47°13'W. b) Profile JD211, 0930Z at 26°02'N, 47°12'W. c) Profile JD202, 0000Z at 25°25'N, 46°00'W. d) Profile JD210, 1330Z at 25°54'N, 47°25'W.

Figure 9. Map of study area showing locations of lines along which sediment thickness and crustal age were picked and binned (thin straight lines). Spreading-segment boundaries are indicated by heavy lines and the extent of Hydrosweep and HMR1 sidescan-sonar coverage is shown by dashes. Selected magnetic anomalies (thin curved lines) are identified, with corresponding crustal ages (Ma) in parentheses. The Central Anomaly Magnetic High (CAMH) is shown by a hachured pattern and records the approximate location of the axial neovolcanic zone in the MAR rift valley.

Figure 10. Bar graph of average sediment thickness vs. age over the MAR flank for the entire region mapped in Figure 4. Bin size = 1 m.y.

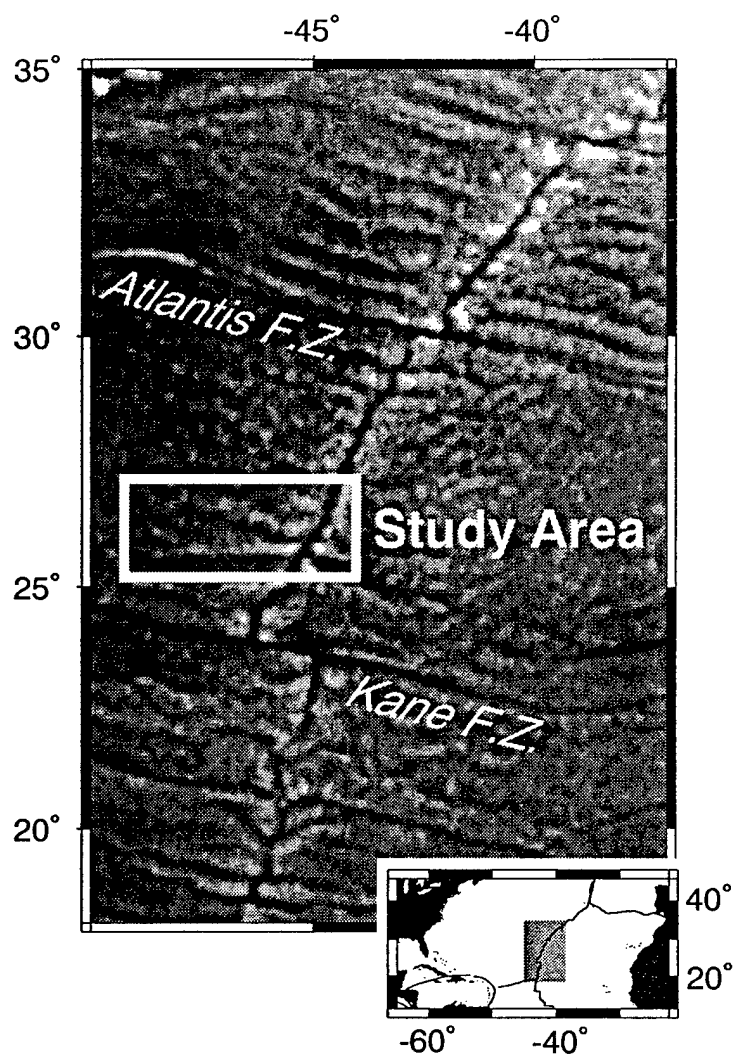


Figure 1

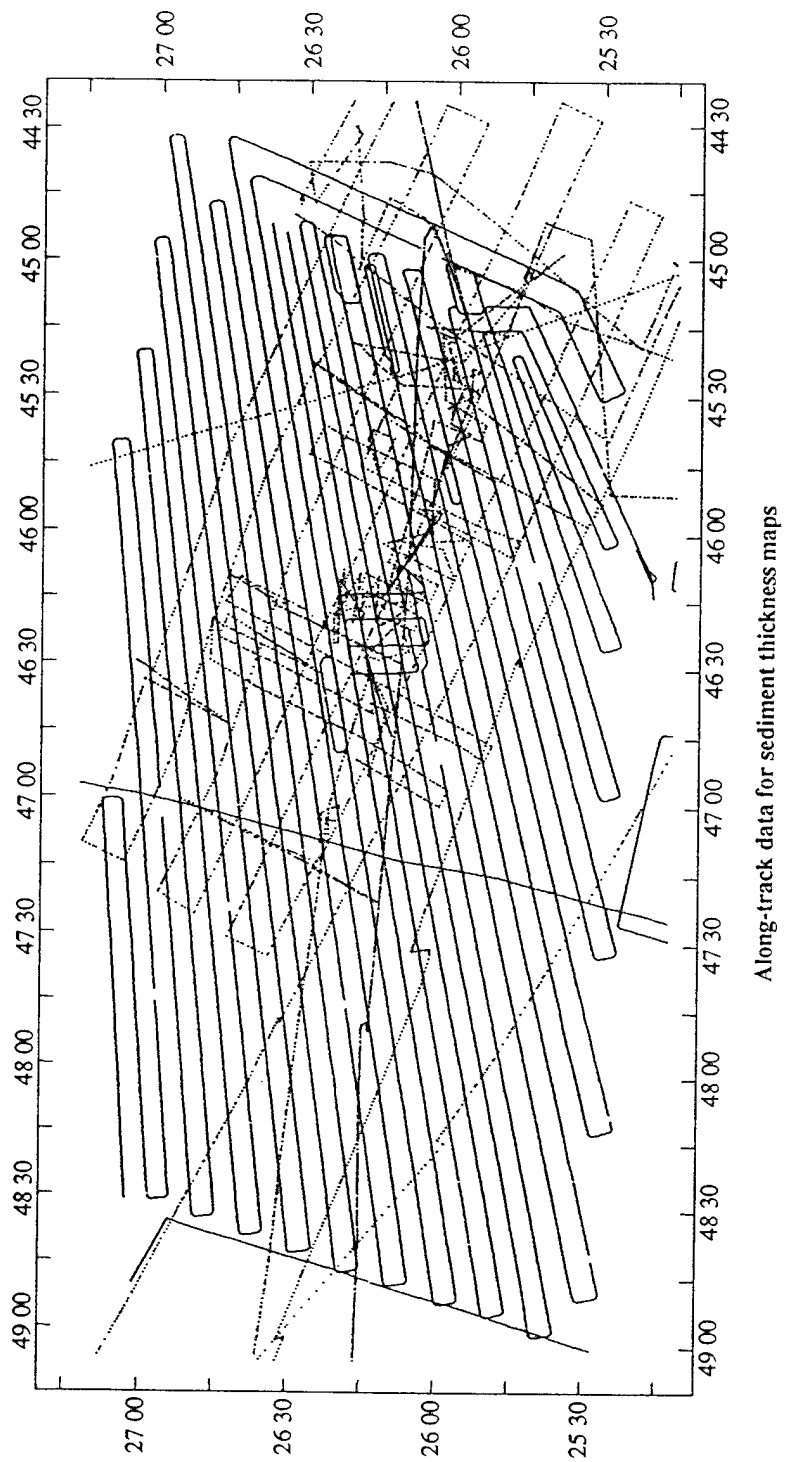


Figure 2

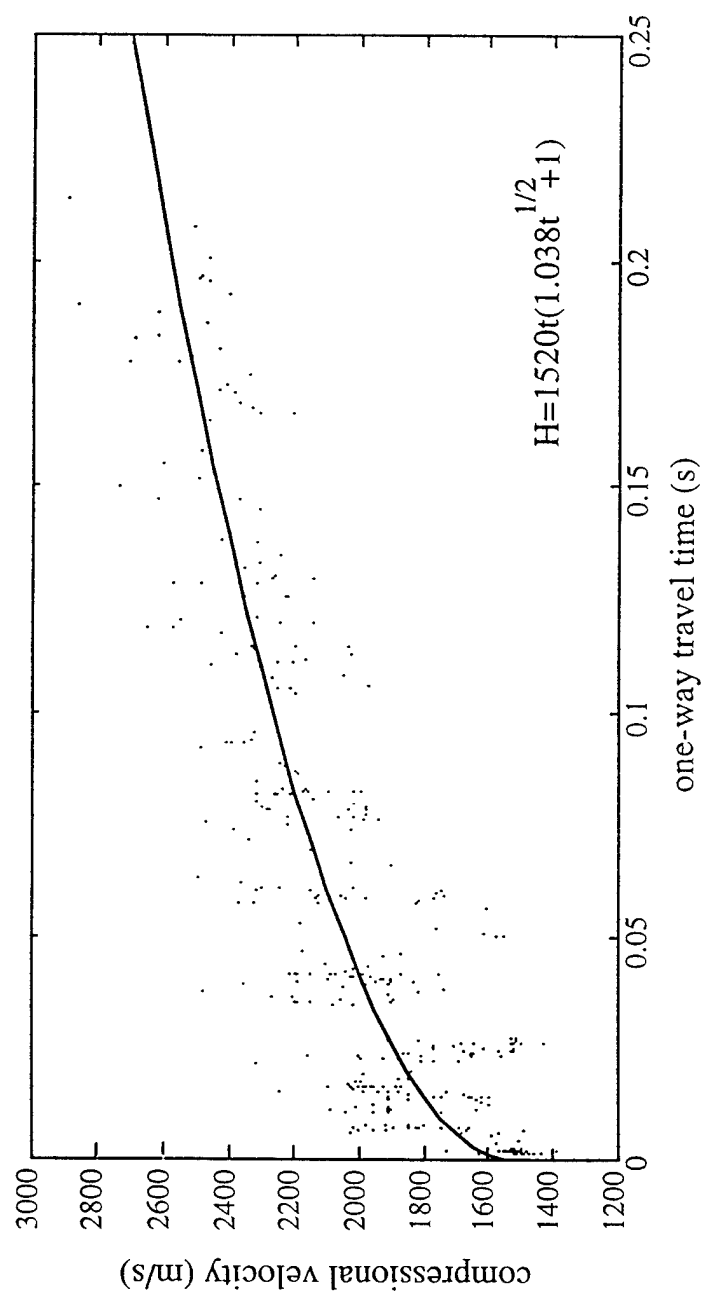


Figure 3

FIGURE 4

Sediment Thickness Maps

(See Jacket Pocket)



Figure 5

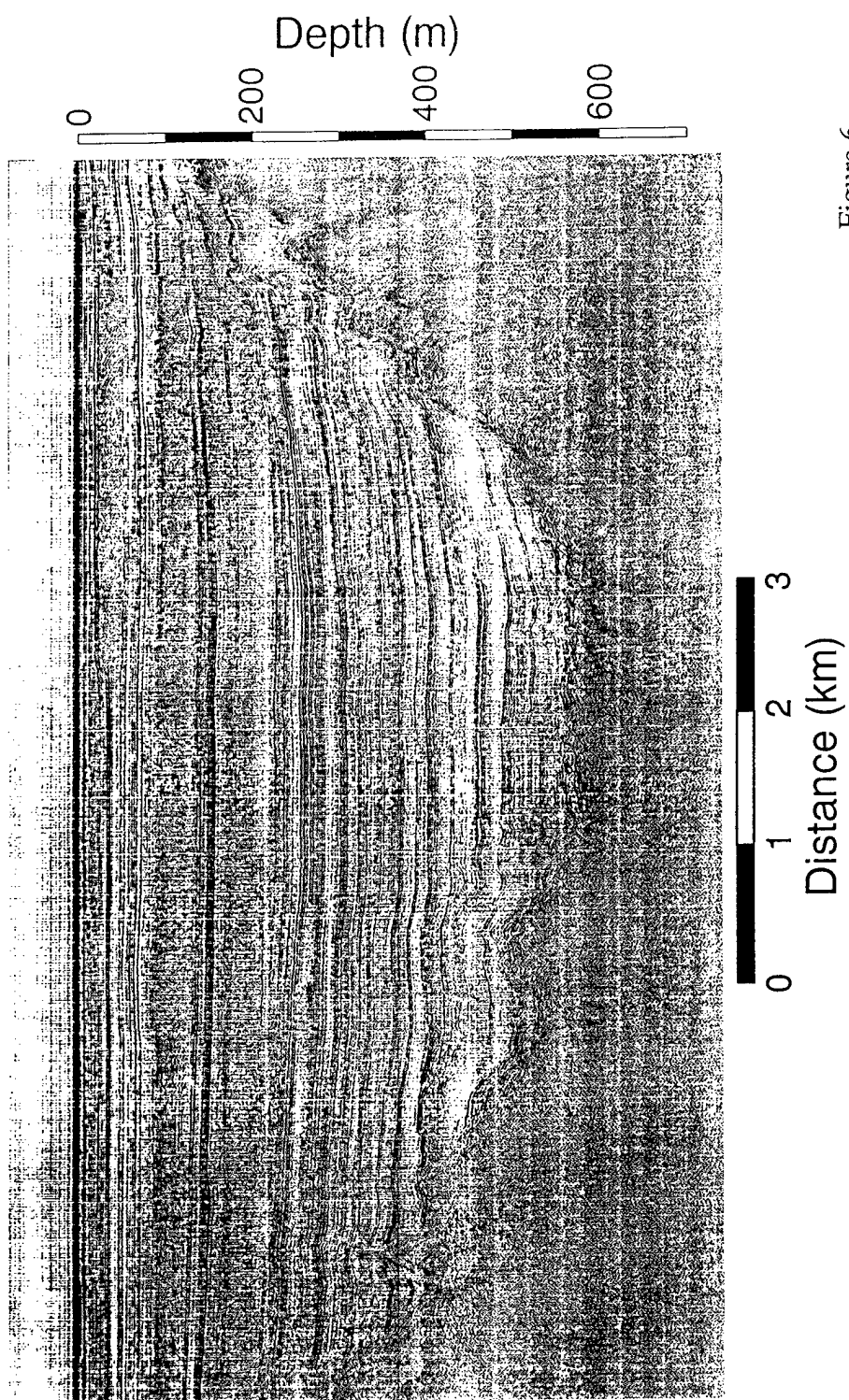


Figure 6

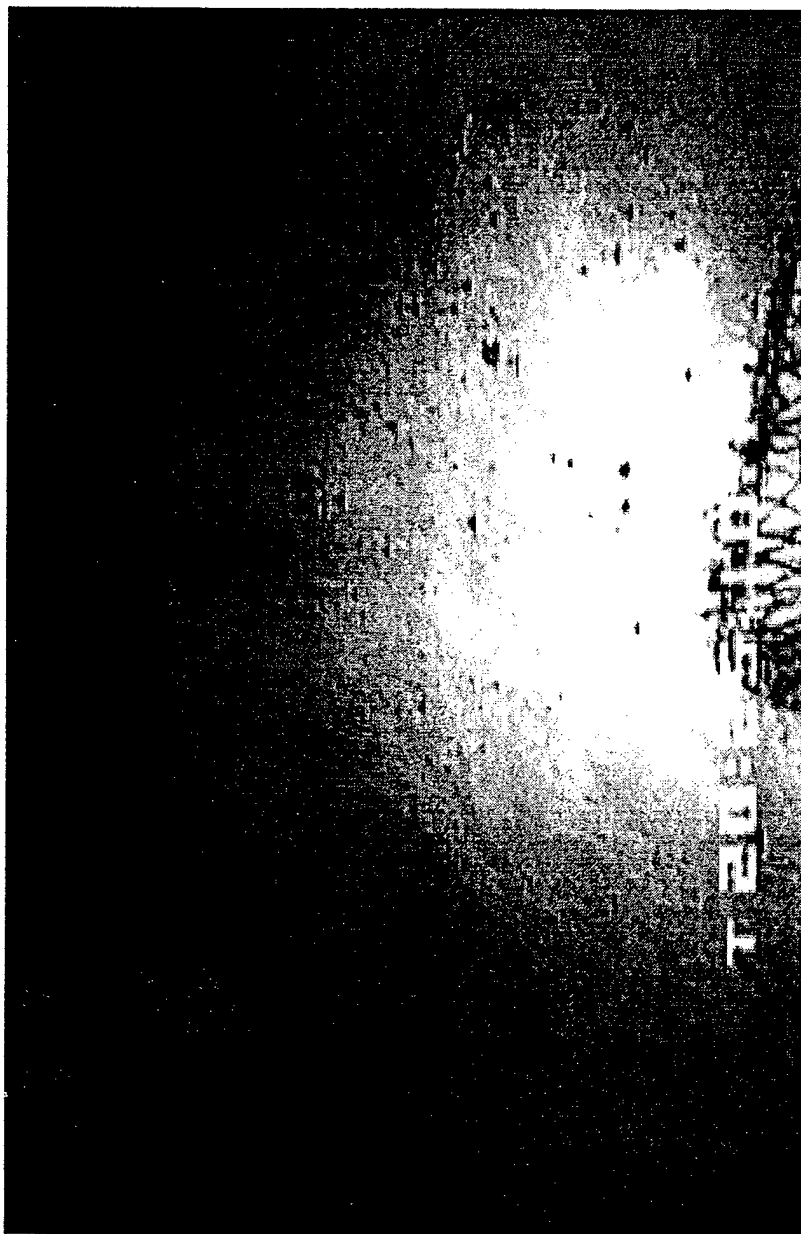


Figure 7

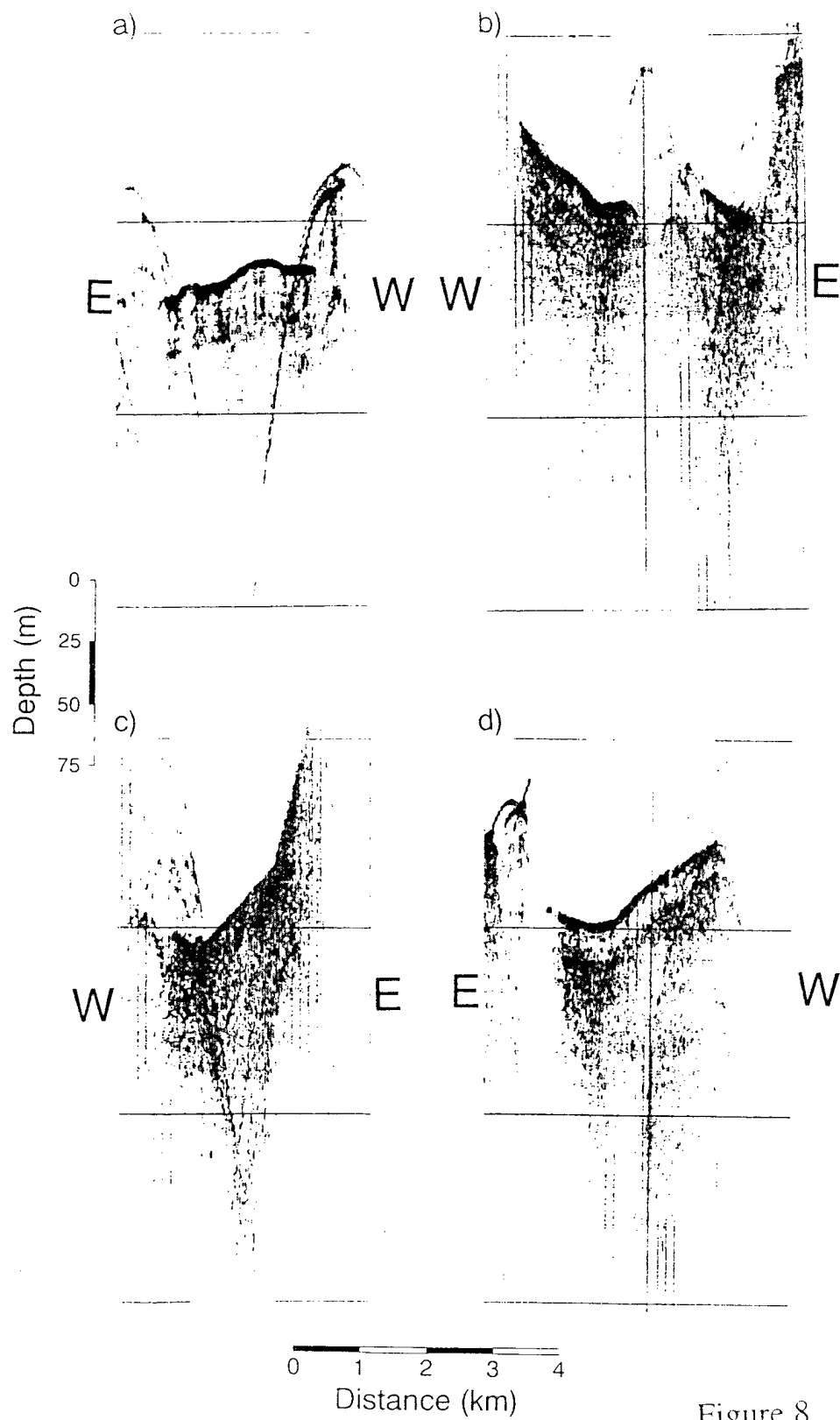


Figure 8

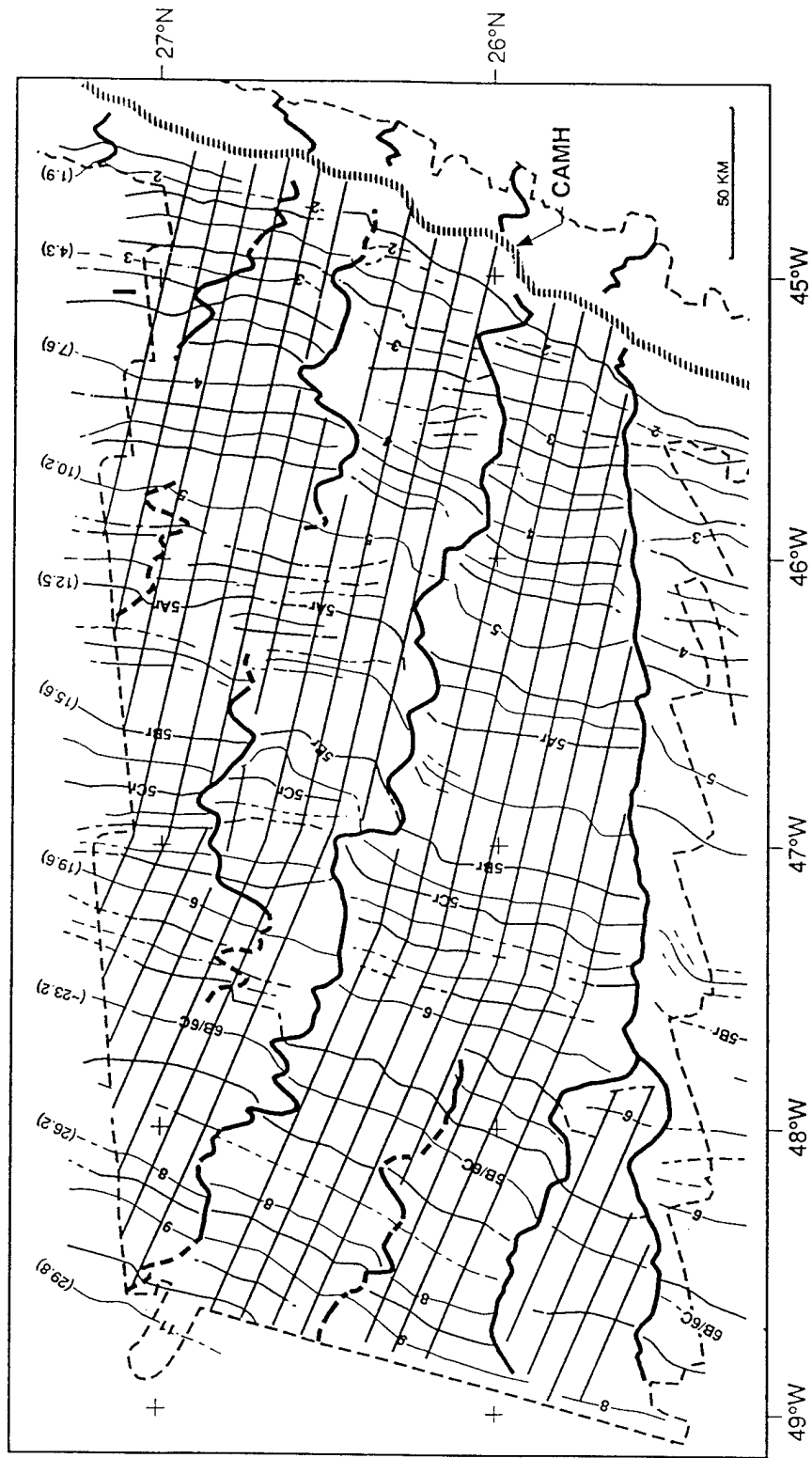


Figure 9

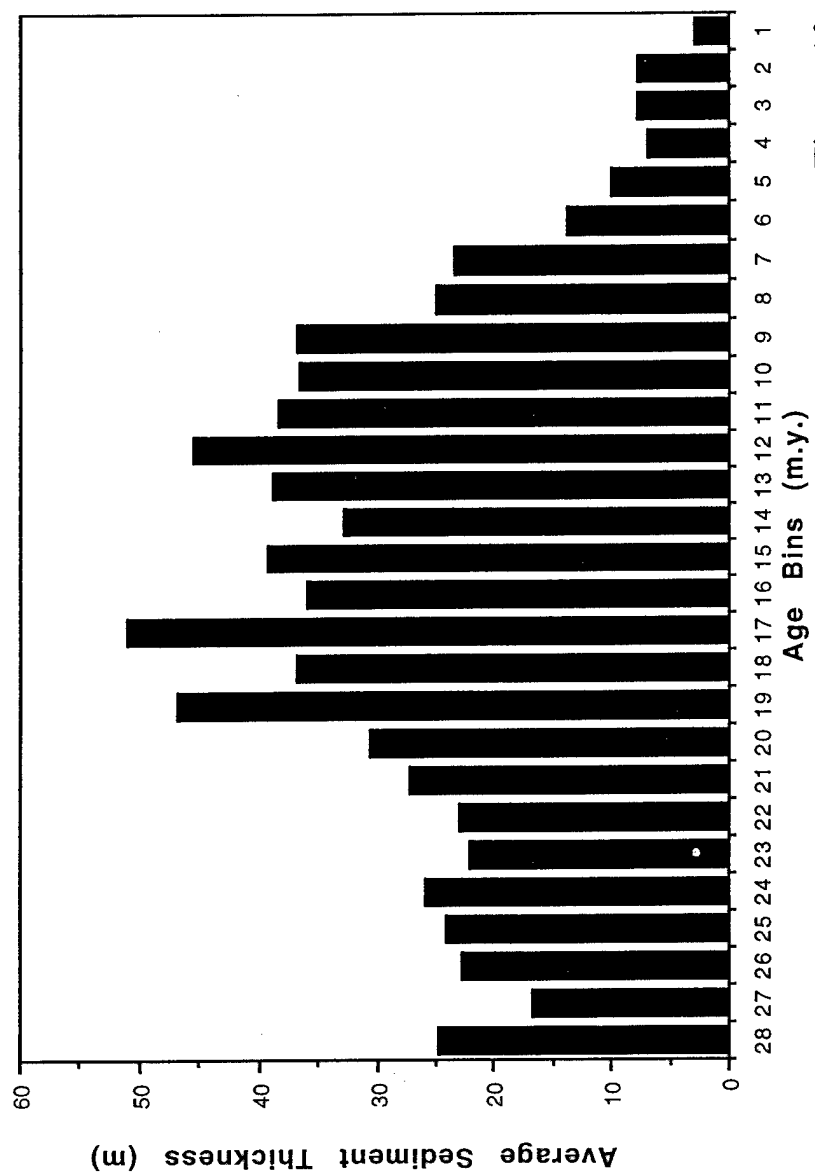


Figure 10

Chapter 3

TECTONIC EXTENSION AT A SLOW-SPREADING MID-OCEAN RIDGE IN SPACE AND TIME: A QUANTITATIVE FAULT STUDY ON THE MID- ATLANTIC RIDGE BETWEEN 25°30' AND 27°10'N

Introduction

The principal processes that govern the morphology of slow-spreading ridges are brittle deformation and magmatism. Constraining the balance between these factors is key to our understanding the formation and evolution of slow-spreading ridges. Although faulting is one of the most important processes generating ridge topography, our understanding of brittle deformation during transport of oceanic crust from the ridge axis to the rift mountains and ridge flank is limited because of restricted off-axis mapping, and because faults can be difficult to distinguish in multibeam bathymetry. In this paper, we outline a method to identify faults from a combined study of bathymetry and sidescan-sonar images and to quantitatively assess the strain accommodated by displacement on faults. Previous studies have estimated brittle strain from the ridge axis to the crest of the rift mountains (Macdonald and Luyendyk, 1977; Searle and Laughton, 1981; Karson and Winters, 1992). We take advantage of a more extensive topographic dataset (Tucholke et al., 1992) to examine the spatial and temporal record of faulting not only within the rift valley but also from the crest of the rift mountains onto 20 Ma crust on the ridge flank.

The plate boundary at slow-spreading ridges is characterized by a 1- to 3-km deep and 15- to 30-km wide rift valley, bounded on either side by rugged topography of the rift mountains (e.g., Needham and Francheteau, 1974; Macdonald and Luyendyk, 1977; Macdonald, 1986; Karson, 1990; Fox et al., 1991). A typical cross-section of a rift valley exhibits an inner floor ~7 km wide where crust is relatively undeformed except by small

fissures and where zero-age crust is accreted at the ridge axis along a neovolcanic ridge. The edge of the inner rift-valley floor (~ 0.6 m.y.) is delineated by major normal faults ("bounding faults", >200 m throw) at the base of the rift-valley walls. Crust is uplifted to the rift mountains on a series of high-angle normal faults, and fault-block terraces define the rift-valley walls. The crest of the rift mountains represents the maximum elevation (~ 2000 m) of the ridge at ~ 15 to 35 km off-axis ($\sim 1.5 - 3.5$ m.y.). From there, crust progressively deepens with age, following a square-root of age relationship predicted by plate cooling models (Parsons and Sclater, 1977; Sclater and Wixon, 1986).

The role of faulting in the formation of mid-ocean-ridge and abyssal-hill topography has been the subject of much research (e.g., Needham and Francheteau, 1974; Rona et al., 1974; Whitmarsh and Laughton, 1976; Macdonald and Luyendyk, 1977; Kappel and Ryan, 1991; Goff et al., 1995). It has been shown that at slow-spreading ridges, most topography is generated by normal faulting parallel to the ridge axis. However, the mechanism that transforms the steep relief of the inward-facing rift-valley wall into subsiding ridge-flank abyssal hills is poorly understood. Hypotheses include systematic development of normal faults dipping away from the ridge axis, reverse faulting, and/or progressive backtilting of fault blocks along existing inward-facing faults (e.g., Needham and Francheteau, 1974; Harrison and Stieltjes, 1977; Macdonald and Luyendyk, 1977; Macdonald and Atwater, 1978; Shaw and Lin, 1993). Although recent microseismicity studies suggest that faulting can occur up to 15 km off-axis (Wolfe et al., 1995), it is unclear how far off-axis faulting contributes to the formation of ridge topography.

Geophysical and geochemical surveys have demonstrated that extensional plate boundaries are segmented at scales of $\sim 10 - 100$ km (Schouten et al., 1985; Macdonald et al., 1988), emphasizing the three-dimensional nature of tectonism and magmatic accretion at mid-ocean ridges (Sempéré et al., 1990, 1993; Purdy et al., 1990). In addition to stable transform faults that laterally offset the ridge axis by $35 - 200+$ km, non-transform

discontinuities with offsets ranging from near-zero to ~30 km delimit the boundaries of spreading segments at slow-spreading ridges (Rona et al., 1976; Searle et al., 1977; Sempéré et al., 1990, 1993). Segments at slow-spreading ridges are characterized by systematic variations in bathymetry and gravity (e.g., Macdonald et al., 1988; Kuo and Forsyth, 1988; Sempéré et al., 1990, 1993) which suggest that segments constitute individual accretionary zones.

According to magmatic accretion models (e.g., Whitehead et al., 1984; Kuo and Forsyth, 1988; Lin et al., 1990), upwelling of mantle diapirs, or melt, focuses at centers of ridge segments and thereby supplies more melt to segment centers than to segment ends. A pronounced "bulls-eye" pattern of mantle Bouguer gravity anomaly (MBA) lows at slow-spreading ridges (Kuo and Forsyth, 1988; Lin et al., 1990) suggests localized, focused, mantle upwelling beneath some segment centers, and it is thought primarily to reflect thickened crust and/or hotter, less dense mantle there. Correlations between along-axis reduction in MBA gravity and increased crustal thickness are supported by seismic refraction studies (Tolstoy et al., 1993).

The along-axis variation in melt supply affects the partitioning of brittle strain within a segment. Such a direct relation was shown by Shaw (1992) and Shaw and Lin (1993). They observed that large-throw, widely-spaced faults interpreted from multibeam bathymetry occur near segment ends where residual mantle Bouguer anomaly (RMBA) highs suggest thin crust. Conversely, relatively small-throw, closely spaced faults are associated with RMBA lows toward centers of ridge segments.

The crustal structure of ridge segments is further complicated by structural asymmetries related to sense of offset at their bounding discontinuities (e.g., Dick et al., 1981; Karson and Dick, 1983, 1984; Collette, 1986; Severinghaus and Macdonald, 1988; Mutter and Karson, 1992; Tucholke and Lin, 1994; Escartín and Lin, 1995). Inside corners (IC) of ridge segments, where crust is formed adjacent to an active discontinuity,

are preferentially elevated and are characterized by thin crust and/or mantle exposures. In contrast, more normal crustal thickness and an intact volcanic carapace are characteristic of segment centers (SC) and of outside corners (OC) formed adjacent to the inactive trace of ridge-axis discontinuities. Faulting style also varies systematically over the along-isochron length of a segment (e.g., Tucholke and Lin, 1994; Cannat et al., 1995; Escartín and Lin, 1995; Tucholke et al., *in press, a*). Faults at ICs typically are irregular in character and have relatively large throws and wide spacing compared to faults at SCs and OCs, which tend to be linear and have small throws.

A geological model recently proposed for structure of segments at slow-spreading ridges suggests that long-lived, low-angle normal (detachment) faults, incised by high angle ($> 45^\circ$) normal faults, occur at most inside corners of segments (Tucholke and Lin, 1994). This model is based not only on data collected from numerous geophysical and geological surveys that show morphological, compositional, and crustal-thickness asymmetries within segments, but also on submersible observations of low-angle normal faults cut by faults dipping 70° - 90° at the eastern inside corner of the Kane Fracture Zone (Karson and Dick, 1983). Low-angle fault surfaces with slip-parallel corrugations (mullions) are now being recognized in bathymetric and sidescan data over IC crust (Cann et al., *in press*; Tucholke et al., 1996). These structures appear to be oceanic analogs of continental metamorphic core complexes that are exposed by low-angle, detachment faulting (Tucholke et al., *in press, a*).

At present there are few observational constraints on the timing and duration of magmatic and tectonic processes at spreading ridges, or on their effect on ridge segmentation. Large cross-isochron variations in RMBA (10 - 20 mGal) on timescales of 2 - 3 m.y. have been documented for the Mid-Atlantic Ridge, and these are thought to be caused by crustal thickness variations that suggest cyclic melt production (Lin et al., 1993;

Pariso et al., 1995; Tucholke et al., *in press, a*). If melt input and crustal accretion are cyclical, there may be a corresponding variation in brittle strain taken up by faults.

In this study, we investigate 1) how fault patterns develop and evolve with time from the rift axis to the ridge flank and 2) how they are spatially related to ridge formation and evolution. We quantitatively assess whether partitioning of brittle strain is consistent with present models of intrasegment structural asymmetries. In addition, we compare regional variations in RMBA against variations in brittle strain to test whether variations in apparent crustal thickness correlate with changes in faulting.

Tectonic Setting

This study focuses on three ridge segments which are separated by non-transform discontinuities. They are located on the MAR between 25°25' and 27°10'N and reach from the MAR axis to ~20 Ma crust (Figure 1). From south to north, the segments are labeled Segments 8, 9, and 10 following the nomenclature of Sempéré et al. (1993). Analysis of Segments 8 and 9 extends from the ridge axis to ~20 Ma crust on the ridge flank; the northern edge of the survey limits our study of Segment 10 to crust \leq 15 Ma. Spreading half-rates have varied from about 18 - 8 mm/yr and have decreased to the lower values over the past 20 m.y. (Tucholke et al., *in press, a*).

The rift morphology of these ridge segments has been described in detail by Sempéré et al. (1993) and Zonenshain et al. (1989), and the axial and ridge-flank morphology is discussed by Tucholke et al. (*in press, a*). Detailed morphology of the segments is shown in the contoured bathymetric map of Figure 2. All three segments exhibit rift valleys that are ~2500 - 2700 m deep and 7 - 20 km wide between the first major inward-facing faults, which are located in ~0.6 Ma crust. These faults delineate the edges of the inner rift-valley floor. The inner rift-valley floor contains a 2 - 4 km-wide neovolcanic ridge with relief of 200 - 700 m. Outside the inner rift-valley floor, the walls

of the rift valley rise steeply across a series of ridge-parallel normal faults to the crest of the rift mountains at 2.5, 1.5, and 3.2 Ma in Segments 8, 9, and 10 respectively. Crust older than the crests of the rift mountains is considered to be the ridge flank and deepens by following a square-root-of-age relation (cf. Sclater and Wixon, 1986).

Off-axis, non-transform discontinuities separate the segments and form bathymetric troughs that strike subparallel to the spreading direction. Meandering of the troughs reflects migration of the segment boundaries along the MAR axis through time. Basement depths within discontinuities vary directly with the magnitude of age offset (Tucholke et al., *in press, a*). Where age offset is zero, no depth anomaly is observed, whereas depth anomaly reaches ~1000 m across the largest offsets (2 - 3 m.y.). Along-isochron basement-depth profiles across the discontinuities are strongly asymmetric, with IC crust averaging ~600 - 700 m shallower than OC crust of comparable age on the opposite side of the discontinuity.

All segments have IC crust along their southern margins and OC crust on their northern margins. There is one significant exception in the < 20 Ma crust studied here: the discontinuity between Segments 9 and 10 is left lateral on ~13 - 19 Ma crust located between 46°18'W and 47°00'W. Here, Segment 9 has two elevated inside corners, and Segment 10 has two deeper outside corners.

Data and Methods

We applied semi-automated fault-detection and measurement techniques to multibeam bathymetry to quantitatively study the brittle strain taken up by faults. We used a combination of the ridge-axis SeaBeam bathymetric data of Purdy et al. (1990) and off-axis Hydrosweep multibeam bathymetry of Tucholke et al. (1992). We also analyzed backscatter images acquired with the Hawaii MR1 (HMR1) sidescan-sonar system.

Our fault-detection and measurement technique is a newly developed method for image processing of rasterized bathymetry. First, "edges" were automatically detected in a

digital raster image of bathymetry using gradient-based, edge-detecting software (Vista v2.1) modified for this study by H. Huang, K. Stewart, and X. Tang (Woods Hole Oceanographic Institution). This technique located individual points which group to form "edges" along the trace of high-dip zones on the seafloor; it also provided dip orientation. All detected edges were then visually compared to HMR1 sidescan-sonar images to discriminate between those edges that represent faults and those that are probably not fault-related. In several locations, interpretations of fault scarps were confirmed by comparison with high-resolution, near-bottom bathymetric and sidescan surveys by Tucholke et al. (*in press, b*). Finally, for those edges identified as faults, fault parameters were derived from original bathymetric data. The following gives details of the steps we followed in fault detection and data analysis:

1. Multibeam bathymetry was converted to a raster image of pixel intensity, where intensity was directly proportional to seafloor depth. Data gaps were filled with interpolated values, and resolution of the raster image was kept the same as that of the gridded bathymetry (1 pixel \approx 200 m).
2. Edges (steepest seafloor gradients) were located from the local maxima in the gradients of a Gaussian smoothed image. A Gaussian filter with a standard deviation of 2 (determined by trial and error) was applied to control the balance between noise and the edges of interest (i.e., faults). Gradients were then calculated for each pixel and all local maxima above a certain threshold were marked as an edge. The threshold was set to 4 degrees to reduce noise and optimize the signal of linear, continuous edges. A minimum edge length of 8 pixels (1600 m) was also applied. This eliminated features too small and discontinuous to be considered faults. Examples of detected edges prior to interpretation are shown in Figure 3.

3. Detected edges were visually compared to HMR1-sidescan-sonar images to identify edges that represent faults and to eliminate edges that are interpreted not to be faults. HMR1 coverage of the study area is complete in each of two primary look directions (NNW and SSE); imagery for both look directions was interpreted in order to identify faults dipping both toward and away from the ridge axis. We applied two criteria to distinguish faults. First, following the technique of Laughton and Searle (1979), strong narrow sidescan echoes were interpreted as fault scarps and wider zones of more diffuse echoes were interpreted as rough volcanic terrain. Second, detected edges were considered to be faults only if they matched with continuous and generally linear sidescan echoes.

4. Edges identified as normal faults were analyzed using the original, 200-m gridded bathymetric depths to determine fault parameters for each detected point along the fault. Fault throw, apparent dip, and apparent heave were first measured in the local direction of maximum dip at 200 m intervals along the strike of the fault. As shown in Figure 4, throw and apparent fault dip are measured directly from bathymetry, and heave is calculated using these parameters. Fault throw was determined from the difference between maximum and minimum bathymetric depths in the local (apparent) dip direction, within a calculated range between faults (Figure 4); the calculated range is half the distance from the edge point of interest to the next closest edge point in the dip direction. Apparent dip was determined from the maximum depth gradient at the local edge point of interest. Apparent heave, h , is calculated as:

$$h = T \cdot \arctan(d), \text{ where } T = \text{throw and } d = \text{apparent dip.}$$

Once apparent heaves and dips were determined, they were geometrically corrected to "true" heave (H) and dip (D) by projecting them onto a line parallel to the average spreading direction in the study area (105°). Only "true" heave and dip are reported in this

study. Fault throws (T) are reported as they were measured because T remains essentially constant regardless of dip direction.

Strain measurements were computed as area strain:

$$\varepsilon = \Delta A / A_0,$$

where ε = area strain, ΔA = change in the area of interest, and A_0 = initial area. The change in area, ΔA , is taken as the total plan-view seafloor expression of all faults lying within an area of interest; it is calculated from the summation of fault heaves of all individual fault points within that area, multiplied by the grid length of each point:

$$\Delta A = \Sigma (H \cdot l_g),$$

where H = fault heave of a point and l_g = point grid length (200 m). It follows that

$$A_0 = A - \Delta A,$$

where A = total area of the seafloor in the area of interest.

Changes in finite strain from area to area may reflect variation in the number of faults, the length of faults, and/or variations in incremental strain along individual faults. To assess the cause of changes in finite strain from area to area, we calculate total fault length (L), fault density (length normalized to area, L/A), and fault heave (H) for different areas within the study region. We use L because it combines the number of faults and their lengths into a single parameter by which to compare changes. By normalizing L by A, we can determine whether strain changes proportionately with fault density.

Spacing between faults was also measured along lines parallel to the average spreading direction (105°). We used 6 equidistant lines per segment so that full along-isochron lengths of segments are represented.

To compare faulting at segment centers and ends, segments were divided into three equally spaced regions. The southern third of each segment is treated as inside-corner crust, the northern third as outside-corner crust, and the middle third as segment-center crust. An exception occurs for 15-19 Ma crust in Segment 9; there, both the southern and

northern third of the segment are inside-corner crust. This method of defining tectonic provinces by along-isochron, intrasegment distance is a simple approximation; it allows first-order variations in fault populations to be compared among the three tectonic settings and avoids the subjectivity involved in detailed interpretation of the complex "boundaries" between tectonic settings.

Crustal ages and segment boundaries were derived from the magnetic data of Tucholke et al. (*in press, a*). Where offsets in magnetic lineations are poorly defined, segment boundaries follow the trace of bathymetric lows.

Limitations

Scarp degradation by mass wasting and the accumulation of debris at the base of fault scarps act to reduce original fault dips and throws (e.g., McAllister, 1995; Allerton, et al., 1995; Tucholke et al., *in press, b*). Therefore, although we measure fault dip at the maximum gradient of fault scarps and fault throw from the base of a fault scarp, reported dips and throws should be considered minimum estimates.

Fault parameter estimates also are subject to smoothing effects caused by the limited horizontal resolution (200 m) of the gridded bathymetry. Structures interpreted to be faults may correspond to zones of closely spaced faults and not to individual fault planes (e.g., Tucholke and Lin, 1994). Thus, measured fault throw of a "single" detected fault may represent the cumulative throw of several smaller-offset faults comprising the fault zone, and measured fault dip may underestimate the dip of individual small-offset faults comprising the fault zone; fault heave, derived from fault throw and dip, consequently may be overestimated. Throughout this study, we treat detected features as individual faults, although it is recognized that they may represent fault zones. The absolute magnitudes of fault dip, heave, and strain are meaningful not for their absolute values, but for quantitative comparisons of relative differences among areas within and between ridge segments in our

study region. The data are also of value for comparison to other studies that have measured these fault components with similar resolution.

A limitation of our technique is that fault length-displacement scaling relationships (e.g., Scholz et al., 1993; Cowie et al., 1994) cannot be readily analyzed. Detected edges are sometimes discontinuous along strike because of local slope reduction (e.g., by mass wasting) and edge-point editing. Therefore, truly continuous faults may have been identified as a set of independent but contiguous edges. This effect is presumed to occur randomly throughout our study area and therefore introduces no consistent bias in our analyses.

Sediment cover can affect fault parameters derived from seafloor topography. Although regional sediment cover is thin (≤ 50 m), local basement depressions can accumulate thick sediments that can mask or diminish the topographic expression of faults (see Chapter 2). Sediment ponds sizable enough to completely or partially mask underlying fault structure occur in the troughs along non-transform discontinuities and in the ridge-parallel valleys between abyssal hills (Chapter 2, Figure 4), especially on 8 - 20 Ma crust where sediment accumulations are relatively large (cf. Chapter 2, Figure 10). In our Hydrosweep data, mappable faults are usually ≥ 100 m high and ≥ 10 km long, so sediment ponds thicker and longer than this can conceal faults. Specific effects of sedimentation and scarp degradation on observed fault parameters are considered in the Discussion.

Regional Fault Patterns

Orientation and Geometry of Faults

Fault distribution out to 20 Ma crust in ridge segments 8, 9, and 10 is shown in Figure 5. Within a segment, the character of faulting tends to change with along-isochron position. On IC crust, faults are irregular to arcuate with widely varying strikes but general

alignment subparallel to either the ridge axis or the adjacent non-transform discontinuity. A good example of this pattern of faulting is exhibited in Segment 9 on 14 - 19 Ma crust, where both the southern and northern edges of the segment are inside corners (Figure 5).

At segment centers, faults generally are linear, and their orientations are orthogonal ($\sim 015^\circ$) to the average plate-spreading direction. Locally, oblique faults associated with small propagating rifts crosscut the ridge-parallel faults at low angles (Kleinrock et al., *submitted*); an example of this faulting pattern occurs in 10-12 Ma crust of Segment 8 (Figure 5). Some SC faults continue onto inside corners of segments and become irregular and variably oriented, while others show no change in pattern but they crosscut or abruptly terminate at irregular IC faults. These relations suggest that there are significant, time-dependent changes in stress orientation at inside corners, and these changes commonly are not in phase with changes in stress at segment centers.

In comparison, faults at outside corners are mostly continuous with those at segment centers, and the distal ends of OC faults terminate at or near non-transform discontinuities. As observed in other studies, OC faults often curve toward the ridge axis within 10-15 km of a discontinuity because of rotation of the stress field (Karson and Dick, 1983; Searle, 1983; Tucholke and Schouten, 1988; Sempéré et al., 1995). This pattern is common in the study area, particularly in Segment 8 (Figure 5), but it is not ubiquitous.

Inward versus Outward-facing Faults

A significant finding of this study is that outward-facing faults, i.e., faults dipping away from the ridge axis, contribute significantly to the tectonic fabric of the ridge flank (Figure 5). The first outward-facing faults recognizable in bathymetry lie outside the bounding faults of the inner rift-valley floor on crust older than ~ 0.6 Ma. Approximately 40% of all faults mapped on this older crust are outward-facing (Figure 6). In comparison, estimates of the number of outward-facing faults along the northern MAR at 23°N and

37°N are 20% and 17%, respectively (Kong et al, 1988; Macdonald and Luyendyk, 1977). This difference is at least partly due to the fact that these estimates were derived from seafloor profiles of near-axis faults (within 7 to ~50 km of the ridge axis); as will be shown later, the proportion of outward-facing faults increases with age in 0.6 to ~3.5 Ma crust.

The most common occurrence of an outward-facing fault is in conjunction with an inward-facing fault (Figures 3 - 5). These fault pairs bound long, linear horsts, thus forming abyssal hills along the centers of segments (e.g., Figure 7). Less commonly, outward-facing faults are not paired with inward-facing faults and they form half-grabens (Figure 8). Half-grabens formed both by inward-facing and outward-facing faults are observed but are atypical of ridge flank topography; however, where these faults occur, their throw can be significant (up to several hundred meters).

Fault Parameters

Fault throw, heave, dip, and spacing vary widely in the study region (Table 1). Measured throws range from 60 to 1540 m, with a mean of 365 m and a standard deviation (σ) of 200 m. These values are similar to those observed elsewhere in the rift mountains of slow-spreading ridges (e.g., Searle and Laughton, 1977; Macdonald and Luyendyk, 1977; Kong et al., 1988; Dauteuil and Brun, 1996). Fault heaves range from 460 to 4650 m with a mean of 1200 m ($\sigma = 530$), and dips range from 4 to 45 degrees (mean = 14 degrees, $\sigma = 7$). As already noted, heaves and dips almost certainly are over- and under-estimated, respectively, because of scarp degradation and limited resolution of the gridded bathymetry. By way of comparison, deep-tow and submersible studies estimate fault dips in other, near-axis regions of the MAR at ~5° to 90° with means of ~30° - 50° (Ballard and Van Andel, 1977; Macdonald and Luyendyk, 1977; Karson and Dick, 1983). Fault spacing within the study area typically is ~2 km, although spacing ranges from 0.5 - 15 km.

A comparison of fault throw and heave for inward- and outward-facing faults indicates that both are statistically identical in range and mean (Table 1), although the range of heaves on outward-facing faults is slightly narrower than that of inward-facing faults. In addition, the distribution of dips on inward- and outward-facing faults is similar (Table 1; Figure 9). These observations are consistent with Macdonald and Luyendyk's (1977) finding that outward-facing faults located outside the MAR rift valley near the crest of the MAR rift mountains at 37°N have throws that are as great as those for inward-facing faults.

Regional Strain Estimates

Measurement of fault parameters allows us to quantify the spatial and temporal partitioning of brittle strain at the plate boundary. We derive brittle strain from total fault length and fault heave in the direction of spreading. Because we use fault dips measured from multibeam bathymetry to calculate fault heave, and because these measurements may underestimate true fault dips, the calculated fault strains almost certainly are greater than true strains. Some studies (e.g., Searle and Laughton, 1981; Carbotte and Macdonald, 1990) have attempted to avoid this difficulty by measuring fault throw either from bathymetry or sidescan-reflection widths and then assuming a fault dip of 45°. Earthquake fault-plane solutions suggest that this dip angle is a reasonable approximation for active normal faults in the seismogenic oceanic lithosphere at slow-spreading ridges (e.g., Sykes, 1967; Solomon et al., 1988; Thatcher and Hill, 1995). High resolution, near-bottom studies of fault geometry show a wide range of dips around this value (e.g., Macdonald and Luyendyk, 1977; Karson and Winters, 1992). The finite strains that we derive are used to make quantitative comparisons of faulting among different tectonic provinces within our study area, but we also calculate finite strains by assuming faults with 45° dips solely as a basis for comparison to other studies.

Area strain, ϵ , is $30 \pm 8\%$ for our entire study area (Segments 8, 9 and 10) and is nearly identical among all three segments (Table 2). However, calculated strain assuming 45° fault dip is only $6 \pm 4\%$. This latter estimate is slightly lower than the range of strains determined in other studies of the MAR. Previous studies have estimated strains of 11 - 18% for faulting within 15 km of the ridge axis (Macdonald and Luyendyk, 1977; Searle and Laughton, 1981; Karson and Winters, 1992). In a global study of focal mechanisms of selected earthquakes at slow-spreading ridges (i.e., earthquakes with source dimensions at least as great as the brittle plate thickness), Solomon et al. (1988) also found that 10-20% of plate separation is accounted for by seismic strain.

Spatial Variations in Faulting Patterns

Correlation with Residual Mantle Bouguer Anomaly

We examined fault patterns and measured strain in relation to residual mantle Bouguer anomaly (RMBA). The RMBA represents a correction of the observed free-air gravity field for the effect of topography at the seafloor and at the crust/mantle interface and the effect of lithospheric cooling with age. RMBA reflects some combination of crustal thickness variations and sub-seafloor density (i.e., temperature) variations (Kuo and Forsyth, 1988; Lin et al., 1990). RMBA highs are associated with regions of thin crust and/or higher lithosphere density, and RMBA lows reflect thicker crust and/or lower density. We divided RMBA gravity into three ranges: low (< 7 mGal), medium (7 to < 15 mGal), and high (> 15 mGal). The resulting anomaly pattern (Figure 10) shows that ICs typically have residual gravity highs (i.e., thin crust), SCs contain residual gravity lows (i.e., thick crust), and OCs have moderate gravity values. This association between residual gravity patterns and intrasegment position has been previously described by Tucholke and Lin (1994) and Escartín and Lin (1995), and the total variation in RMBA is

equivalent to variation of more than 3 km in apparent crustal thickness (Tucholke and Lin, 1994).

Individual fault data-points were assigned gravity values correlative with their location (Figure 10). We observe that fault throw and heave correlate directly with RMBA (Table 3). Mean fault throw is ~115 m (36%) greater in crust associated with residual gravity highs than that associated with residual gravity lows, and mean fault heave is about 180 m (16%) greater. Fault offsets in areas of intermediate gravity values are only slightly higher than those in areas of gravity lows, but they are considerably less than offsets in areas of gravity highs. There are no differences in fault dips among the different gravity regimes.

We also compared the percentage of outward-facing faults, based on total fault length, with the different gravity regimes (Table 3). The percentage of outward-facing faults increases consistently with increasing RMBA value, and in regions of high RMBA (thin crust) it is approximately double that in regions of low RMBA (thicker crust).

Finally, we examined changes in finite strain and fault density in relation to residual gravity (Table 3). Strain, ϵ , associated with RMBA highs (27%) is much greater than that at RMBA lows (16%). Fault density, L/A , also is greater in areas with gravity highs compared to that with gravity lows. Values of ϵ and L/A in areas of intermediate gravity are similar to values associated with gravity highs.

Correlation with Intrasegment Position

Fault spacing varies with tectonic setting within a segment (Figure 11). Histograms of fault spacing measured along the inside corners, segment centers and outside corners of the three segments studied show distributions with ranges of <1 to 20 km and peaks at 1 - 2 km. Fault spacing is closer at segment centers than at segment ends in Segments 8 and 9 (Figure 12), and differences between spacings at inside and outside corners are negligible.

However, this relationship does not hold for Segment 10, where there is a slightly greater percentage of closely spaced faults on inside-corner crust, and fault spacing at the segment center and outside corner is comparable.

Although fault spacing appears to relate to intrasegment position, we find no comparable relation with magnitude of fault offset (Table 4). Even though mean fault throw (405 m) and heave (1260 m) at inside corners are slightly greater than those at segment centers and outside corners (355 m and 325 m, and 1150 m and 1145 m, respectively), large standard deviations of these values make the differences statistically insignificant.

However, fault density (L/A), and thus brittle strain taken up by faults, does vary significantly with intrasegment position (Table 5). On average, finite strain and fault density are highest at inside corners and steadily decrease through the segment centers to outside corners. It is possible that strain at outside corners is underestimated because of sediment cover. OC crust is generally deeper than IC and SC crust, and it dips gently into adjacent discontinuities where sediment accumulations are greatest (Chapter 2, Figure 4).

Temporal Record of Faulting

To examine temporal changes in faulting and to assess the effects of aging on fault-scarp morphology, we have grouped faults by crustal age. In Figure 13, a plot of the percentage of outward-facing faults shows an increase from approximately 10 - 15% percent in < 1 Ma crust to ~40% on 3 - 4 Ma crust located at the crest of the rift mountains. On crust older than 3 - 4 Ma, the mean percentage of outward-facing faults remains at ~40%. There is no significant variation of this pattern with intrasegment position (Figure 13).

In Figure 14, we compare off-axis changes in finite strain, fault length, fault density, and mean fault heave partitioned by fault-facing direction over time for each of the

three segments studied. Inward-facing faults consistently exhibit a significant decrease in ϵ from the edge of the inner rift-valley floor toward the crest of the rift mountains. However, heave on these faults, H , remains nearly constant over the same region. Therefore, most of the observed decrease in strain must be attributable to changes in fault density, L/A , and L/A does proportionately decrease toward the crest of the rift mountains. This suggests either that the amount of brittle strain is actually decreasing with age in the rift-valley walls, or that brittle strain has been approximately constant but the cumulative length of detectable faults has been reduced with age.

On outward-facing faults, we observe a consistent increase in ϵ with age for all segments over the same time interval, i.e., from the bounding fault of the inner rift-valley floor to the crest of the rift mountains (Figure 14). Outward-facing faults are not observed within the rift valley inboard of the bounding faults, but we observe an increase in L/A on the rift-valley walls towards the crest of the rift mountains. Like inward-facing faults, average heave along outward-facing faults changes very little with distance from the ridge axis. The off-axis increase in ϵ appears to reflect the progressive growth of new, outward-facing faults within the rift-valley walls.

Farther off-axis on the ridge flank, ϵ on both inward- and outward-facing faults varies by as much as 25% on time scales of ~ 3 million years, but the overall trend is one of slowly decreasing strain with crustal age (Figure 14). Heave remains nearly constant with age. Therefore, the change in ϵ must be related to a decrease in L/A . The overall decrease is approximately 2% per m.y. for Segment 8, and 1% and 4% per m.y. for Segments 9 and 10 respectively.

Discussion

The balance between magmatic and tectonic extension is reflected in spatial and temporal variations in brittle strain recorded in the population of off-axis faults. Based on geometrically derived fault heaves, we estimate average brittle strain on the Mid-Atlantic Ridge at 26°N on 0.6 - 29 Ma crust to be a maximum of ~30%. If fault dips of 45° are assumed, strain estimates are reduced to ~6%, at the low end of values previously derived from near-axis studies of the Mid-Atlantic Ridge. Our observations indicate that magmatic accretion at the Mid-Atlantic Ridge accounts for greater than 70% and possibly as much as 94% of total plate separation. However, brittle extension on normal faults is fundamental to forming abyssal hills on the ridge flank, and it varies systematically within segments.

Effects of scarp degradation and sedimentation on fault parameters

Before interpreting the variation in fault parameters off-axis, we must consider how scarp degradation and sedimentation can affect these parameters. The degradation of fault scarps by erosion and by talus deposition at the scarp base can reduce measurable fault lengths, throws and dips (McAllister, 1995; Allerton et al., 1995). A study of high-resolution, near-bottom surveys of fault scarps in our study area on crust of ages 4, 11, and 24 Ma revealed that faults scarps appear to progressively degrade with time due to mass-wasting and abrasion processes (Tucholke et al., *in press, b*).

We observe that the mean heave derived from measured fault throws and dips is nearly constant with crustal age (Figure 14), but there is long-term reduction in L/A (and thus ϵ) probably caused by mass wasting. Why does mass-wasting not appear to affect heave (derived from throw and dip)? It is conceivable that reduction in measured fault throws and dips over time are roughly proportional to one another and that the derived heaves thus remain constant. In fact, in Figure 15a, plots of mean fault throws and dips in Segments 8, 9, and 10 versus crustal age both show reductions with time. By comparing

the measured throws and dips to theoretical throws and dips that would be necessary to maintain a constant heave for the study area (e.g., 1200 m, Figure 15b) we do observe that throws and dips change proportionately to maintain a nearly constant mean heave of 1200 - 1400 m. Thus the data are consistent with the idea that fault scarps degrade progressively with time; this degradation reduces L and L/A , but it is not reflected in heave. It would appear that as a fault scarp ages, dip is reduced by scarp erosion while fault throw is reduced by the build up of talus and sediment on the hanging wall.

Sedimentation also can affect measured fault strain by complete or partial burial of fault scarps, thus reducing measured fault lengths and L/A . There is increasing sediment cover with age on crust up to ~17 Ma (Chapter 2, Figure 10), and sediment cover is a likely additional cause of the long-term decreases in L/A and ϵ (Figure 14).

Intrasegment variations in faults

Ridge segmentation studies suggest that focused magmatic upwelling results in greater supply of melt to the centers of segments than to their ends (e.g., Whitehead et al., 1984; Kuo and Forsyth, 1988; Lin et al., 1990; Lin and Phipps Morgan, 1992). Thus, extension at segment centers is more likely to be taken up by magmatic accretion, while brittle extension at segment ends should be enhanced. Our results tend to confirm this. Fault throw, fault density, area strain, and possibly fault heave all increase towards ICs (Tables 4, 5). These parameters are roughly comparable at SCs and OCs, although they may be underestimated on deep OC crust near discontinuities because of increased sediment cover. Fault spacing tends to increase towards both ICs and OCs (Figure 12).

It is likely that our fault-detection technique does not measure many of the low-angle faults that are thought to be a primary cause of crustal thinning at inside corners (Dick et al., 1981; Brown and Karson, 1988; Karson, 1990; Tucholke and Lin, 1994). Recently identified low-angle fault surfaces on megamullions at inside corners have dips as low as 1°

- 2°, and they appear to have attained these low dips by isostatic adjustment and "roll-over" of the footwall (Tucholke et al., 1996). If this is a common effect, our values for strain at inside corners may be considerably underestimated.

Comparison of fault parameters against residual gravity anomaly values shows that brittle strain, and fault throw, heave, and density all markedly increase with increasing RMBA (Table 3) and thus in thinner crust. These trends are accentuated compared to IC versus SC/OC differences even though crust is thinner at the segment ends, and especially at the inside corner (Tucholke et al., 1994; Escartín and Lin, 1995). This difference may be caused in part by our assignments of IC, SC, and OC tectonic settings, each representing an arbitrary one-third of along-isochron segment length without regard to geological or geophysical constraints; in comparison, the boundaries of the gravity anomaly values are well defined. Also, intrasegment division of tectonic province along isochrons does not account for temporal, cross-isochron variations in crustal thickness suggested by changes in RMBA.

These results indicate that faulting is enhanced in regions of thin crust, suggesting that where magma supply is relatively low, plate separation is compensated by increased brittle extension. However, Escartín and Lin (1995) also have correlated off-axis, positive residual gravity anomalies with regions where crust has been thinned by normal faulting (particularly at ICs), suggesting that decreased magma supply alone may not account for crustal thinning. These ideas are further developed in later discussion of faulting in the rift valley by considering temporal variations in magma supply.

Intersegment Comparison

Variations in fault parameters differ greatly among ridge segments. The variations are reflected in the strain parameters listed in Table 5. For example, differences in area strain (ϵ) between intrasegment provinces (IC versus SC/OC) are greater for Segment 8

than Segment 9, but they are considerably less for Segment 10. Similarly, variation in fault spacing between segment centers and segment ends is well defined for Segments 8 and 9 but is not discernible for Segment 10 (Figure 12).

The magnitude of IC to SC/OC variations in intrasegment faulting may be related to the magnitude of a segment's offset with the adjacent segment. Segment 8 is bounded by well defined, continuous non-transform discontinuities throughout its length, with offsets ranging from 10 to 58 km. The discontinuity bounding Segment 9 on its north side (between Segments 9 and 10) is offset by only 10 km or less throughout its length, with zero offset on 10.2 to 13.9 Ma crust. The discontinuity bounding Segment 10 on its north side also has an offset of ≤ 10 km with zero offset on 7 and 10.2 Ma crust.

These observations suggest that where segment boundaries are marked by large offsets, intrasegment variations in faulting are more pronounced. Larger offsets are sites where thicker, colder lithosphere abuts the spreading axis across the offset. Therefore, it is reasonable to expect that magmatism becomes more reduced at segment ends near larger offsets, resulting in increased brittle extension.

Faulting in the rift valley

Variations in fault parameters with distance from the ridge axis allow us to address the role of faulting in the formation of the rift valley. The apparent strain on both inward- and outward-facing faults shows marked changes in the rift-valley walls, but beyond the crest of the rift mountains on the ridge flank, strain is generally constant or decreases with crustal age (Figure 14). These observations suggest that faulting is limited to the rift-valley walls, and that there is no significant faulting on the ridge flank.

Strain on faults within the rift-valley wall is partitioned differently for inward-facing and outward-facing faults (Figure 14). Inward-facing faults show relatively high strains near the edge of the inner rift-valley floor, but strains decrease with crustal age. This

observation suggests that inward-facing faults are active only at the inner rift-valley bounding faults and that little or no further slip occurs on these faults in the rift-valley walls. The reduction in strain on inward-facing faults with crustal age may be explained by reduction in fault scarp exposure either because of aging effects on inactive faults or because of reverse motion on previously active normal faults. Aging of faults reduces fault throw and dip by erosion, talus buildup, and/or sedimentation (Figure 16), and although this may not change measured fault heave (Figure 15) the lengths (and therefore L/A) of inward-facing inactive faults will decrease over time. Thus, aging of faults results in decreased area strain as measured from fault scarp exposure. Reverse faulting is discussed below.

In comparison, strain on outward-facing faults steadily increases with crustal age in the rift-valley walls (Figure 14). The increasing strain suggests that outward-facing faults develop higher in the rift-valley walls than inward-facing faults. This idea is supported by the fact that the percentage of outward-facing faults increases from near-zero in the lower rift-valley walls to ~40% at the crest of the rift mountains (Figure 13). Further, the increase in strain with crustal age indicates that outward-facing faults are actively growing, as increases in measurable area strain occur when the rate at which fault scarps are exposed by fault growth exceeds the rate at which fault scarps are degraded by aging processes (Figure 16). We also suggest that most of the outward-facing faults delineated in our study are major normal faults that crosscut previously active inward-facing faults. These outward-facing faults are not simply antithetic faults formed by collapse in hanging walls; if this were the case, the observed growth of the outward-facing faults would have to be accompanied by growth (increasing area strain) of the inward-facing master faults with crustal age, which is not the case. Antithetic faults have been documented at fast-spreading ridges as clusters of faults with small throws (Carbotte and Macdonald, 1994), and they

may exist at the MAR, but they do not explain the large, individual, outward-facing faults detected in this study.

The transition from predominantly inward- to outward-facing active faults with distance from the ridge axis is consistent with cross-ridge changes in the stress regime. Studies of the stresses at mid-ocean ridges indicate that pure shear is an unlikely mechanism for creation of the rift valley. For example, lateral variations in viscous head pressure associated with asthenospheric upwelling during extension (Lachenbruch, 1976), and bending moments due to plate thickening (Phipps Morgan et al., 1987) create vertical stresses that are balanced during horizontal stretching. Tapponier and Francheteau (1978) argued that isostatic recovery in response to vertical shear stresses will cause rotation in the stress field at a distance of about 8 - 15 km from the axis. They predict that "steep outward-facing normal faults will be activated for isostatic recovery." In addition, Tapponier and Francheteau (1978) argued that the rotation of the stress field will reduce the possibility of reverse faulting in the outer portions of the rift valley. From these considerations, and our observations of faulting in the rift-valley walls, we conclude that observed changes in the fault parameters of inward-facing faults reflect the effects of aging, not reverse faulting, on inactive inward-facing faults.

Our observations account for rift-valley morphology. The rift valley itself is maintained along the inward-facing normal faults at the base of the rift-valley wall. Reduction of rift-valley relief is then accommodated by outward-facing faults in the upper portions of the rift-valley wall, forming horsts and grabens. This scenario has been suggested in the past (Needham and Francheteau, 1974; Harrison and Stieltjes, 1977; Macdonald and Luyendyk, 1977), but limited off-axis surveying of the MAR found few outward-facing faults in support of this conclusion.

The observed growth of outward-facing faults is at odds with conclusions of Carbotte and Macdonald (1990), who noted that cross-ridge variations in thermal structure

favor the occurrence of inward-facing faults because outward-facing faults need to overcome greater stresses to break through thicker, older lithosphere. There are several observations, however, that suggest this model may not apply at slow-spreading ridges. First, a recent structural study of the moderate-to-slow spreading ocean crust in the Troodos ophiolite of Cyprus reports a crush zone in mid-crust at the base of the sheeted dike complex. This zone constitutes a sub-horizontal decoupling horizon that partitions deformation within the crust (Agar and Klitgord, 1995). The crush zone is developed during rotation of the upper crustal section in domino-style faulting. If such mid-crustal failure occurred at the Mid-Atlantic Ridge, it could allow the formation of outward-facing faults. However, it is yet unclear whether the findings at Troodos may be applicable to the slow-spreading Mid-Atlantic Ridge.

Second, although thermal models predict a relatively steep thermal gradient near the ridge axis, the brittle/plastic transition also has a pressure dependence (G. Hirth, *personal communication*) that decreases the significance of the thermal gradient as a determinant of brittle lithospheric thickness near the ridge axis. Thus the mechanical base of the lithosphere is probably deeper near the ridge axis than predicted from thermal structure alone, and there may not be a significant mechanical preference for fault-facing directions based on thermal-thickness variations.

Finally, there is increasing evidence that serpentinite is an important constituent of the lower crust and upper mantle at slow-spreading ridges (e.g., Aumento and Loubat, 1971; Dick, 1989; Zonenshain et al., 1989; Cannat, 1993; Tucholke and Lin, 1994), and its occurrence could limit the brittle-layer thickness to less than or equal to the crustal thickness away from the ridge axis. Serpentinite is weak, and its presence favors the localization of strain and the formation of weak faults (Reinen, 1991; Escartín et al., 1996). Formation of serpentinite is favored in the retrograde conditions of the upper mantle away from the ridge axis, where serpentine is stable at lithospheric pressures and temperatures

<400° - 500°C (Caruso and Chernovsky, 1979; Ulmer and Trommsdorff, 1995). Serpentine is formed by hydration of olivine and/or pyroxene, and therefore depends on exposure of these minerals to water. Studies of seismicity at slow-spreading ridges suggest that most teleseismic events occur deep below the rift valley (Solomon et al., 1988), suggesting that faults may provide pathways for water to the base of the crust beneath the rift axis, and thereby supply the means for serpentinization.

Based on the above observations, we present a model of faulting in the rift valley (Figure 17a). We envision that along the edges of the rift valley, the principal locus of extension is the inward-facing faults that bound the inner rift-valley floor. The location of the inner-valley bounding faults most likely is controlled by the depth of the brittle/plastic transition (Harper, 1985), which, to the extent that it follows thermal structure, is relatively shallow near the spreading axis. As new oceanic crust is formed at the spreading axis, the bounding fault migrates away from the axis, and a new inboard fault is formed when the stress necessary for continued slip on the bounding fault exceeds the stress needed to break a new fault nearer the axis (Bicknell et al., 1988). Therefore, the fault spacing of inward-facing faults (mean ≈ 2 km) reflects the average distance that the bounding fault is carried off-axis before the next fault is formed. Higher up in the rift-valley walls, outward-facing faults develop and sole into the relatively weak serpentinite that was formed where the bounding faults penetrated the lower crust to the upper mantle.

The observation that there are nearly twice as many outward-facing faults in regions of high RMBA (thin crust) compared to that of low RMBA (Table 3) is explained by comparing faulting models in Figure 17. During magmatic extension (Figure 17a), crust formed at the ridge axis is relatively thick, and therefore few faults reach to or below the base of the crust. As a consequence, water does not penetrate the shallow mantle and formation of serpentinization is limited, and few outward-facing faults, which sole in serpentinites, are created. In contrast, during relatively amagmatic extension crust is

relatively thin (Figure 17b), and near-axis faulting often extends to or below the base of the crust, allowing penetration of water and enhancing serpentinization. Serpentinization of the upper mantle forms a weak decoupling layer at the base of the crust, and outward-facing faults would be favored over inward-facing faults in the upper rift-valley wall because of rotation of stress vectors (Tapponier and Francheteau, 1978). For these reasons, the creation of outward-facing faults would be enhanced in regions of thin crust.

Our fault model is consistent with observed seismicity at the Mid-Atlantic Ridge. Centroid depths of teleseismic events occur deep (1 - 6 km) below the bottom of the rift valley (Solomon et al., 1988), in agreement with most slip occurring on the inward-facing bounding faults, as observed in our data. The lack of teleseismic activity beneath the rift mountains suggests that outward-facing faults there do not generate large-moment events, although microearthquakes have been recorded up to ~15 km off axis at 29°N (Wolfe et al., 1995). The presence of serpentine on a fault may result in aseismic creep (Reinen, et al., 1991); if outward-facing faults sole in serpentinites at depth, or even incorporate mobile (e.g., diapiric) serpentinites along the fault plane in deeper parts of the crust, they may be relatively aseismic or have greatly reduced seismic moments.

Ridge-flank faults

On crust beyond the crest of the rift mountains, ϵ and L/A show a general decrease with age, indicating that there is no significant fault slip on the ridge flank (Figure 14). Study of sediment ponds shows almost no disturbance that can be attributed to faulting. However, one example of rollover structure is developed in sediments that were initially deposited in a flat-lying pond, and it indicates recent ridge-flank fault activity on an outward-facing fault in 13 Ma crust (Figure 18). This is the only clear example of off-axis faulting we observe in reflection profiles throughout the study area, suggesting that although faulting can occur in relatively old crust, it is not common. Thus abyssal hills

represent largely fossil topographic relief that originated within the rift-valley walls. The long-term trend of decreasing ϵ and L/A with age probably is best explained by scarp degradation and increasing burial by sediments, although we cannot rule out the possibility that there has been a long-term increase in brittle strain over the past 20 m.y.

Short-term variations in fault parameters on the ridge flank must reflect either aging effects on fault scarps, variations in sediment cover, or temporal variations in faulting within the rift valley. It is unlikely that scarp degradation or sedimentation are variable enough at these small spatial scales to explain the changes, so temporal variations in near-axis faulting probably are responsible. The changes occur at ~3 m.y. intervals. Tucholke et al. (*in press, a*) have pointed out that cross-isochron variations in residual gravity occur at 2 - 3 m.y. intervals, and they attribute these variations to cyclic fluctuations in magmatic supply at the ridge axis. Although cross-isochron correlations between fault parameters and RMBA have not been made, regional variations in fault parameters do correlate with RMBA (Table 3). This suggests that off-axis variations in faulting most likely reflect temporal changes in magmatic versus relatively amagmatic extension at the Mid-Atlantic Ridge. Variation in off-axis faulting with fluctuations in magma supply is consistent with the faulting model presented in Figure 17.

Conclusions

Analyses of fault data from the western flank of the northern Mid-Atlantic Ridge provide new constraints on the role of faulting in the formation of topography at slow-spreading ridges. The fault-detection technique developed for this study is well suited for quantitatively characterizing regional fault geometry, and it has allowed us to compare spatial and temporal variability of faulting in three ridge segments that span ~300 km from

zero-age crust at the spreading axis to 20 Ma crust on the ridge flank. The following summarizes our conclusions:

1. Creation of both rift-valley and abyssal-hill topography is controlled by faulting on inward- and outward-facing faults. Uplift of crust to the crest of the rift mountains is accommodated by extension on normal faults that dip toward the ridge axis, with slip being concentrated on faults near the base of the rift-valley walls. Reduction of rift-valley relief into the rift mountains is accomplished by outward-facing faults that are active in the upper rift-valley walls. Outward-facing faults account for 40% of the faults observed on the ridge flank. The generation of pairs of inward- and outward-facing faults results in common horst and graben terrain that forms most abyssal hills. Facing-directions of faults may be controlled by thermal gradients near the ridge, but other explanations, such as the development of a decoupling horizon due to near-axis formation of serpentinites, favor the formation of outward-facing faults away from the rift valley and better support our observations. There is no significant faulting beyond the crest of the rift mountains on crust $> 3 - 4$ Ma.

2. Fault populations show strong differences in geometry, density and strain with intrasegment position. Observations at inside-corner crust are consistent with faulting of relatively thick, cold lithosphere with limited magmatic extension: strains are large and fault spacings tend to be greater than those at segment centers. At segment centers, faults are longer, more linear, more closely spaced, and have smaller offsets and lower strains; this pattern suggests a thinner brittle lid and more magmatic extension. Comparison of brittle strain between individual ridge segments suggests that strain near segment ends is enhanced with increasing magnitude of offset between segments.

3. Short-term (~ 3 m.y.) temporal variations in brittle strain observed off-axis on the ridge flank most likely reflect changes in magmatic versus relatively amagmatic extension at the ridge axis. Regionally, high fault density and high fault strain correlate

with increased residual mantle Bouguer anomaly (thin crust) attributable to relatively amagmatic extension. Similarly, low fault densities and low strains correlate with reduced RMBA (thick crust) attributable to more magmatic extension.

Acknowledgments

We are grateful to K. Stewart, X. Tang, and H. Huang for testing various automated image analysis techniques and developing software in a usable format for fault detection and measurement. For stimulating discussions, we thank J. Escartín, G. Hirth, D. Smith, and P. Clift. This research was supported by the Office of Naval Research under Grants N00014-90-J-1621 and N00014-94-1-0466. G.E.J. was also supported by ONR Grant N00014-93-1-1153 (AASERT).

References

- Agar, S. M., and K. D. Klitgord, A mechanism for decoupling within the oceanic lithosphere revealed in the Troodos ophiolite, *Nature*, 374, 232-238, 1995.
- Allerton, S., B. J. Murton, R. C. Searle, and M. Jones, Extensional faulting and segmentation of the Mid-Atlantic Ridge north of the Kane Fracture Zone (24°00' N to 24°40'N), *Mar. Geophys. Res.*, 17, 37-61, 1995.
- Aumento, F., and H. Loubat, The Mid-Atlantic Ridge near 45°N. XVI. Serpentinized ultramafic intrusions, *Can. J. Earth Sci.*, 8, 631-663, 1971.
- Ballard, R. D., and T. H. Van Andel, Morphology and tectonics of the inner rift valley at lat 36°50'N on the Mid-Atlantic Ridge, *Geol. Soc. Am. Bull.*, 88, 507-530, 1977.
- Bicknell, J. D., J.-C. Sempéré, and K. C. Macdonald, Tectonics of a fast spreading center: A Deep-Tow and Sea Beam survey on the East Pacific Rise at 19°30'S, *Mar. Geophys. Res.*, 9, 25-46, 1988.
- Brown, J. R., and J. A. Karson, Variations in axial processes on the Mid-Atlantic Ridge: The median valley of the MARK area, *Mar. Geophys. Res.*, 10, 109-138, 1988.
- Cann, J. R., D. K. Blackman, D. K. Smith, E. McAllister, B. Janssen, S. Mello, E. Averginso, and A. R. Pascoe, Corrugated slip surfaces formed at the intersections of the Mid-Atlantic Ridge with the Atlantis Transform Fault, *Nature*, (in press).
- Cannat, M., Emplacement of mantle rocks in the seafloor at mid-ocean ridges, *J. Geophys. Res.*, 98, 4163-4172, 1993.
- Cannat, M., C. Mével, M. Maia, C. Deplus, C. Durand, P. Gente, P. Agrinier, A. Belarouchi, G. Dubuisson, E. Humler, and J. Reynolds, Thin crust, ultramafic exposures and rugged faulting patterns at the Mid-Atlantic Ridge (22°-24°N), *Geology*, 23, 49-52, 1995.
- Carbotte, S. M., and K. C. Macdonald, Causes of variation in fault-facing direction on the ocean floor, *Geology*, 18, 749-752, 1990.
- Carbotte, S. M., and K. C. Macdonald, Comparison of seafloor tectonic fabric at intermediate, fast, and superfast spreading ridges: Influence of spreading rate, plate motions, and ridge segmentation on fault patterns, *J. Geophys. Res.*, 99, 13609-13631, 1994.
- Caruso, L. J., and J. Chernovsky, The stability of lizardite, *Can. Mineral.*, 17, 757-769, 1979.
- Chen, Y., and W. J. Morgan, A nonlinear rheology model for mid-ocean ridge axis topography, *J. Geophys. Res.*, 95, 17583-17604, 1990.

- Collette, B. J., Fracture zones in the North Atlantic: Morphology and model, *J. Geol. Soc. Lon.*, 143, 763-774, 1986.
- Cowie, P. A., A. Malinverno, W. B. F. Ryan, and M. H. Edwards, Quantitative fault studies on the East Pacific Rise: A comparison of sonar imaging techniques, *J. Geophys. Res.*, 99, 15205-15218, 1994.
- Dauteuil, O., and J.-P. Brun, Deformation partitioning in a slow spreading ridge undergoing oblique extension: Mohns Ridge, Norwegian Sea, *Tectonics*, 15, 4, 870-884, 1996.
- Dick, H. J. B., Abyssal peridotites, very slow spreading ridges and ocean ridge magmatism. In: A. D. Saunders and M. J. Norry (Eds.), *Magmatism in the Ocean Basins*. Geol. Soc. Special Publ., 24, 71-105, 1989.
- Dick, H. J. B., W. B. Bryan, and G. Thompson, Low-angle faulting and steady-state emplacement of plutonic rocks at ridge-transform intersections, *EOS, Trans. Am. Geophys. Union*, 62, 406, 1981.
- Escartín, J., *Ridge Segmentation, Tectonic Evolution and Rheology of Slow-Spreading Oceanic Crust..* Ph.D. Thesis, Massachusetts Institute of Technology/Woods Hole Oceanographic Institution, 209 pp., 1996.
- Escartín, J., and J. Lin, Ridge offsets, normal faulting, and gravity anomalies of slow spreading ridges, *J. Geophys. Res.*, 100, 6163-6177, 1995.
- Fox, J., N. R. Grindlay, and K. C. Macdonald, The Mid-Atlantic Ridge (31°S-34°30'S): Temporal and spatial variations of accretionary processes, *Mar. Geophys. Res.*, 13, 1-20, 1991.
- Goff, J. A., B. E. Tucholke, J. Lin, G. E. Jaroslow, and M. C. Kleinrock, Quantitative analysis of abyssal hills in the Atlantic Ocean: A correlation between inferred crustal thickness and extensional faulting, *J. Geophys. Res.*, 100, 22509-22522, 1995.
- Harper, G. D., Tectonics of slow spreading mid-ocean ridges and consequences of a variable depth to the brittle/ductile transition, *Tectonics*, 4, 395-409, 1985.
- Harrison, C. G. A., and L. Stieltjes, Faulting within the median valley, *Tectonophysics*, 38, 137-144, 1977.
- Kappel, E. S., and W. B. F. Ryan, Sea Beam bathymetry along the Mid-Atlantic Ridge provides evidence of abyssal hill formation, *EOS, Trans. Am. Geophys. Union*, 72, 44, 467, 1991.
- Karson, J. A., Seafloor spreading on the Mid-Atlantic Ridge: Implications for the structure of ophiolites and oceanic lithosphere produced in slow-spreading environments. In:

- J. Malpas, E. M. Moores, A. Panyiotou and C. Xenophontos (Eds), *Ophiolites: Oceanic Crustal Analogues*. Geol. Surv. Dept., Nicosia, Cyprus, 547-555, 1990.
- Karson, J. A., and H. J. B. Dick, Tectonics of ridge-transform intersections at the Kane Fracture Zone, Mar. Geophys. Res., 6, 51-98, 1983.
- Karson, J. A., and H. J. B. Dick, Deformed and metamorphosed oceanic crust on the Mid-Atlantic Ridge, *Ophioliti*, 9, 279-302, 1984.
- Karson, J. A., and A. T. Winters. Along-axis variations in tectonic extension and accommodation zones in the MARK Area, Mid-Atlantic Ridge 23° N latitude. In: L. M. Parson, B. J. Murton and Browning (Eds.), *Ophiolites and their Modern Oceanic Analogues*. Geol. Soc. Spec. Publ., 60, 107-116, 1992.
- Kong, L., R. S. Detrick, P. J. Fox, L. A. Mayer, and W. B. F. Ryan, The morphology and tectonics of the MARK area from SeaBeam and Sea MARC I observations (Mid-Atlantic Ridge 23°N), Mar. Geophys. Res., 10, 59-90, 1988.
- Kuo, B. Y., and D. W. Forsyth, Gravity anomalies of the ridge-transform system in the south Atlantic between 31° and 34.5°S: Upwelling centers and variations in crustal thickness, Mar. Geophys. Res., 10, 205-232, 1988.
- Lachenbruch, A. H., Dynamics of a passive spreading center, J. Geophys. Res., 81, 1883-1901, 1976.
- Laughton, A. S., and R. C. Searle, Tectonic processes on slow spreading ridges. In: M. Talwani, C. G. Harrison and D. E. Hayes (Eds.), *Deep Drilling Results in the Atlantic Ocean: Ocean Crust*. Am. Geophys. Union, Maurice Ewing Series 2, Washington, D.C., 15-32, 1979.
- Lin, J., and E. M. Parmentier, Mechanisms of lithospheric extension at mid-ocean ridges, Geophys. J., 96, 1-22, 1989.
- Lin, J., and J. Phipps Morgan, The spreading rate dependence of three-dimensional mid-ocean ridge gravity structure, Geophys. Res. Lett., 19, 13-16, 1992.
- Lin, J., G. M. Purdy, H. Schouten, J.-C. Sempéré, and C. Zervas, Evidence from gravity data for focused magmatic accretion along the Mid-Atlantic Ridge, Nature, 344, 627-632, 1990.
- Lin, J., B. E. Tucholke, and M. C. Kleinrock, Off-axis "boudin-shaped" gravity lows on the western flank of the Mid-Atlantic Ridge at 25°25' - 27°10'N: Evidence for long-term pulses in magmatic accretion in spreading segments, EOS, Trans. Am. Geophys. Union, 74, 380, 1993.

- Macdonald, K. C., The crest of the Mid-Atlantic Ridge: Models for crustal generations processes and tectonics. In: P. R. Vogt and B. E. Tucholke (Eds.), *The Geology of North America, Volume M, The Western North Atlantic Region*. Geol. Soc. Amer., Boulder, 51-68, 1986.
- Macdonald, K. C., and T. M. Atwater, Evolution of rifted ocean ridges, *Earth Planet. Sci. Lett.*, 39, 319-327, 1978.
- Macdonald, K. C., P. J. Fox, L. J. Perram, M. F. Eisen, R. M. Haymon, S. P. Miller, S. M. Carbotte, M.-H. Cormier, and A. N. Shor, A new view of the mid-ocean ridge from the behavior of ridge-axis discontinuities, *Nature*, 335, 217-225, 1988.
- Macdonald, K. C., and B. P. Luyendyk, Deep-tow studies of the structure of the Mid-Atlantic Ridge crest near lat 37°N, *Geol. Soc. Am. Bull.*, 88, 621-636, 1977.
- McAllister, E., *Tectonics of a slow spreading ridge*. Ph.D. Thesis. The University of Leeds, 177 pp., 1995.
- Mutter, J. C., and J. A. Karson, Structural processes at slow-spreading ridges, *Science*, 257, 627-634, 1992.
- Needham, H. D., and J. Francheteau, Some characteristics of the rift valley in the Atlantic Ocean near 36°48' North, *Earth Planet. Sci. Lett.*, 22, 29-43, 1974.
- Neumann, G. A., and D. W. Forsyth, The paradox of the axial profile: Isostatic compensation along the axis of the Mid-Atlantic Ridge?, *J. Geophys. Res.*, 98, 17891-17910, 1993.
- Pariso, J. E., and J.-C. Sempéré, Temporal and spatial variations in crustal accretion along the Mid-Atlantic Ridge (29°-31°30'N) over the last 10 m.y.: Implications from a three-dimensional gravity study, *J. Geophys. Res.*, 100, 17781-17794, 1995.
- Parsons, B., and J. G. Sclater, An analysis of the variation of ocean floor bathymetry and heat flow with age, *J. Geophys. Res.*, 82, 803-827, 1977.
- Phipps Morgan, J., E. M. Parmentier, and J. Lin, Mechanisms for the origin of mid-ocean ridge axial topography: Implications for the thermal and mechanical structure of accreting plate boundaries, *J. Geophys. Res.*, 92, 12823-12836, 1987.
- Purdy, G. M., J.-C. Sempéré, H. Schouten, D. L. Dubois, and R. Goldsmith, Bathymetry of the Mid-Atlantic Ridge, 24° - 31°N: A map series, *Mar. Geophys. Res.*, 12, 247-252, 1990.

- Reinen, L. A., J. D. Weeks, and T. E. Tullis, The frictional behavior of serpentinite: Implications for aseismic creep on shallow crustal faults, *Geophys. Res. Lett.*, 18, 10, 1921-1924, 1991.
- Rona, A., R. N. Harbison, B. G. Bassinger et al., Tectonic fabric and hydrothermal activity of Mid-Atlantic Ridge Crest (Lat. 26°N), *Geol. Soc. Am. Bull.*, 87, 661-674, 1976.
- Rona, A., R. N. Harbison, and S. A. Bush, Abyssal hills of the eastern central North Atlantic, *Mar. Geol.*, 16, 275-292, 1974.
- Scholz, C. H., N. H. Dawers, J.-Z. Yu, and M. H. Anders, Fault growth and fault scaling laws: Preliminary results, *J. Geophys. Res.*, 98, 21951-21961, 1993.
- Schouten, H., K. D. Klitgord, and J. A. Whitehead, Segmentation of mid-ocean ridges, *Nature*, 317, 225-229, 1985.
- Sclater, J. G., and L. Wixon, The relationship between depth and age and heat flow and age in the western North Atlantic. In: P. R. Vogt and B. E. Tucholke (Eds.), *The Geology of North America, Volume M, The Western North Atlantic Region*. *Geol. Soc. Am.*, Boulder, 257-270, 1986.
- Searle, R. C., and A. S. Laughton, Sonar studies of the Mid-Atlantic Ridge and Kurchatov Fracture Zone, *J. Geophys. Res.*, 82, 5313-5328, 1977.
- Searle, R. C., and A. S. Laughton, Fine-scale sonar study of tectonics and volcanism of the Reykjanes Ridge, *Ocean. Acta.*, 5-13, 1981.
- Sempéré, J.-C., P. Blondel, A. Briaies, T. Fugiwara, L. Géli, N. Isezaki, J. E. Pariso, L. Parson, P. Patriat, and C. Rommevaux, The Mid-Atlantic Ridge between 29°N and 31°30'N in the last 10 Ma, *Earth Planet. Sci. Lett.*, 130, 45-55, 1995.
- Sempéré, J.-C., J. Lin, H. Brown, H. Schouten, and G. M. Purdy, Segmentation and morphotectonic variations along a slow-spreading center: The Mid-Atlantic Ridge (24°00'N-30°40'N), *Mar. Geophys. Res.*, 15, 153-2000, 1993.
- Sempéré, J.-C., G. M. Purdy, and H. Schouten, Segmentation of the Mid-Atlantic Ridge between 24°N and 30°40'N, *Nature*, 344, 427-431, 1990.
- Severinghaus, J., and K. C. Macdonald, High inside corners at ridge-transform intersections, *Mar. Geophys. Res.*, 9, 353-367, 1988.
- Shaw, P. R., Ridge segmentation, faulting and crustal thickness in the Atlantic Ocean, *Nature*, 358, 490-493, 1992.
- Shaw, P. R., and J. Lin, Causes and consequences of variations in faulting style at the Mid-Atlantic Ridge, *J. Geophys. Res.*, 98, 21839-21851, 1993.

- Solomon, S. C., Y. Huang, and L. Meinke, The seismic moment budget of slowly spreading ridges, *Nature*, 334, 469-481, 1988.
- Sykes, L. R., Mechanism of earthquakes and nature of faulting on the mid-oceanic ridges, *J. Geophys. Res.*, 72, 2131-2153, 1967.
- Tapponnier, P., and J. Francheteau, Necking of the lithosphere and the mechanics of slowly accreting plate boundaries, *J. Geophys. Res.*, 83, 3955-3870, 1978.
- Thatcher, W., and D. Hill, A simple model for the fault-generated morphology of slow-spreading mid-oceanic ridges, *J. Geophys. Res.*, 100, 561-570, 1995.
- Tolstoy, M., A. J. Harding, and J. A. Orcutt, Crustal thickness on the Mid-Atlantic Ridge: Bull's-eye gravity anomalies and focused accretion, *Science*, 262, 726-729, 1993.
- Tucholke, B. E., and J. Lin, A geological model for the structure of ridge segments in slow-spreading oceanic crust, *J. Geophys. Res.*, 99, 11937-11958, 1994.
- Tucholke, B. E., J. Lin, and M. C. Kleinrock, Crustal structure of spreading segments on the western flank of the Mid-Atlantic ridge at 25°25'N to 27°10'N, *EOS, Trans. Am. Geophys. Union*, 73, 537, 1992.
- Tucholke, B. E., J. Lin, and M. C. Kleinrock, Mullions, megamullions, and metamorphic core complexes on the Mid-Atlantic Ridge, *EOS, Trans. Am. Geophys. Union*, 77, 724, 1996.
- Tucholke, B. E., J. Lin, M. C. Kleinrock, M. A. Tivey, T. B. Reed, J. Goff, and G. E. Jaroslow, Segmentation and crustal structure of the western Mid-Atlantic Ridge flank, 25°30' - 27°10'N and 0 - 29 m.y., *J. Geophys. Res.*, (in press, a).
- Tucholke, B. E., and H. Schouten, Kane Fracture Zone, *Mar. Geophys. Res.*, 10, 1-39, 1988.
- Tucholke, B. E., W. K. Stewart, and M. C. Kleinrock, Long-term denudation of ocean crust in the central North Atlantic Ocean, *Geology*, (in press, b).
- Ulmer, P., and Trommsdorff, Serpentine stability to mantle depths and subduction related magmatism, *Science*, 268, 858-861, 1995.
- Whitehead, J. A., H. J. B. Dick, and H. Schouten, A mechanism for magmatic accretion under spreading centers, *Nature*, 312, 146-148, 1984.
- Whitmarsh, R. B., and A. S. Laughton, A long-range sonar study of the Mid-Atlantic Ridge crest near 37°N (FAMOUS area) and its tectonic implications, *Deep Sea Res.*, 23, 1005-1023, 1976.

- Wolfe, C. J., G. M. Purdy, D. R. Toomey, and S. C. Solomon, Microearthquake characteristics and crustal velocity structure at 29°N on the Mid-Atlantic Ridge: The architecture of a slow spreading ridge, *J. Geophys. Res.*, 100, 24449-24472, 1995.
- Zonenshain, L. P., M. I. Kuzmin, A. Lisitsin et al., Tectonics of the Mid-Atlantic rift valley between the TAG and MARK areas (26-24°N): Evidence for vertical tectonism, *Tectonophysics*, 159, 1-23, 1989.

Table 1: Fault Parameters of Inward- and Outward-Facing Faults

Parameter	Inward	Outward
Dip (°):		
Range	4 - 45	4 - 45
Mean	14 ± 7	14 ± 7
Median	13	13
Throw (m):		
Range	60 - 1520	60 - 1540
Mean	365 ± 205	370 ± 195
Median	315	330
Heave (m):		
Range	460 - 4650	510 - 3350
Mean	1180 ± 550	1215 ± 495
Median	1050	1125

Table 2: Area Strain by Ridge Segment

Segment(s)	ϵ	ϵ_{45°
8, 9, & 10	0.30 ± 0.08	0.06 ± 0.04
8	0.30 ± 0.09	0.06 ± 0.04
9	0.31 ± 0.06	0.06 ± 0.05
10	0.29 ± 0.09	0.05 ± 0.04

Table 3: Fault and Strain Parameters Versus RMBA Values

Parameter	Low RMBA (< 7 mGal)	Intermd. RMBA (7 - 15 mGal)	High RMBA (>15 mGal)
Dip (°):			
Range	4 - 43	4 - 45	4 - 45
Mean	14 ± 7	14 ± 6	15 ± 7
Median	12	13	14
Throw (m):			
Range	60 - 1490	60 - 1520	60 - 1490
Mean	320 ± 185	345 ± 180	435 ± 215
Median	270	300	390
Heave (m):			
Range	520 - 4850	460 - 4880	510 - 6500
Mean	1120 ± 480	1160 ± 490	1300 ± 595
Median	1015	1060	1180
% of Outward Facing Faults:	27%	39%	53%
ε:	0.16	0.24	0.27
L (km):	1470	2890	1916
L/A (km ⁻¹):	0.125	0.166	0.163

Table 4: Fault Parameters Associated with Intrasegment Province

Parameter	IC	SC	OC
Dip (°):			
Range	4 - 45	4 - 44	4 - 43
Mean	14 ± 7	15 ± 7	14 ± 6
Median	13	13	12
Throw (m):			
Range	60 - 1540	75 - 1540	60 - 1500
Mean	405 ± 210	355 ± 195	325 ± 170
Median	360	300	285
Heave (m):			
Range	460 - 4650	510 - 3250	535 - 2475
Mean	1260 ± 595	1150 ± 470	1145 ± 470
Median	1130	1050	1045

Table 5: Strain Parameters Associated with Intrasegment Province by Segment

Region	ϵ	L (km)	L/A (km⁻¹)	H (km)
<i>Segment 8:</i>				
IC	0.51	1219	0.211	1.230
SC	0.26	390	0.156	1.122
OC	0.21	822	0.143	1.141
Ends (Ave.)	0.36	2040	0.177	1.195
<i>Segment 9:</i>				
IC	0.44	1248	0.282	1.297
SC	0.29	590	0.131	1.162
OC	0.26	552	0.125	1.184
Ends (Ave.)	0.35	1800	0.203	1.261
<i>Segment 10:</i>				
IC	0.35	433	0.182	1.240
SC	0.33	511	0.185	1.180
OC	0.26	396	0.166	1.108
Ends (Ave.)	0.30	829	0.174	1.174

Figure Captions

1. Simplified map of merged Hydrosweep multibeam bathymetry of Tucholke et al. (1992) and along-axis SeaBeam bathymetry of Purdy et al. (1990). Contour interval is 1 km. Segment boundaries, as identified by Tucholke et al. (*in press, a*) are indicated by black lines; solid segment boundaries have right-stepping offsets, and dashed boundaries are left-stepping. White circles identify segments. Crustal ages are indicated by numbers and bold lines at edge of survey. The rift-valley floor encompasses crust approximately < 0.6 Ma.
2. Detailed map of merged Hydrosweep and SeaBeam (along ridge axis) multibeam bathymetry; contour interval is 100 m (from Tucholke et al., *in press, a*).
3. Example of detected edges using image processing technique described in text superimposed on a) multibeam bathymetry, and b, c) mosaicked HMR1 sidescan sonar images, prior to hand-editing of processing artifacts and removal of non-fault edges. Each edge consists of individual data points spaced 200 m apart; east-dipping edge points are identified by black or blue crosses and west-dipping points are red. This example site is located in Segment 8 on ~ 7 Ma crust. Map coordinates are in Universal Transverse Mercator units; see Figure 4 for latitude and longitude.
4. Example of the automated technique employed in measuring fault parameters. Fault throw and dip are measured directly from bathymetry and fault heave is geometrically derived. Map of bathymetry (top) is overlain by detected fault edges (black dots) The cross-section A-A', shown at bottom, is oriented in the direction of maximum local dip (i.e., apparent dip) at point "X" along the fault edge. Vertical (throw) and horizontal (apparent heave) offset are calculated for each such point along the fault edge. Example site is the same as in Figure 3.
5. Map of all inward- (blue) and outward- (red) facing normal faults identified in this study. Segment boundaries are marked by gray lines, and the ridge axis by heavy black lines. Thin black lines indicate crustal ages (Ma). The strike of most faults is subparallel to average plate-boundary orientation, marked by arrow in upper left corner.

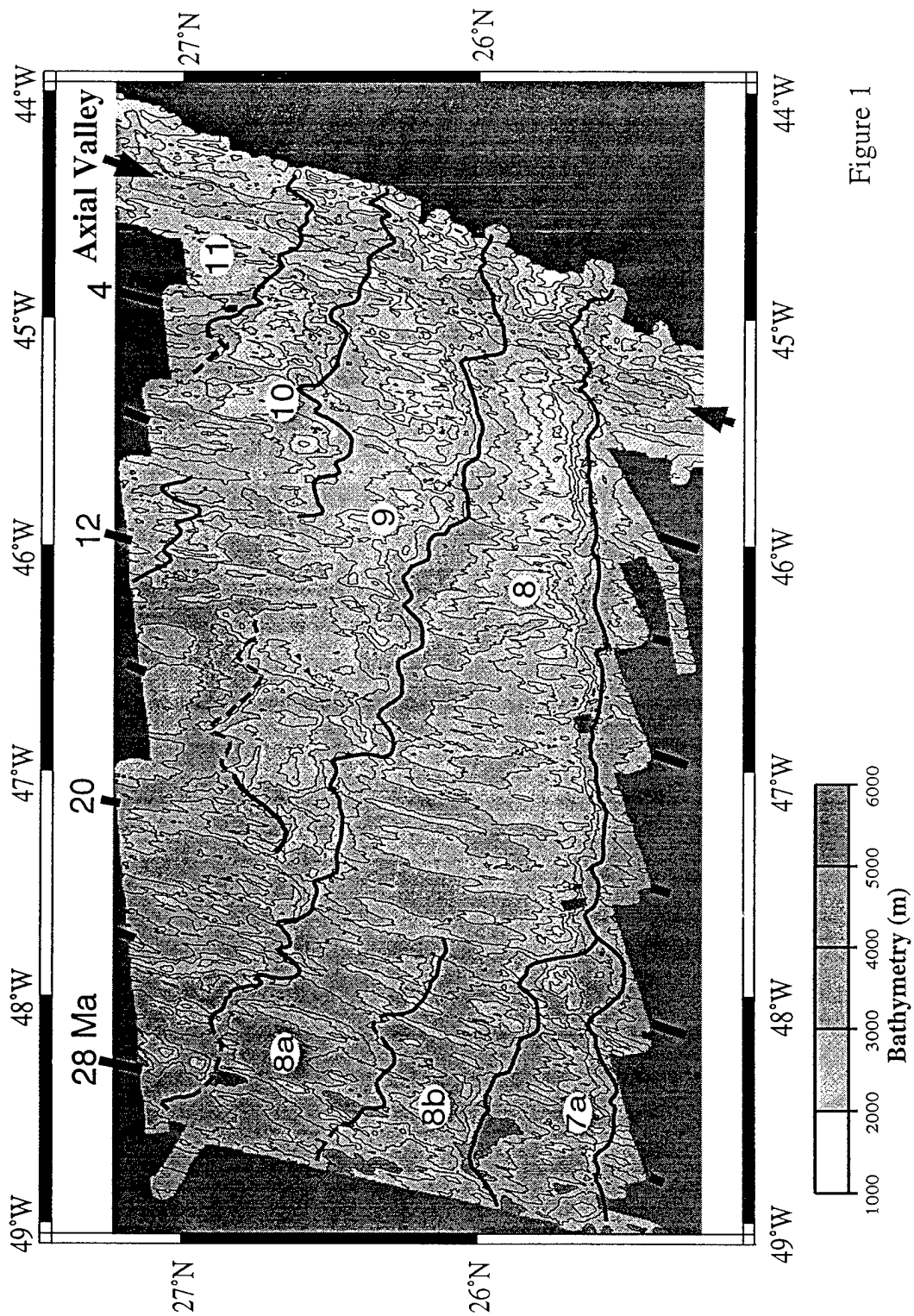
Pairs of closely spaced inward- and outward- facing faults are common, and they form elongate horsts (abyssal hills).

6. a) Histograms of fault spacing for inward- and outward-facing faults. Population bin sizes are 1 km. b) Fraction of the number of inward- and outward-facing closely spaced (≤ 2 km) faults within the total fault population; in the population of closely spaced faults, there are relatively more inward- than outward-facing faults.
7. Bathymetric map of a horst (ridge marked by arrow) formed by an inward-facing (east-dipping) and outward-facing (west-dipping) pair of faults (Segment 9, ~ 6 Ma crust). Such horsts commonly form abyssal hills on the ridge flank. Contour interval is 100 m.
8. Bathymetric map of a large outward-facing (west-dipping) fault that is not associated with a complementary east-dipping fault to form a horst (Segment 10, ~ 7 Ma crust). Fault throw is ~ 700 m. Contour interval is 100 m.
9. Histograms of fault dips for inward- and outward-facing faults. The populations of fault dips for both fault types are similar in range and distribution, although there are fewer outward-facing faults in each population bin. Bin sizes are 1 degree.
10. Map of residual mantle Bouguer anomaly (RMBA) with superimposed fault locations from Figure 5. Gravity values are < 7 mGal in dark gray areas, 7 to ≤ 15 mGal in medium gray areas, and > 15 mGal in light gray areas. RMBA data are from Tucholke et al. (*in press, a*). Segment boundaries are marked by black lines.
11. Histograms of fault spacing at inside corners, segment centers, and outside corners of Segments 8, 9, and 10. Bin size = 1 km.
12. Fraction of the number of closely spaced (≤ 2 km) faults within the total population of faults for each tectonic province by individual segment. In Segments 8 and 9, there are relatively more closely spaced faults at the segment center than at the segment ends.

13. Percentage of outward-facing fault-edge points within the total number of edge points, plotted against crustal age for all segments. Percentages were calculated for 1 m.y. age bins by intrasegment province; IC = solid line, SC = dashed line, and OC = dotted line. The percentage of outward-facing faults increases from near zero at the ridge axis to ~40% on ~ 3 - 4 Ma crust (indicated by heavy horizontal line), and it remains nearly constant on older crust.
14. Plots of fault parameters versus crustal age for individual ridge segments. Arrows indicate the age of the crest of the rift mountains in each segment. Solid lines are totals for all faults, bold dashed lines are inward-facing faults, and thin dashed lines are outward-facing faults. Data are in 1 m.y. age bins. See text for description of fault parameters.
15. a) Plots of mean throws and dips for all faults in Segments 8, 9, and 10 versus crustal age. Values are for 1 m.y. age bins. Error bars indicate 1σ standard deviation. b) Plot of mean throw versus dip (asterisks) calculated for (a) and (b). Dashed lines represent the geometrical relationship between fault throw and dip needed to maintain constant heave, labeled in meters; solid line indicates constant mean heave for our study area. The plot suggests that the mean fault heaves, geometrically derived from measured fault throws and dips, may remain relatively constant even though throws and dips decrease over time.
16. Schematic illustration of how mass-wasting and sedimentation may affect fault parameters for inactive (left) and actively growing faults (right) through time (t_1 to t_3) on the rift-valley walls. Gray shading indicates exposed, measurable fault surface. Unshaded regions indicate reduction in the measurable fault surface due to deposition of talus and sediments at the base of the fault scarp. H remains relatively constant with time because of reduction in both dip and throw (see Figure 15), but L and L/A (and thus ϵ) change significantly, as indicated.
17. Schematic cross-sections of the Mid-Atlantic Ridge from the ridge axis (right) out to ~5.5 Ma crust (no vertical exaggeration). Active faults (solid lines) and inactive faults (dashed) are located in accord with our observations. Isotherms are derived from Lin and Parmentier (1989) assuming a Nusselt number = 6. Serpentinities are indicated by

the hatched pattern. a) Model for thick crust formed during relatively magmatic extension; few inward-facing faults reach the mantle, serpentinization is minimized, and outward-facing faults thus form rarely and only in locations where serpentinites create a thin brittle lid. b) Model for thin crust formed during relatively amagmatic extension; inward-facing faults commonly reach the mantle, a serpentinite layer is well developed, and outward-facing faults readily form in the thin brittle lid.

18. Single-channel seismic reflection profile over 13 Ma crust showing a rollover structure in ponded sediments that suggests recent off-axis faulting. The fault is located at 26°26'N, 46°43'W in Segment 9. Profile JD218, 0000Z, R/V Ewing Cruise 9208.



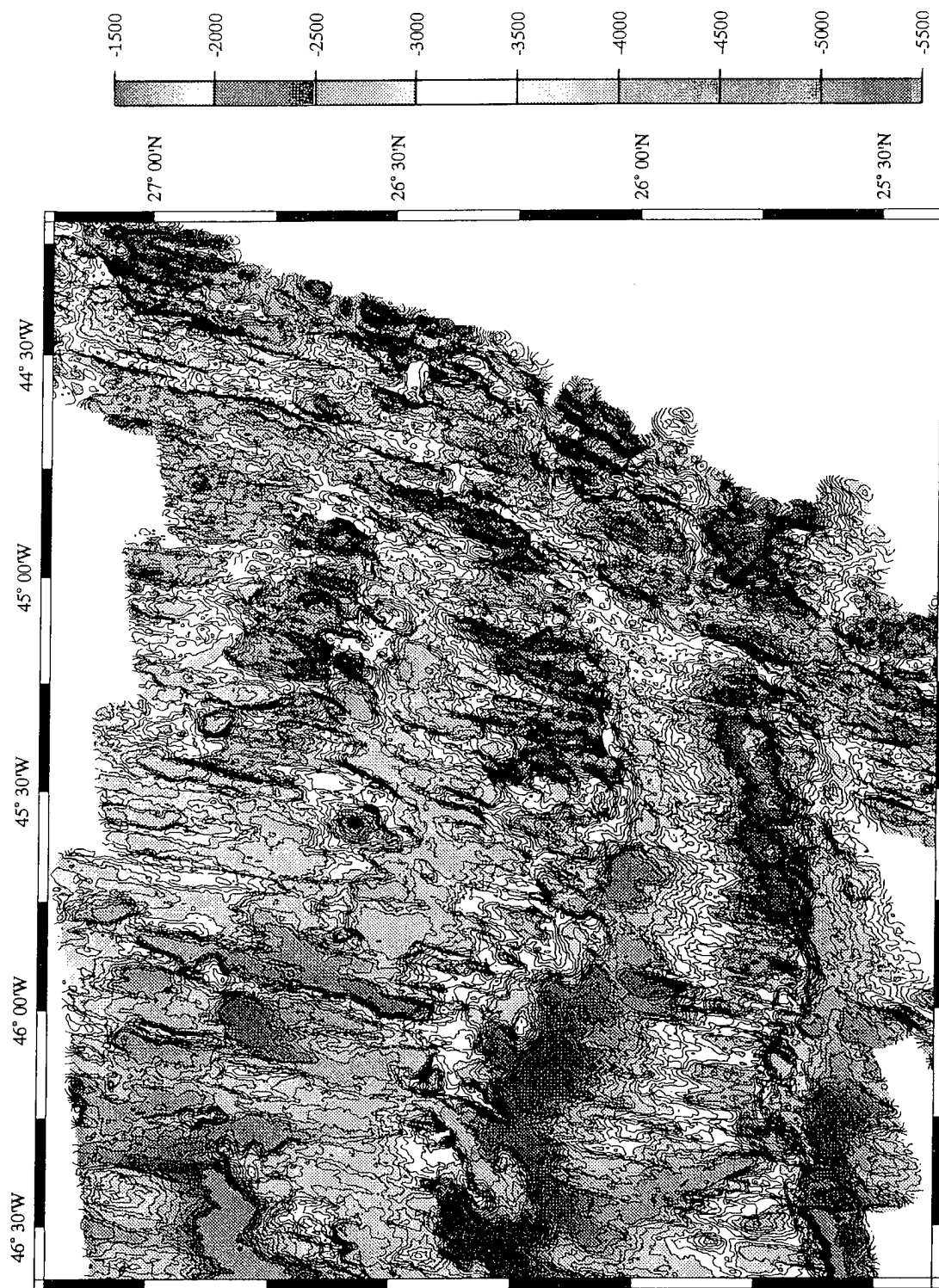


Figure 2 (first half)

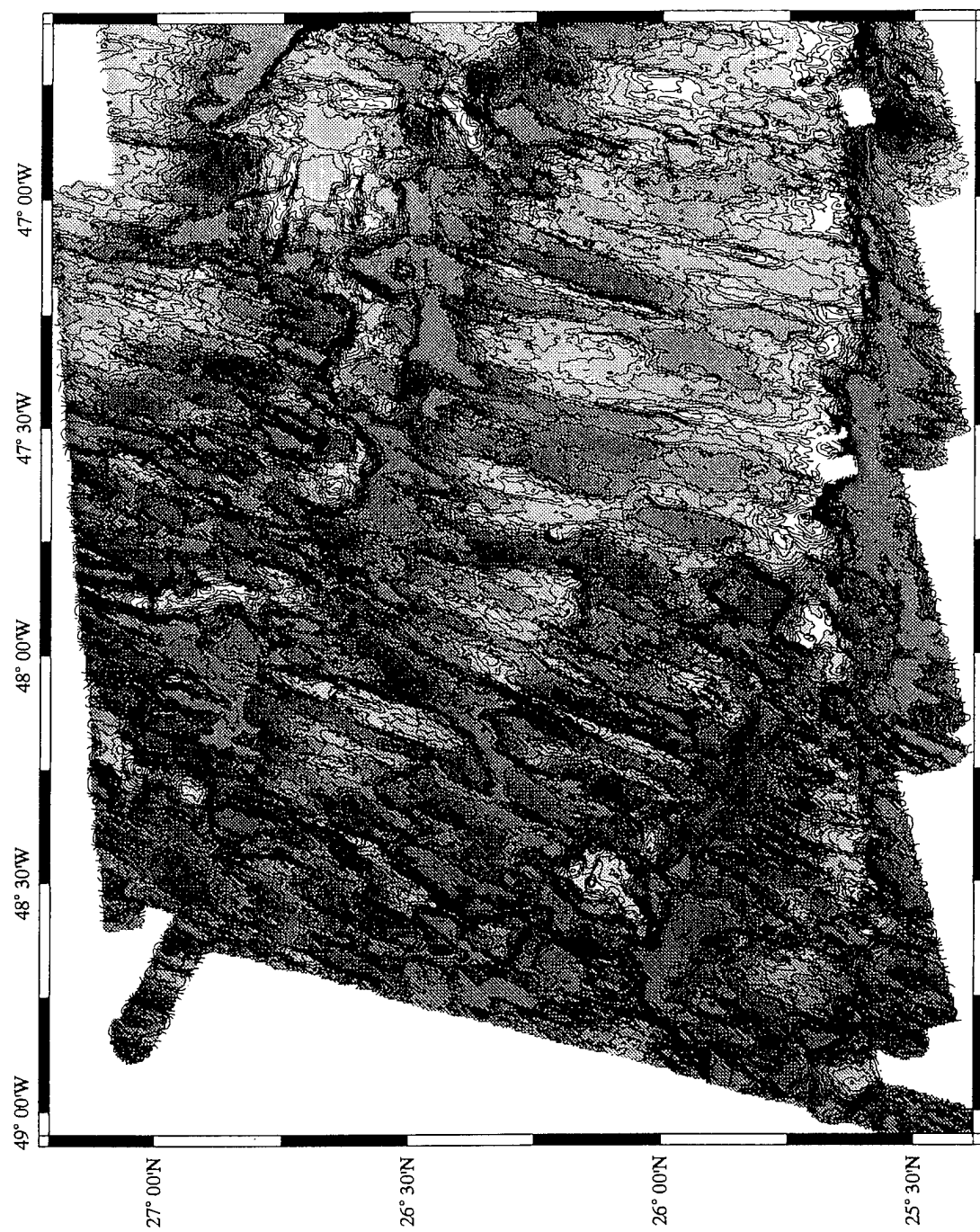


Figure 2 (second half)

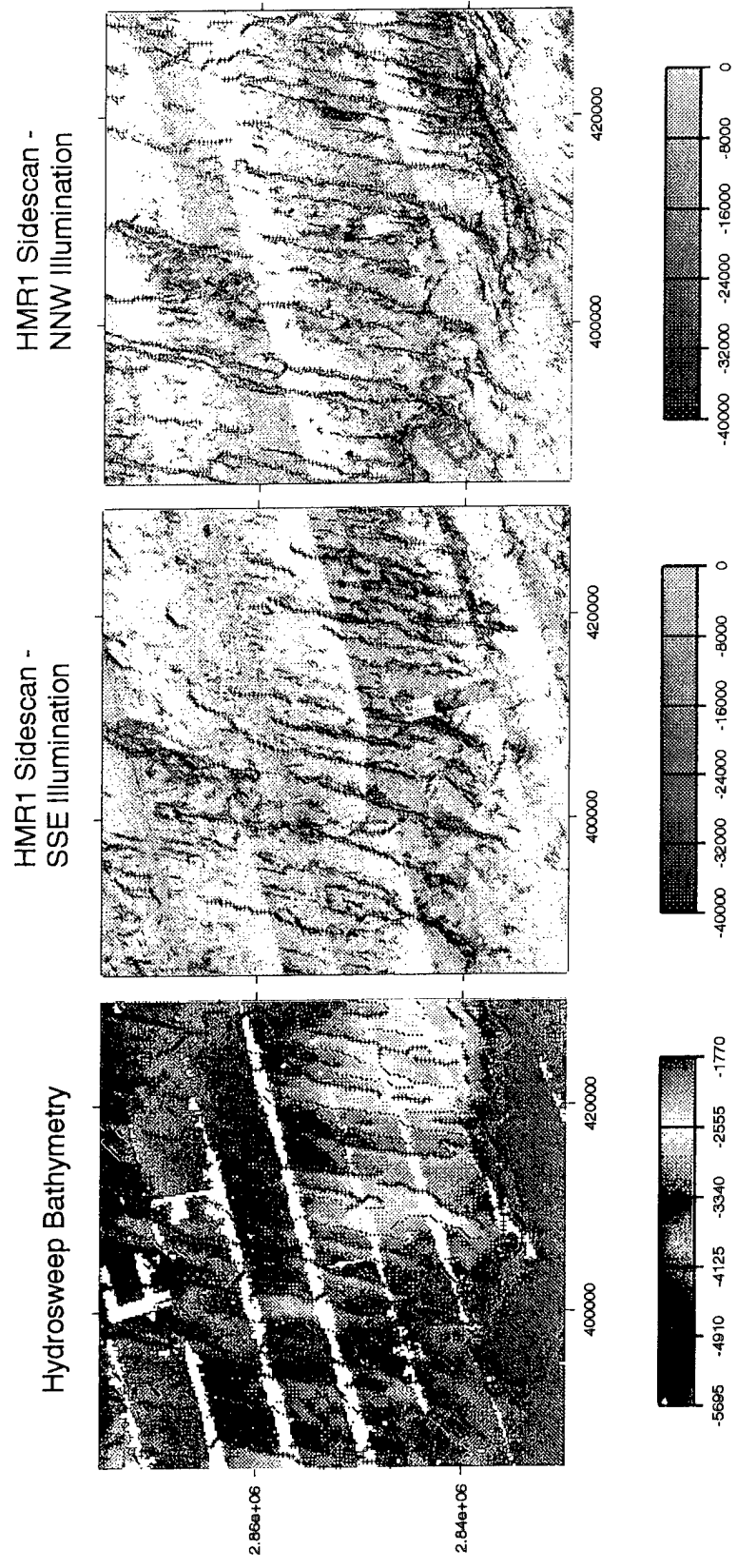


Figure 3

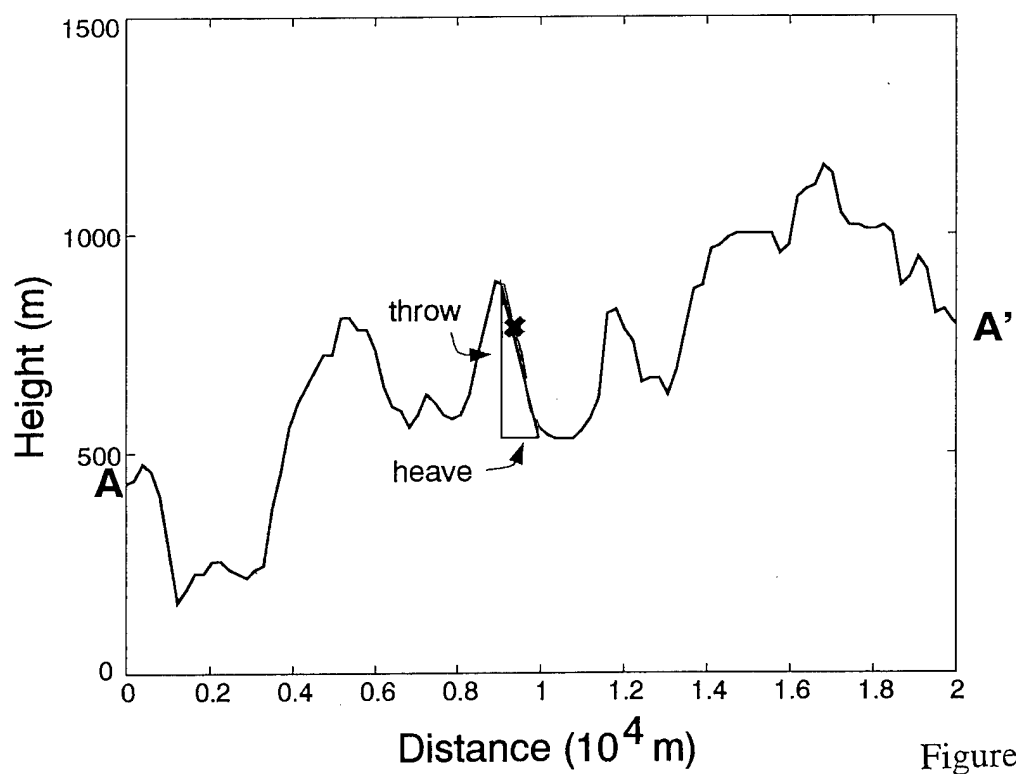
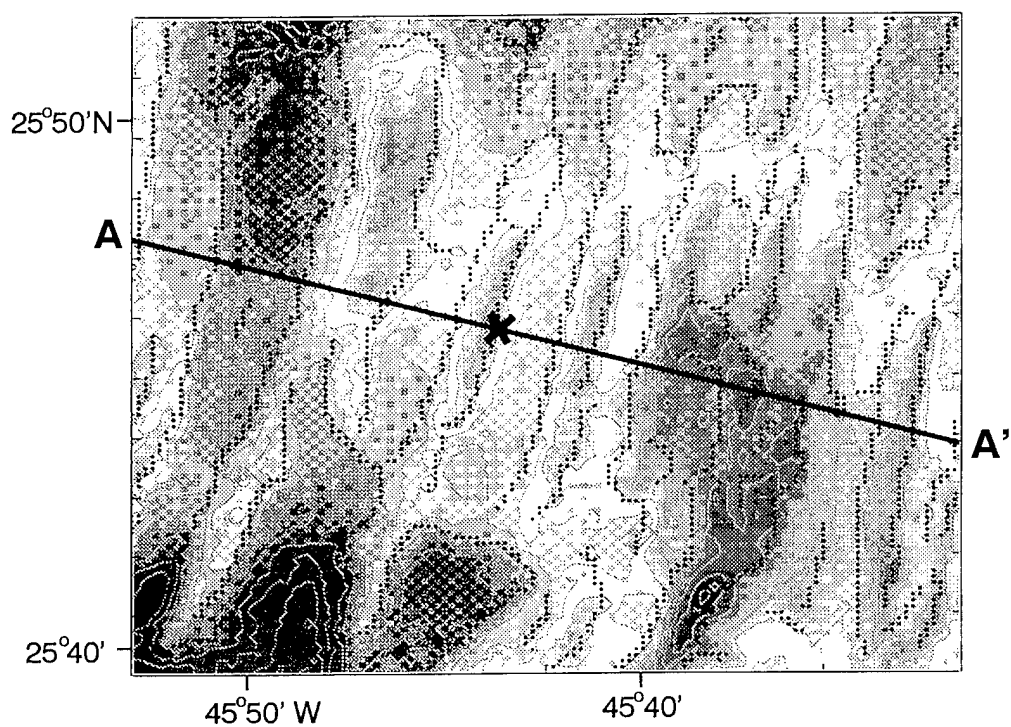


Figure 4

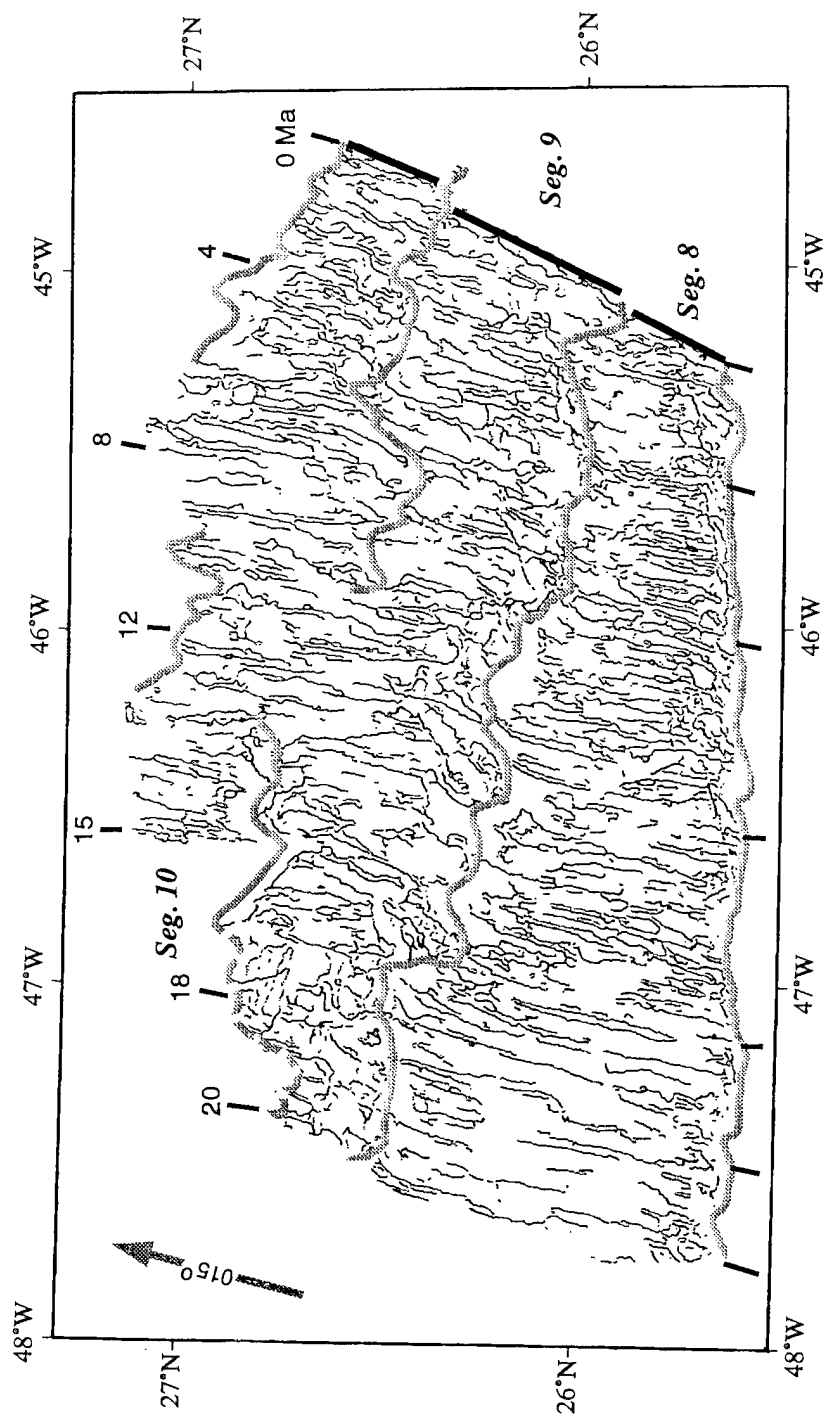


Figure 5

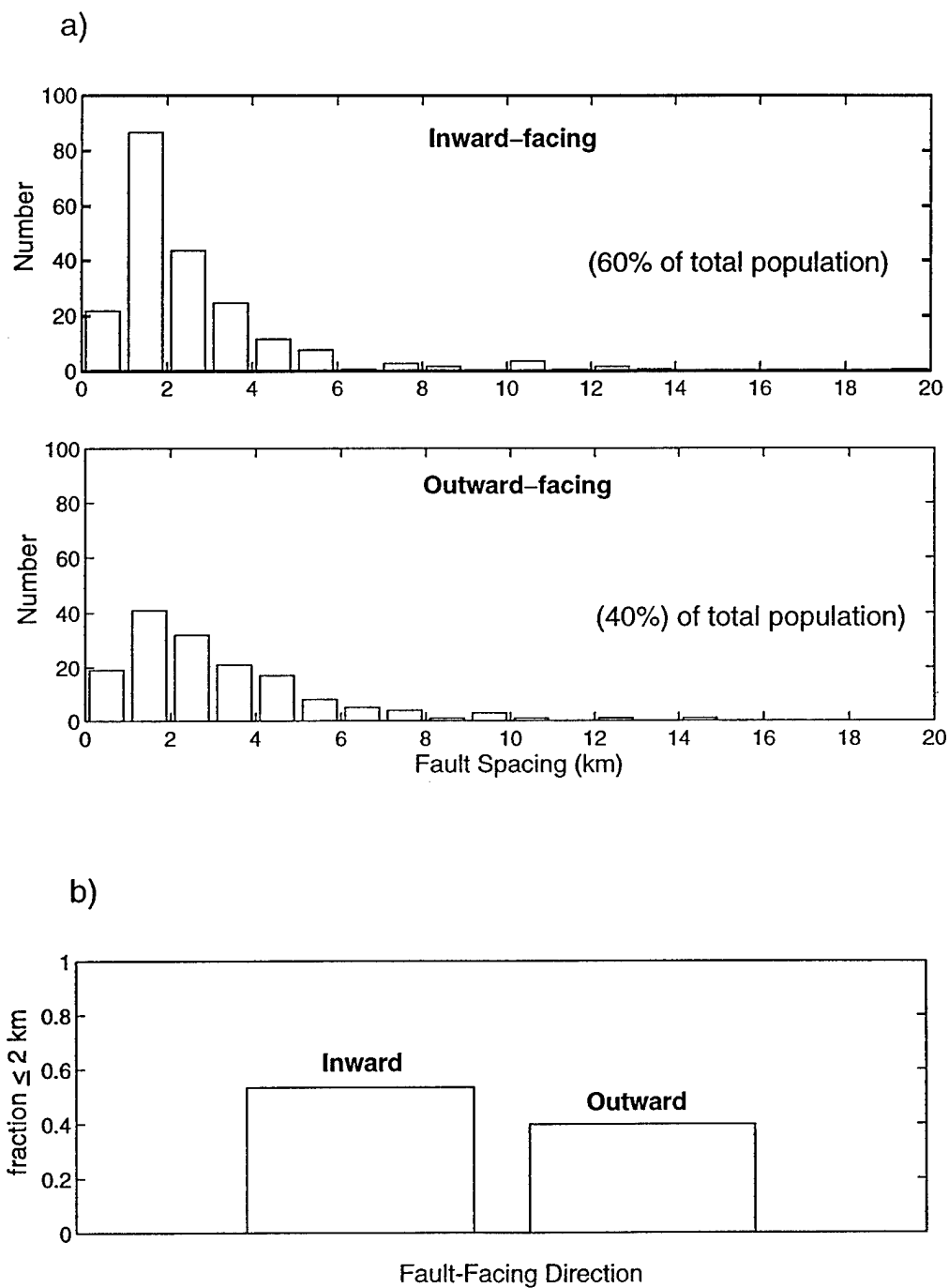


Figure 6

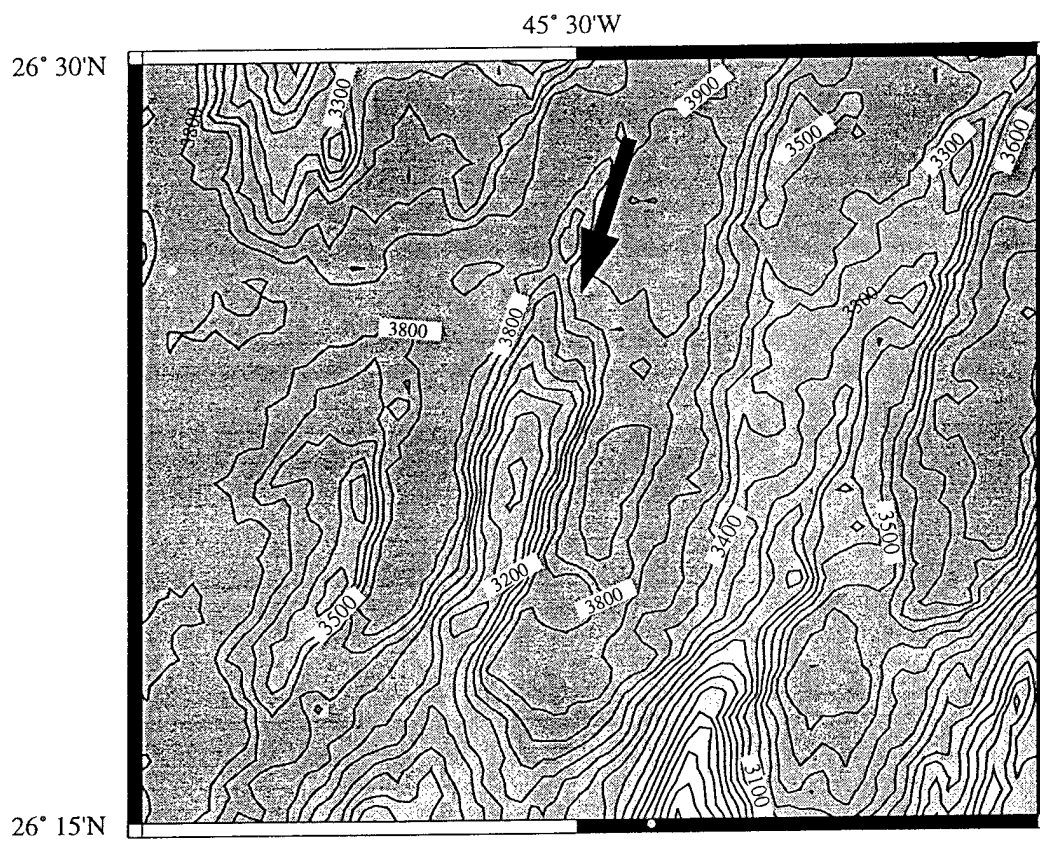


Figure 7

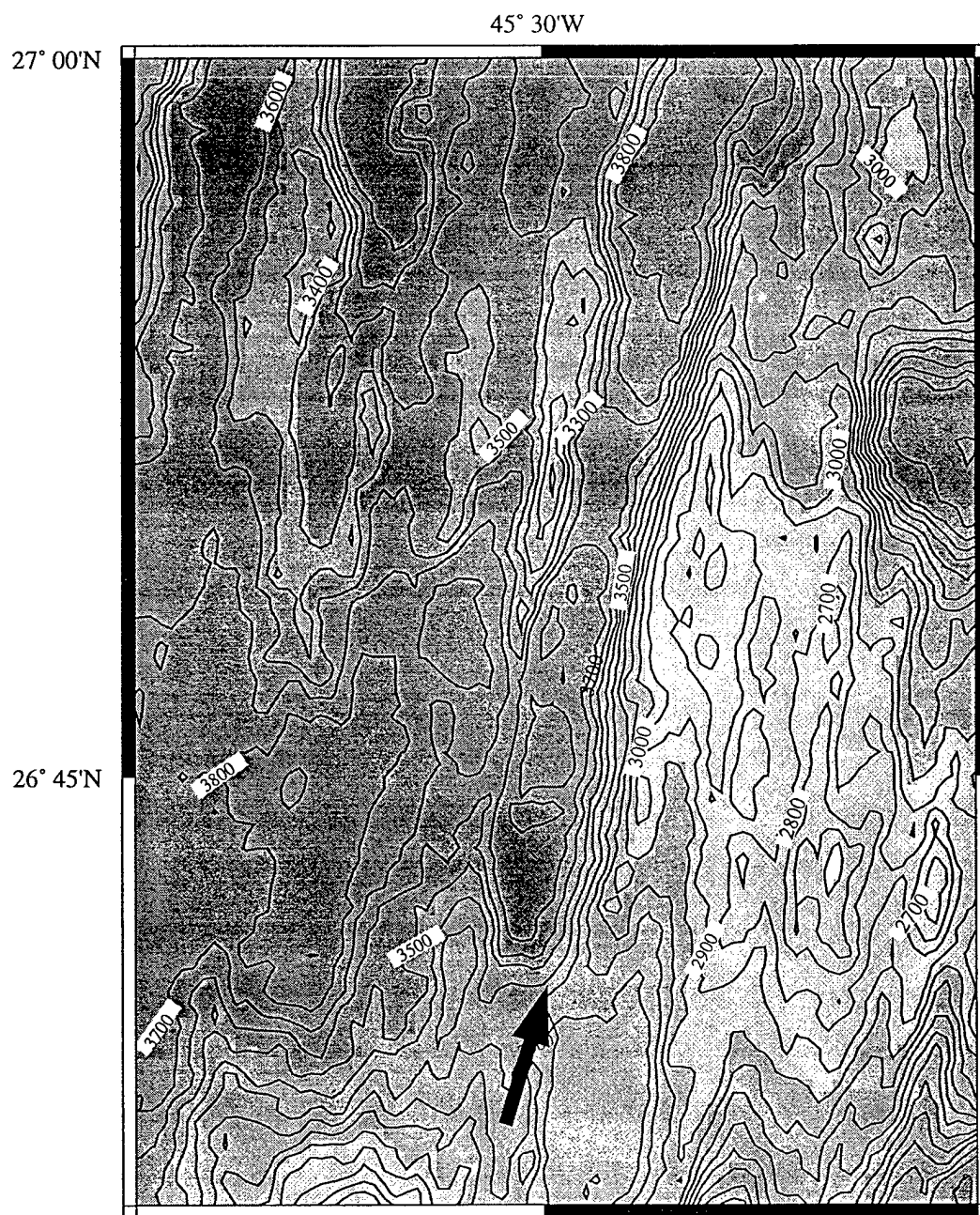


Figure 8

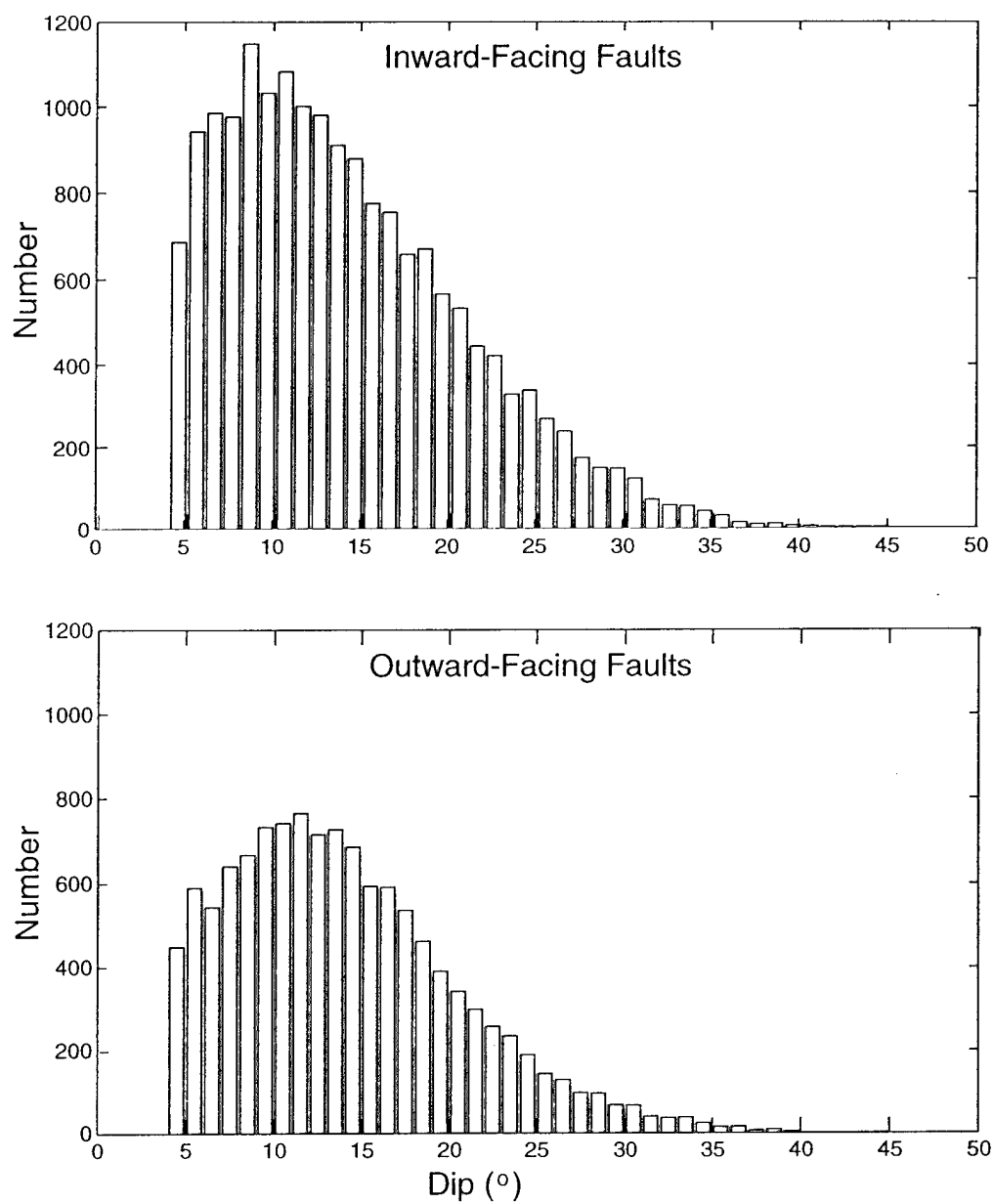


Figure 9

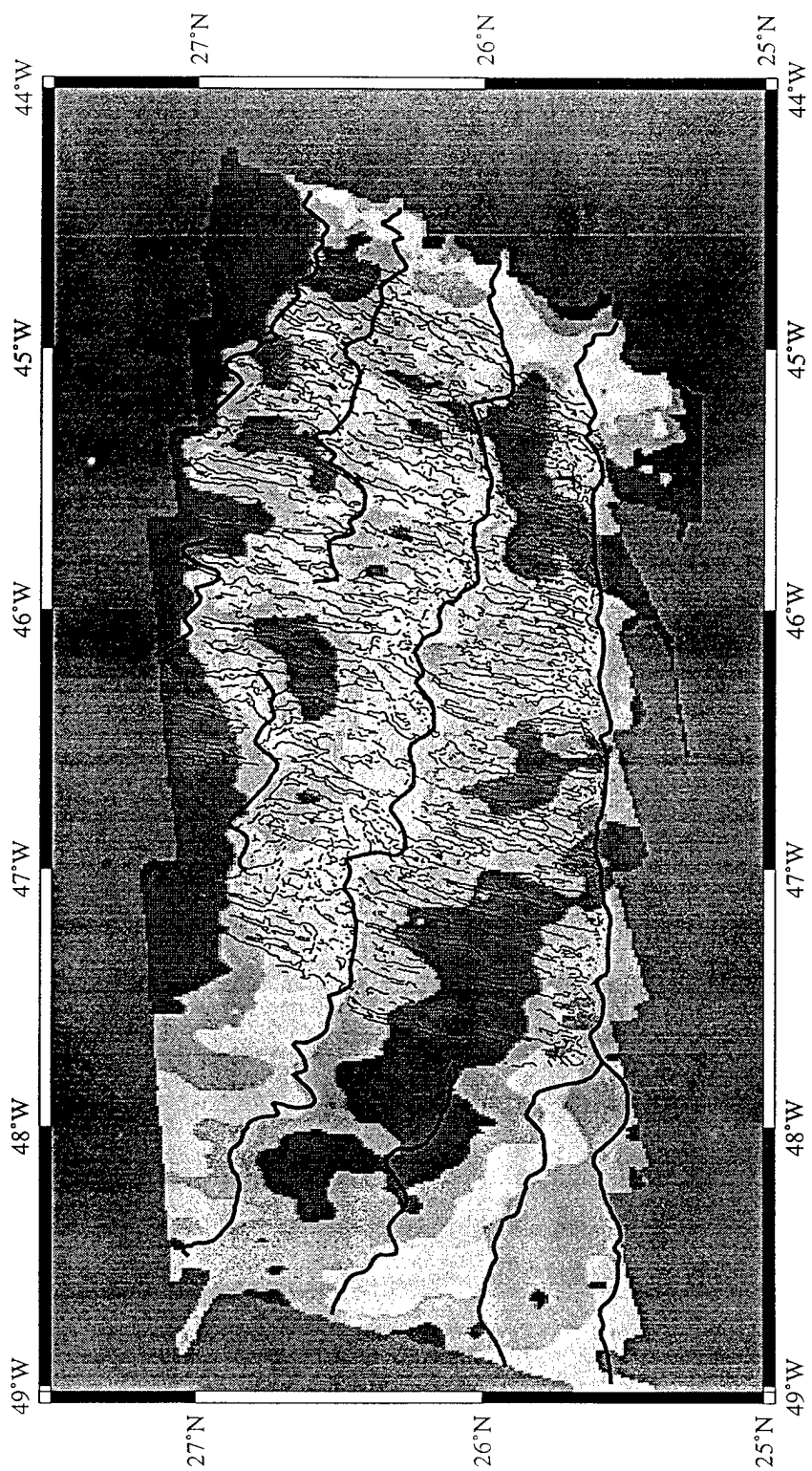


Figure 10

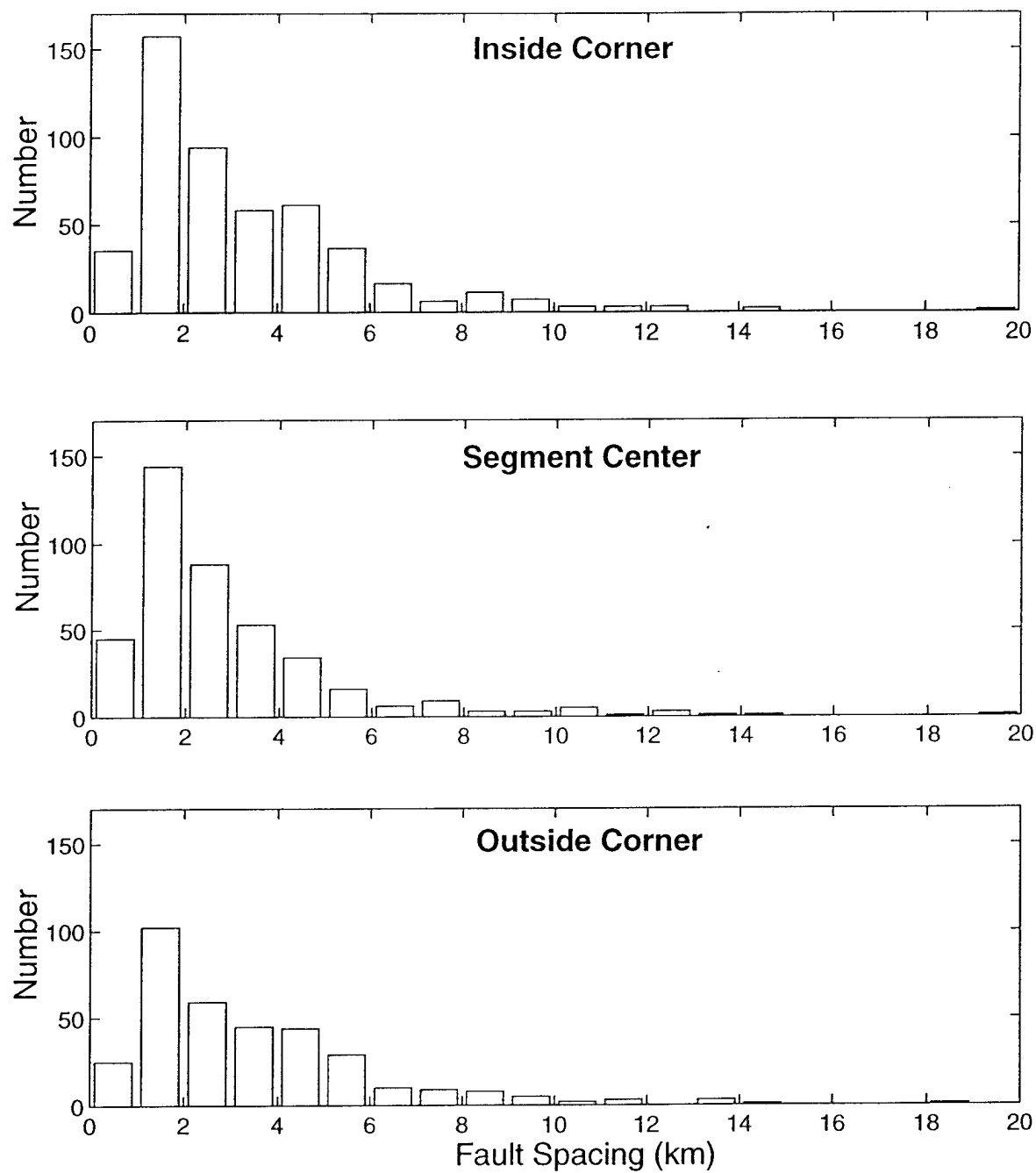


Figure 11

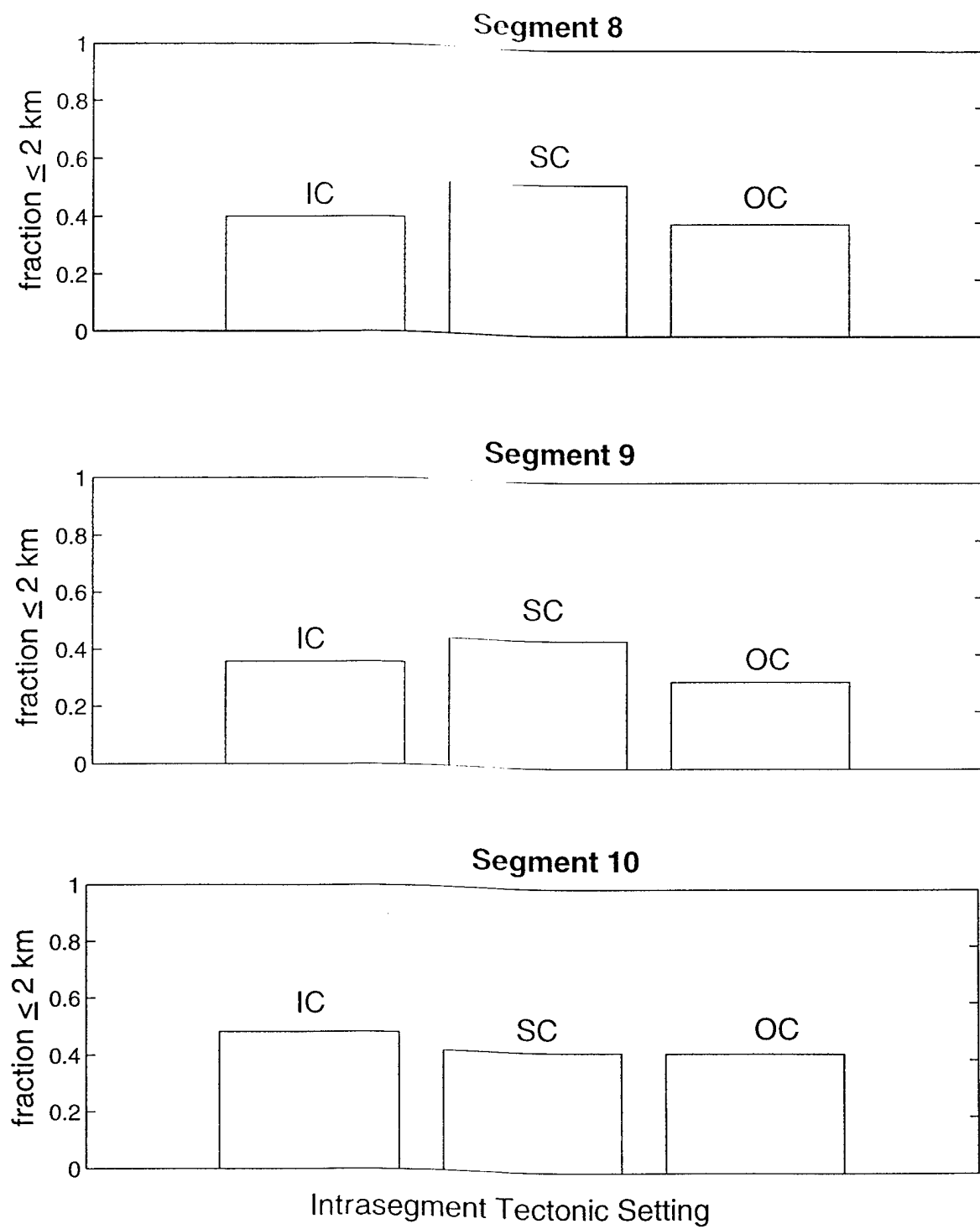


Figure 12

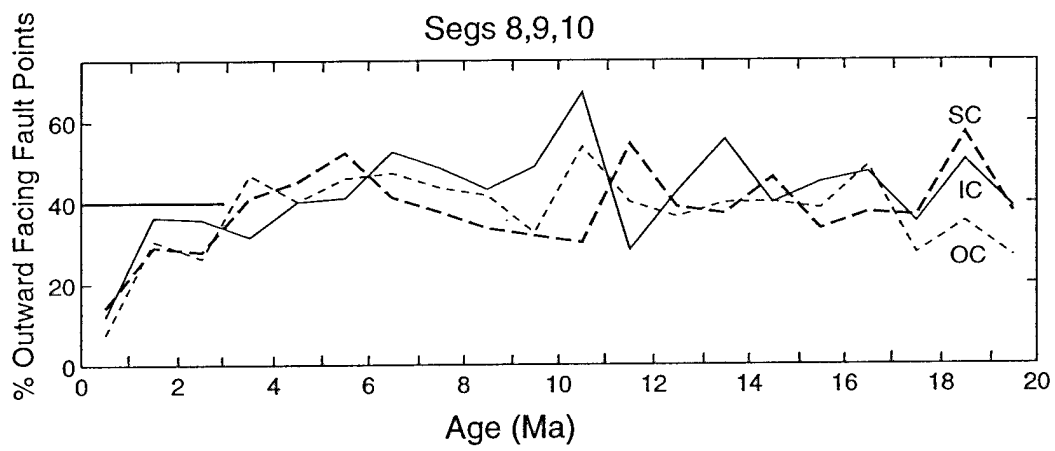


Figure 13

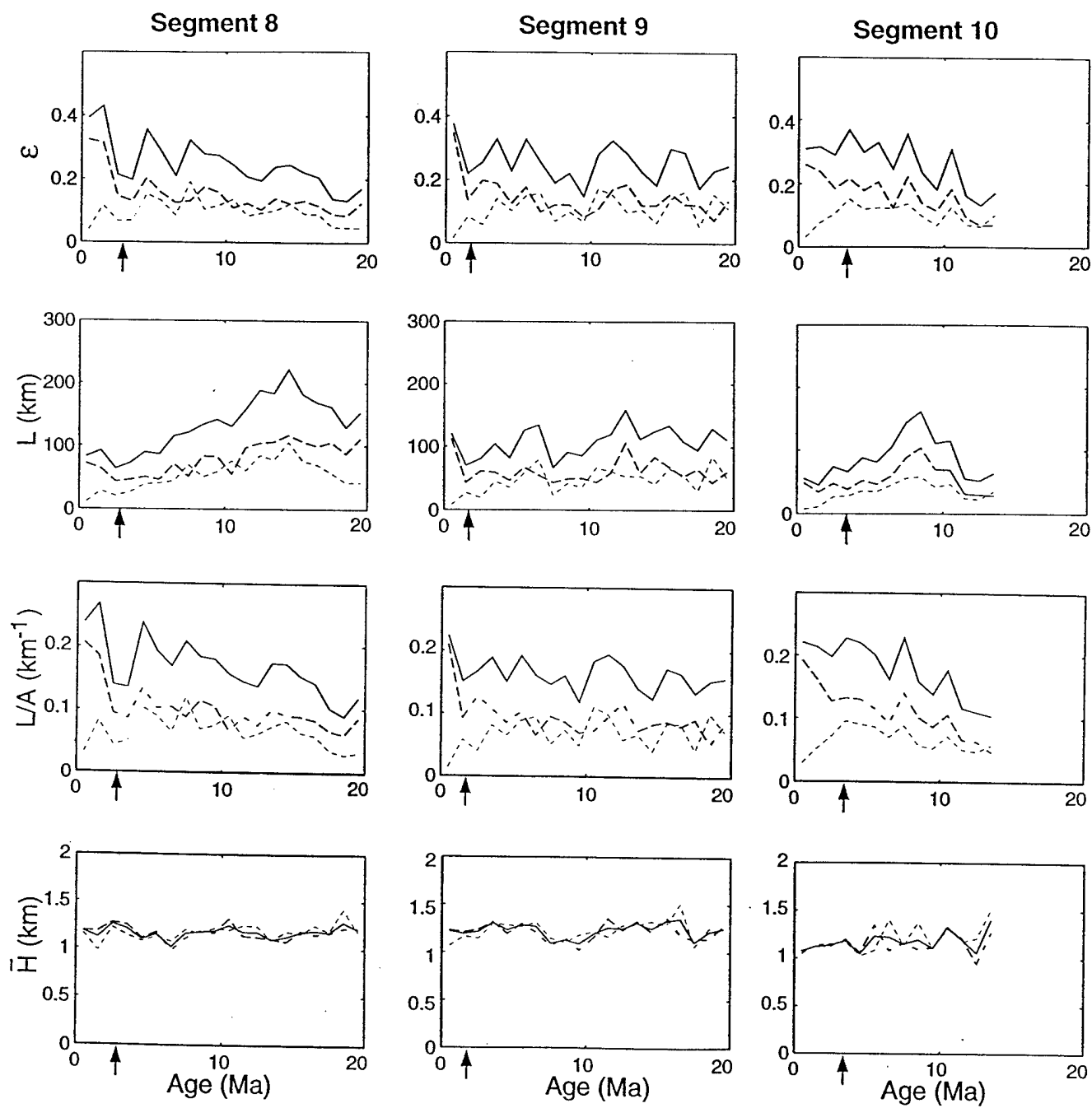
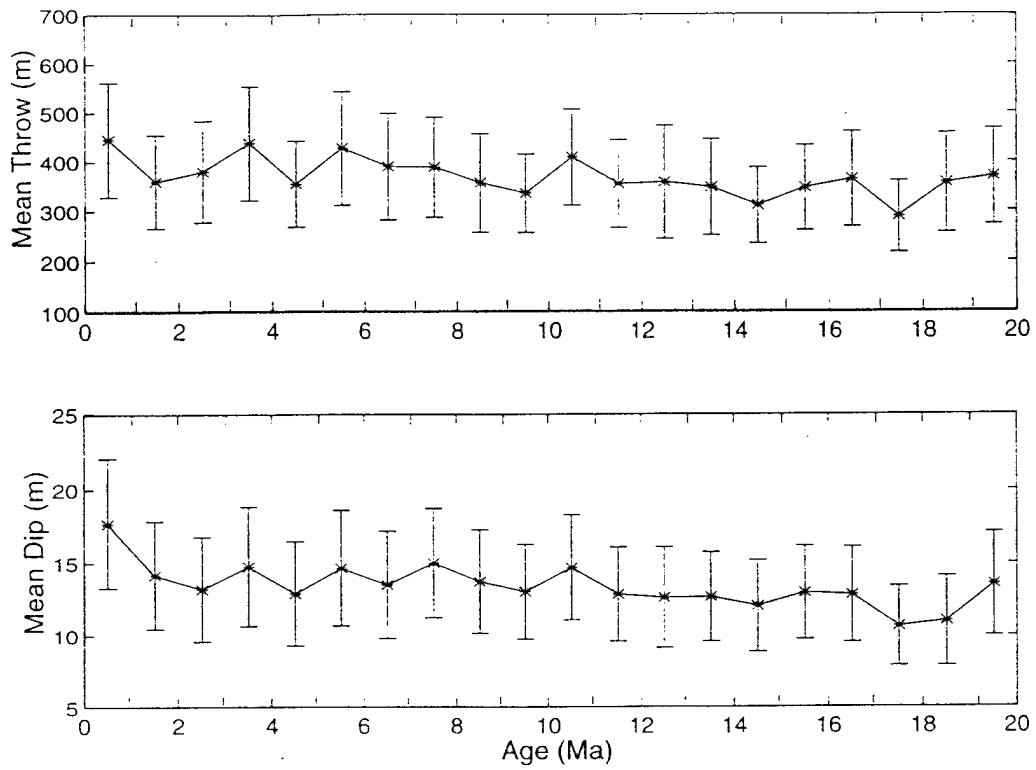


Figure 14

a)



b)

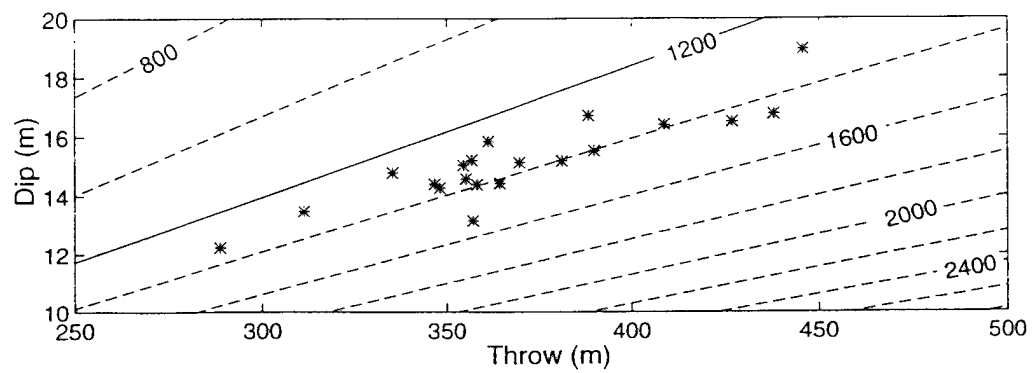


Figure 15

RIFT-VALLEY WALL

Horizontal Views into Fault Faces

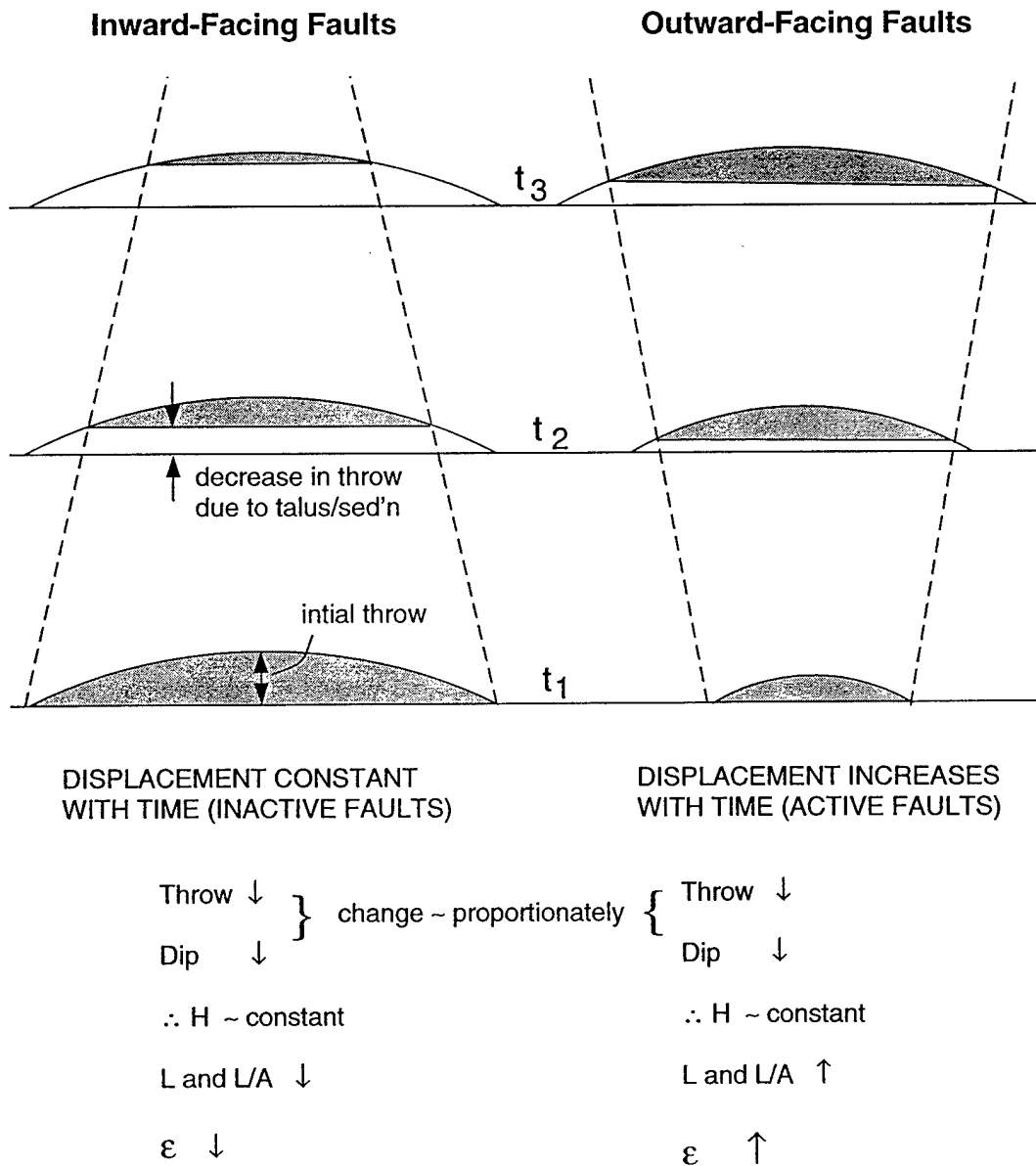


Figure 16

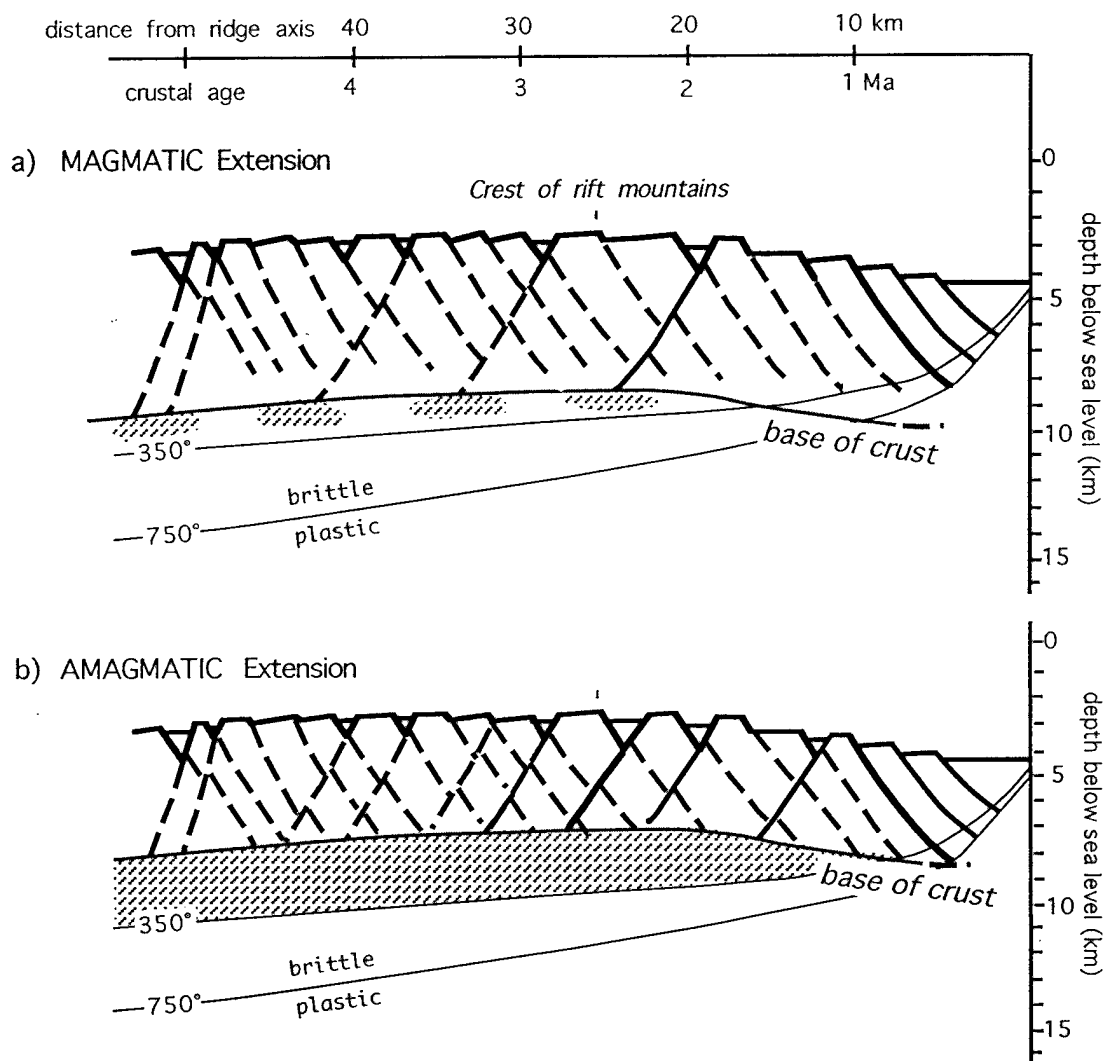


Figure 17

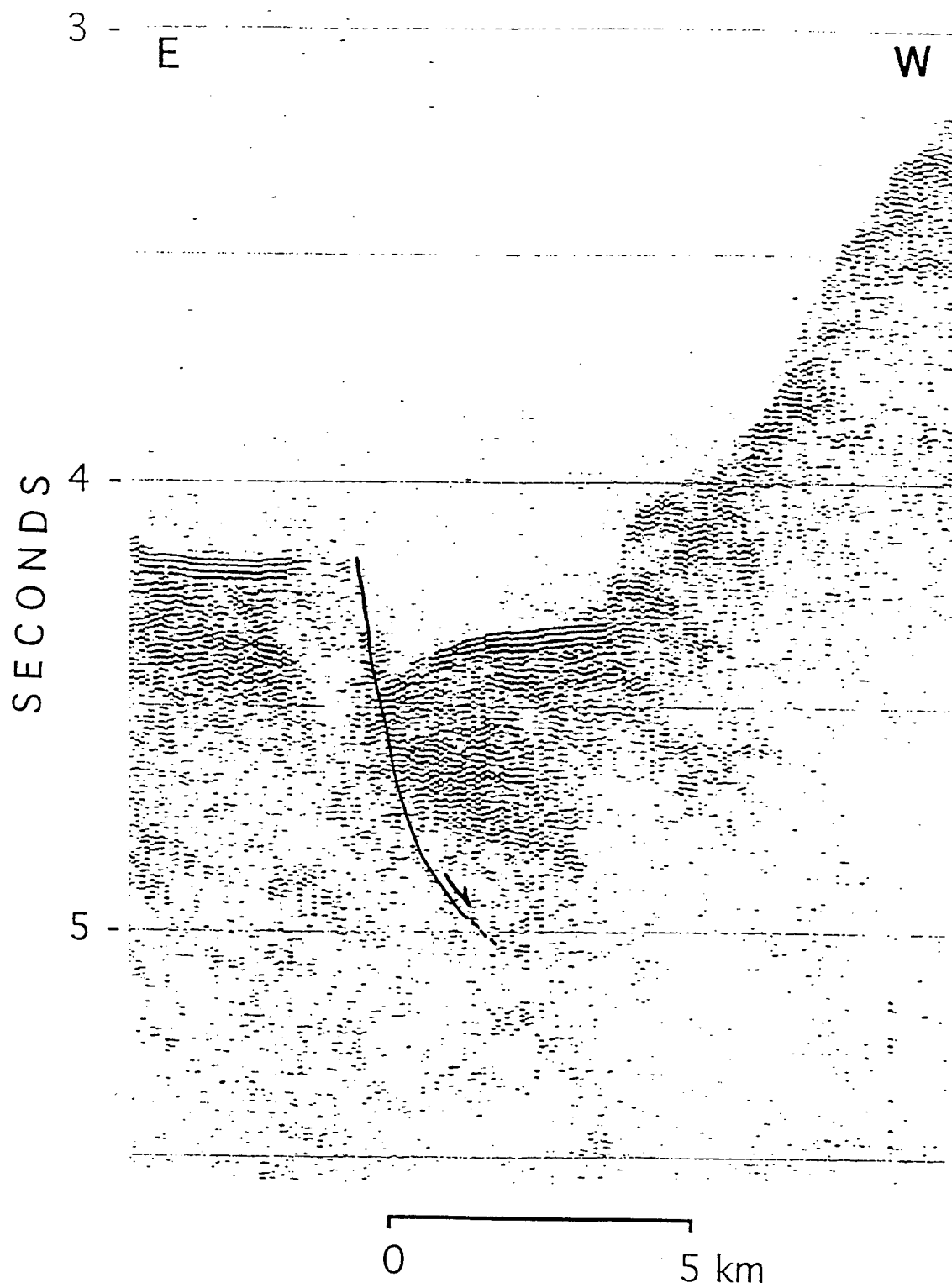


Figure 18

Chapter 4

RECORD OF SEAMOUNT PRODUCTION AND OFF-AXIS EVOLUTION IN THE WESTERN NORTH ATLANTIC OCEAN, 25°25' - 27°10'N

Introduction

The connection between seamount volcanism and crustal construction at mid-ocean ridges has been the subject of much discussion (Fornari et al., 1987; Batiza, 1989; Shen et al., 1993; Scheirer and Macdonald, 1995). At fast-spreading ridges such as the East Pacific Rise, near-circular, submarine volcanoes (seamounts) are abundant on the ridge flanks but are only rarely found at the ridge axis (e.g., Fornari et al., 1987; Scheirer and Macdonald, 1995). Volcanism leading to the formation of the seamounts on the flanks of the East Pacific Rise is thought to be separate from that occurring at the ridge axis (Scheirer and Macdonald, 1995). In comparison, seamounts in the Atlantic are observed both at the axis of the slow-spreading Mid-Atlantic Ridge (MAR) and on its flanks (e.g., Litvin and Rudenko, 1973; Kong et al., 1988; Batiza et al., 1989; Epp and Smoot, 1989; Smith and Cann, 1990, 1992; Sempéré et al., 1993). Surprisingly little is known about how volcanoes generated at the MAR are modified by faulting as crust is uplifted from the ridge axis to the crest of the rift mountains. Even less is known about abundances, size distributions, and spatial locations of any volcanic remnants. Furthermore, there are few studies (Batiza et al., 1989; Epp and Smoot, 1989) comparable to those in the Pacific to provide information about the construction of off-axis volcanoes in the slowly spreading crust of the Atlantic, despite its importance to understanding how magma is supplied spatially and temporally to the crust during its formation and evolution.

To obtain a better understanding of the record of on- and off-axis volcanism at the MAR, we analyzed an extensive new multibeam and side-scan sonar dataset collected along

the western flank of the northern MAR between 25°25'N and 27°10'N and extending from the ridge axis to ~29 Ma crust (Figure 1). We examine the seamount populations within this region and investigate 1) modification of seamounts during tectonic transport away from the ridge axis, 2) the question of on- and off-axis volcanism, 3) the effects of seafloor aging on seamount morphology, and 4) temporal variations in seamount generation. Because our study area spans numerous ridge segments, we also examine the relationship of seamount volcanism to ridge segmentation (i.e., to along-isochron position in segment and to across-isochron crustal thickness inferred from gravity). Finally, we evaluate variation in seamount population against variation in regional residual mantle Bouguer anomaly, and we compare the seamount populations of adjacent segments to determine whether intersegment relationships exist.

Geological Background

The Mid-Atlantic Ridge is a slow-spreading (≤ 15 mm/yr half-rate), divergent plate margin typically marked by a 1.5 - 3 km deep, 15 - 30 km wide axial rift valley. The rift valley contains an axial volcanic ridge ~200 - 700 m high and a few kilometers wide that runs most of the length of the floor of the innermost portion of the rift valley; this ridge is considered to be the predominant site of volcanic activity within the rift valley (Smith and Cann, 1990). The walls of the rift valley are composed of a series of backtilted ridges uplifted along inward-facing normal faults, and in the upper portions of the valley walls, the mean topographic gradient is diminished by extension along outward-facing normal faults (Chapter 3). The uplifted fault blocks and tilted ridges peak at a depth of ~2000 m on 1.5 - 3.2 Ma crust, forming the crest of the rift mountains. Older seafloor is considered to be the "ridge flank", and it progressively deepens with age, roughly following a square-root-of-age relation (cf. Sclater and Wixon, 1986). The detailed fault analysis in Chapter 3 suggests that there is little, if any, faulting beyond the crest of the rift mountains.

Ridge segmentation is a fundamental feature of the Mid-Atlantic Ridge, and it may be controlled by focused mantle upwelling and magmatic accretion, as has been suggested by geodynamic experiments (Whitehead et al., 1984) and bathymetric and gravity observations (Kuo and Forsyth, 1988; Lin et al., 1990; Blackman and Forsyth, 1992; Morris and Detrick, 1991). Focused mantle upwelling models suggest that there is an orderly spatial pattern to magmatic and tectonic processes at the segment scale. At the ridge axis, the seafloor is shallower and the crust is thicker at the centers of ridge segments than at their ends (e.g., Kuo and Forsyth, 1988; Lin et al., 1990; Tolstoy et al., 1993). It is as yet unclear whether focused magmatic accretion directly affects the supply of melt to the upper crust and its subsequent eruption (Cannat, 1996). If there is a direct relationship, then intrasegment patterns in the construction and distribution of volcanic edifices might be expected to reflect spatial and temporal magmatic patterns. Recently, Smith et al. (1995) analyzed variations in seamount morphology along eight ridge segments on the inner rift-valley floor of the MAR, but they found no correlation between seamount morphology and along-axis position within each segment.

Off axis, tectonic deformation overprints the record of axial volcanism and creates intrasegment asymmetries in seafloor morphology and crustal thickness. Elevated seafloor, residual gravity highs, and exposures of lower crustal/upper mantle rocks along the inside corners (IC) of ridge-axis discontinuities testify to cross-axis asymmetry in tectonic extension at slow-spreading ridges (Severinghaus and Macdonald, 1988; Tucholke and Lin, 1994; Escartín and Lin, 1995). Off-axis studies of these asymmetries suggest that oceanic crust, on average, is thinner along ICs of ridge segments than at segment centers (SCs) or outside corners (OCs) (Pariso et al., 1995; Tucholke et al., *in press, a*). In addition, cross-isochron variations in residual gravity anomalies suggest that episodic crustal thickening and thinning occurs with a period of roughly 2 - 3 m.y., and this has been attributed to cyclical variations in melt input from the upwelling asthenosphere (Lin et

al., 1993; Pariso et al., 1995; Tucholke et al., *in press, a*). If across-isochron variations in crustal thickness are due to temporal variations in melt supply, there might be a temporal correlation in melt supply between adjacent segments. However, Pariso et al. (1995) compared off-axis crustal thickness variations of individual segments along the MAR at 29° - 31°30'N and found little correlation of melt supply between segments.

The most recent investigation of off-axis seamounts in the North Atlantic was by Epp and Smoot (1989), who hypothesized that seamounts are only built where plume material is injected at the ridge axis. From their study, Epp and Smoot (1989) concluded that no seamounts are formed at the ridge axis between the Kane and Atlantis Fracture Zones. This subsequently was found to be incorrect. Smith and Cann (1990, 1992) identified more than 450 seamounts on the inner rift-valley floor of the MAR between 24° - 30°N alone, demonstrating that seamount volcanism plays a major role in crustal construction at the MAR. However, the extent to which seamounts exist off-axis in this region of the Atlantic remained uncertain.

A study of the rift valley and ridge flanks of the southern Mid-Atlantic Ridge at 26°S, conducted by Batiza et al. (1989), documented 50 off-axis seamounts with heights ≥ 50 m on crust between ~1 Ma and 7 Ma, and 38 seamounts located on crust younger than ~1 Ma. Batiza et al. (1989) noted that the observed density of seamounts (i.e., the number of seamounts per unit area) decreases with increasing age, suggesting either that seamounts are destroyed or buried during transport out of the rift valley, or that the rate of seamount production varies on the inner rift-valley floor. However, these researchers interpreted the occurrence of relatively fresh appearance of lavas dredged from some off-axis seamounts to mean that the ridge-flank seamounts probably originated outside the rift valley.

Studies of seamount population density, distribution, and morphology on the rift-valley floor (e.g., Smith and Cann, 1990, 1992; Smith et al., 1995; Head et al., 1996) have led to a general model for eruptions at the MAR. Smith et al. (1995) proposed that

fissure eruptions on the inner rift-valley floor produce low-relief flows and build volcanic edifices. If the fissure eruption focuses to a number of discrete vents, a hummocky ridge a few km in length is formed. A seamount is formed by the rapid evolution of a fissure eruption to a single vent. Restriction of fissure eruptions to a narrow zone causes construction of an axial volcanic ridge as individual flows and edifices pile upon one another.

Study Area

This paper investigates the seamount populations from a portion of the Mid-Atlantic Ridge located north of the Kane Fracture Zone from 25°25'N to 27°10'N (Figure 1; Chapter 2, Figure 1). An overview of the regional ridge-axis geology is given by Sempéré et al. (1993) and the ridge-axis and ridge-flank geology is discussed by Tucholke et al. (*in press, a*).

The area studied encompasses nine ridge segments; both bounding non-transform discontinuities are known for six of them (Segments 7a, 8a, 8b, 8, 9, and 10; Figure 1). Segments 7, 8, 9, 10, and 11 are currently active segments with well defined rift valleys having relief of approximately 2500 - 2700 m. Each of these segments contains an inner rift-valley floor that averages 7 km wide and is delineated for the most part by inward-facing bounding faults with throws typically greater than ~200 m. The inner rift-valley floor of Segment 9 includes the active Trans-Atlantic Geotraverse (TAG) hydrothermal field located at 26°08'N; the TAG area has been the focus of intense geological and geophysical study (e.g., Rona et al., 1976; Temple et al., 1979; Karson and Rona, 1990; Kleinrock and Humphris, *in press*).

Off axis, ridge segments are well defined by non-transform discontinuities. About 22 - 24 Ma, a distinct counterclockwise change in relative plate motion occurred that rotated the prevailing orientation of abyssal hills, faults, and magnetic anomalies from 024° to

015°, with coeval changes in plate-boundary segmentation patterns (Tucholke et al., *in press, a*). Segments 8a and 8b combined to form Segment 8, and Segment 9a was divided into Segments 9 and 10. Segment 7a died out before 19 Ma. Segments 8, 9, and 10 have persisted to the present. The along-isochron lengths of these segments vary from ~35 - 100 km, reflecting along-axis migration of the segment boundaries through time; Segment 8 has steadily shrunk to a length of ~35 km. The discontinuities between ridge segments vary in offset magnitude from 0 - 58 km (0 - 3 m.y.). Segment offsets have been predominantly right-stepping, but at times the boundaries between Segments 9/10 and 10/11 have been left-stepping or have had zero offset (Chapter 3).

As discussed in Chapter 2, sediment cover is highly variable across the study area. The thickest sediments are in sediment ponds within crustal depressions. The thickest ponds (up to 800 m) are in relatively deep depressions along the non-transform discontinuities. Ridge-parallel valleys between abyssal hills in the adjacent ridge segments also accumulate ponded sediments with a typical thickness range of ~50 - 350 m. However, the basement ridges between ponds rarely have sediments greater than ~10 m thick. Sediment thickness averaged along crustal isochrons shows a trend of increasing sediment cover with increasing crustal age up to ~17 Ma crust. Farther off axis, thicknesses decrease to ~25 m on 28 - 29 Ma crust (Chapter 2, Figure 10).

Data and Methods

We combined two separate bathymetric datasets to obtain nearly 100% bathymetric coverage of an ~75,000 km² area of the Mid-Atlantic Ridge and its western flank (Figure 1). We used the Sea Beam bathymetry data of Purdy et al. (1990) that covered the rift valley and the rift mountains out to ~30 km off axis. Hydrosweep bathymetry collected during Ewing Cruise 9208 (Tucholke et al., 1992) provided off-axis coverage ~400 km

westward to 26 - 29 Ma crust. Both multibeam bathymetric datasets were gridded at 200 m intervals using similar gridding and contouring algorithms.

Seamounts were identified in 20-m-contour bathymetric maps as near-circular topographic highs with plan-view aspect ratios of ≤ 2 , following Smith and Cann's (1990, 1992) criteria for seamount identification. Smith and Cann (1990, 1992) identified features greater than 50 m in relief as seamounts on the inner rift-valley floor; we increased this height to 60 m to identify seamounts more confidently within the rougher, irregularly sedimented terrain of the rift mountains and the ridge flank, but only seamounts with heights ≥ 70 m are incorporated in the seamount statistics.

For each seamount we recorded latitude, longitude, and minimum depth of the seamount top, and latitude, longitude, and water depth of the endpoints of the minimum and maximum plan-view shape axes. Recording of these parameters was partially automated by use of an on-screen interactive computer program developed for this study with the help of Scott Garland of JungleWare, Inc. The shape parameters derived from these measurements are minimum basal diameter, D_{\min} ; maximum basal diameter, D_{\max} ; average basal water depth, D_b , taken as the average of the four basal depths recorded; seamount height, h , the difference between D_b and summit depth; height-to-diameter ratio $\xi_d = h/D_b$; and ϕ_{\max} , the strike of D_{\max} .

We use the methodology of Jordan et al. (1983) and Smith and Jordan (1988) to characterize and objectively compare the density (number of seamounts per area) and characteristic size of seamount populations. The seamount size distribution is assumed to be nearly exponential over a large range in heights. That is, the average number of seamounts with summit height $h \geq H$ has the expected value:

$$v(H) = v_0 e^{-\beta H},$$

where v_0 is the *expected* number of seamounts per unit area ("expected population density"), and β^{-1} is the *characteristic height* of the population. For this analysis, we

sorted seamounts into height bins of 25 m starting with a minimum height of 70 m, and found that the seamount populations in our study area are well characterized by the exponential model. Therefore, the seamount populations can be described by the two parameters v_0 and β^{-1} . In the following discussions instead of presenting v_0 , the expected number per m^2 , we present a more intuitive value, v_{ot} , number per $10^3 km^2$ ($v_{ot} = v_0 * 10^9$). Uncertainties in the parameters are given as one standard deviation.

In order to investigate temporal changes in the population and shape parameters, seamount were assigned the same age as the underlying crust, as dated from magnetic anomalies (Tucholke et al., *in press, a*). Seamounts located on the inner rift-valley floor are referred to as *axial seamounts* and have ages less than or equal to ~ 0.6 Ma; those located outside the inner rift-valley floor are considered to be *off-axis* seamounts and range in age from $\sim 0.6 - 29$ Ma.

Hawaii MR1 (HMR1) long-range sidescan sonar images of the seafloor were used to examine the ages of seamounts relative to adjacent seafloor. The HMR1 data (Tucholke et al., 1992) provide 100-200% seafloor coverage in both NNW and SSE look directions. We first examined the backscatter from off-axis seamounts to determine if recent lava flows cover adjacent, sedimented seafloor. At mid-ocean ridges, a relatively steady rain of pelagic sediment produces an almost linear decay in average backscatter strength away from the ridge axis, and regions of high backscatter locate surfaces where sediment does not significantly attenuate the backscatter signal (Mitchell, 1993). Our analysis showed that no off-axis seamounts have high backscatter relative to surrounding seafloor, suggesting that the seamounts are approximately the same age as the crust on which they were built.

We also investigated the sidescan-sonar imagery for geological relations between faults and seamounts. Dissection of a seamount by faults indicates that the seamount was formed prior to faulting, i.e., prior to exiting the rift valley (Chapter 3). Growth of a

seamount's volcanic apron over a fault indicates that the seamount postdates the fault, and thus must have been formed on crust beyond the inner rift-valley bounding fault. We found no evidence of seamounts being constructed across pre-existing faults, although many seamounts are crosscut by faults. We conclude from this that the observed seamounts were constructed on the inner rift-valley floor and that off-axis volcanism is not important in our study area.

From work done on sediment thickness (Chapter 2), we recognize that there are regions where sediment thickness is > 60 m, the minimum height of seamounts identified in this study. Seamounts that fit our counting criteria in these regions may be masked or buried by sediments. These effects are considered later when we interpret the results of our study.

Seamount Population Comparisons

In the following we characterize and compare seamount populations based on the parameters of seamount shape, population density, and characteristic height. We compare the axial seamount population to the population of all off-axis seamounts to establish differences between these two regions. Next, variations of seamount populations with age are examined for changes associated with lateral transport of crust during seafloor spreading, with temporal changes in seamount production, and with the effects of aging. Seamount population parameters of individual segments are also compared with one another to investigate intersegment relationships. Finally, we examine how seamount population variations may be related to ridge segmentation; this is accomplished by comparing seamount populations to variations in crustal thickness as inferred from residual mantle Bouguer gravity anomaly patterns, and to intrasegment tectonic setting.

Axial Versus Off-axis Seamount Populations

We identified 86 axial and 1290 off-axis seamounts with heights ranging from 60 m to 560 m (Figure 1). In addition, there are many seamount-like topographic highs in the off-axis bathymetry that have heights greater than 60 m, but that have a plan-view shape forming only a portion of a circle and whose aspect ratio is greater than 2. Although many of these may be seamounts that have been dissected by faults, according to our identification criteria they are not identified as seamounts and they are excluded from this study.

Population characteristics of off-axis seamounts differ significantly from those of axial seamounts. Number of seamounts versus seamount height is plotted in Figure 2 for the axial and off-axis seamount populations. Also shown (in the lower panels) is the best fitting exponential model to the data. The characteristic height of the off-axis population is estimated as $\beta^{-1} = 51 \pm 1$ m, which is significantly lower than that estimated for the axial seamounts, $\beta^{-1} = 92 \pm 4$ m (Table 1). Likewise, the seamount population density is significantly lower off axis ($v_{ot} = 58 \pm 2$ per 10^3 km²) than on axis ($v_{ot} = 76 \pm 9$ per 10^3 km²).

Shapes of seamounts, characterized by basal diameter, height-to-diameter ratio, and plan-view aspect ratio, also show marked differences between the axial and off-axis populations. The basal diameter, D_b , of axial seamounts ranges from 700 m to 2650 m, which is narrower than the range for off-axis seamounts (275 - 3125 m). The mean height-to-diameter ratio of seamounts increases from $\xi_d = 0.09 \pm 0.02$ on-axis to $\xi_d = 0.13 \pm 0.04$ off-axis (Figure 3). Plan-view aspect ratios of off-axis seamounts also are shifted to higher mean values (Figure 4).

Orientations of seamounts, ϕ_{max} , are shown in Figure 5. Orientations of axial seamounts vary widely and do not show a distinctive trend compared to off-axis seamounts. Off-axis seamounts of age 0.6 - 22 Ma have orientations that trend

approximately $355^{\circ} - 020^{\circ}$, and older seamounts of age 22 - 28 Ma have orientations of approximately $000^{\circ} - 035^{\circ}$. The counterclockwise shift in ϕ_{\max} ca. 22 Ma is consistent with a marked counterclockwise change in spreading direction from $\sim 114^{\circ}$ to $\sim 105^{\circ}$ at that time (Tucholke et al., *in press, a*).

Temporal Variations in Seamount Population

Our study of backscatter from seamounts in HMR1 sidescan data and the observed geological relations between seamounts and faults suggest that all seamounts are formed at the ridge axis. The following discussion of temporal variations in seamount population is based on this assumption.

We measured cross-isochron variations in seamount populations to examine 1) how seamounts are modified during tectonic transport from the inner rift-valley floor to the ridge flank, 2) the effects of seafloor-aging processes, and 3) temporal changes in axial seamount production. We divided the seamount population into nine age bins as follows: 0 - 0.6 Ma, the axial seamounts; 0.6 - 2 Ma, seamounts located off-axis and generally on the lower walls of the rift valley; 2 - 4 Ma, seamounts on the upper walls of the rift valley and along the crest of the rift mountains; and in 4 m.y. intervals out to 28 Ma on the ridge flank. Age bins off-axis were selected to be large enough to provide a statistically robust sample in each bin, and yet small enough to highlight details of age-related variations in population, especially near the ridge axis where faults are active (Table 1, Figure 6).

Overall, the expected population density (v_{ot}) of off-axis seamounts is less than that at the ridge axis (Figure 6a). However, this change does not occur immediately as crust is transported beyond the inner rift-valley bounding faults; on crust 0.6 - 2 Ma, the population density is approximately the same as that on the inner rift-valley floor. It is only in the upper rift-valley walls and on the ridge flank, on crust older than 2 Ma, that density

significantly decreases. Expected seamount population density decreases steadily on crust older than 2 Ma, reaching a minimum ($v_{ot} = 42 \pm 3$ per 10^3 km^2) on crust of age 8 - 16 Ma. On crust older than 16 Ma, seamount density increases significantly to $v_{ot} = 65 \pm 5$ per 10^3 km^2 at 20 - 24 Ma and then again decreases on older crust.

Characteristic height of seamounts also changes over time (Figure 6b). The characteristic height of the axial population is $\beta^{-1} = 92 \pm 4$ m. Interestingly (and unlike seamount population density, which remains constant) a dramatic decrease in β^{-1} occurs immediately off-axis in the lower rift-valley walls on crust 0.6 - 2 Ma ($\beta^{-1} = 69 \pm 4$ m). On crust older than 2 Ma, the seamount populations show an overall, progressive decrease in characteristic height with increasing crustal age.

To examine trends in seamount shape parameters over time, we plot both height-to-diameter ratio and plan-view aspect ratio against seamount height for all age bins (Figure 7). We distinguish between 2 - 3 Ma and 3 - 4 Ma seamounts to gain insight into near-axis changes in seamounts, but data for the more statistically robust 2 - 4 Ma age bin are given in Table 1. Figure 7a shows the running means of height-to-diameter ratio, ξ_d , versus h . Axial seamounts and those in the lower rift-valley walls (0.6 - 2 Ma) have approximately constant height-to-diameter ratios over the entire height range. In comparison, seamounts located on crust older than 3 Ma have both higher values of ξ_d and a positive correlation of ξ_d with h . This suggests that the diameters of seamounts of all sizes are being altered off-axis, but that large (tall) seamounts are more likely to be modified. Seamounts in the upper rift-valley walls, age 2 - 3 Ma, show a dramatic increase in height-to-diameter ratios of larger seamounts.

Running mean of plan-view aspect ratios, D_{min}/D_{max} , versus h in each age bin is shown in Figure 7b. D_{min}/D_{max} of axial seamounts are lower than those of older, off-axis seamounts, but the standard deviation in all populations is large, suggesting that differences

between populations are not statistically significant, particularly for taller seamounts where the number of seamounts sampled is small.

The effects of sediment accumulation on seamount population statistics were also examined (Figure 8). To determine whether off-axis seamount density is influenced by seamount burial, average sediment thickness (Chapter 2) was correlated to seamount densities (in 2 m.y. age bins) as a function of crustal age for each of the three longest-lived segments (Segments 8, 9, and 10). In this case, we use the *observed* seamount densities (number of counted seamounts divided by area, n/A) because of the small sample sizes in the 2 m.y. age bins. The plots of sediment thickness and observed seamount density versus crustal age (Figure 8) indicate that there is a negative correlation between sediment thickness and the number of seamounts in a given area. The best correlation between observed seamount density and sediment accumulation is in Segment 8 ($r = -0.63$). In general, however, correlations are weak and sediment cover appears to have no significant effect on observed seamount abundance. Partial burial of seamounts by sediment will uniformly reduce the heights of all seamounts; thus it will cause no change in the distribution of seamount sizes as measured by characteristic height, β^{-1} .

Intersegment Variations in Seamount Population

Seamount population parameters for individual segments (Table 2) were also compared to one another. Only segments that contain > 60 seamounts and that are bounded by identified discontinuities were included (Segments 7a, 8a, 8, 9, and 10; Figure 1). Seamount population parameters estimated for Segments 8a and 8b were compared to those estimated for Segment 8. Expected seamount population density is similar in Segments 8a ($v_{ot} = 86 \pm 8$) and 8b ($v_{ot} = 81 \pm 10$), and significantly higher than the density estimated for Segment 8 ($v_{ot} = 65 \pm 4$). The estimated characteristic height of the population is significantly higher in Segment 8a ($\beta^{-1} = 55 \pm 3$) and Segment 8 ($\beta^{-1} = 51 \pm 2$) than in

Segment 8b ($\beta^{-1} = 45 \pm 3$). These relationships suggest that similar densities of seamounts were produced at the spreading axis of Segments 8a and 8b, but that seamounts were taller in 8a. After the two segments merged (Segment 8), the population of seamounts formed at the axis retained a large characteristic height like Segment 8a, but their number decreased significantly.

Comparison of seamount population parameters estimated for Segments 8, 9, and 10 show a significant northward trend of increased v_{ot} and β^{-1} from segment to segment (Table 2). We also compared these segments in terms of number of observed seamounts per 1000 km² (n/A) versus time (Figure 9). In general, there are no strong correlations among the three segments; the best correlation is between Segments 8 and 9 ($r = 0.57$).

Seamount Population Variations Correlated with Gravity Signature

To investigate possible relations between seamount production and inferred crustal thickness, we compared seamount parameters with residual mantle Bouguer anomaly (RMBA). RMBA is calculated by removing the gravity effects of seafloor topography, a constant-thickness crust, and the thermal effects of lithospheric cooling (Kuo and Forsyth, 1988; Lin et al., 1990; Lin and Phipps Morgan, 1992). It reflects variations in crustal thickness and/or density. Residual gravity lows represent regions of thicker crust and/or lower-density mantle compared to regions of RMBA highs. To make regional comparisons of seamount populations with variations in RMBA, we divided the residual gravity into three ranges: low (< 7 mGal), intermediate (7 to ≤ 15 mGal), and high (> 15 mGal). Figure 10 shows the anomaly pattern with locations of identified seamounts. Ridge segments are associated with marked regional patterns of RMBA highs and lows. Segment 8 exhibits low residual gravity overall, suggesting that its crust is relatively thick. In contrast, Segment 9 is marked by RMBA highs, indicating thinner crust. Segment 10 contains a mixed pattern of residual gravity highs and lows. Within individual segments,

inside corners tend to be regions with gravity highs (thin crust), and segment centers and outside corners correspond to regions of low and intermediate gravity (thick and intermediate crust), respectively (Tucholke and Lin, 1994; Escartín and Lin, 1995). Across isochrons, residual gravity anomalies fluctuate by 10 - 20 mGal with a period of ~2 - 3 Ma, suggesting cyclical changes up to ~2 km in crustal thickness (Lin et al., 1993; Tucholke et al., *in press, a*).

Estimates of the seamount population parameters for each of the three ranges in residual gravity are listed in Table 3. The estimated density of seamounts in regions of low to intermediate residual gravity ($v_{ot} = \sim 70$ per 10^3 km²) is significantly greater than that in regions of residual gravity highs ($v_{ot} = \sim 50$ per 10^3 km²). However, the characteristic heights ($\beta^{-1} \sim 55$ m to 61 m) are comparable for all gravity values. Therefore, areas with inferred thicker crust (low RMBA) have more seamounts per unit area than areas of thin crust (high RMBA). Average seamount heights in both these regions, however, are similar.

Temporal variations in gravity and in the observed number of seamounts per area (n/A) were compared for Segments 8, 9, and 10 (Figure 11a). We observe no significant correlation between across-isochron n/A and residual gravity; all correlation coefficients are small ($r < |0.34|$). However, the mean RMBA used in each crustal-age bin incorporates significant along-isochron variations; these smooth out the cross-isochron gravity signal, so it is not clear that the apparent lack of correlation between n/A and residual gravity is meaningful. Unfortunately, other methods of comparison, such as relating seamount population to gravity values along single across-isochron gravity profiles, would require using very small numbers of seamounts and thus would not produce robust results.

Finally, we compared across-isochron residual gravity anomaly variations of individual segments to each other (Figure 11b) to check for intersegment correlations in RMBA that may exist but that are not reflected in the intersegment seamount population

comparisons (Figure 9). There are no significant correlations between the segments ($r \leq 0.391$), but again, the along-isochron averaging of the RMBA may affect this result.

Intrasegment Variations in Seamount Population

Data were obtained for intrasegment subsets of seamount population parameters to investigate variations in seamount density and characteristic height over along-isochron segment length. We examined only those seamounts lying within segments where both bounding non-transform discontinuities are well defined (Segments 7a, 8, 8a, 8b, 9, and 10; Figure 1). Segments were divided into inside-corner, segment-center, and outside-corner provinces in two ways. First, to objectively compare intrasegment variations, IC, SC, and OC provinces were each defined as one-third of the along-isochron distance between non-transform discontinuities, as was done for intrasegment fault analyses in Chapter 3. This method was chosen to highlight along-isochron differences in seamount population that might be related to three-dimensional magmatic upwelling at the centers of segments. Second, IC crust was defined as 14% of the along-isochron distance from the boundary at the IC edge of the segment. This position reflects the approximate, average limit of irregular, arcuate, and oblique faults that are typical of IC crust (Chapter 3). Outside-corner crust is defined as 30% of the segment length from the outside-corner segment boundary, and the remainder of the area is considered to be SC crust. This second method allows for examination of possible correlations between seamount population and intrasegment variations in tectonic setting. Where discontinuity offset is zero and the segment boundary is essentially undefined, crust is assigned to the same tectonic setting as that of younger crust along the flowline of the segment, where the discontinuity is defined. Table 4 lists population characteristics in relation to along-isochron position for the two methods described.

Comparison of characteristic heights and expected seamount population densities (Table 4) shows no significant differences in the population parameters with respect to intrasegment position using either method of grouping seamounts by along-isochron distance.

Discussion

Using multibeam bathymetry, 86 axial and 1290 off-axis seamounts were identified in an area of 75,000 km² on the western flank of the MAR, 25°25'N to 27°10'N, indicating that seamounts are a common morphological feature of the North Atlantic seafloor. Our observations further suggest that seamount-producing volcanism occurs primarily on the inner rift-valley floor, and that few, if any, seamounts are formed on the rift-valley walls or the ridge flank. This interpretation is based on five observations: 1) seamounts are a ubiquitous volcanic product on the inner rift-valley floor of the MAR between 24° - 30°N (e.g., Smith and Cann, 1990; 1992), 2) side-scan sonar images show no strong backscatter from off-axis seamounts that would suggest off-axis formation, 3) faults commonly cut off-axis seamounts, 4) there is no bathymetric or sidescan-sonar evidence for off-axis growth of seamount aprons over pre-existing fault scarps, and 5) off-axis seamount-population density is significantly less than that of axial seamounts.

Based on the assumption that seamounts observed off-axis were formed on the inner rift-valley floor, off-axis changes in seamount parameters record the effects of faulting as seamounts are transported out of the rift valley, the effects of seafloor aging (sedimentation and mass-wasting), and temporal variations in axial seamount production. Along-isochrons, variations in seamount population parameters help to constrain spatial patterns of melt delivery with respect to ridge segmentation.

Modification of Seamounts During Transport Off-axis

The existence of abundant off-axis seamounts that originated on the inner rift-valley floor provides strong evidence that large sections of seafloor remain remarkably intact as they are transported up the rift-valley walls and onto the ridge flank (e.g., Figure 12). At the same time, off-axis changes in seamount density, size, and shape suggest that faulting destroys some seamounts and strongly modifies others. These changes are concentrated in the rift-valley walls (0.6 - 4 Ma crust).

To understand these effects, we summarize changes in the seamount population from the ridge axis to the ridge flank (Figure 13). At the top of the figure is a conceptual cross-section that highlights fault patterns that are consistent with the faulting analysis in Chapter 3 and with our seamount observations.

Axial Seamounts

On the inner rift-valley floor where seamounts are generated (Zone 1, Figure 13), faults are discontinuous and have small throws (typically <50 m; Zonenshain et al., 1989). Expected population density, height, and shape parameters of axial seamounts therefore are little affected by faulting. Head et al. (1996) show that the density of seamounts on the inner rift-valley floor of the MAR must be controlled by the amount of magma delivered to the crust, its ability to erupt, and the style of emplacement (low-relief flow versus edifice). Similarly, the height to which a seamount builds depends on several variables, most important of which are magma volume and pressure within the magma reservoir (Head et al., 1996). Plan-view shapes of seamounts on the inner rift-valley floor have aspect ratios that range between 1 (circular) and 2, the upper limit of our identification criterion. An elongate plan-view shape may be caused by a) eruption through a fissure rather than a more restricted vent, b) partial burial by subsequent, closely adjacent volcanism, and/or c) the influence of pre-existing topography on edifice construction. We expect that the orientation

of the long-axes of seamounts, ϕ_{\max} , will be similar to the strike of the rift valley. Although many seamounts show this trend (Figure 5), there is a large variation in orientation.

0.6 - 2 Myr

The first major modification of the seamount population occurs just beyond the first major bounding fault at the foot of the rift-valley walls on 0.6 to 2 Ma crust (Zone 2, Figure 13), and we attribute this modification to faulting. A strong indication that seamounts are faulted off-axis is the change in distribution of seamount orientations (Figure 5) from widely varying on-axis to a more definitive trend that generally parallels the strike of extensional normal faults on the ridge flank (Chapter 3). Fault analysis (Chapter 3) suggests that uplift of fault blocks in the lower rift-valley walls occurs predominantly along normal, inward-facing faults. Inward stepping of a bounding fault captures a large section of the inner rift-valley floor, typically ≥ 2 km wide (Chapter 3). This locally dissects seamounts but also preserves whole seamounts on the crustal block between faults. On 0.6 - 2 Ma crust, we observe a significant decrease in characteristic height of the seamount population ($\beta^{-1} = 69 \pm 4$ m) compared to that on younger crust ($\beta^{-1} = 92 \pm 4$ m). However, there is no change in expected seamount population density, height-to-diameter ratio, and plan-view aspect ratio (Figure 13). These observations suggest that during initial transport of seafloor out of the rift valley, few seamounts are destroyed, but many are affected by faulting.

To explain the reduction in seamount height, we must consider the geomorphic effects of faulting. The effect is shown in Figure 14, where a remnant of a seamount (red) sits on the uplifted footwall. Less than half of the seamount was removed by faulting, and the remnant remains subcircular with an aspect ratio < 2 . The part of the seamount downfaulted with the hanging wall usually is degraded to the point where it is no longer

recognized as part of the original seamount. In our identification and picking of seamount parameters, the base of the seamount on the faulted end of the short diameter (D_{\min} , orthogonal to the fault) typically was picked at the break in slope atop this debris pile on the hanging wall. This depth normally is shallower than the basal depths at the other diameter ends; the resulting effect is that the averaged basal depths of faulted seamounts are reduced, and therefore their characteristic height is also reduced.

Another possible way to reduce seamount height without reducing expected population density would be to downthrow the summit with the hanging wall, i.e., to fault away more than half of the seamount. Although this undoubtedly occurs, it is highly likely to create a plan-view aspect ratio > 2 for the remnant on the footwall. Such elongate fragments, by definition, are not recognized as seamounts in this study.

Just as it affects seamount heights, faulting also reduces seamount diameter because only the remnant on the footwall is measured. The fact that height-to-diameter ratio, ξ_d , does not change, even though characteristic height decreases significantly, suggests that mean heights and diameters of faulted seamounts are reduced proportionally.

Although Figure 7b suggests there may be an increase in the mean D_{\max}/D_{\min} of the off-axis seamount population, these changes are not statistically significant, as is readily apparent in the bottom panel of Figure 13. Nonetheless, the distribution of D_{\max}/D_{\min} within the on- and off-axis populations (Figure 4) clearly does show a decrease in low aspect ratios and a shift towards higher aspect ratios in the off-axis population. Thus many originally near-circular seamounts on <0.6 Ma crust are reshaped by faulting in the rift-valley walls.

2 - 4 Myr

Significant reductions in seamount population density (v_{ot}) occur on crust 2 - 4 Ma, suggesting that faulting continues to modify seamounts in the upper rift-valley walls to the crest of the rift mountains (1.5 - 3.2 Ma; Zone 3, Figure 13). As discussed in Chapter 3, new, outward-facing faults appear high in the rift-valley walls. They cut fault blocks previously uplifted along inward-facing faults, forming horst and graben terrain. The outward-facing faults also cut seamounts, much as the inward-facing faults did on younger crust. We examined fault-facing direction for those seamounts on > 0.6 Ma crust that are cut by faults and found that 27% are cut on their western flanks by outward-facing faults, 56% are cut on their eastern flanks by inward-facing faults, and 17% are cut by both. These percentages are similar to the finding (Chapter 3) that 40% of all ridge-flank faults are outward-facing.

In contrast to 0.6 - 2 Ma crust, seamounts are now being destroyed. Although expected seamount density decreases on 2 - 4 Ma crust, characteristic height, β^{-1} , remains constant (Figure 13). To maintain the characteristic height of the population, as observed, all sizes of seamounts must be destroyed equally.

At the same time, the height-to-diameter ratio (ξ_d) of seamounts on 2 - 4 Ma crust is increased by faulting in the upper rift-valley walls (Figure 13). Because characteristic heights are constant, the increase in height-to-diameter ratio indicates that seamount diameters must decrease. Thus faulting appears to reduce average seamount diameter but not height, unlike 0.6 - 2 Ma crust where β^{-1} and ξ_d were reduced proportionately. The cause of this change is not clear. Mean plan-view aspect ratio, D_{max}/D_{min} , does not change compared to younger crust.

Based on the fault analysis in Chapter 3, there are few, if any, active faults on the ridge flank beyond the crest of the rift mountains. Therefore, changes in seamount population characteristics on crust older than 4 Ma are not caused by faulting but reflect either the effects of crustal-aging processes or temporal changes in seamount production. The aging processes (sedimentation and denudation) are considered first; once their effect is known, it is easier to recognize which variations in off-axis seamount population parameters may be attributable to temporal changes in axial seamount production. The effects of sedimentation on observed seamount density (Figure 8) and characteristic height have already been discussed, and it was found that sediment cover has little to no effect on these population parameters.

A second aging effect is denudation. Submarine denudation has been identified only recently as a significant process affecting ocean crust (Cann et al., 1992; Allerton et al., 1995; Tucholke et al., *in press, b*). We observe evidence of mass wasting and erosion on the flanks of some off-axis seamounts in the form of 1) scalloping of scarps and 2) decreased slope gradients characteristic of talus deposition at the seamount base (Figure 15). Because there is no active faulting on the ridge flank, much of the marked trend of decreasing characteristic height with age (Figure 6b) may be caused by denudation, which acts to degrade the size of seamounts over time.

Because there is no significant seamount construction on the ridge flank, and because off-axis faulting tends to decrease seamount population density, off-axis increases in seamount abundance might be interpreted as a temporal increase in seamount production (Figure 6a). The peak in seamount density (ca. 24 - 22 Ma) is coeval with a major, plate-reorientation event (Tucholke et al., *in press, a*), and it could relate to changes in melt supply associated with the plate-boundary reorganization. However, the increase in

seamount density also could reflect a period of unusually limited faulting. Our fault analysis in Chapter 3 did not extend to ≥ 20 Ma crust, so we cannot test this concept.

Seamount Populations in Relation to Ridge Segmentation

Seamount population densities and characteristic heights do not change along isochrons (Table 4). There are not enough on-axis seamounts in our study area to be certain that this is true on the rift-valley floor, but the fact that this is a robust observation for off-axis seamounts implies that it also applies on-axis. This is surprising for two reasons: 1) On-axis, gravity studies (Kuo and Forsyth, 1988; Lin et al., 1990) and seismic studies (Tolstoy et al., 1993) suggest that crust is thickest near segment centers, and therefore that magmatism might be strongest near segment centers. 2) With respect to off-axis observations, the cross-rift structure at segment ends suggests fundamentally asymmetric distribution of volcanic upper crust and plutonic lower crust to outside and inside corners (Dick et al., 1981; Karson, 1990; Tucholke and Lin, 1994).

Consider first the question of seamount production at the ridge axis. The apparent along-axis uniformity of seamount abundance and characteristic height implies uniform melt supply. This could be accomplished either by injection from magma bodies that are evenly distributed along the ridge axis or by melt that is evenly distributed along-axis from a magma source at the segment center. In either case, if melt is initially supplied to the segment center by deep-seated upwelling, it must be redistributed along-axis at shallow crustal levels. Either system of melt distribution could create similar seamount population.

However, it is possible that seamount production is not uniform along axis and that we simply cannot detect the variations. For example, seamounts actually may be more abundant at segment centers than at segment ends, but seamounts constructed at the segment centers may be buried more often by subsequent volcanic flows, thus reducing their apparent population density and heights. This is consistent with overall along-axis

topography and morphology of axial volcanic ridges which do suggest that the volume and style of volcanic construction vary along axis; the ridges are well defined bathymetric highs near the segment center, but they lose definition and become discontinuous toward the ends of segments (Sempéré et al., 1990).

It is also surprising that there is no off-axis difference in seamount population parameters between inside and outside corners of ridge segments (Table 4b). IC crust is characteristically a region of highly strained, thin crust (high RMBA) with irregular, large-throw normal faults and low-angle detachment faults (Chapter 3); the low-angle detachment faulting is thought to remove much of the volcanic crustal carapace from inside corners (footwalls) and retain it at outside corners (hanging walls) (Tucholke and Lin, 1994; Escartín and Lin, 1995). Strain at OC crust also is less disruptive, with brittle extension being accommodated on relatively small-throw normal faults; crustal thicknesses at OCs remain comparable to those on axis (Chapter 3; Tucholke and Lin, 1994; Escartín and Lin, 1995). Based on these distinctions, it seems reasonable to expect that seamount population parameters would differ between inside and outside corners, e.g., that seamount population densities would be lower at ICs where more seamounts might be destroyed in the highly extended crust or removed to the OC hanging wall by detachment faulting. We do observe that seamount densities are relatively low in regions of high RMBA, i.e., thin crust (Table 3) but this observation does not extend to ICs where RMBA also is generally elevated. It may be that our artificial assignment of some percentage (30%, or 14%) of segment length to "IC crust" explains the problem; such an assignment ignores and smoothes local (e.g., cross-isochron) variations in RMBA that relate to crustal strain and crustal thinning, and it therefore may mask possible correlations with seamount population.

Significant differences in observed seamount populations between ridge segments (Table 2; Figure 9) suggest that seamount-forming volcanic processes are separate and distinct between individual spreading segments. Intersegment differences in RMBA within

our study area (Figure 11), and on the MAR at 29° - 31°30'N (Pariso et al., 1995), also suggest there are no segment-to-segment correlations in magmatism; each ridge segment appears to operate independently from neighboring spreading cells.

The trend of increasing seamount population densities and characteristic heights from Segment 8 through Segment 9 to Segment 10 is noteworthy; it may reflect increased magma supply towards the north. However, until seamount distribution is mapped farther to the north, it cannot be determined whether this is part of a regional trend (e.g., increasing proximity to the Azores hotspot) or whether it is only a local phenomenon.

Summary

The major conclusions of this study are:

1. We identified 86 axial and 1290 off-axis seamounts (near-circular volcanoes) that are ≥ 60 m high on the western flank of the Mid-Atlantic Ridge from approximately 25°25'N to 27°10'N, and extending from the inner rift-valley floor to ~29 Ma crust. Analysis of sidescan-sonar images and bathymetry shows no evidence for construction of seamounts off axis, indicating that seamount construction occurs primarily on the inner rift-valley floor of the Mid-Atlantic Ridge in this region.

2. Abundance of off-axis seamounts shows that large sections of oceanic crust are carried intact through the rift-valley wall to the ridge flank on > 4 Ma crust. However significant changes in seamount population density, size distribution, and shape are caused by faulting between ~0.6 and 3 - 4 m.y. off-axis. During initial transport of seamounts out of the rift valley (0.6 - 2 m.y.), few seamounts are destroyed by (inward-facing) faults, but seamount height is significantly decreased. In the upper portions of the rift valley, on crust 2 - 4 Ma, additional faults (outward-facing) destroy and degrade a significant number of seamounts. These results are consistent with evidence that outward-facing faults in the

upper portions of the rift-valley walls lead to higher densities of off-axis faults and also form horst and graben terrain (Chapter 3).

3. Beyond the crest of the rift mountains faulting is no longer active, and changes in the off-axis seamount population reflect long-period crustal aging processes and temporal changes in seamount production that occurred at the ridge axis. We attribute a steady decline in characteristic height of the seamount population with crustal age to the cumulative effects of mass-wasting. A marked increase in seamount density on ~20 - 24 Ma crust may have been caused by an increase in axial seamount production at that time, or it may reflect reduced seamount destruction related to reduced density of faults.

4. Seamount population density estimated for the entire off-axis seamount population has a positive correlation to crustal thickness (as inferred from gravity data), suggesting that increased seamount production accompanies increased magma input to the rift valley. However, intra-segment variations in seamount population characteristics do not appear to correlate with IC, SC, and OC tectonic setting or their associated differences in RMBA. It is unclear whether this effect is real or whether it is an artifact of the way the tectonic settings were defined (i.e., as percentages of segment length, rather than as detailed, but subjectively interpreted, geological boundaries).

5. There are no variations in measured seamount density with along-axis position within individual ridge segments. There are two possible explanations: a) Along-axis production of seamounts is actually uniform, in which case melt delivery in the shallow crust must also be relatively uniform along-axis, irrespective of how it is supplied to the base of the crust by deep-seated magmatic processes. b) Seamount production varies along-axis, but along-axis variations in the style of volcanism prevent its topographic identification. In particular, complete or partial burial of segment-center seamounts by subsequent volcanic flows might reduce their population density and characteristic heights to values similar to those at segment ends.

Acknowledgments

We thank Scott Garland for help in developing the software for seamount identification, Tamara Osychny for help in data entry, and Lori Dolby for assistance in map processing. We also thank Javier Escartín for constructive comments. This research was supported by ONR Grants N00014-93-1-1153 (AASERT), N0014-94-1-0319, N0014-94-1-0466, and N00014-90-J-1621.

References

- Allerton, S., B. J. Murton, R. C. Searle, and M. Jones, Extensional faulting and segmentation of the Mid-Atlantic Ridge north of the Kane Fracture Zone (24°00' N to 24°40'N), *Mar. Geophys. Res.*, 17, 37-61, 1995.
- Batiza, R., P. J. Fox, P. R. Vogt, S. C. Cande, N. R. Grindlay, W. G. Melson, and T. O'Hearn, Morphology, abundance, and chemistry of near-ridge seamounts in the vicinity of the Mid-Atlantic Ridge ~26°S, *J. Geol.*, 97, 209-220, 1989.
- Blackman, D. K., and D. W. Forsyth, The effects of plate thickening on three-dimensional, passive flow of the mantle beneath mid-ocean ridges. In: J. Phipps Morgan, D. K. Blackman, and J. M. Sinton (Eds.), *Mantle Flow and Melt Generation at Mid-Ocean Ridges*, *Geophys. Mono.* 71, 311-326, 1992.
- Cann, J., D. K. Smith, M. E. Dougherty, J. Lin, B. Brooks, S. Spencer, C. J. MacLeod, E. McAllister, R. A. Pascoe, and J. A. Keeton, Major landslides in the MAR median valley, 25° - 30°N: Their role in crustal construction and plutonic exposure, *EOS, Trans. Am. Geophys. Union*, 73, 569, 1992.
- Cannat, M., How thick is the magmatic crust at slow spreading oceanic ridges?, *J. Geophys. Res.*, 101, 2847-2857, 1996.
- Epp, D., and N. C. Smoot, Distribution of seamounts in the North Atlantic, *Nature*, 337, 254-257, 1989.
- Escartín, J., and J. Lin, Ridge offsets, normal faulting, and gravity anomalies of slow spreading ridges, *J. Geophys. Res.*, 100, 6163-6177, 1995.
- Fornari, D. J., R. Batiza, and M.-A. Luckman, Seamount abundances and distribution near the East Pacific Rise 0°-24°N based on SeaBeam data, *Geophys. Mono.*, 43, 13-21, 1987.
- Head, J. W., L. Wilson, and D. K. Smith, Mid-ocean ridge eruptive vent morphology and substructure: Evidence for dike widths, eruption rates, and evolution of eruptions and axial volcanic ridges, *J. Geophys. Res.*, 101, 28265-28280.
- Jordan, T. H., W. Menard, and D. K. Smith, Density and size distribution of seamounts in the Eastern Pacific inferred from wide-beam sounding data, *J. Geophys. Res.*, 88, 10508-10518, 1983.
- Karson, J. A., and P. A. Rona, Block-tilting, transfer faults, and structural control of magmatic and hydrothermal processes in the TAG area, Mid-Atlantic Ridge 26°N, *Geol. Soc. Am. Bull.*, 102, 1635-1645, 1990.

- Kleinrock, M. C., and S. E. Humphris, Structural asymmetry of the TAG rift valley: Evidence from a near-bottom survey for episodic spreading, *Nature*, (in press).
- Kong, L., R. S. Detrick, P. J. Fox, L. A. Mayer, and W. B. F. Ryan, The morphology and tectonics of the MARK area from Sea Beam and Sea MARC I observations (Mid-Atlantic Ridge 23°N), *Mar. Geophys. Res.*, 10, 59-90, 1988.
- Kuo, B. Y., and D. W. Forsyth, Gravity anomalies of the ridge-transform system in the South Atlantic between 31° and 34.5°S: Upwelling centers and variations in crustal thickness, *Mar. Geophys. Res.*, 10, 205-232, 1988.
- Lin, J., and J. Phipps Morgan, The spreading rate dependence of three-dimensional mid-ocean ridge gravity structure, *Geophys. Res. Lett.*, 19, 13-16, 1992.
- Lin, J., G. M. Purdy, H. Schouten, J.-C. Sempéré, and C. Zervas Evidence from gravity data for focused magmatic accretion along the Mid-Atlantic Ridge, *Nature*, 344, 627-632, 1990.
- Lin, J., B. E. Tucholke, and M. C. Kleinrock, Off-axis "boudin-shaped" gravity lows on the western flank of the Mid-Atlantic Ridge at 25°25' - 27°10'N: Evidence for long-term pulses in magmatic accretion in spreading segments, *EOS, Trans. Am. Geophys. Union*, 74, 380, 1993.
- Litvin, V. M., and M. V. Rudenko, Distribution of seamounts in the Atlantic, *Dokl. Acad. Sci. USSR Earth Sci. Sect., Engl. Transl.*, 213, 223-225, 1973.
- Mitchell, N. C., A model for attenuation of backscatter due to sediment accumulations and its application to determine sediment thicknesses with GLORIA sidescan sonar, *J. Geophys. Res.*, 98, 22477-22493, 1993.
- Morris, E., and R. S. Detrick, Three-dimensional analysis of gravity anomalies in the MARK area, Mid-Atlantic Ridge 23°N, *J. Geophys. Res.*, 96, 4355-4366, 1991.
- Pariso, J. E., and J.-C. Sempéré, Temporal and spatial variations in crustal accretion along the Mid-Atlantic Ridge (29°-31°30'N) over the last 10 m.y.: Implications from a three-dimensional gravity study, *J. Geophys. Res.*, 100, 17781-17794, 1995.
- Purdy, G. M., J.-C. Sempéré, H. Schouten, D. L. Dubois, and R. Goldsmith, Bathymetry of the Mid-Atlantic Ridge, 24° - 31° N: A map series, *Mar. Geophys. Res.*, 12, 247-252, 1990.
- Rona, P. A., R. N. Harbison, B. G. Bassinger, R. B. Scott, and A. J. Nalwalk, Tectonic fabric and hydrothermal activity of Mid-Atlantic Ridge Crest (Lat. 26°N), *Geol. Soc. Amer. Bull.*, 87, 661-674, 1976.

- Scheirer, D. S., and K. C. Macdonald, Near-axis seamounts on the flanks of the East Pacific Rise, 8°N to 17°N, *J. Geophys. Res.*, 100, 2239-2259, 1995.
- Sclater, J. G., and L. Wixon. The relationship between depth and age and heat flow and age in the western North Atlantic. In: P. R. Vogt and B. E. Tucholke (Eds.), *The Geology of North America, Volume M, The Western North Atlantic Region*. Boulder, Colorado: Geol. Soc. Amer., 257-270, 1986.
- Sempéré, J.-C., J. Lin, H. Brown, H. Schouten, and G. M. Purdy, Segmentation and morphotectonic variations along a slow-spreading center: The Mid-Atlantic Ridge (24°00'N-30°40'N), *Mar. Geophys. Res.*, 15, 153-200, 1993.
- Severinghaus, J., and K. C. Macdonald, High inside corners at ridge-transform intersections, *Mar. Geophys. Res.*, 9, 353-367, 1988.
- Shen, Y., D. W. Forsyth, D. S. Scheirer, and K. C. Macdonald, Two forms of volcanism: Implications for mantle flow and off-axis crustal production on the west flank of the southern East Pacific Rise, *J. Geophys. Res.*, 98, 17875-17889, 1993.
- Smith, D. K., and J. R. Cann, Hundreds of small volcanoes on the median valley floor of the Mid-Atlantic Ridge at 24-30°N, *Nature*, 344, 427-431, 1990.
- Smith, D. K., and J. R. Cann, The role of seamount volcanism in crustal construction at the Mid-Atlantic Ridge (24°-30°N), *J. Geophys. Res.*, 97, 1645-1658, 1992.
- Smith, D. K., and J. R. Cann, Building the crust at the Mid-Atlantic Ridge, *Nature*, 365, 707-715, 1993.
- Smith, D. K., S. E. Humphris, and W. B. Bryan, A comparison of volcanic edifices at the Reykjanes Ridge and the Mid-Atlantic Ridge at 24°-30°N, *J. Geophys. Res.*, 100, 22485-22498, 1995.
- Smith, D. K., and T. H. Jordan, Seamount statistics in the Pacific Ocean, *J. Geophys. Res.*, 93, 2899-2918, 1988.
- Temple, D. G., R. B. Scott, and P. A. Rona, Geology of a submarine hydrothermal field, Mid-Atlantic Ridge, 26°N latitude, *J. Geophys. Res.*, 84, 7453-7466, 1979.
- Tolstoy, M., A. J. Harding, and J. A. Orcutt, Crustal thickness on the Mid-Atlantic Ridge: Bull's-eye gravity anomalies and focused accretion, *Science*, 262, 726-729, 1993.
- Tucholke, B. E., and J. Lin, A geological model for the structure of ridge segments in slow-spreading ocean crust, *J. Geophys. Res.*, 99, 11937-11958, 1994.
- Tucholke, B. E., J. Lin, and M. C. Kleinrock, Crustal structure of spreading segments on the western flank of the Mid-Atlantic ridge at 25°25'N to 27°10'N, *EOS, Trans. Am. Geophys. Union*, 73, 537, 1992.

- Tucholke, B. E., J. Lin, M. C. Kleinrock, M. A. Tivey, T. B. Reed, J. Goff, and G. E. Jaroslow, Segmentation and crustal structure of the western Mid-Atlantic Ridge flank, 25°25' - 27°10'N and 0 -29 m.y., *J. Geophys. Res.* (in press, a).
- Tucholke, B. E., W. K. Stewart, and M. C. Kleinrock, Long-term denudation of ocean crust in the central North Atlantic Ocean, *Geology* (in press, b).
- Whitehead, J. A., H. J. B. Dick, and H. Schouten, A mechanism for magmatic accretion under spreading centers, *Nature*, 312, 146-148, 1984.
- Zonenshain, L. P., M. I. Kuzmin, A. P. Lisitsin, Yu. A. Bogdanov, and B. V. Baranov, Tectonics of the Mid-Atlantic rift valley between the TAG and MARK areas (26° - 24°N): Evidence for vertical tectonism, *Tectonophys.*, 159, 1-23, 1989.

Table 1. Population Characteristics Associated with Crustal Age

Age (Ma)	n	Area (10^3 km^2)	β^{-1} (m)	V_{ot} (# per 10^3 km^2)	ξ_d	D_{max}/D_{min}
Axial	86	2.8	91.53 ± 3.72	75.96 ± 8.5	0.09 ± 0.02	1.32 ± 0.23
Off-axis:						
0.6 to 28	1290	70.7	51.20 ± 1.21	58.33 ± 1.63	0.13 ± 0.04	1.44 ± 0.25
0.6 to 2	85	2.8	69.16 ± 3.65	74.57 ± 8.44	0.09 ± 0.02	1.36 ± 0.27
2 to 4	97	4.1	70.05 ± 3.42	58.51 ± 6.20	0.13 ± 0.06	1.42 ± 0.26
4 to 8	178	8.5	74.11 ± 2.49	52.20 ± 3.99	0.13 ± 0.04	1.44 ± 0.26
8 to 12	179	10.4	69.07 ± 2.93	42.24 ± 3.19	0.14 ± 0.05	1.46 ± 0.25
12 to 16	182	11.8	61.16 ± 2.84	41.53 ± 3.12	0.13 ± 0.04	1.43 ± 0.25
16 to 20	207	11.8	56.75 ± 2.22	52.70 ± 3.76	0.12 ± 0.04	1.45 ± 0.24
20 to 24	200	9.9	52.12 ± 2.56	65.36 ± 4.65	0.13 ± 0.04	1.46 ± 0.26
24 to 28	162	11.5	51.08 ± 2.45	47.22 ± 3.80	0.13 ± 0.04	1.45 ± 0.25

Table 2. Population Characteristics Associated with Individual Segments

Segment	n	Area (10 ³ km ²)	β^{-1} (m)	v_{ot} (# per 10 ³ km ²)
7a	60	4.2	59.78 \pm 4.84	50.69 \pm 6.55
8a	124	5.6	54.90 \pm 2.84	85.93 \pm 7.88
8b	74	4.6	44.89 \pm 2.87	80.95 \pm 9.82
8	292	18.5	50.75 \pm 2.33	64.60 \pm 3.79
9	228	11.2	57.75 \pm 2.13	74.52 \pm 5.06
10	245	9.2	68.39 \pm 2.52	80.39 \pm 5.23

Table 3. Off-axis Population Characteristics Associated with RMBA

RMBA	n	Area (10^3 km^2)	β^{-1} (m)	v_{ot} (# per 10^3 km^2)
Low	472	22.9	58.32 ± 1.96	70.71 ± 3.29
Medium	595	32.1	55.08 ± 1.51	69.63 ± 2.88
High	298	20.5	61.44 ± 1.88	50.20 ± 2.99

Table 4. Population Characteristics Associated with Along-Isochron Position

Province	n	Area (10 ³ km ²)	β^{-1} (m)	v_{ot} (# per 10 ³ km ²)
a)				
IC (33%)	352	18.0	56.46 \pm 1.70	73.35 \pm 4.00
SC (33%)	362	18.0	58.14 \pm 1.97	71.44 \pm 3.79
OC (34%)	355	18.6	56.27 \pm 2.23	68.00 \pm 3.65
b)				
IC (14%)	167	9.5	52.75 \pm 2.43	71.09 \pm 5.62
SC (56%)	588	28.7	56.38 \pm 1.53	74.83 \pm 3.12
OC (30%)	313	16.4	55.74 \pm 2.37	68.58 \pm 3.92

Figure Captions

Figure 1. Gray-scale bathymetric contour map of combined SeaBeam and Hydrosweep multibeam bathymetry. Circles show locations of identified seamounts; circle size is proportional to mean seamount diameter. Segment boundaries and the MAR axis, defined by Tucholke et al. (*in press, a*), are indicated by thin black lines. Numbers denote segment identifications corresponding to those of Sempéré (1993). Crustal ages (Ma) are indicated by numbers and bold lines at edge of survey. Inner rift-valley floor contains crust approximately < 0.6 Ma.

Figure 2. (a, b) Binned height distributions of axial and off-axis seamounts ≥ 70 m high. (c, d) Number of axial and off-axis seamounts versus seamount height. Stars are binned counts in 25-m height bins; crosses are cumulative counts. Open circle data are not included in the statistical analyses because of the small numbers of seamounts at these heights. Maximum likelihood fits to the data show that the distributions can be modeled with exponential size-frequency curves (solid line for fit of cumulative data; dashed line for binned data). Definitions of population parameters, β^{-1} and v_{ot} , are given in text.

Figure 3. Histograms of the distribution of seamount height-to-diameter ratio, ξ_d , for all axial and off-axis seamounts.

Figure 4. Histograms of the distribution of plan-view aspect ratio, D_{max}/D_{min} , for all axial and off-axis seamounts.

Figure 5. Rose diagrams showing the strike of seamount orientations, as determined by seamount D_{max} (long-axis), for three age groupings. Normalized frequency distribution is indicated by circles in 0.2 fractional increments.

Figure 6. Population parameters of (a) expected seamount density, v_{ot} , and (b) characteristic height, β^{-1} , plotted against crustal age. Ranges of age bins and errors of one standard deviation are shown by bars. Values are given in Table 1.

Figure 7. Running mean of seamount shape parameters versus height for seamount populations sorted by age. Dashed lines indicate maximum bounds of errors ($1-\sigma$) for axial

(< 0.6 Ma; gray) and off-axis (2 - 28 Ma; black) seamounts. Running means were derived using height step sizes of 10 m and ranges of 60 m.

Figure 8. Combined plots comparing observed seamount density (n/A, solid curve) and mean sediment thickness (dashed curve) against crustal age. Data are shown for 2 m.y. age bins. Correlation coefficients, r , between the two data plots are given. Sediment thickness data from Chapter 2, Figure 10.

Figure 9. Plot comparing observed seamount density (n/A) of Segments 8 (solid line), 9 (heavy dashed line), and 10 (light dashed line) versus crustal age. Data are shown for 2 m.y. age bins. Correlation coefficients, r , compare pairs of curves indicated in subscript.

Figure 10. Map of residual mantle Bouguer anomaly (Tucholke et al., *in press*, a) with seamount locations (circles) superimposed. Shaded gravity contours are: < 7 mGal (dark gray), 7 to \leq 15 mGal (medium gray), and > 15 mGal (light gray). Associated seamount population characteristics are listed in Table 3. Segment boundaries as in Figure 1.

Figure 11. a) Combined plots comparing observed seamount density (n/A, solid curve) and mean RMBA (dashed curve) against crustal age for Segments 8, 9 and 10. b) Plot of mean RMBA for individual segments versus crustal age. Data are shown for 2 m.y. age bins. RMBA was calculated as the mean of the gridded gravity data values within each crustal age bin for a given segment. Correlation coefficients, r , between the data plots are given.

Figure 12. Shaded three-dimensional bathymetric relief of a fossil, axial volcanic ridge transported intact onto ridge flank and now on 25 Ma crust. Seamount height and diameter are approximately 250 m and 2 km, respectively. Aspect ratio is ~ 1 .

Figure 13. Upper panel: Schematic cross-section showing pattern of normal faulting to explain observations of inward- and outward-facing faults based on fault analysis in Chapter 3. Inactive faults are indicated by dashed lines. Circled numbers relate to local fault pattern: 1) the relatively unfaulted inner rift-valley floor, 2) the lower walls of the rift valley where faults are predominantly inward-facing, 3) upper rift-valley wall to the crest of the rift mountains, where outward-facing faults are active, 4) ridge flank where there are no

active faults. Lower panels: Plots of estimated seamount density, v_{ot} ; characteristic height, β^{-1} ; height-to-diameter ratio, ξ_d ; and plan-view aspect ratio, D_{max}/D_{min} , versus crustal age/distance from the ridge axis. Errors of one standard deviation about the estimated parameter are shown on the y-axis.

Figure 14. Three-dimensional texture map of SeaBeam bathymetry (color) overlain with TOBI deep-tow sidescan backscatter intensity (gray scale) within the MAR rift valley. North is toward the upper right, and image is ~10 km east to west. Sidescan illumination is orthogonal to vehicle track. Bathymetric depths in the image range from approximately 3100 to 3650 m. The faulted seamount indicated has height of ~140m, long-axis diameter of 1200 m, and plan-view aspect ratio of 2. Throw of inner rift-valley bounding fault that cuts the seamount is ~180 m. Axial volcanic ridge shown is comprised of fissured, hummocky terrain without identifiable seamounts.

Figure 15. Shaded three-dimensional bathymetric relief of ~2 - 3 Ma seafloor with 50 m bathymetric contours. Top is north. Bathymetric depths range from approximately 2500 to 3500 m. Arrows locate examples of off-axis seamounts cut by an east-dipping ridge-parallel, normal fault. Crustal ages indicated by bold lines with numbers.

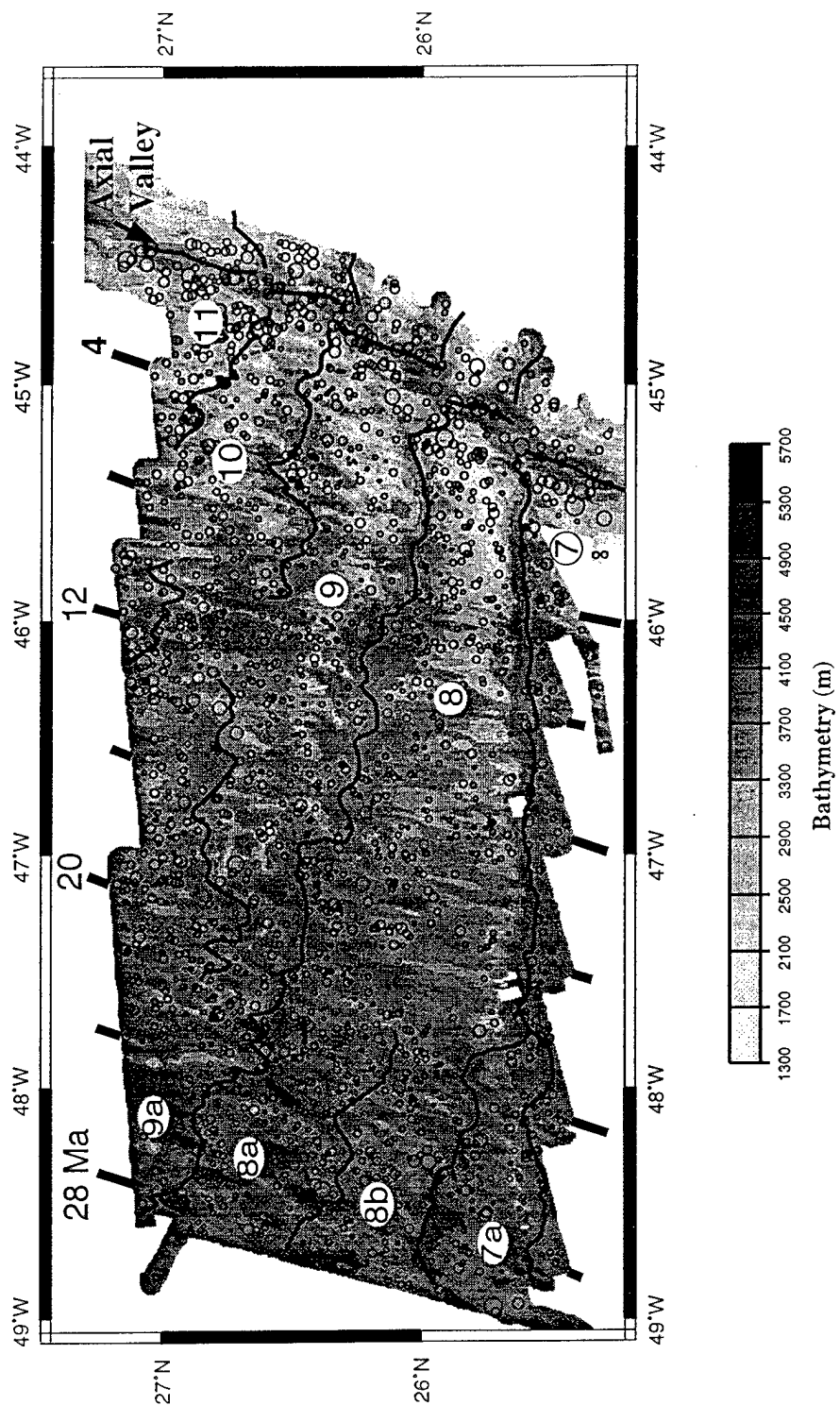


Figure 1

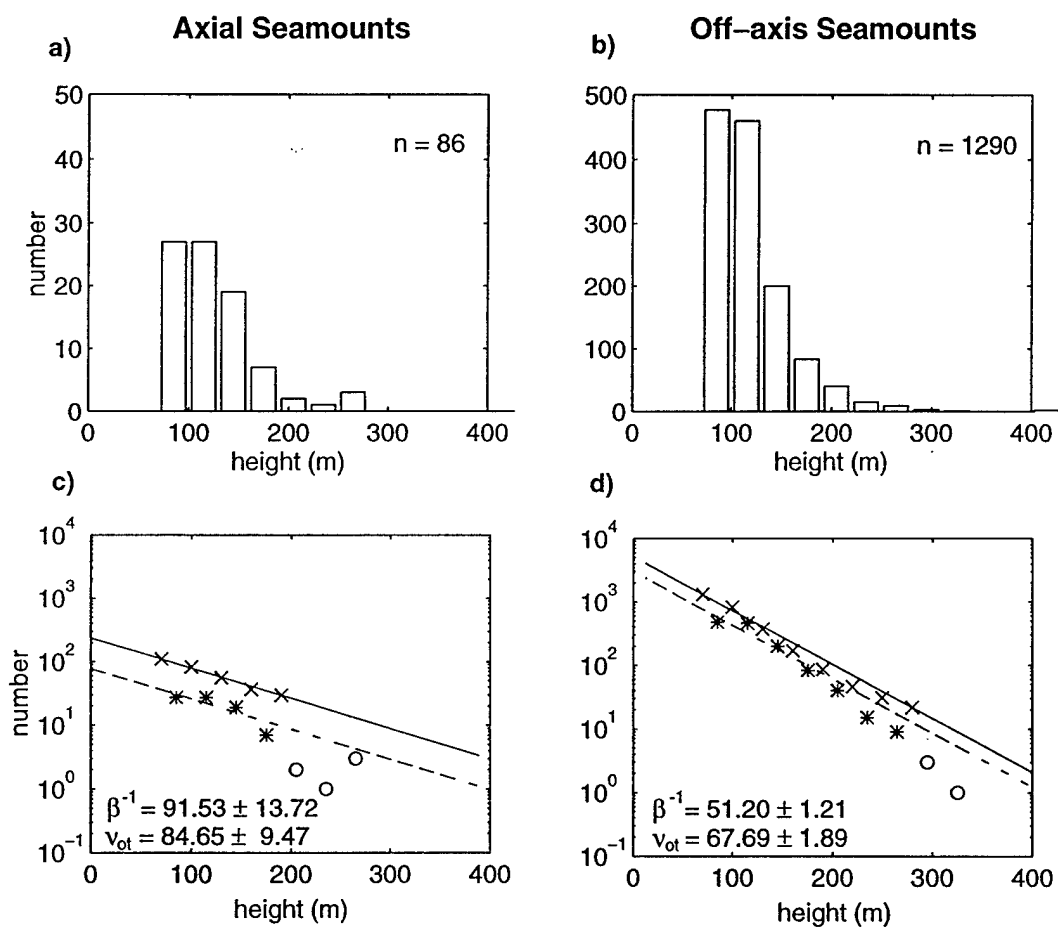


Figure 2

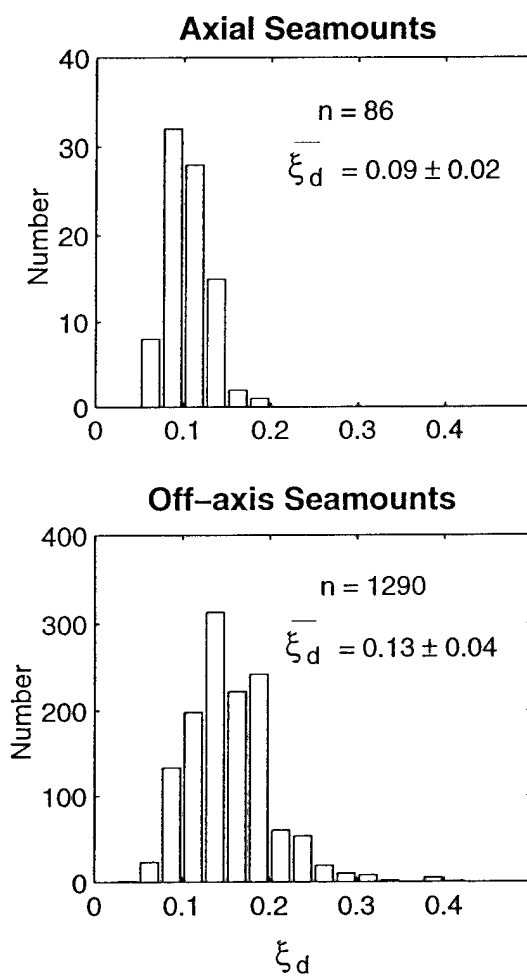


Figure 3

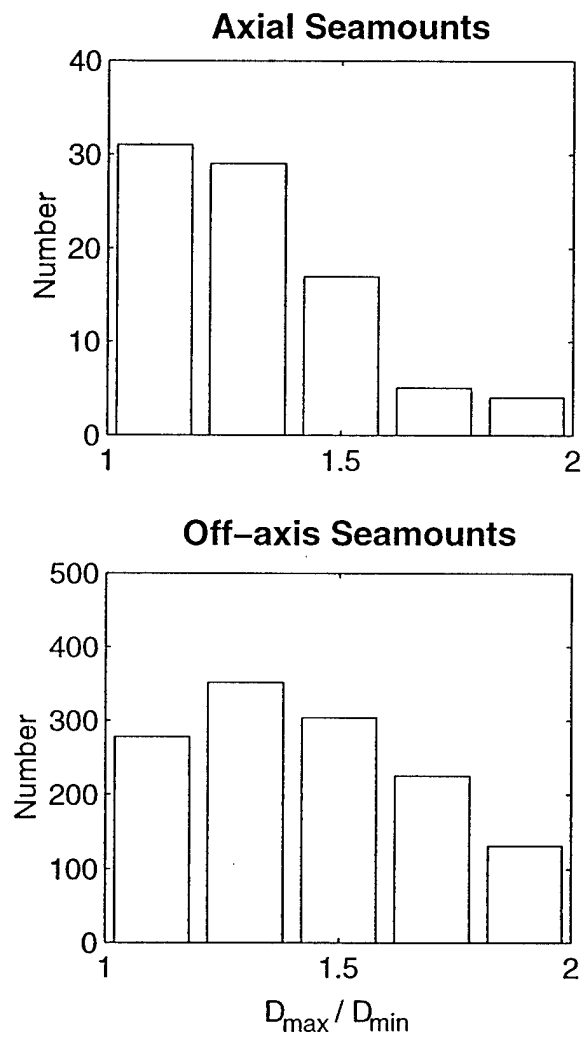


Figure 4

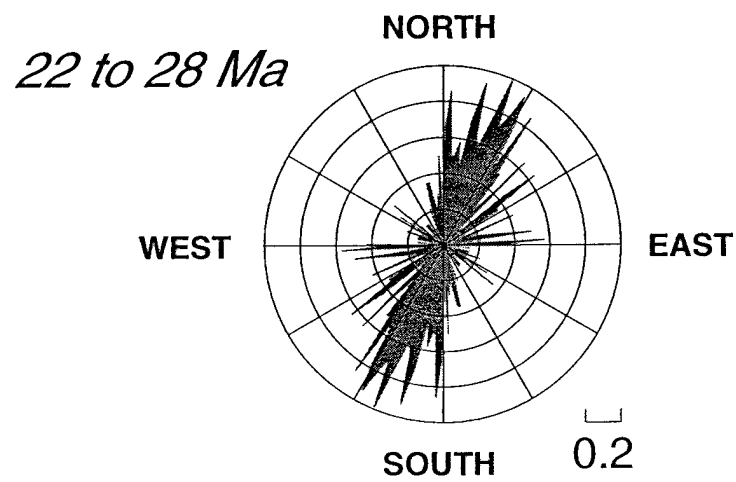
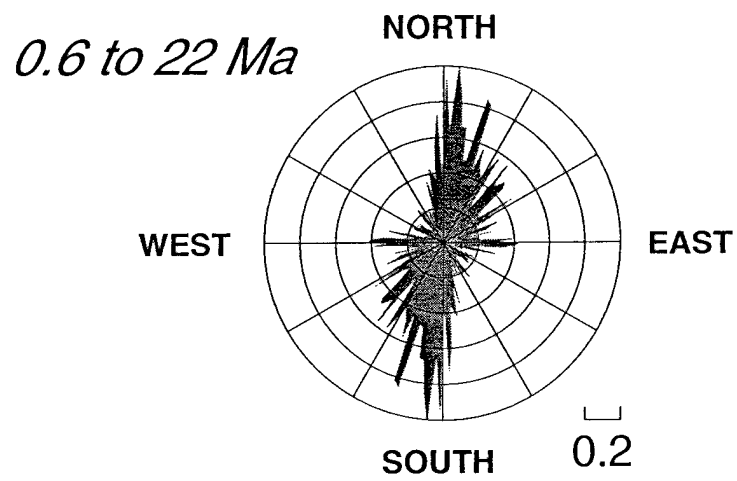
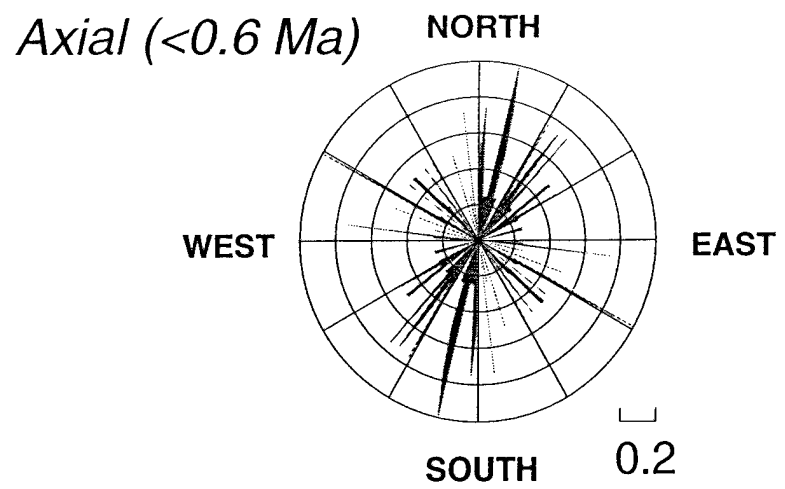
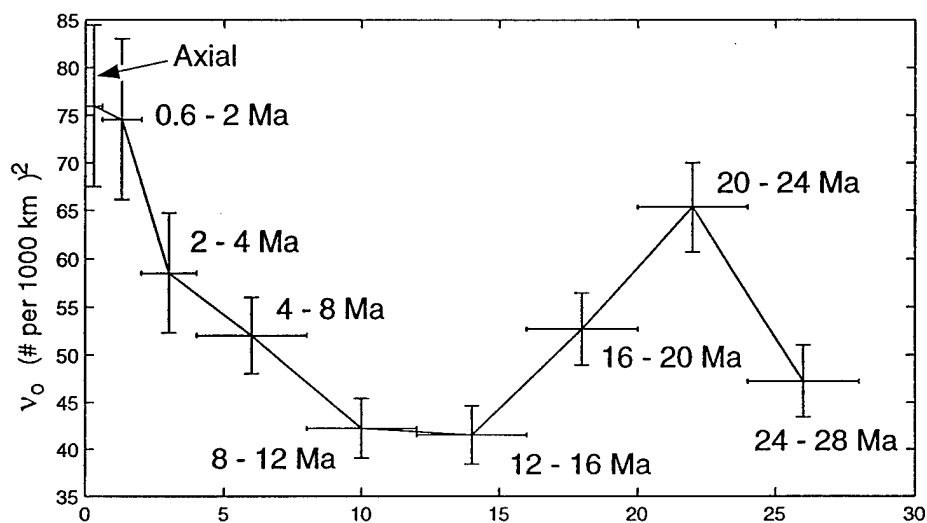


Figure 5

a)



b)

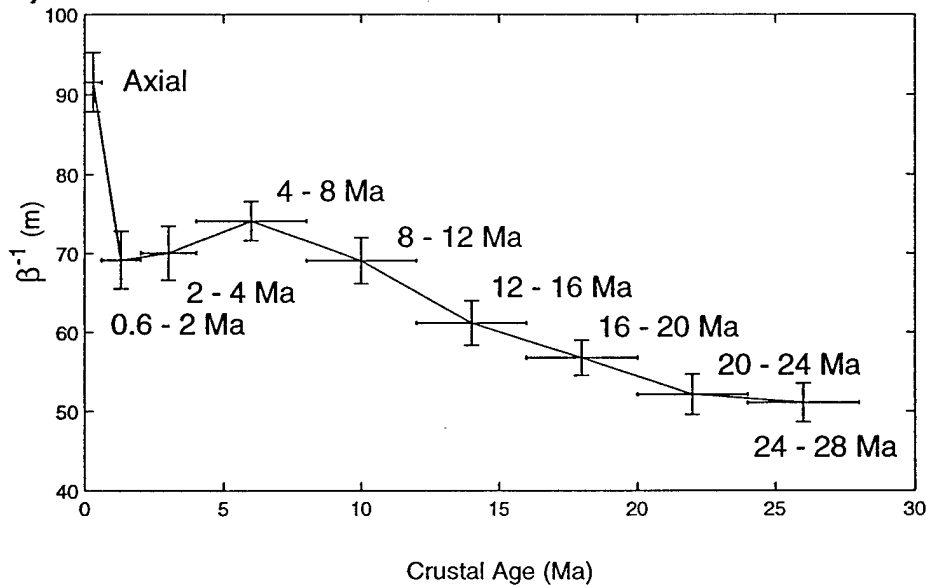
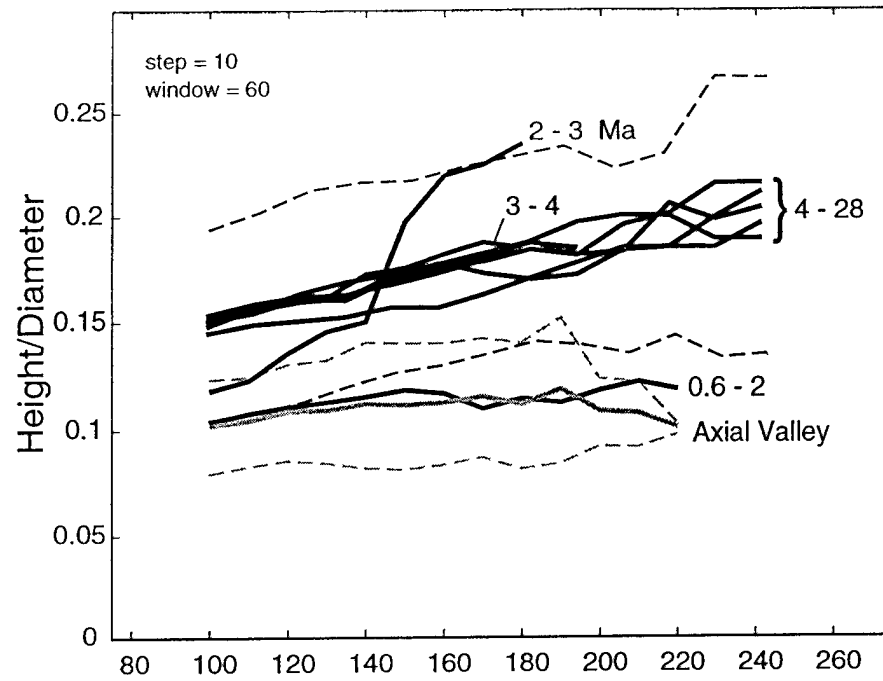


Figure 6

a)



b)

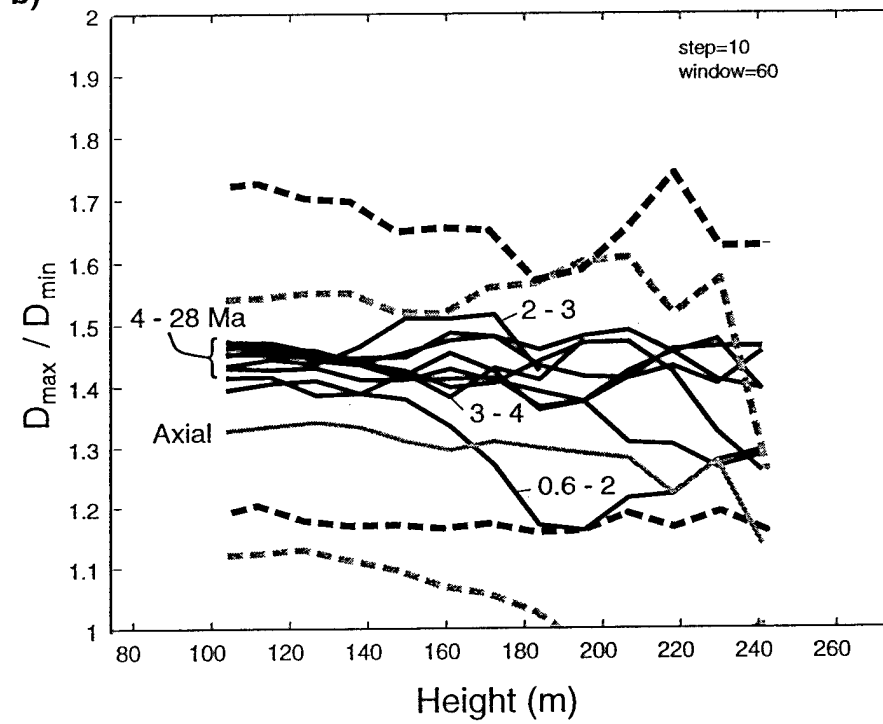


Figure 7

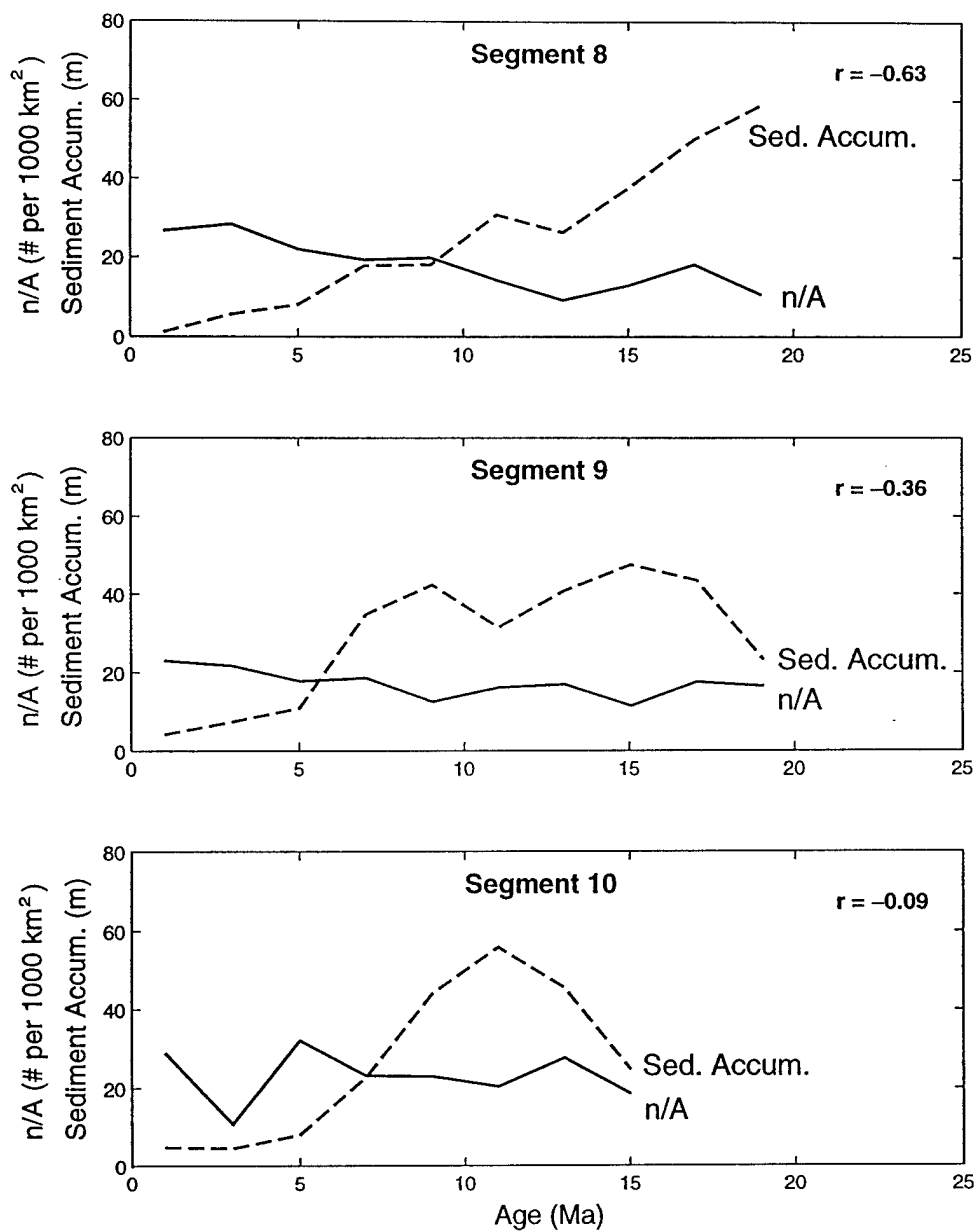


Figure 8

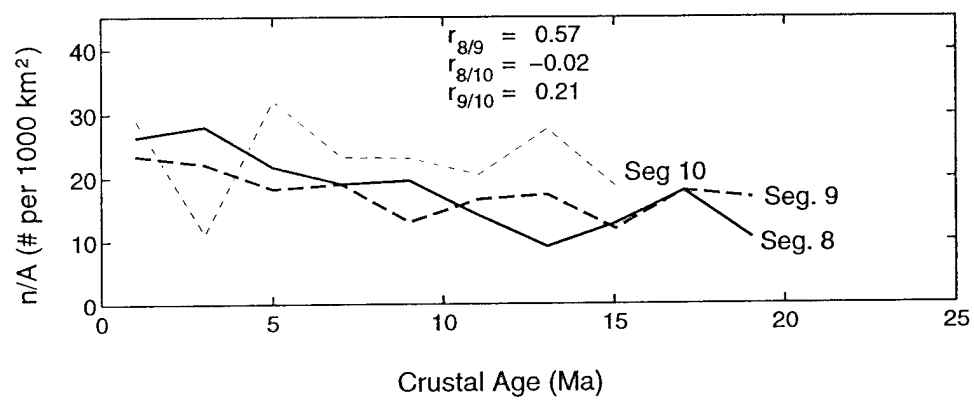


Figure 9

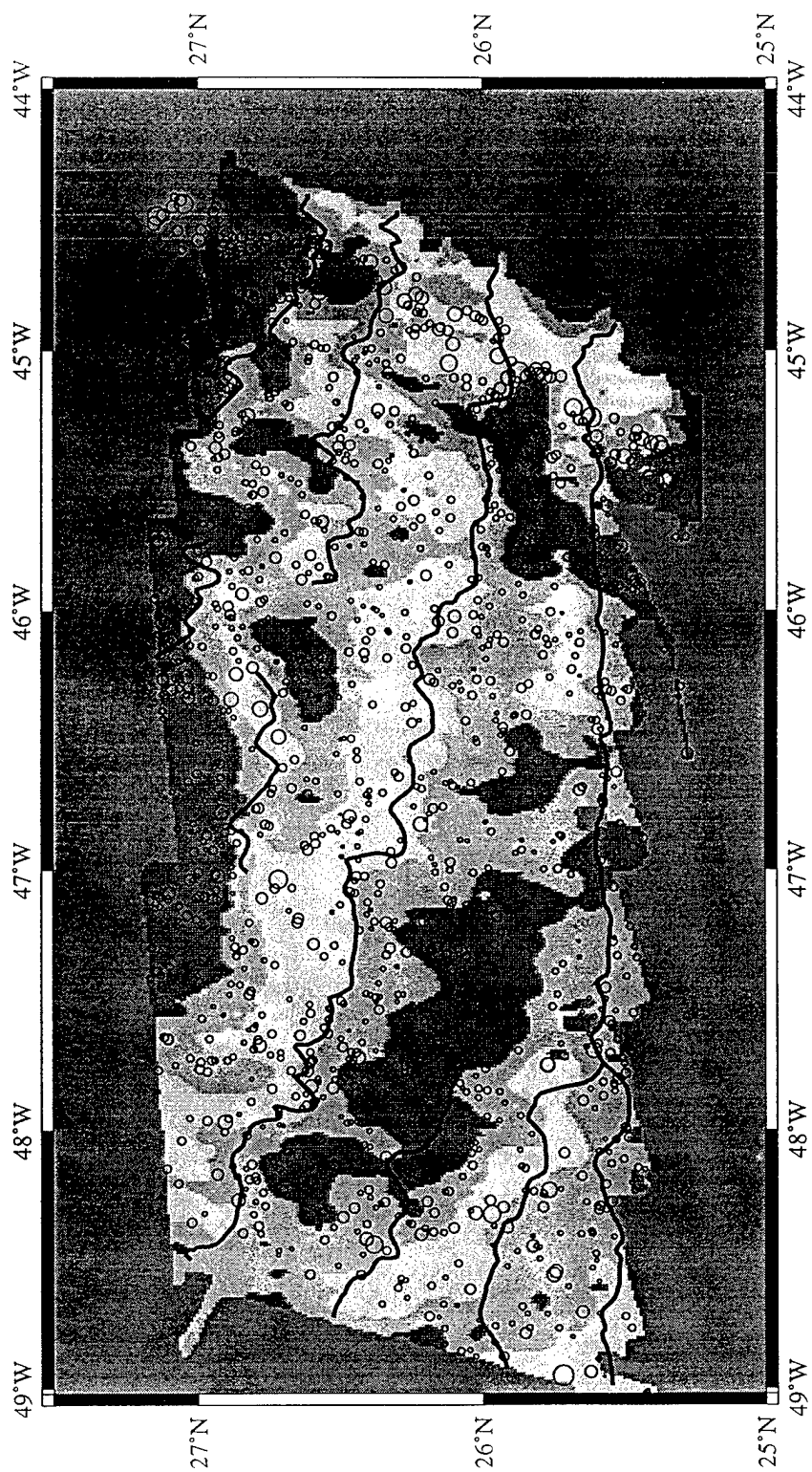
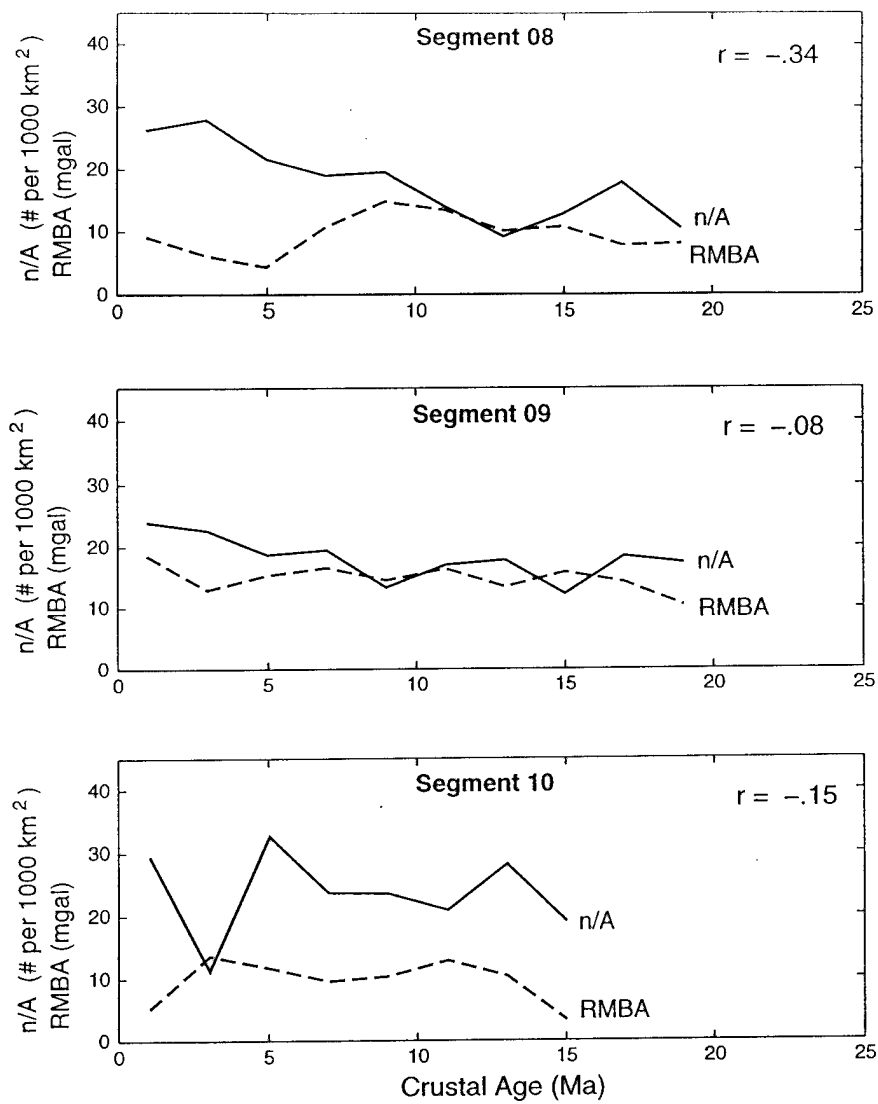


Figure 10

a)



b)

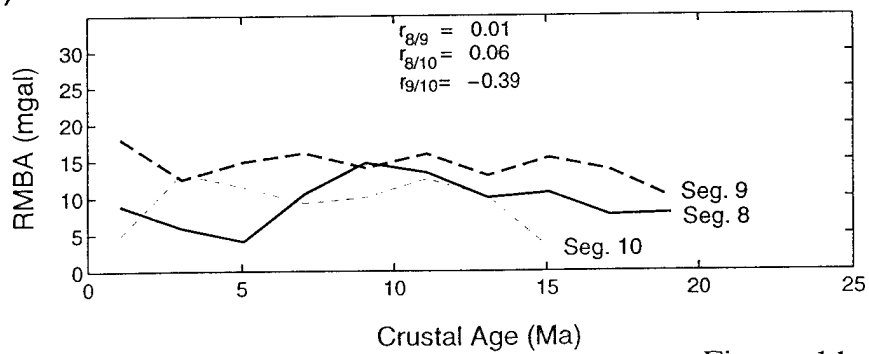


Figure 11

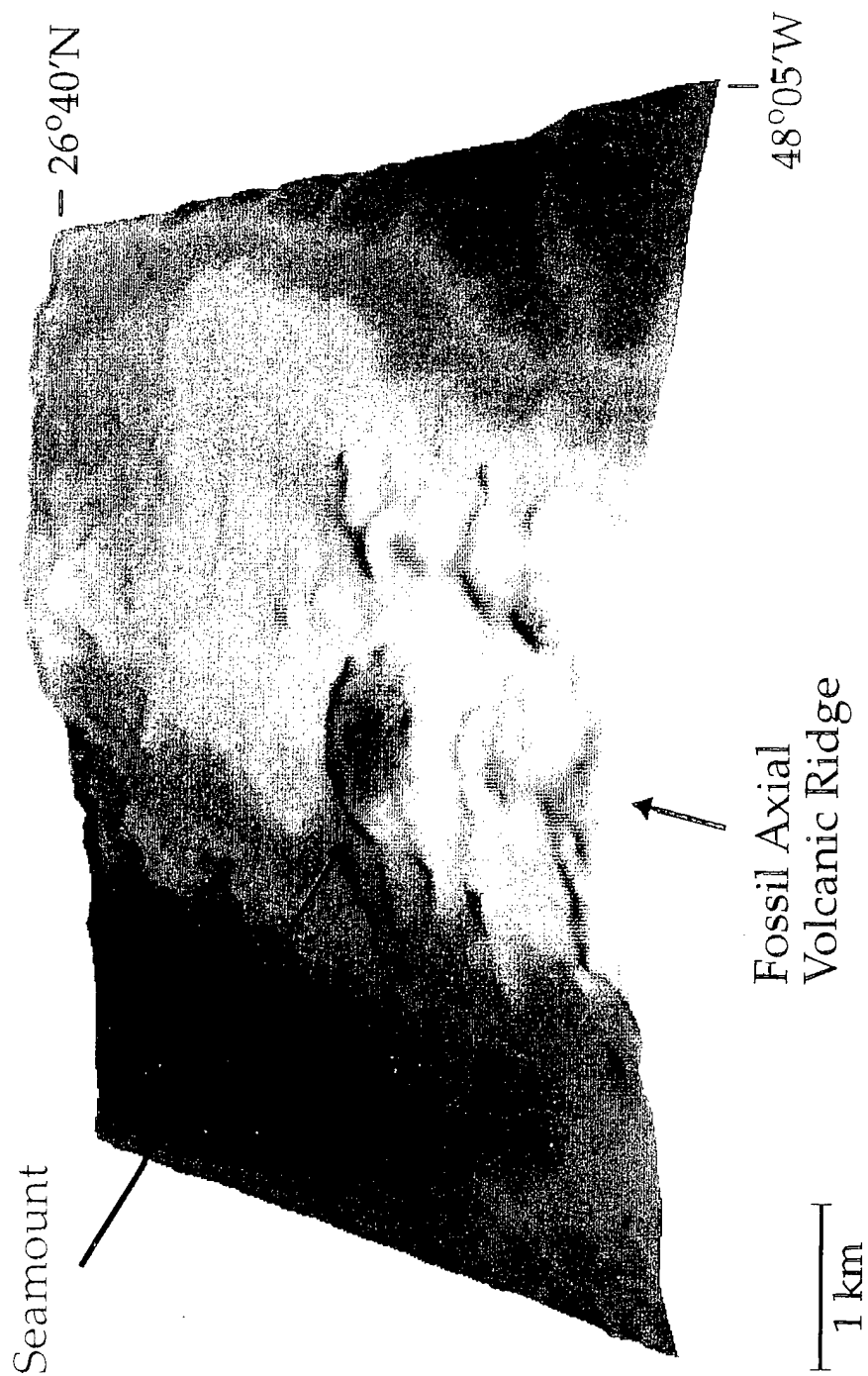


Figure 12

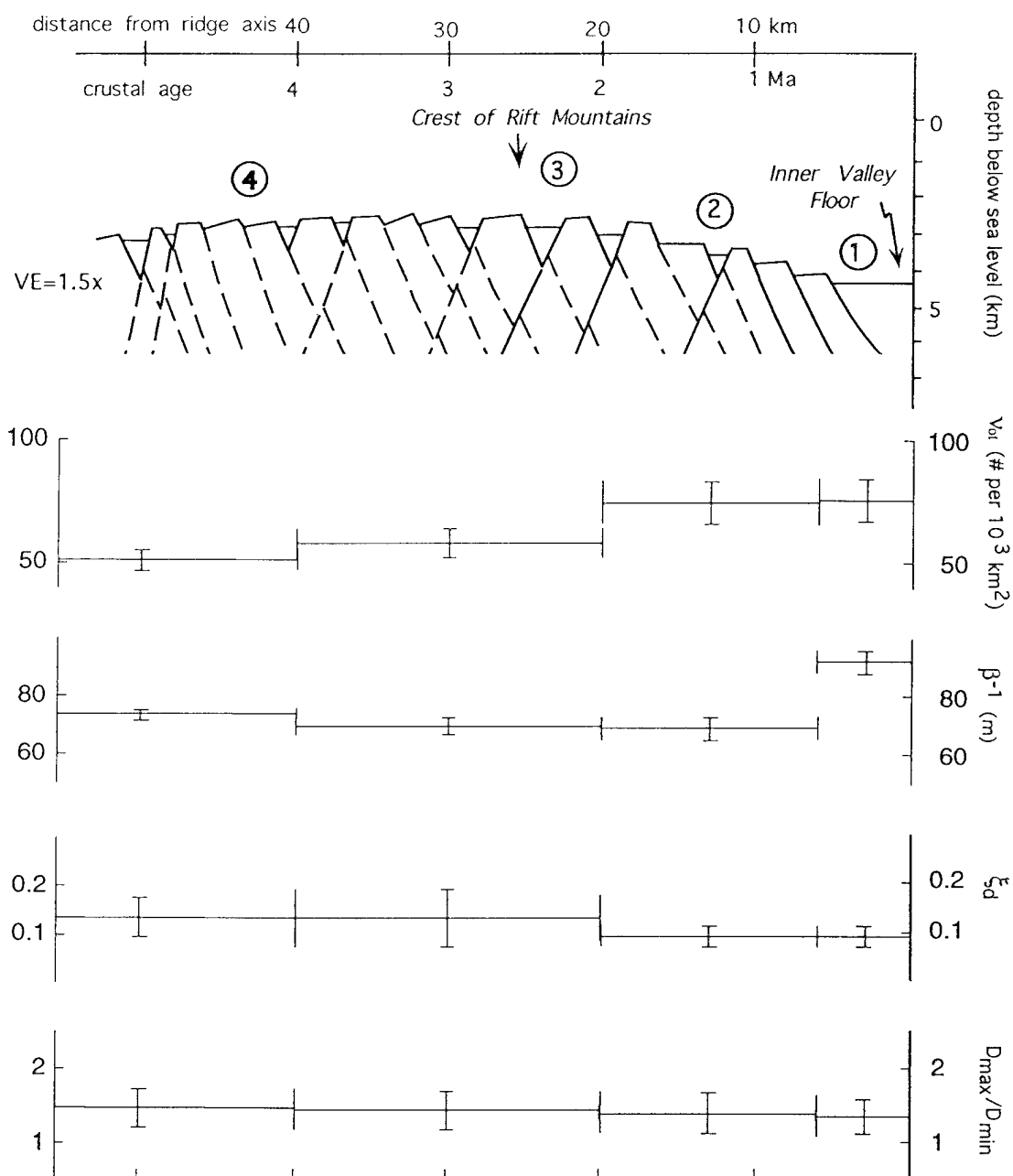


Figure 13

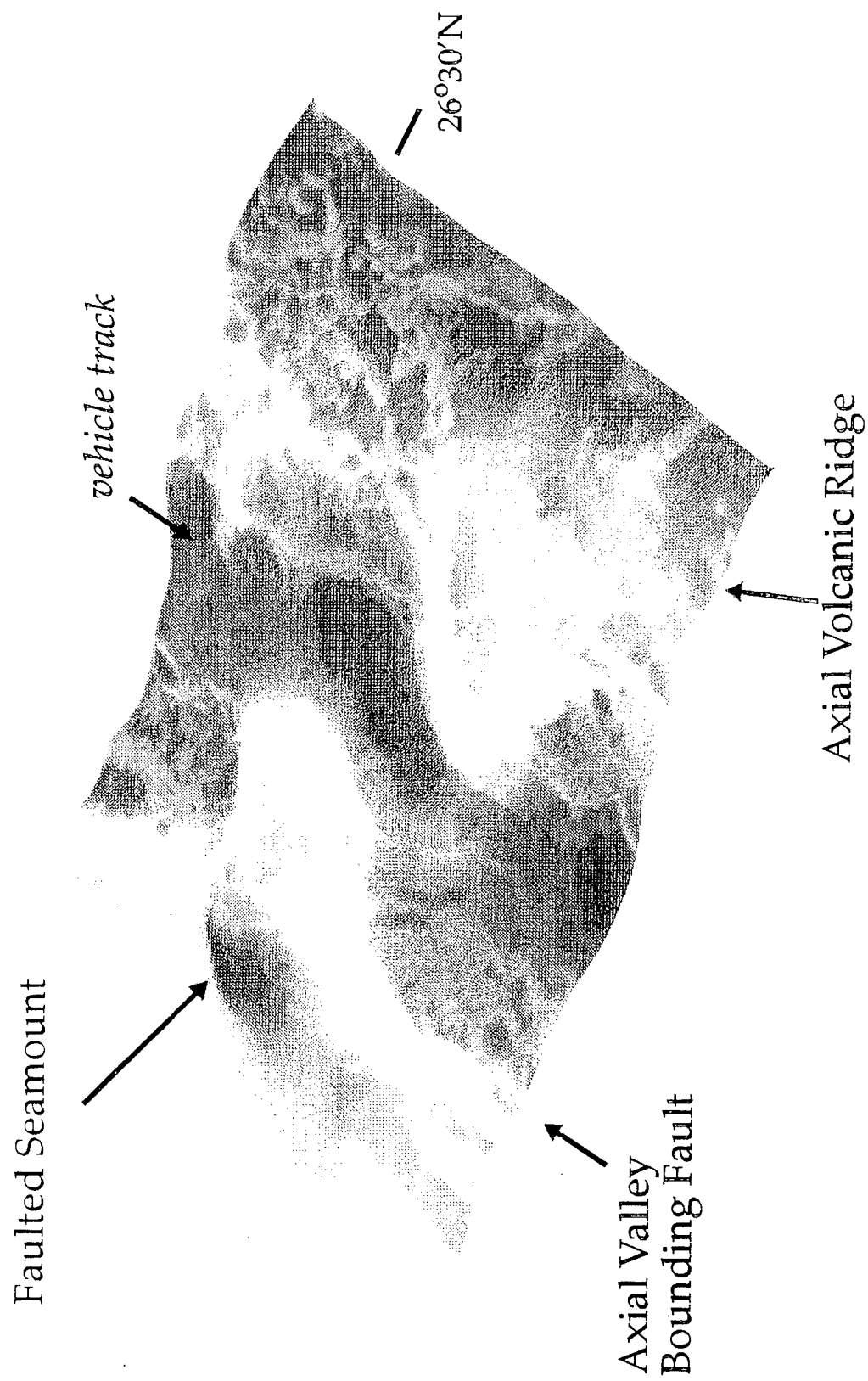
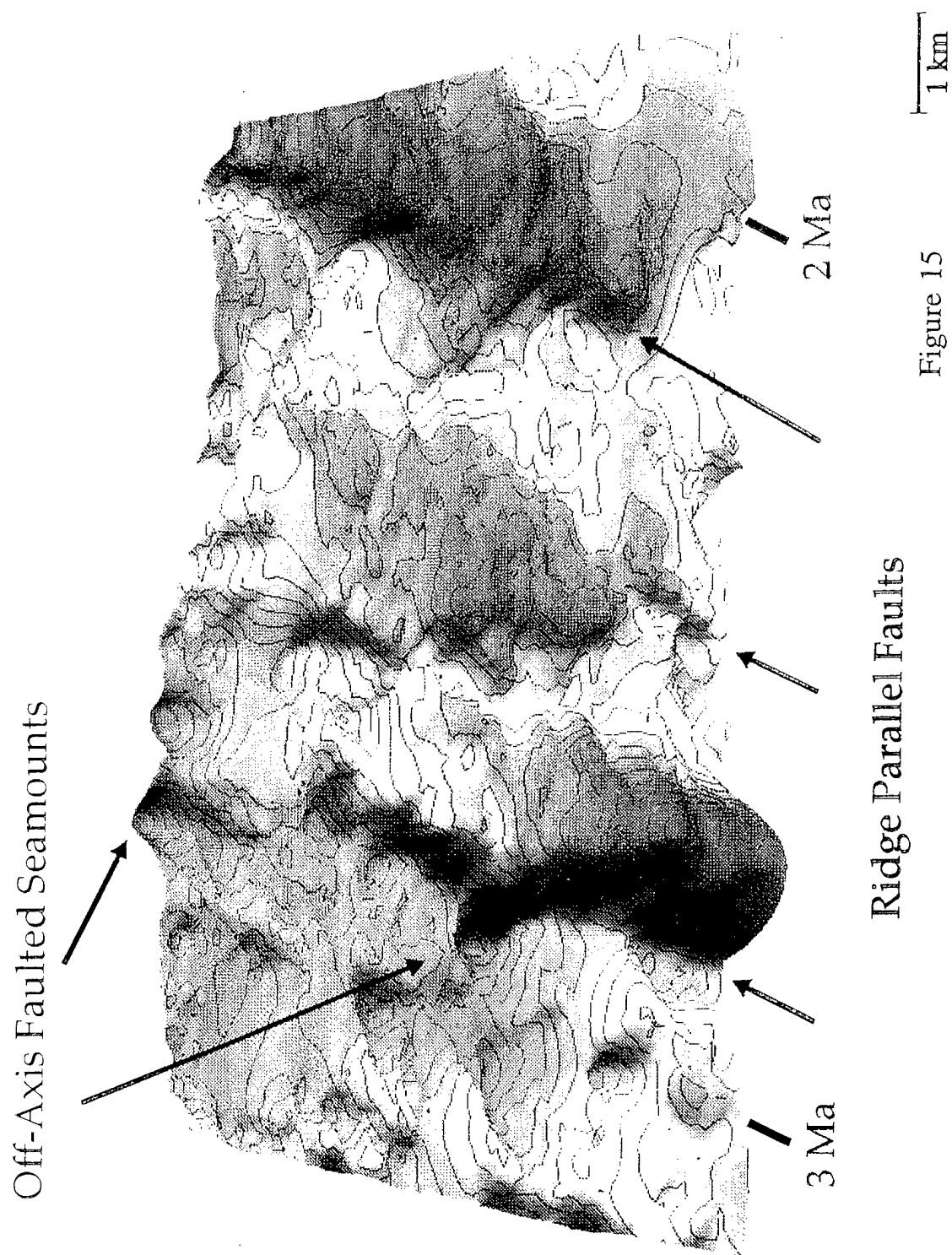


Figure 14



Chapter 5

ABYSSAL PERIDOTITE MYLONITES: IMPLICATIONS FOR GRAIN-SIZE SENSITIVE FLOW AND STRAIN LOCALIZATION IN THE OCEANIC LITHOSPHERE

Gary E. Jaroslow, Greg Hirth, and Henry J. B. Dick
Tectonophysics, 256 (1996) 17-37

Abyssal peridotite mylonites: implications for grain-size sensitive flow and strain localization in the oceanic lithosphere

G.E. Jaroslow ^{*,1}, G. Hirth, H.J.B. Dick

Department of Geology and Geophysics, Woods Hole Oceanographic Institution, Woods Hole, MA 02543, USA

Received 17 April 1995; accepted 14 August 1995

Abstract

Microstructures preserved in abyssal peridotites dredged from the oceans record several different physical regimes of deformation. Fabrics associated with deformation processes at slow-spreading mid-ocean ridges form two major classes of abyssal peridotites based on detailed microstructural observations. The most abundant class are medium- to coarse-grained tectonites with microstructures that reflect deformation processes during mantle upwelling and emplacement to the base of the lithosphere. These tectonites give geothermometric temperatures of $\sim 755^\circ\text{C}$ or higher, interpreted to represent lower temperature limits for diffusive exchange in coarse-grained abyssal peridotites during cooling. This conclusion is consistent with flow laws for olivine at these temperatures. The second class of abyssal peridotites, previously largely undescribed for the mid-ocean ridge environment, include fine-grained mylonites associated with faulting and shear zones that develop during extension and cooling of the oceanic lithosphere when the brittle-plastic transition extends into mantle rocks. These mylonites give temperatures of $\sim 600^\circ\text{C}$, which we suggest represent a lower temperature limit for plastic deformation. Reduced grain size in mylonites allows for diffusive exchange to continue to these low temperatures. Relict augen in the mylonitic samples preserve equilibration temperatures similar to those exhibited by the coarse-grained tectonites.

Based on flow laws for olivine, we suggest that deformation in some fine-grained mylonites occurred by diffusion creep down to $\sim 600^\circ\text{C}$. Rheological data for olivine indicate that dislocation creep is not likely to occur at this temperature. We conclude that a reduction in grain size by cataclasis, or dynamic recrystallization, resulted in a transition in deformation mechanisms from dislocation- to diffusion-creep during uplift (and/or cooling). The observation of these fine-grained mylonites indicates that shear zones that extend into the upper mantle will be weaker than expected if deformation was accommodated by brittle processes or dislocation creep. Weak faults may promote the development of long-lived detachments in the upper mantle. This inference supports mid-ocean-ridge tectonic models that suggest that ultramafic rocks exposed at the inside corners of ridge-axis discontinuities are exhumed along long-lived detachment faults.

1. Introduction

The structural evolution of mid-ocean ridges depends critically on the rheological properties of the

oceanic lithosphere. Current rheological models for the oceanic lithosphere are based largely on laboratory experiments, geophysical observations, and theoretical studies (e.g., Carter and Avé Lallemant, 1970; Brace and Kohlstedt, 1980; Chen and Molnar, 1983; Rutter and Brodie, 1988). A complementary approach to understanding ocean lithosphere rheology is reconstructing deformation histories using a

^{*} Corresponding author.

¹ Also: MIT/WHOI Joint Program in Oceanography, Woods Hole Oceanographic Institution, Woods Hole, MA 02543, USA.

combination of microstructural, petrological, and geochemical observations and analyses of natural peridotites (e.g., Cannat et al., 1992; Agar, 1994).

Microstructures of mantle rocks record compositional, thermal, and stress conditions of the asthenosphere and lithosphere that affect the mechanical response of the oceanic lithosphere during seafloor spreading. Deformation textures in abyssal peridotites can be used to distinguish between asthenospheric flow fabrics associated with mantle upwelling beneath mid-ocean ridges and plastic deformation fabrics associated with emplacement of these rocks at the seafloor (Nicolas et al., 1980). In addition, the thermal history of peridotites during uplift can be estimated using spinel–olivine geothermometry (e.g., Fabries, 1979; Ozawa, 1983). By combining microstructural observations, geothermometry, and flow law information, deformation histories reflected in the fabrics of ultramafic rocks emplaced at the seafloor can be resolved and the dominant deformation mechanisms in the upper mantle constrained.

Plastic deformation in the upper mantle can be accommodated by either diffusion creep, in which strain rate depends linearly on stress, or by dislocation creep in which strain rate follows a power law relationship with stress (e.g., Karato et al., 1986). Both theoretical and experimental studies demonstrate that diffusion creep, which is controlled by diffusive mass transport along either grain boundaries or grain matrices, is strongly dependent on grain size. In contrast, dislocation creep is normally grain-size insensitive. Experimental studies show that the activation energy for dislocation creep is greater than that for diffusion creep (e.g., Cooper and Kohlstedt, 1984; Karato and Wu, 1993; Hirth and Kohlstedt, 1995a). Thus, a reduction in grain size and decrease in temperature may result in a change in the operative deformation mechanism in the upper mantle (e.g., Rutter and Brodie, 1988; Handy, 1989).

Partially serpentinized mantle peridotite is the most abundant rock type dredged from fracture zones and inside corners of ridge/transform intersections at slow-spreading mid-ocean ridges (Dick, 1989; Tucholke and Lin, 1994). Ultramafic rocks are also commonly dredged along rift-valley walls and on fault scarps in rift mountains far from transforms (Aumento and Loubat, 1971; Skolotnev et al., 1989; Cannat, 1993; Silant'ev et al., 1996). These observa-

tions indicate that faults that extend down to the upper mantle play an important role in the structural evolution of slow-spreading oceanic lithosphere.

There are many different mechanisms that can promote a transition from broadly distributed deformation in the asthenosphere to more localized deformation and fault development in the lithosphere. For example, strain localization during uplift and/or cooling may result from geometrical weakening due to lattice-preferred orientation originating from asthenospheric flow (Karato and Wu, 1993). In addition, heterogeneities in lithospheric rheology may spatially focus deformation, and influence fault development (e.g., Ranalli and Murphy, 1987; Handy, 1989). Grain size reduction produced by cataclasis or dynamic recrystallization may further influence strain localization (e.g., Evans and Wong, 1985; Tullis et al., 1990; Drury et al., 1991). As a zone of weakness develops, strain can be localized into narrow zones of highly concentrated deformation (Drury et al., 1991).

In this study, we present microstructural and geothermometric data from naturally deformed upper-mantle rocks that place direct constraints on deformation conditions leading to fault development in the lithosphere at slow-spreading ridges. These results indicate a transition from dislocation to diffusion creep occurs during uplift of lithospheric peridotites due to a reduction in grain size and concomitant decrease in temperature. This transition in deformation processes results in localized deformation that occurs at much lower stresses than predicted by either Byerlee's law for brittle failure (Byerlee, 1978) or by flow laws for dislocation creep (Chopra and Paterson, 1981; Karato et al., 1986).

2. Geologic setting

Abyssal peridotites are sampled from three distinct environments at ocean ridges: (1) rift-valley walls adjacent to and far from transform faults; (2) transform-valley walls; and (3) scarps in the rift mountains away from both transforms and rift valleys. A generic location map is shown in Fig. 1.

Exposures of plutonic mylonites on rift-valley walls include material exposed directly on fault surfaces and in debris flows consisting of blocky talus

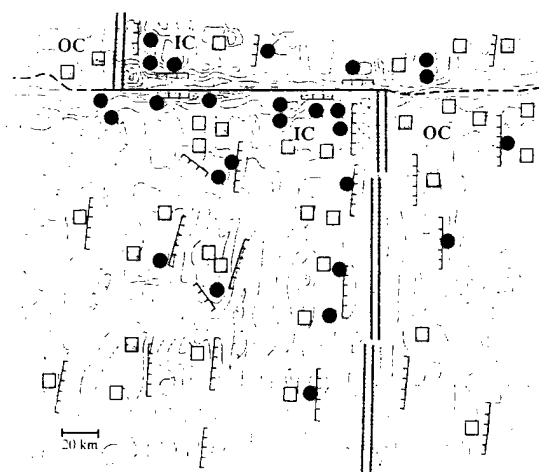


Fig. 1. Schematic map of a large-offset transform at a slow-spreading ridge showing the distribution of ultramafic rocks. This map was constructed by combining observations from the Atlantic II and Kane Fracture Zones (after Dick, 1989). Dots indicate possible peridotite mylonite exposures, and squares indicate those for basalt. Contour interval is 500 m. Maximum depth is around 6500 m. The inferred zone of present-day extension is shown by parallel lines and stippling highlights the neovolcanic ridge. The active transform is shown by the heavy solid line and its inactive trace by the heavy dashed line. IC = inside corner, and OC = outside corner of the ridge-transform intersection. Major normal faults are indicated by thin straight lines with teeth pointing in down-dip directions.

ranging from sand- to house-sized boulders. Both low- (30°) and high- (60°) angle fault surfaces exposing plutonic rocks on rift-valley walls have been observed using deep-towed cameras and submersibles. Peridotites and gabbros sampled directly from relatively low-angle fault surfaces are commonly mylonitized and metamorphosed in the amphibolite or greenschist facies (Karson and Dick, 1983; Karson and Dick, 1984; Karson et al., 1995); however, mylonitic deformation is not pervasive. Samples collected from joint surfaces and cross-faults cutting such surfaces may be either mylonitized or preserve asthenospheric flow fabrics (Karson and Dick, 1983; Karson and Dick, 1984; Karson et al., 1995).

The faults exposing mantle peridotites on rift-valley walls are believed to principally represent major low-angle faults striking parallel to the rift valleys and extending to mantle depths; the geometry of

these faults at depth is unknown. The origin of these low-angle faults is somewhat controversial. Karson and Dick (1983) suggested that these faults represent rotated high-angle normal faults. In contrast, Dick et al. (1981), Dick (1989), and Dick et al. (1991) suggest these are long-lived, primary, low-angle faults that are responsible for dismemberment of the crustal section and unroofing of plutonic rocks from beneath rift-valley-floor volcanics. In addition, at least two hypotheses have been described for termination of the normal faults at depth. Karson and coworkers have suggested that faults flatten with depth, forming detachment faults analogous to those in the basin and range province of the western U.S. (Karson et al., 1987; Hurst et al., 1990; Karson, 1990; Karson and Winters, 1992). Others suggest that the faulting dies out into the zone of upwelling beneath the ridge axis (Dick et al., 1981, 1991; Mevel et al., 1991; Tucholke and Lin, 1994). Finally, some of the exposed peridotites on rift-valley walls have been interpreted to represent serpentinite diapirism along high-angle faults (Aumento and Loubat, 1971; Bonatti, 1976; Silant'ev et al., 1996). Resolution of these models explaining the exposure of plutonic rocks on rift-valley walls depends not only on knowing the geometry of faults at mid-ocean ridges, but also on an improved understanding of the rheology of the lithosphere.

Much less data documenting the nature of faulting on transform walls are available, and the nature of the deformation fabrics in these regions is not well constrained. However, peridotite mylonites are also observed in these areas. Walls of transform valleys are commonly quite steep and consist of a 'staircase' of high-angle normal faults paralleling the transform (Francheteau et al., 1976; OTTER Team, 1984; OTTER Team, 1985). Seafloor can be uplifted several kilometers in these regions. For example, at St. Paul's Rocks in the equatorial Atlantic, transform walls are exposed at the sea surface. Several observations suggest that mylonitization occurs due to faulting and extension of the lower crust and mantle beneath the rift valley floors, and that it is not produced along faults associated with uplift along transform walls. In deep-tow surveys at ridge-transform intersections, transform-wall faults appear to intersect (and presumably cut) many of the faults exposed along rift-valley walls. Mylonites, drilled in

a 500-m-thick section of gabbro exposed on a wave-cut terrace at Hole 735B on the crest of the transverse ridge flanking the Atlantis II Fracture Zone on the Southwest Indian Ridge (SWIR), were apparently oriented orthogonal to the transform (Dick et al., 1991). Similarly, the foliation in peridotite mylonites exposed above sealevel on the transverse ridge flanking St. Paul's Fracture Zone, at St. Paul's Rocks, is observed at right angles to the flanking transform wall and is parallel to the axis of the Mid-Atlantic Ridge (Melson et al., 1972).

Mylonites are also observed along scarps in the rift mountains away from both transforms and rift valleys (Aumento and Loubat, 1971). These scarps may simply represent faults and associated debris on fossil rift-valley walls. However, the abundance of peridotites dredged along the Hudson 45°N geotransverse across the Mid-Atlantic Ridge does increase into the rift mountains away from the rift valleys (Aumento et al., 1971). This observation suggests that active emplacement of mantle peridotites to the seafloor may continue in the rift mountains beyond the rift-valley walls.

3. Sample selection

Peridotite mylonites constitute a major textural class at slow-spreading ocean ridges. In our collections from eleven different fracture zones at slow spreading ridges, peridotite mylonites were recovered in ~20% (14 of 65) of all peridotite-bearing dredge hauls (Fisher et al., 1985; Dick, 1989; Dick et al., 1991). By weight, the mylonites comprise 14.3% of all peridotites documented. In the 14 dredges containing mylonites, the mylonites constitute 44.7% by weight, and 4 of these dredges record >90% peridotite mylonites (up to 357 kg in one dredge). In addition, on Southeast Islet at St. Paul's Rocks, where peridotite mylonites are subaerially exposed, the zone of mylonites measures at least 67 m in thickness (the breadth of the island normal to the strike of the foliation). These observations indicate that peridotite mylonites do not necessarily represent small localized shear zones, but may comprise relatively broad zones of deformation.

The majority of our samples come from land-slips and debris flows and thus represent a nearly random

sampling of the rocks associated with shallow faulting. Mass wasting is a characteristic feature of the geomorphology of transform walls; debris flows and rock slides characterize most of the rocks observed during submersible and deep-tow traverses of transform walls (e.g., Francheteau et al., 1976; OTTER Team, 1984, 1985; Karson and Dick, 1983). Land slides/slump scars on the walls of transforms often indicate that 10's of km² may be involved in a single slip. Thus, rocks from deep within the fault block exposed by mass wasting can constitute the majority of the material exposed in such debris flows. Because most dredged samples come from land-slips and debris flows, we do not know which of the mylonites selected for this study should be attributed to faulting beneath the rift valley rather than along transforms. However, in-situ mylonites have only been observed on faults parallel to rift-valley walls, as described above.

We examined approximately one thousand thin sections representing the entire range of altered and deformed peridotites dredged from the Arctic, Atlantic, Caribbean and Indian oceans. Therefore, samples from all of the major slow-spreading (<50 mm/yr full rate) ocean ridges, except the Nansen-Gakkel Ridge, were studied. Our sampling does not include peridotites from fast-spreading ridges. The 37 mylonite samples listed in Table 1 were studied in detail, and we assume that these samples are representative of plastic deformation microstructures in peridotites from slow-spreading ridges. However, there may be some bias introduced by systematically selecting the least-altered rocks (<20% serpentine); most abyssal peridotites examined contain greater than 65% serpentine. The majority of the samples were collected by the Woods Hole Oceanographic Institution. Additional samples were provided by the Scripps Institution of Oceanography (courtesy of R.L. Fisher) and the University of Rhode Island (courtesy of J.-G. Schilling).

4. Analytical techniques

Microstructural observations were made using transmitted and reflected light microscopy on ultrathin (<10–20 µm) sections, and using a Philips

Table 1
List of peridotite mylonite samples studied with recovery locations

Sample	Locality/Site	Latitude	Longitude	Water depth (m)
<i>Knipovich Ridge:</i>				
En 26-71	Spitzbergen FZ/E wall	79°22.8'N	02°38.7'E	3200–2000
<i>Mid-Atlantic Ridge:</i>				
AII 20:9-1	Romanche FZ	10°45.0'N	43°18.0'W	4990–3490
AII 20:9-4	Romanche FZ	10°45.0'N	43°18.0'W	4990–3490
<i>Southwest Indian Ridge:</i>				
PS 86:4-36	North FZ/wall	52°07.0'S	14°09.2'E	3800–2790
AII 107:60-4	Shaka FZ/SE wall	53°25.7'S	09°09.1'E	5399–4207
AII 107:60-44	Shaka FZ/SE wall	53°28.8'S	09°11.4'E	5399–4207
AII 107:60-58	Shaka FZ/SE wall	53°25.2'S	09°14.3'E	5399–4207
AII 107:61-74	Shaka FZ/SE wall	53°25.1–25.2'S	09°11.9–16.7'E	4418–4063
AII 107:61-75	Shaka FZ/SE wall	53°25.1–25.2'S	09°11.9–16.7'E	4418–4063
AII 107:61-76	Shaka FZ/SE wall	53°25.1–25.2'S	09°11.9–16.7'E	4418–4063
AII 107:61-78	Shaka FZ/SE wall	53°25.1–25.2'S	09°11.9–16.7'E	4418–4063
AII 107:61-83	Shaka FZ/SE wall	53°25.1–25.2'S	09°11.9–16.7'E	4418–4063
IO 11-76 58-23	Islas Orcadas FZ/SE wall	54°05.5'S	06°23.9'E	3580–2960
IO 11-76 58-30	Islas Orcadas FZ/SE wall	54°05.5'S	06°23.9'E	3580–2960
IO 11-76 60-102	Islas Orcadas FZ/SE wall	54°05.5'S	06°23.9'E	2780–2500
IO 11-76 60-126	Islas Orcadas FZ/SE wall	54°05.5'S	06°23.9'E	2780–2500
Prot 5:15-25	Andrew Bain FZ	47°–641.9'S	32°09.6'E	4400–4000
Prot 5:18-1	Prince Edward FZ	46°31.5–32.5'S	33°45.8–47.1'E	5100–4800
Prot 5:18-2	Prince Edward FZ	46°31.5–32.5'S	33°45.8–47.1'E	5100–4800
Prot 5:18-6	Prince Edward FZ	46°31.5–32.5'S	33°45.8–47.1'E	5100–4800
Prot 5:18-8	Prince Edward FZ	46°31.5–32.5'S	33°45.8–47.1'E	5100–4800
Prot 5:18-10	Prince Edward FZ	46°31.5–32.5'S	33°45.8–47.1'E	5100–4800
Prot 5:18-11	Prince Edward FZ	46°31.5–32.5'S	33°45.8–47.1'E	5100–4800
Prot 5:18-12	Prince Edward FZ	46°31.5–32.5'S	33°45.8–47.1'E	5100–4800
Prot 5:18-16	Prince Edward FZ	46°31.5–32.5'S	33°45.8–47.1'E	5100–4800
Prot 5:18-25	Prince Edward FZ	46°31.5–32.5'S	33°45.8–47.1'E	5100–4800
Prot 5:18-30	Prince Edward FZ	46°31.5–32.5'S	33°45.8–47.1'E	5100–4800
Prot 5:18-40	Prince Edward FZ	46°31.5–32.5'S	33°45.8–47.1'E	5100–4800
Prot 5:19-32	Prince Edward FZ	46°30.4–31.0'S	33°49.9–55.0'E	3900–2700
Prot 5:19-33	Prince Edward FZ	46°30.4–31.0'S	33°49.9–55.0'E	3900–2700
Prot 5:17-1	Prince Edward FZ/MTR	46°22.7–23.6'S	33°30.5–31.2'E	2380–2050
INMD 8-8 HD4	Discovery FZ	41°51.8'S	42°39.6'E	4120–3650
INMD 8-8 HD5	Discovery FZ	41°51.8'S	42°39.6'E	4120–3650
INMD 8-8 HD12	Discovery FZ	41°51.8'S	42°43.6'E	4120–3650
INMD 8-13 HD1	Gallieni FZ	36°42.1–42.3'S	52°13.7–16.0'E	5300–4750
INMD 8-13 HD4	Gallieni FZ	36°42.1–42.3'S	52°13.7–16.0'E	5300–4750
RC 27-9:18-7	Atlantis II FZ/E wall	32°07.1'S	57°06.0'E	4899–4170

Abbreviations in locality column are as follows: FZ = fracture zone; MTR = median tectonic ridge.

EM420 transmission electron microscope (TEM). Orientations of crystallographic axes were measured using a universal stage. Grain sizes were measured by the mean linear intercept method (Pickering, 1976) using a measurement grid superimposed on reflected

light microphotographs; gridlines were oriented parallel and perpendicular to deformation fabrics.

Mineral compositions were obtained using a Jeol 733 Superprobe at the electron microprobe facility at the Massachusetts Institute of Technology. Natural

and synthetic minerals were used as primary silicate standards. The principal spinel standard used was chromite 52NL11. Silicate and oxide analyses have been corrected using Bence–Albee correction procedures (Bence and Albee, 1968). Ferric iron in spinels was calculated on the basis of spinel stoichiometry (8 positive charges, 3 cations).

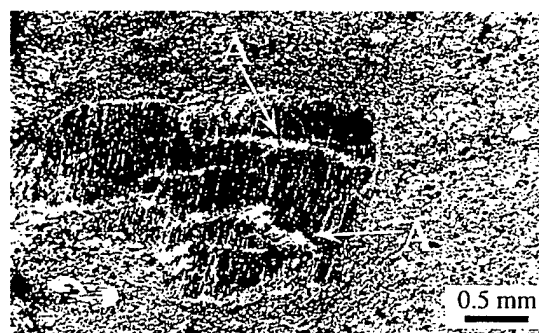
5. Primary mineralogy and high-temperature alteration

The abyssal peridotites studied are predominantly harzburgites and lherzolites with occasional dunites; all are spinel-bearing. About one third of the peridotites contain plagioclase, although these samples were collected from only a few dredge hauls. Typical harzburgites consist of 60–90% olivine, 10–40% orthopyroxene, 0–5% clinopyroxene, and 0–1.5% spinel. Typical lherzolites have 50–80% olivine, 10–40% orthopyroxene, 5–10% clinopyroxene, and 0–1.5% spinel.

Hydrothermal alteration in the peridotites studied ranges from upper-amphibolite/lower-granulite (550°–700°C) to lower-greenschist facies (350°–450°C). Post-kinematic alteration sequences are generally consistent with the progressive hydration–cooling sequence observed in ultramafic rocks from the Islas Orcadas Fracture Zone (Kimball et al., 1985). High-temperature incipient alteration occurs in the form of clinopyroxene altering to amphibole, and orthopyroxene to talc or talc plus olivine, along cleavage planes and kink-bands. Microfractures and veins are filled with amphibolite to greenschist facies metamorphic assemblages. In this case, the vein-filling minerals are amphibole, talc, (high-birefringent) serpentine, secondary olivine, and chlorite; these phases are stable at maximum temperatures of 825°, 600°, 510°, 510°, and 450°C, respectively (Hemley et al., 1977; Robinson et al., 1981). In one sample, AII 107:61–83, the end of macroscopic ductile deformation is marked by microcracks that cross-cut foliation but are filled with the relatively anhydrous assemblage of granular plagioclase, clinopyroxene, pargasitic hornblende, and olivine, suggesting vein filling in the upper amphibolite or granulite facies. In general, veins of amphibole and talc are commonly crosscut by later generations of chlorite veins with

opaque oxides, followed by serpentine veins. With progressive hydration, early-generation alteration veins may further retrograde to lower temperature assemblages. Clustered laths of amphiboles are common as well, usually in association with clinopyroxene and talc products, and occasionally with chlorite reaction rims about altered spinel. In moderately serpentinized samples, bastite textures are common. The latest-stage alteration is marked by pervasive chloritization and serpentinization. As previously noted, the peridotite mylonites selected for detailed microstructural study were chosen in part because low-grade alteration was not pervasive.

Synkinematic alteration in the peridotite mylonites studied is not common, but evidence for high-temperature synkinematic alteration is exhibited



a



b

Fig. 2. Optical micrographs of synkinematic alteration. (a) Veins filled with amphibole (arrows) cross-cut orthopyroxene porphyroclast but do not continue into recrystallized matrix. Sample AII 107:60–4. (b) Vein filled with olivine, pyroxene, and amphibole is folded within fine-grained matrix that has been subsequently altered. Sample AII 107:60–44.

in most of the suite from the Shaka Fracture Zone, SWIR. For example, in sample AII 107:60-4, synkinematic veins filled with amphibole cross-cut pyroxene porphyroclasts but do not extend into the surrounding recrystallized matrix (Fig. 2a). In sample AII 107:60-44, veins of secondary olivine, pyroxene, and amphibole are folded, also suggesting amphibolite-facies synkinematic alteration (Fig. 2b).

6. Microstructure

We have identified two major classes of abyssal peridotites based on microstructural observations: coarse granular tectonites and fine-grained mylonites. Most coarse granular peridotites have olivine and orthopyroxene grains that are large (1–10 mm), nearly equant, and exhibit curvilinear grain boundaries often meeting at triple-grain junctions (Fig. 3a). In some cases, the coarse granular abyssal peridotites contain elongate orthopyroxene grains and have small amounts of recrystallization along their grain boundaries, although serpentinization may overprint finer features (Fig. 3b). Similar coarse granular textures have been described for mantle xenoliths in basalt, ophiolitic peridotites, and abyssal peridotites, and are referred to as protogranular or coarse porphyroclastic (Mercier and Nicolas, 1975; Nicolas et al., 1980; Boudier and Nicolas, 1982). These deformation textures are interpreted to form from flow associated with mantle upwelling and late-stage emplacement at the base of the crust beneath mid-ocean ridges (Nicolas et al., 1980). Therefore it is reasonable to assume that at some point in their history all abyssal peridotites had this type of microstructure, although later-stage deformation may overprint it.

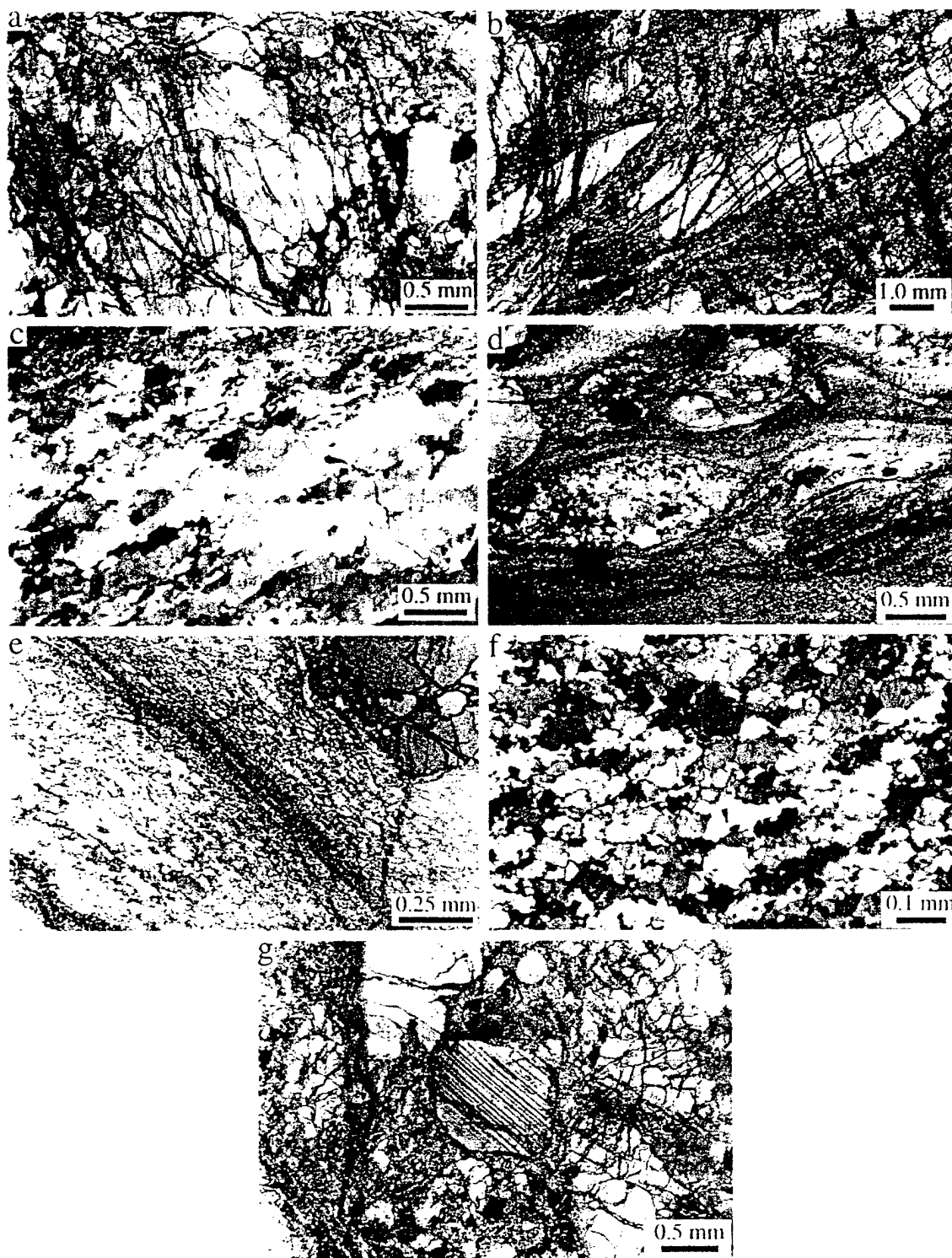
The mylonitic peridotites have S–C fabrics that overprint the original asthenospheric flow textures to various degrees. Mylonitic textures vary between samples; the shape and mineralogy of porphyroclasts, the extent of recrystallization, and recrystallized grain size reflect variations in rheological conditions during textural development.

The mylonitic texture in abyssal peridotites that shows the most similarity to coarse granular textures is distinguished by ribbons of homogeneously flattened olivine grains, as shown in Fig. 3c. These ribbons may partly form from kinking and recrystal-

lization of the original coarse-grained fabric. Olivine grain size averages $\sim 300 \mu\text{m}$. These grains exhibit sweeping undulatory extinction, extensive subgrain development, and gypsum-plate analysis indicate a strong lattice-preferred orientation with a statistical preferred maximum (010) parallel to the foliation. In some cases, such as shown in the upper quarter of Fig. 3c, a fine-grained (5–100 μm) matrix of recrystallized olivine and pyroxene surrounds polycrystalline augen with the ribbon-like microstructure.

A second mylonitic texture that exhibits more pronounced grain size reduction is shown in Fig. 3d and Fig. 3e. The porphyroclasts are composed of well-rounded to elongate crystals of olivine or pyroxene with grain sizes ranging from approximately 100 μm to $> 10 \text{ mm}$. In addition, polycrystalline porphyroclasts are observed in these mylonites. An extremely fine-grained (sometimes $< 5 \mu\text{m}$) matrix of recrystallized grains surrounds the porphyroclasts, and although the extent of recrystallization varies, it can be as high as 80%. In relatively coarse-grained ($> 10 \mu\text{m}$) deformation bands where crystallographic orientations can be measured optically with a universal stage, there is a relatively strong lattice-preferred orientation (Fig. 4). Within finer-grained ($< 10 \mu\text{m}$) regions, quantitative measurement of crystallographic axes is impractical, but qualitative optical observations suggest that these regions have weak or no lattice-preferred orientation and decrease in the amount of grain elongation (Fig. 5). These observations indicate that crystallographic fabric decreases in intensity with decreasing grain size. TEM observations show that within fine-grained regions, where olivine grain size is less than $\sim 2 \mu\text{m}$, small fractions of pyroxene with grain size $< 1 \mu\text{m}$ are often distributed between recrystallized olivine grains (Fig. 6a), possibly inhibiting the migration of grain boundaries and retarding grain growth (e.g., Olgaard, 1990). In pyroxene-free regions, where recrystallized grain size of olivine is greater than $\sim 2 \mu\text{m}$, grain growth occurs unimpeded by secondary phases (Fig. 6b).

A third mylonitic texture that is relatively uncommon is noteworthy in that it lacks obvious strain features such as porphyroclastic fabric, undulatory extinction, or large degrees of grain flattening, which characterize the other mylonitic textures described above. As shown in Fig. 3f, these mylonites have a



weakly banded, granular structure of nearly equant to slightly flattened grains of recrystallized olivine. Recrystallization is nearly complete in these samples, with a mean recrystallized grain size of $\sim 25 \mu\text{m}$. This microstructure resembles that of the polycrystalline porphyroclasts shown in Fig. 3d. Olivine porphyroclasts are rare or nonexistent, and the occasional pyroxene and spinel porphyroclasts are rounded and relatively small ($< 1 \text{ mm}$).

Cataclastically deformed peridotites are not included as a separate microstructural classification in this study because by definition their texture reflects deformation in the brittle field. In practice, it is often difficult to distinguish between fine-grained cataclastic and mylonitic textures using optical microscopy. For example, some peridotites dredged from the Prince Edward Fracture Zone, SWIR, have porphyroclastic textures with at most a weak foliation (Fig. 3g). The olivine and pyroxene porphyroclasts in these peridotites are large, up to 3 mm and 8 mm respectively, often well rounded and/or elongate, and they may exhibit a weak lattice-preferred orientation. Aside from the porphyroclastic texture of these rocks, deformation is recorded as kink-bands and bent cleavage planes in pyroxene and undulose extinction in both pyroxene and olivine. The matrix, which comprises $< 30\%$ of the rock, is fine-grained ($< 10 \mu\text{m}$) and contains angular to rounded grains, but does not strictly resemble fault breccia.

Spinel habit in abyssal peridotite mylonites varies within and between individual samples and does not appear to correlate with deformation fabric classifications. Spinel has a variety of habits in the mylonites studied, as listed in Tables 2 and 3. It exists as vermicular exsolutions in pyroxene, rounded blebs distributed at triple-junction grain boundaries, randomly distributed euhedral to anhedral crystals, and

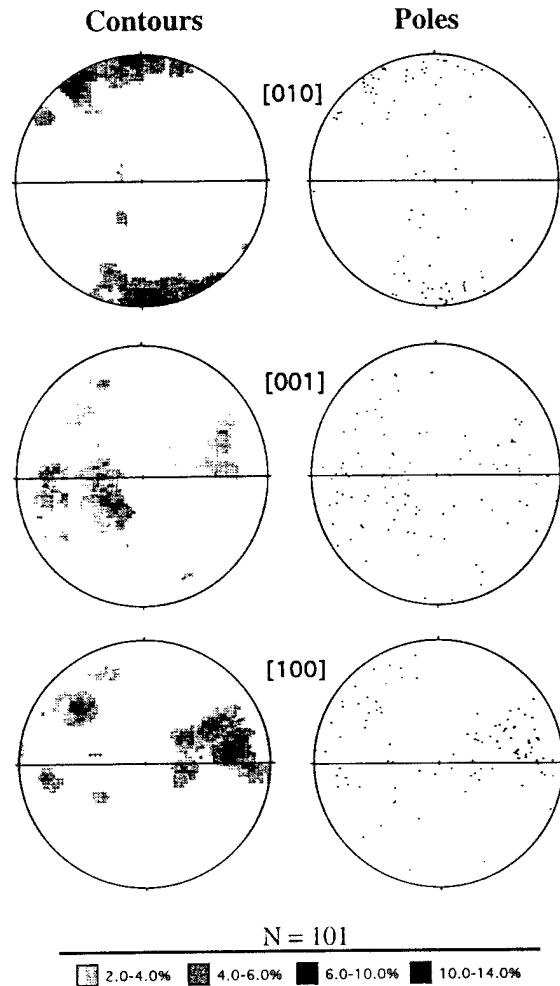


Fig. 4. Lower-hemisphere, equal-area stereonet plots of the orientation of olivine crystallographic axes in coarse-grained ($> 10 \mu\text{m}$) regions of sample AII 107:61-83. Shaded densities represent percentage per 1% area. Foliation is oriented along the east-west axis and is marked by the solid line. A relatively strong lattice-preferred orientation is displayed with an [100] lineation plunging $\sim 30^\circ$ from the plane of the thin section.

Fig. 3. Optical micrographs of abyssal peridotite textures. (a) Coarse granular texture. Large olivine crystals typically exhibit curvilinear grain boundaries. Sample Prot 5:29-25 from the Prince Edward Fracture Zone, SWIR. (b) Orthopyroxene grains show large degree of flattening observed in many coarse-grained peridotites. Olivine matrix has been completely serpentinized. Sample PS 86:4-36B from the North Fracture Zone, SWIR. (c) Olivine microstructure indicative of dislocation creep. Grains exhibit undulatory extinction and homogeneous flattening (similar to Regime II dislocation creep in quartz aggregates described by Hirth and Tullis, 1992). Sample Prot 5:18-2. (d) Porphyroclastic microstructure illustrates localized reduction in size of dynamically recrystallized grains between impinging polycrystalline aggregate porphyroclasts. Foliation within the ultrafine-grained ($< 10 \mu\text{m}$) matrix is pronounced in dark tails of pyroxene. Sample AII 107:61-83. (e) Recrystallized grains have an average grain size of $18.3 \mu\text{m}$. Grain size within the fine grain deformation bands averages $7.1 \mu\text{m}$. Sample AII 107:61-83. (f) Mylonite with extensive dynamic recrystallization. Sample EN 26:26-71. (g) Weakly foliated fabric with well-rounded clinopyroxene porphyroclast in a fine grained matrix. Sample Prot 5:19-1 from the Prince Edward Fracture Zone, SWIR.

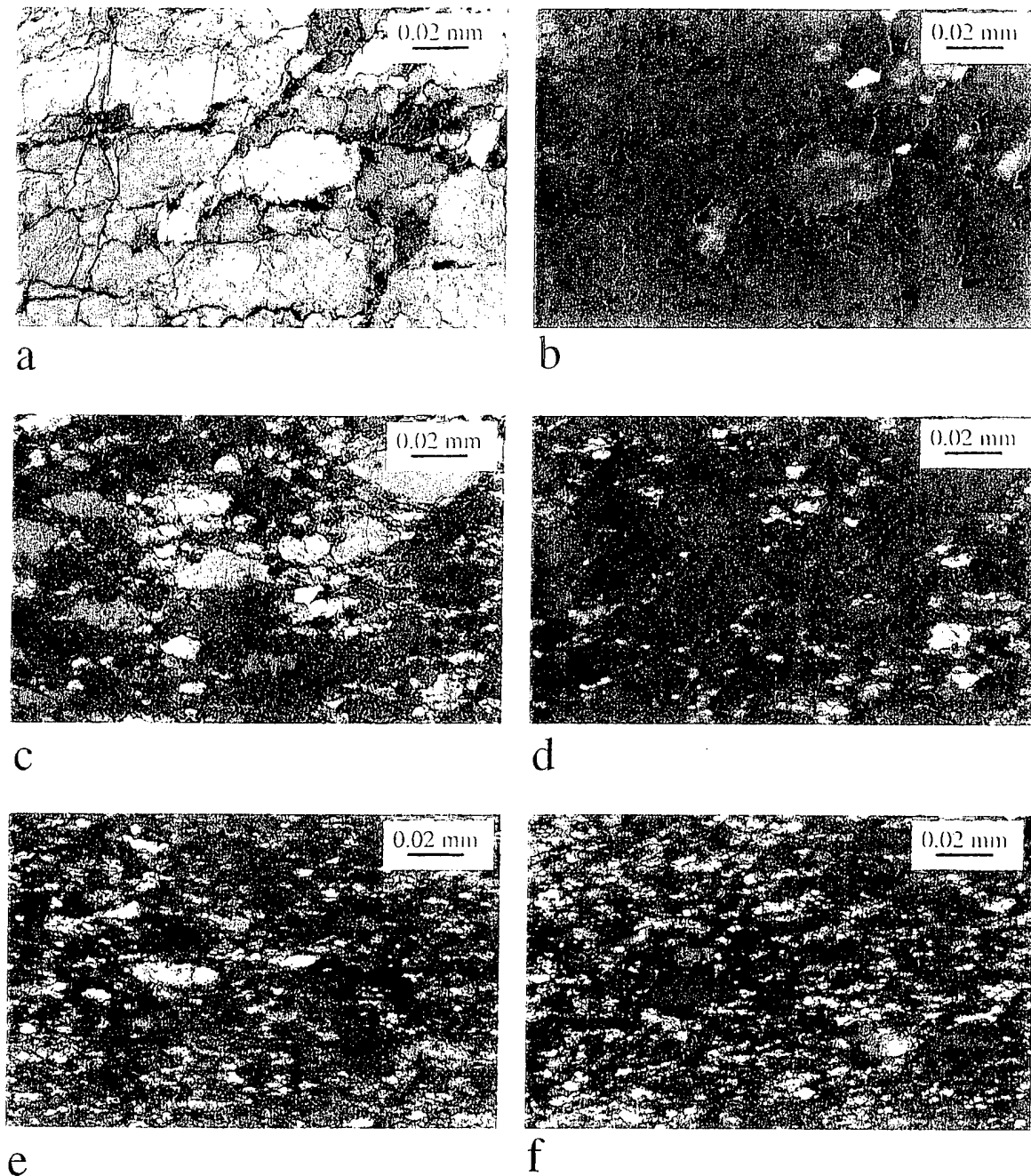


Fig. 5. Optical micrographs of olivine crystallographic orientations in sample AII 107:61-83 (cross-polarizers with gypsum plate addition). Micrograph pairs are oriented at complementary extinction angles ($\sim 90^\circ$). (a, b) Coarse-grained ($> 10 \mu\text{m}$) region exhibits flattened grains, strong lattice-preferred. This microstructure is indicative of deformation by dislocation creep. (c, d) Fine-grained (5–20 μm) region exhibiting relatively weak lattice-preferred orientation and reduction in the amount of grain flattening. This region may represent a transition between dislocation to diffusion creep processes. (e, f) Within the finest-grained regions ($< 5 \mu\text{m}$), lattice orientation appears to be nearly random and deformation is interpreted to occur by diffusion creep.

as holly-leaf shapes associated with pyroxene. Holly-leaf-shaped spinel has previously been correlated with porphyroclastic fabrics in peridotite xenoliths, and interpreted as evidence for post-kinematic growth (Mercier and Nicolas, 1975). Although the same correlation can be made for abyssal peridotite mylonites, holly-leaf-shaped spinels occur infrequently and cannot be used as consistent geological markers.

7. Geothermometry

7.1. Geothermometer

The Mg–Fe exchange equilibrium between spinel and olivine is temperature-dependent. Although numerous geothermometers have been calibrated based on the partitioning of Mg^{2+} and Fe^{2+} between olivine and spinel (e.g., Irvine, 1965; Jackson, 1969; Evans and Frost, 1975; Fabries, 1979; Engi, 1983), the olivine–spinel geothermometer of Sack and Ghiorso (1991) was chosen for this study because it has been calibrated for low temperatures (400°–1400°C) and pressures, and for natural complex sys-

tems. It was developed to define equilibration temperatures for subassemblages of olivine plus spinel in ultramafic rocks metamorphosed in the greenschist–granulite facies. Olivine–spinel geothermometry was selected over pyroxene geothermometry because the exchange of Mg^{2+} and Fe^{2+} between olivine and spinel occurs at temperatures below those at which pyroxenes cease to equilibrate (Henry and Medaris, 1980).

To obtain equilibration temperatures of thermal events, the olivine–spinel geothermometer is applied to core–core pairs of spinel and olivine (average composition) in peridotite samples with deformation textures representative of the classifications defined in this paper. Cores of olivine and spinel in natural peridotites generally preserve Mg^{2+} – Fe^{2+} distributions established during high temperature exchange, and are more likely to have uniform compositions than regions near grain boundaries (Ozawa, 1983).

Mylonite samples selected for geothermometry are listed in Tables 2 and 3. Both relict (porphyroclast) and recrystallized (neoblast) spinel/olivine pairs were analyzed. If relict and recrystallized grains could not be distinguished by optical microscopy, coarse grains of olivine and spinel (> 0.3 mm) were

Table 2
Representative average compositions of olivine in abyssal peridotite mylonites

Sample	Sample type	MgO	Al ₂ O ₃	SiO ₂	CaO	TiO ₂	Cr ₂ O ₃	MnO	FeO	NiO	Total	Mg#
EN 26:26-71	F	49.781	0.000	40.903	0.016	0.079	0.030	0.119	9.101	0.375	100.403	0.91
AII 107:60-4	L	49.063	0.029	40.620	0.008	0.061	0.000	0.102	9.247	0.358	99.486	0.90
AII 107:60-4	F	48.775	0.000	40.554	0.044	0.058	0.000	0.124	9.691	0.331	99.576	0.90
AII 107:61-78	L	48.436	0.009	40.849	0.024	0.071	0.000	0.144	9.414	0.357	99.302	0.90
AII 107:61-78	F	48.356	0.000	40.944	0.039	0.041	0.112	0.071	9.275	0.358	99.194	0.90
AII 107:61-83	L	49.245	0.014	40.761	0.037	0.040	0.017	0.126	9.493	0.368	100.099	0.90
AII 107:61-83	F	49.589	0.016	40.694	0.024	0.037	0.047	0.114	9.644	0.358	100.520	0.90
IO 11-76:60-126	F	48.708	0.011	40.367	0.043	0.046	0.129	0.091	9.403	0.186	98.984	0.90
PROT 5:18-2	L	49.549	0.051	40.811	0.014	0.012	0.013	0.151	9.170	0.356	100.125	0.91
PROT 5:18-2	F	49.412	0.030	40.788	0.011	0.025	0.075	0.130	9.374	0.269	100.112	0.90
PROT 5:18-6	L	48.035	0.000	40.236	0.024	0.044	0.038	0.122	10.606	0.374	99.476	0.89
PROT 5:18-6	F	47.664	0.000	40.529	0.011	0.072	0.042	0.149	11.156	0.246	99.867	0.88
PROT 5:18-40	L	49.108	0.019	40.826	0.024	0.026	0.048	0.068	9.484	0.337	99.940	0.90
PROT 5:18-40	F	49.371	0.000	41.001	0.020	0.063	0.029	0.129	9.871	0.352	100.836	0.90
INMD 8-13 HD4	L	49.235	0.019	40.709	0.008	0.037	0.102	0.153	9.114	0.354	99.728	0.91
INMD 8-13 HD4	F	48.286	0.084	41.398	0.066	0.015	0.088	0.127	8.960	0.284	99.309	0.91
RC27-9:18-7	L	48.914	0.046	41.038	0.000	0.042	0.017	0.136	9.975	0.353	100.520	0.90
RC27-9:18-7	F	49.306	0.040	40.958	0.040	0.049	0.000	0.144	9.673	0.345	100.555	0.90

Abbreviations are as follows: L = large grains (porphyroclasts); F = fine grains (neoblasts); Mg# = Mg/(Mg + Fe).

Table 3
Representative average compositions of spinel in abyssal peridotite mylonites

Sample	Sample type	Habit	Ave. grain size (μm)	MgO	Al_2O_3	SiO_2	CuO	TiO_2	Cr_2O_3	MnO	FeO	Fe_2O_3	NiO	Total	Mg#	Cr#	Fe^{3+} + #
EN 26: 26-71	L	S	1000	17.311	38.240	0.020	0.020	0.062	28.769	0.163	11.190	3.787	0.140	99.700	0.73	0.34	0.04
EN 26: 26-71	F	B	30	16.367	42.822	0.058	0.037	0.032	23.449	0.143	13.050	2.560	0.166	98.683	0.69	0.27	0.03
AIH 107: 60-4	L	S	500	17.378	45.004	0.027	0.000	0.076	21.958	0.142	12.260	2.867	0.177	99.888	0.72	0.25	0.03
AIH 107: 60-4	F	B	50	16.271	44.218	0.029	0.000	0.048	21.685	0.168	13.520	2.860	0.128	98.926	0.68	0.25	0.03
AIH 107: 61-78	L	A	1100	18.766	50.804	0.000	0.008	0.000	14.380	0.171	10.655	4.645	0.380	99.808	0.76	0.16	0.05
AIH 107: 61-78	F	B	40	17.692	48.877	0.000	0.032	0.006	16.222	0.213	11.867	4.073	0.273	99.256	0.73	0.18	0.04
AIH 107: 61-83	L	S	1400	19.827	51.112	0.092	0.000	0.074	14.143	0.097	9.230	4.440	0.361	99.373	0.79	0.16	0.04
AIH 107: 61-83	F	A	90	18.675	49.426	0.085	0.006	0.055	15.508	0.106	10.775	4.510	0.288	99.432	0.76	0.17	0.05
Prot 5: 18-2	L	S	800	16.508	40.733	0.015	0.025	0.017	25.468	0.143	12.710	3.685	0.128	99.431	0.70	0.30	0.04
Prot 5: 18-6	L	H	1000	17.969	49.198	0.020	0.000	0.084	16.063	0.108	11.937	4.357	0.318	100.052	0.73	0.18	0.04
Prot 5: 18-6	F	H	20	17.386	51.584	0.046	0.020	0.042	13.304	0.110	12.913	3.210	0.204	98.818	0.71	0.15	0.03
Prot 5: 18-23	L	A	300	18.169	50.874	0.033	0.011	0.080	14.167	0.141	11.546	3.460	0.210	98.692	0.74	0.16	0.04
Prot 5: 18-23	F	B	20	15.992	44.921	0.080	0.031	0.110	19.897	0.212	13.855	3.065	0.185	98.346	0.67	0.23	0.03
Prot 5: 18-40	L	A,H	800	20.468	52.830	0.000	0.000	0.046	13.168	0.094	8.740	4.640	0.279	100.265	0.81	0.14	0.05
Prot 5: 18-40	F	B	20	17.147	46.656	0.047	0.000	0.048	18.459	0.130	12.680	3.930	0.162	99.259	0.71	0.21	0.04
INMD 8-13 HD4	L	H	400	19.327	51.123	0.080	0.000	0.040	15.537	0.072	10.280	3.110	0.197	99.764	0.77	0.17	0.03
INMD 8-13 HD4	F	H	10	17.788	49.010	0.128	0.058	0.000	16.652	0.098	11.685	2.410	0.202	98.030	0.73	0.19	0.02
RC27-9: 18-7	L	E	800	20.216	52.136	0.018	0.026	0.135	14.541	0.056	9.080	3.545	0.264	100.016	0.80	0.16	0.04
RC27-9: 18-7	F	B	10	11.902	26.383	0.146	0.054	0.250	38.574	0.279	17.490	3.510	0.117	98.705	0.55	0.50	0.04

Abbreviations are as follows; L = large grains (porphyroclasts); F = fine grains (neoblasts); A = anhedral; E = euhedral; S = subhedral; B = rounded blebs; H = holly-leaf-shaped; Mg# = $\text{Mg}/(\text{Mg} + \text{Fe})$; Cr# = $\text{Cr}/(\text{Cr} + \text{Al})$; Fe^{3+} # = $\text{Fe}^{3+}/(\text{Fe}^{3+} + \text{Al} + \text{Cr})$.

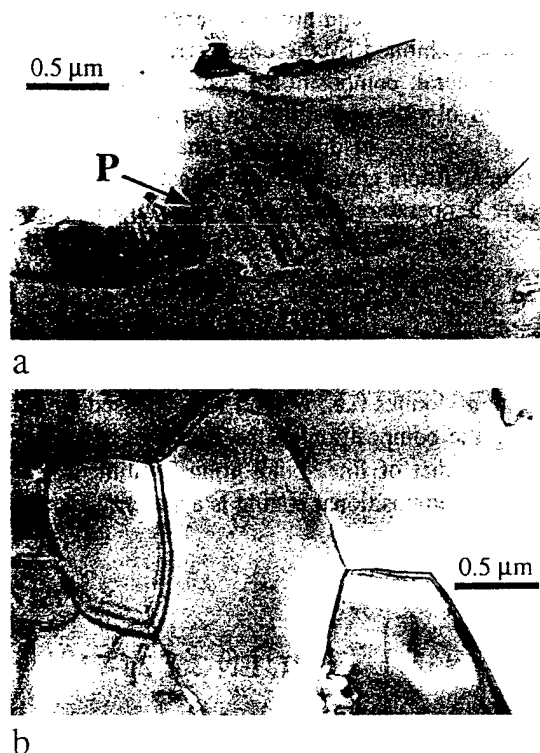


Fig. 6. TEM micrographs of ultrafine-grained matrix. Sample AII 107:61-83. (a) In regions where recrystallized olivine grain size is $< \sim 2 \mu\text{m}$, the presence of pyroxene inhibits grain growth. (b) In regions where recrystallized olivines are $> \sim 2 \mu\text{m}$, grain growth is not impeded by a second phase.

selected as potential primary relict phases and fine grains ($< 0.1 \text{ mm}$) were selected as potential recrystallized phases. All of the mylonitic samples have some degree of hydrothermal alteration; however, spinels included in our geothermometric analysis have no optical or chemical evidence of alteration. Spinel was not included in this study if they showed optical evidence of resorption or alteration, if they were identified from high $\text{Cr}/(\text{Cr} + \text{Al})$ and low $\text{Mg}/(\text{Mg} + \text{Fe})$ values as being hydrothermally altered (e.g., Kimball, 1990), or if they were in contact with metamorphic assemblages.

7.2. Equilibrium temperatures

The equilibration temperatures of porphyroclast and neoblast spinel/olivine pairs from thirteen mylonite samples are summarized in Table 4 and Fig. 7.

Table 4

Grain sizes and geothermometrically derived temperatures of olivine/spinel pairs

Sample	Neoblast T ($^{\circ}\text{C}$)	Porphyro- clast T ($^{\circ}\text{C}$)	Grain size (μm)	
			neoblast	porphyro- clast
EN 26:26-71	586	751	20	1000
AII 107:60-4	586	624	50	500
AII 107:61-78	577	650	40	1100
AII 107:61-83	671	800	70	1400
PROT 5:18-2	619	633	10	800
PROT 5:18-6	599	735	20	1000
PROT 5:18-23	572	688	50	300
PROT 5:18-40	600	844	20	800
INMD 8-13 HD4	555	705	10	400
RC 27-9:18-7	692	854	10	800

In order to compare the equilibration temperatures obtained for the peridotite mylonites to those of non-mylonitic abyssal peridotites, the equilibrium

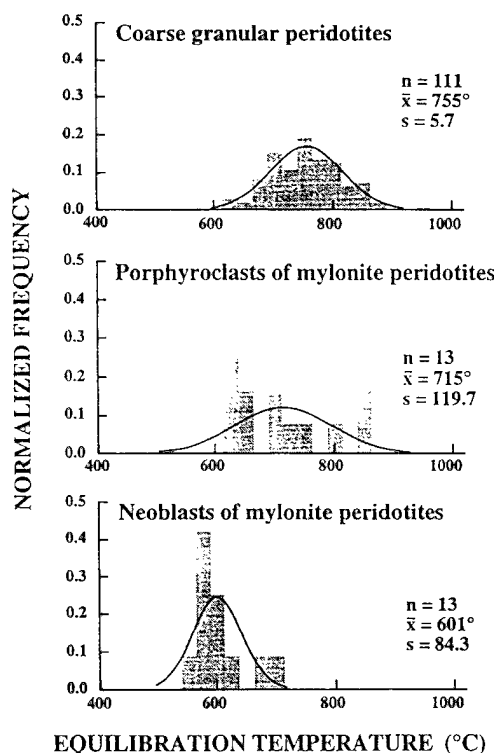


Fig. 7. Normalized histograms (shaded bars) and frequency distribution curves of olivine/spinel equilibration temperatures calculated for 111 coarse granular peridotites, and 13 porphyroclast and neoblast pairs in mylonitic peridotites (listed in Table 4).

temperatures of 111 spinel/olivine pairs from coarse granular peridotites in the W.H.O.I. rock collection have been calculated as well.

Normalized distributions of equilibration temperatures calculated for both mylonitic and coarse granular peridotites indicate that equilibration temperatures for the mylonites ($\sim 600^\circ\text{C}$) are significantly lower than those calculated for the coarse granular tectonites ($\sim 755^\circ\text{C}$). The standard deviation of the temperature distribution for neoblast grains in mylonites is fairly large due to the small number of samples; however, the range in temperatures is relatively narrow (137°) and the only overlap with coarse granular peridotites is in the low-end temperature tail of the distribution curve for coarse granular peridotites. Equilibration temperatures of relict porphy-

roclasts preserve equilibration temperatures similar to those exhibited by the coarse-grained peridotites.

In general, compositional zoning at the interface between olivine and spinel in peridotites can be a useful indicator of diffusive exchange during cooling. In addition, grain size may affect the geothermometric temperature because the exchange of Mg–Fe depends on the diffusion length scale. The cores of large grains may preserve higher temperatures than their rims, and coarse grains may preserve higher temperatures than fine grains (Ozawa, 1983). The influence of grain size on the temperatures calculated for the mylonites (i.e., 600°C) was assessed by comparing the composition of the rims of coarse spinel grains to that of fine spinel grains within the same sample. Compositional zoning is apparent in some of

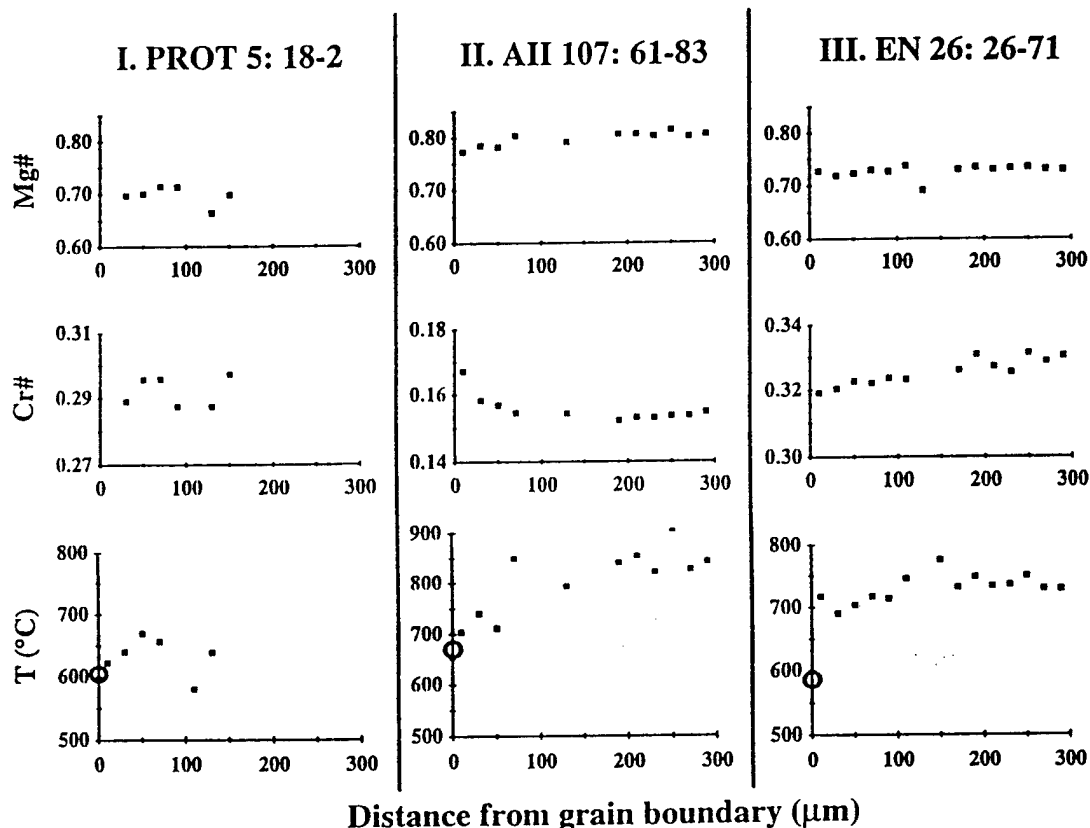


Fig. 8. Profiles of zoning in coarse-grained spinel porphyroclasts. Distance from grain boundary reflects distance from rim towards core. $\text{Mg\#} = \text{Mg}/(\text{Mg} + \text{Fe})$. $\text{Cr\#} = \text{Cr}/(\text{Cr} + \text{Al})$. Circles indicate temperatures derived for fine-grained spinel/olivine pairs within the same sample.

the samples examined, as illustrated in Fig. 8. However, fine grains in other samples have calculated temperatures that are significantly different than rim compositions of associated porphyroclasts (e.g., Fig. 8, sample III).

8. Discussion

Rheological conditions in the oceanic lithosphere at slow-spreading ridges are reflected in the textural development and geothermal histories of plastically deformed peridotites during emplacement to the seafloor. The recovery of both coarse granular and mylonitic abyssal peridotites with the same mineralogy from closely associated fault blocks indicates that they may have had comparable uplift histories. Therefore, the textural and geothermal differences between these rocks reflect factors other than cooling rate. The mylonites studied record a sequence in deformation history of successively finer-grained microstructures overprinting each other. The observed decrease in recrystallized grain size is consistent with an increase in stress associated with uplift (i.e., cooling).

8.1. Effects of grain-size reduction on strain localization in peridotite mylonites

Strain localization in ductile shear zones can be enhanced if grain-size reduction results in a transition to diffusion creep. The mylonite illustrated in Fig. 3d exhibits both large single crystal and polycrystalline porphyroclasts surrounded by a highly strained, fine-grained matrix. This microstructure indicates that the strength of the rock was strongly dependent on grain size. The finest-grained regions of this sample ($\leq 10 \mu\text{m}$) have weak or no lattice-preferred orientations (Fig. 5). In contrast, coarser-grained regions exhibit strong lattice-preferred orientation and pronounced grain flattening (Figs. 4 and 5). These textural observations suggest that a transition from dislocation to diffusion creep occurred with decreasing grain size.

To investigate the role of grain-size reduction, we compare our microstructural observations to the results of deformation experiments on dry olivine aggregates. In particular, we use flow laws for both

Table 5
Parameters for olivine flow laws

	Dislocation creep	Diffusion creep
A ($\text{s}^{-1} \text{MPa}^{-n} (\mu\text{m})^{-m}$)	2.4×10^5	1.8×10^7
Q (kJ/mol)	540	315 ± 35
n	3.5	1
m	0	-3

Parameters for dislocation creep are taken from Chopra and Paterson (1984). Parameters Q , n , and m for diffusion creep are taken from Hirth and Kohlstedt (1995a); parameter A was derived from Group A data in Hirth and Kohlstedt (1995a).

dislocation and diffusion creep to construct deformation mechanism maps. The general form of the flow laws used for both deformation regimes is:

$$\dot{\epsilon} = A \exp(-Q/RT) \sigma^n d^m$$

where $\dot{\epsilon}$ is strain rate, A is an empirical constant, Q is the activation energy for flow, R is the gas constant, T is absolute temperature, σ is flow stress, and d is grain size. Deformation mechanism maps were calculated using the flow law parameters in Table 5 and are shown for temperatures of 600° and 755° in Fig. 9; these temperatures represent those calculated for mylonitic peridotites and coarse granular tectonites, respectively. In addition, a deformation mechanism map for 1300°C is shown for comparison to asthenospheric and experimental conditions. Estimates for the dynamic recrystallized grain size in olivine are plotted in all three deformation mechanism maps using the piezometer of van der Wal et al. (1993). The deformation mechanism maps show that the diffusion creep field expands with decreasing temperature due to the smaller activation energy of diffusion creep relative to that of dislocation creep. The transition from dislocation creep to diffusion creep, suggested by the finest-grained mylonite microstructures, is also supported by the deformation mechanism maps in Fig. 9. At 600°C and a grain size of $\leq 10 \mu\text{m}$, the deformation mechanism maps demonstrate that diffusion creep would be the dominant deformation mechanism at geologically reasonable strain rates and stresses.

While the deformation mechanism maps show that diffusion creep would be the dominant deformation mechanism at grain sizes of $\leq 10 \mu\text{m}$ and temperatures of $\sim 600^\circ\text{C}$, a question remains as to

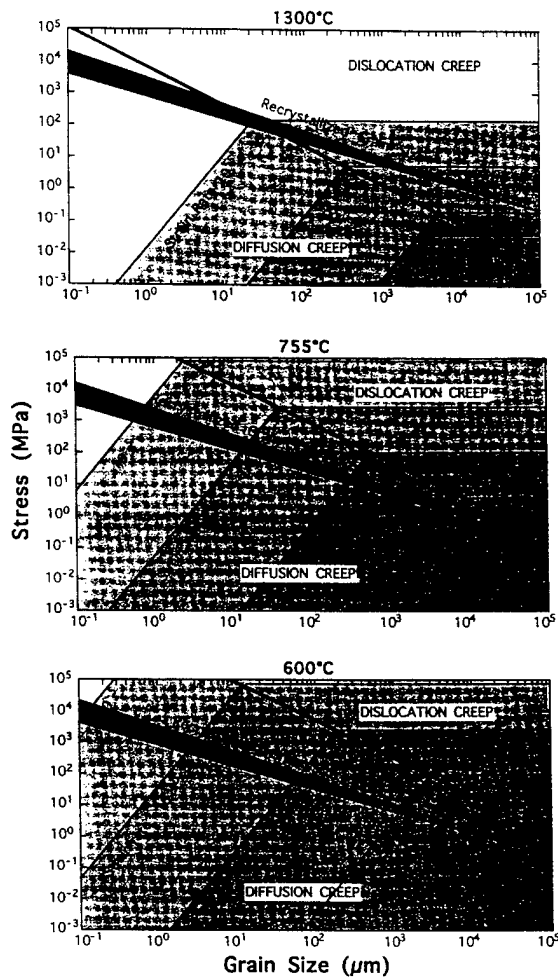


Fig. 9. Deformation mechanism maps for olivine, constructed from the constitutive flow laws using parameters listed in Table 5. Dark shaded region indicates recrystallized grain size–stress relationships derived by van der Wal (1993).

how such a small grain size was achieved. Microstructural observations indicate that the finest-grained mylonitic textures overprint coarser-grained fabrics formed in the dislocation creep regime. Thus, it is possible that the grain-size reduction is accommodated by dynamic recrystallization. However, at a grain size of $10\ \mu\text{m}$, the piezometer relationship plotted in Fig. 9 falls within the diffusion creep regime at all temperatures up to $\sim 1300^\circ\text{C}$. Because the driving force for dynamic recrystallization (i.e., gradients in dislocation density) is only produced in

the dislocation creep regime, it is unlikely that piezometer relationships are applicable in the diffusion creep regime (e.g., Karato and Wu, 1993). In addition, even at conditions where the piezometer relationship falls within the dislocation creep regime for a grain size of $10\ \mu\text{m}$, the stresses and strain rates are geologically unreasonable.

While the analysis presented above suggests that dynamic recrystallization cannot result in a reduction in grain size to $\sim 10\ \mu\text{m}$, several caveats must be addressed. (1) TEM observations of the finest-grained mylonites show considerable amounts of pyroxene in the fine-grained regions. In this case, pyroxene may act as a pinning-phase inhibiting grain growth during dynamic recrystallization. (2) Grain-size sensitive dislocation creep processes may expand the dislocation creep field to smaller grain sizes than shown in Fig. 9. In rock deformation experiments, grain-size sensitive flow has been observed in the dislocation creep regime associated with grain boundary migration recrystallization (e.g., Tullis and Yund, 1985) and grain boundary sliding (e.g., Hirth and Kohlstedt, 1995b). Microstructural observations of flattened grains with weak lattice-preferred orientation and grain sizes of $5\text{--}20\ \mu\text{m}$ (Fig. 5c, Fig. 5d) support the possibility that grain-size sensitive dislocation creep processes may have been operable. Although grain-size sensitive dislocation creep processes may be operative at these fine grain sizes, there are currently no flow laws to confirm whether these deformation processes are applicable at these conditions. (3) Finally, indications of synkinematic hydrothermal alteration that we observe in fine-grained mylonites support high-temperature cataclasis as a mechanism for grain-size reduction. Once grain size was reduced, deformation may have proceeded by diffusion creep.

8.2. Interpretation of geothermometry

Coarse granular textures in peridotites are attributed to grain boundary migration during high-temperature deformation ($> 1000^\circ\text{C}$) (Gueguen and Nicolas, 1980; Nicolas et al., 1980). Olivine–spinel geothermometry performed in this study indicates that the equilibrium temperature for coarse granular peridotites is $\sim 755^\circ\text{C}$ or above. Because the microtextures preserved in these rocks reflect high-temper-

ature deformation, we deduce that 755°C represents the blocking temperature for diffusive exchange during static uplift (cooling) of the coarse-grained tectonites.

In contrast, temperatures calculated for the mylonites are significantly lower (~600°C). Based on the following observations, we believe 600°C reflects the blocking temperature for Mg–Fe equilibration accommodated by grain boundary diffusion, or possibly diffusion in spinel, and thus represents the lower temperature limit for plastic deformation. In samples where compositional zoning is observed, temperatures calculated for fine-grained spinels are similar to those for porphyroclastic rims within the same sample. This observation suggests that in these samples, the temperature of 600°C reflects an enhancement of diffusive exchange during cooling due to reduction in diffusion distances, which is associated with the reduced grain size. However, in the finest-grained samples that lack obvious zoning, 600°C may reflect the continuation of plastic deformation accommodated by diffusion creep, consistent with the deformation mechanism maps. In addition, evidence for upper-amphibolite/lower-granulite facies veins cross-cutting the foliation in almost all peridotite mylonites examined is consistent with brittle or semi-brittle deformation and fracture at temperatures $\leq \sim 600^\circ\text{C}$. The inference that plastic deformation continues down to 600°C in fine-grained mylonites narrows the 'temperature gap' noted by Cannat et al. (1992) between the experimentally determined lower limits of ductile deformation in olivine (700°–1000°C) and the formation of sheared serpentine veins at temperatures below 350°C.

9. Implications for tectonics of slow-spreading mid-ocean ridges

The distribution of strain within the oceanic lithosphere depends critically on the rheological properties of mantle shear zones. Fig. 10 is a schematic diagram of the variation of the mechanical strength of the lithosphere at depth. At shallow depths, frictional failure is characterized by the linear relationship between differential stress and depth (e.g., Byerlee, 1978). As the brittle strength increases with depth, it eventually reaches the brittle–plastic transition,

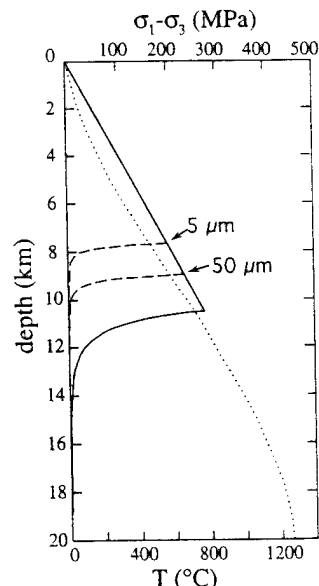


Fig. 10. Schematic diagram for the mechanical strength of the upper mantle with respect to depth at a slow-spreading mid-ocean ridge. The dotted curve represents an inferred geotherm for 1-Ma lithosphere at a slow-spreading (1 cm/yr) ridge with a Nusselt thermal conductivity factor of 6 (based on Lin and Parmentier, 1989). The upper line represents brittle strength based on Byerlee's law for frictional sliding. The lower curves are based on the inferred geotherm and represent ductile strength of the olivine mantle. Dashed curves reflect deformation by diffusion creep at indicated grain sizes. The solid curve is for deformation by grain-size insensitive dislocation creep.

where the strength of the lithosphere is at a maximum. With increasing depth, the strength decreases rapidly due to an increase in temperature. We emphasize that it is unlikely that transitions in the brittle/plastic behavior of the mantle occur at discrete boundaries; both field and experimental observations demonstrate that the brittle–plastic transition in rocks occurs over a wide range of conditions and involves several different deformation mechanisms (Carter and Kirby, 1978; Kirby, 1983; Ross and Lewis, 1989; Evans et al., 1990; Hirth and Tullis, 1994). For example, evidence of high-temperature synkinematic alteration suggests deformation mechanisms in part may be semi-brittle. However, the observation of diffusion creep (or at least grain-size sensitive creep) indicates that shear zones, characterized by intense grain-size reduction, will be signifi-

cantly weaker than predicted by Byerlee's law (Fig. 10).

Establishment of a localized zone of weakness in the lithosphere could result in long-lived faults. Such zones of weakness are required for tectonic models that suggest that ultramafic rocks exposed at inside-corners of mid-ocean ridge discontinuities are exhumed along detachment faults (Dick et al., 1981; Dick, 1989; Karson, 1991; Mevel and Cannat, 1991; Mevel et al., 1991; Tucholke and Lin, 1994). The longevity of these detachment faults may contribute to the relatively wide fault spacing observed in regions where ultramafic rocks are exposed. The deformation textures and equilibration temperatures of the abyssal peridotite mylonites analyzed in this study support the existence of such detachment faults at the base of the ocean crust beneath mid-ocean ridges by providing evidence that strain localization in the oceanic lithosphere can result in localized reduction in the strength of the mantle.

10. Conclusions

Microstructural observations and geothermometric analyses of abyssal peridotite mylonites indicate that plastic deformation along shear zones in the oceanic lithosphere can occur at temperatures as low as 600°C. The microstructures preserved in the finest grained mylonites suggest a strong correlation between strain localization and grain-size reduction. This observation is consistent with extrapolations of olivine flow laws that demonstrate that a stress induced reduction in grain size and concomitant cooling can result in a transition from dislocation creep to grain-size sensitive diffusion creep during uplift. The microstructure of coarse-grained mylonites reflect steady state flow by dislocation creep.

These observations suggest that localized shear zones, characterized by intense grain-size reduction, will be weaker than expected if deformation was accommodated by frictional sliding (i.e., Byerlee's law) or dislocation creep. The presence of such zones of weakness in the oceanic lithosphere may promote the existence of long-lived faults in the upper mantle at slow-spreading ridges. This hypothesis supports tectonic models that attribute the emplacement of upper crustal/lower mantle rocks at

the seafloor to normal extension along low-angle detachment faults.

Acknowledgements

This paper is dedicated to Neville Carter, without whom it would never have been written. Henry Dick took rock mechanics from Neville while he was a graduate student at Yale University. Neville's fundamental research on mantle rheology and courses inspired much of Henry's thesis work on the origin and emplacement of the Josephine Peridotite, and led to Henry's early attempt to integrate shallow mantle deformation and melt transport into his thesis. Neville's influence led Henry to appreciate the potential applications of rock mechanics for understanding crustal and mantle evolution, leading him to recruit Gary Jaroslow to work on the abyssal peridotite mylonites described in this paper and to encourage Greg Hirth to join the staff at Woods Hole.

This paper represents the results of a cooperative research project begun under the auspices of the W.M. Keck Geodynamics Program at Woods Hole Oceanographic Institution, and has been supported by funds provided by the Van Allen Clark Chair (Henry Dick), by NSF grants OCE-9417404, and the W.H.O.I. Education Office. We thank B. Tucholke, D. Kelley and M. Cannat for helpful discussions. In addition, we thank J. Tullis, R.A. Yund, and N. Shimizu for providing access to their laboratories. Finally, we appreciate the helpful reviews of A. Kronenberg and J. Ross.

References

- Agar, S.M., 1994. Rheological evolution of the ocean crust: a microstructural view. *J. Geophys. Res.*, 99(B2): 3175–3200.
- Aumento, F., Loncarevic, B.D. and Ross, D.I., 1971. Hudson Geotraverse: geology of the Mid-Atlantic Ridge at 45°N. *Philos. Trans. R. Soc. London, Ser. A*, 268: 623–650.
- Aumento, F. and Loubat, H., 1971. The Mid-Atlantic Ridge near 45°N, XVI. Serpentinized ultramafic intrusions. *Can. J. Earth Sci.*, 8: 631–663.
- Bence, A.E. and Albee, A.L., 1968. Empirical correction factors for the electron microanalysis of silicates and oxides. *J. Geol.*, 76: 382.
- Bonatti, E., 1976. Serpentine protrusions in the oceanic crust. *Earth Planet. Sci. Lett.*, 32: 107–113.

- Boudier, F. and Nicolas, A., 1982. Peridotite microtextures. In: G.J. Borradaile, M.B. Bayly and C.M. Powell (Editors), *Atlas of Deformational and Metamorphic Rock Fabrics*. Springer-Verlag, New York, NY, pp. 384–385.
- Brace, W.F. and Kohlstedt, D.L., 1980. Limits on lithospheric stress imposed on laboratory experiments. *J. Geophys. Res.*, 85(B11): 6248–6252.
- Byerlee, J.D., 1978. Friction of rocks. *Appl. Geophys.*, 116: 615–626.
- Cannat, M., 1993. Emplacement of mantle rocks in the seafloor at mid-ocean ridges. *J. Geophys. Res.*, 98(B3): 4163–4172.
- Cannat, M., Bideau, D. and Bougault, H., 1992. Serpentinized peridotites and gabbros in the Mid-Atlantic Ridge axial valley at 15°37'N and 16°52'N. *Earth Planet. Sci. Lett.*, 109: 87–106.
- Carter, N.L. and Avé Lallemant, H.G., 1970. High temperature flow of dunite and peridotite. *Geol. Soc. Am. Bull.*, 81: 2181–2202.
- Carter, N.L. and Kirby, S.H., 1978. Transient creep and semibrittle behavior in crystalline rocks. *Pure Appl. Geophys.*, 116: 807–839.
- Chen, W.-P. and Molnar, P., 1983. Focal depths of intracontinental and intraplate earthquakes and their implications for the thermal and mechanical properties of the lithosphere. *J. Geophys. Res.*, 88(B5): 4183–4212.
- Chopra, P.N. and Paterson, M.S., 1981. The experimental deformation of dunite. *Tectonophysics*, 78: 453–473.
- Chopra, P.N. and Paterson, M.S., 1984. The role of water in the deformation of dunite. *J. Geophys. Res.*, 89: 7861–7876.
- Cooper, R.F. and Kohlstedt, D.L., 1984. Sintering of olivine and olivine–basalt aggregates. *Phys. Chem. Miner.*, 11: 5–6.
- Dick, H.J.B., 1989. Abyssal peridotites, very slow spreading ridges and ocean ridge magmatism. In: A.D. Saunders and M.J. Norry (Editors), *Magmatism in the Ocean Basins*. Geol. Soc. London, Spec. Publ., 24: 71–105.
- Dick, H.J.B., Bryan, W.B. and Thompson, G., 1981. Low-angle faulting and steady-state emplacement of plutonic rocks at ridge-transform intersections. *EOS (Trans. Am. Geophys. Union)*, 62: 406.
- Dick, H.J.B., Schouten, H., Meyer, P.S., Gallo, D.G., Bergh, H., Tyce, R., Patriat, P., Johnson, K.T.M., Snow, J. and Fischer, A., 1991. Tectonic evolution of the Atlantis II Fracture Zone. *Proc. ODP, Sci. Results*, 118: 359–358.
- Drury, M.R., Vissers, R.L.M., van der Wal, D. and Hoogerduijn Strating, E.H., 1991. Shear localisation in upper mantle peridotites. *Pure Appl. Geophys.*, 137(4): 439–460.
- Engi, M., 1983. Equilibria involving Al–Cr spinel: Mg–Fe exchange with olivine. Experiments, thermodynamic analysis and consequences for geothermometry. *Am. J. Sci.*, 283-A: 29–71.
- Evans, B.W. and Frost, B.R., 1975. Chrome–spinel in progressive metamorphism — a preliminary analysis. *Geochim. Cosmochim. Acta*, 39: 959–972.
- Evans, B.W. and Wong, T.-F., 1985. Shear localization in rocks induced by tectonic deformation. In: Z. Bazant (Editor), *Mechanics of Geomaterials*. John Wiley, New York, NY, pp. 189–210.
- Evans, B.W., Fredrich, J.T. and Wong, T.-F., 1990. The brittle–ductile transition in rocks: recent experimental and theoretical progress. *Am. Geophys. Union, Geophys. Monogr.*, 56: 1–20.
- Fabries, J., 1979. Spinel–olivine geothermometry in peridotites from ultramafic complexes. *Contrib. Mineral. Petrol.*, 69: 329–336.
- Fisher, R.L., Natland, J.H. and Dick, H.J.B., 1985. Shipboard Description and Inventory of Rocks Dredged on PROTEA Expedition, Leg 5, in the Southwest Indian Ocean. Scripps Institute of Oceanography, La Jolla, CA. Rep. 85-15, 223 pp.
- Francheteau, J., Choukroune, P., Hekinian, R., Le Pichon, X. and Needham, H.D., 1976. Oceanic fracture zones do not provide deep sections in the crust. *Can. J. Earth Sci.*, 13: 1223–1235.
- Gueguen, Y. and Nicolas, A., 1980. Deformation of mantle rocks. *Annu. Rev. Earth Planet. Sci.*, 8: 119–144.
- Handy, M.R., 1989. Deformation regimes and the rheological evolution of fault zones in the lithosphere: the effects of pressure, temperature, grain size and time. *Tectonophysics*, 163: 119–152.
- Hemley, J.J., Montoya, J.W., Shaw, D.R. and Luce, R.W., 1977. Mineral equilibria in the MgO–SiO₂–H₂O system. II. Talc–antigorite–forsterite–anthophyllite–enstatite stability relations and some geologic implications in the system. *Am. J. Sci.*, 277: 353–383.
- Henry, D.J. and Medaris, L.G., Jr., 1980. Application of pyroxene and olivine–spinel geothermometers to spinel peridotites in southwestern Oregon. *Am. J. Sci.*, 280-A: 211–231.
- Hirth, G. and Kohlstedt, D.L., 1995a. Experimental constraints on the dynamics of the partially molten upper mantle: deformation the diffusion creep regime. *J. Geophys. Res.*, 100(B2): 1981–2001.
- Hirth, G. and Kohlstedt, D.L., 1995b. Experimental constraints on the dynamics of the partially molten upper mantle. 2. Deformation the dislocation creep regime. *J. Geophys. Res.*, 100(B8): 15,441–15,449.
- Hirth, G. and Tullis, J., 1992. Dislocation creep regimes in quartz aggregates. *J. Struct. Geol.*, 14(2): 145–159.
- Hirth, G. and Tullis, J., 1994. The brittle–plastic transition in experimentally deformed quartz aggregates. *J. Geophys. Res.*, 99(B6): 11,731–11,747.
- Hurst, S.D., Karson, J.A. and Moores, E.M., 1990. Nodal basins at slow spreading ridge-transform intersections: a comparison to the central portion of the Troodos ophiolite. In: J. Malpas, E.M. Moores, A. Panayiotou, C. Xanophontos (Editors), *Proceedings of the Symposium 'TROODOS 1987'*. Geological Survey Department, pp. 125–129.
- Irvine, T.N., 1965. Chromian spinel as a petrogenetic indicator, Part 1. Theory. *Can. J. Earth Sci.*, 2: 648–672.
- Jackson, E.D., 1969. Chemical variation in coexisting chromite and olivine in chromite zones of Stillwater complex. *Econ. Geol. Monogr.*, 4: 41–71.
- Karato, S.-I. and Wu, P., 1993. Rheology of the upper mantle: a synthesis. *Science*, 260: 771–778.
- Karato, S.-I., Paterson, M.S. and Fitzgerald, J.D., 1986. Rheology of synthetic olivine aggregates: influence of grain size and water. *J. Geophys. Res.*, 91(B8): 8151–8176.

- Karson, J.A., 1990. Seafloor spreading on the Mid-Atlantic Ridge: implications for the structure of ophiolites and oceanic lithosphere produced in slow-spreading environments. In: J. Malpas, E.M. Moores, A. Panyiotou and C. Xenophontos (Editors), *Ophiolites: Oceanic Crustal Analogues*. Geological Survey Department, Nicosia, Cyprus, pp. 547–555.
- Karson, J.A., 1991. Accommodation zones and transfer faults: integral components of Mid-Atlantic Ridge extensional systems. In: T. Peters, A. Nicolas and R.J. Coleman (Editors), *Ophiolite Genesis and Evolution of Oceanic Lithosphere*. Ministry of Petroleum and Minerals, Sultanate of Oman, pp. 21–37.
- Karson, J.A. and Dick, H.J.B., 1983. Tectonics of ridge-transform intersections at the Kane Fracture Zone. *Mar. Geophys. Res.*, 6: 51–98.
- Karson, J.A. and Dick, H.J.B., 1984. Deformed and metamorphosed oceanic crust on the Mid-Atlantic Ridge. *Ophiolite*, 9: 279–302.
- Karson, J.A. and Winters, A.T., 1992. Along-axis variations in tectonic extension and accommodation zones in the MARK Area, Mid-Atlantic Ridge 23°N latitude. In: L.M. Parson, B.J. Murton and P. Browning (Editors), *Ophiolites and their Modern Oceanic Analogues*. Geol. Soc. London, Spec. Publ., 60: 107–116.
- Karson, J.A., Thompson, G., Humphris, S.E., Edmond, J.M., Bryan, W.B., Brown, J.R., Winters, A.T., Pockalny, R.A., Casey, J.F., Campbell, A.C., Klinkhammer, G., Palmer, M.R., Kinzler, R.J. and Sulanowska, M.M., 1987. Along-axis variations in seafloor spreading in the MARK area. *Nature*, 328: 681–685.
- Karson, J.A., Cannat, M., Miller, J. and Scientific Party, 1995. Proceedings of the Ocean Drilling Program, Scientific Results, 153. Ocean Drilling Program, College Station, TX, in press.
- Kimball, K.L., 1990. Effects of hydrothermal alteration on the compositions of chromian spinels. *Contrib. Mineral. Petrol.*, 105: 337–346.
- Kimball, K.L., Spear, F.S. and Dick, H.J.B., 1985. High temperature alteration of abyssal ultramafics from the Islas Orcadas Fracture Zone, South Atlantic. *Contrib. Mineral. Petrol.*, 91: 307–320.
- Kirby, S.H., 1983. Rheology of the lithosphere. *Rev. Geophys. Space Phys.*, 21(6): 1458–1487.
- Lin, J. and Parmentier, E.M., 1989. Mechanisms of lithospheric extension at mid-ocean ridges. *Geophys. J.*, 96: 1–22.
- Melson, W.G., Hart, S.R. and Thompson, G., 1972. St. Paul's Rocks, Equatorial Atlantic: petrogenesis, radiometric ages, and implications on sea-floor spreading. In: R. Shagan (Editor), *Studies in Earth and Space Sciences: The Hess Volume*. Geol. Soc. Am. Mem., 132: 241–272.
- Mercier, J.-C.C. and Nicolas, A., 1975. Textures and fabrics of upper-mantle peridotites as illustrated by xenoliths from basalts. *J. Petrol.*, 16(2): 454–487.
- Mevel, C. and Cannat, M., 1991. Lithospheric stretching and hydrothermal processes in oceanic gabbros from slow-spreading ridges. In: T. Peters, A. Nicolas and R.J. Coleman (Editors), *Ophiolite Genesis and Evolution of the Oceanic Lithosphere*. Ministry of Petroleum and Minerals, Sultanate of Oman, pp. 293–312.
- Mevel, C., Cannat, M., Gente, P., Marion, E., Auzende, J.M. and Karson, J.A., 1991. Emplacement of deep crustal and mantle rocks on the west median valley wall of the MARK area (MAR, 23°N). *Tectonophysics*, 190: 31–53.
- Nicolas, A., Boudier, F. and Bouchez, J.-L., 1980. Interpretation of peridotite structures from ophiolitic and oceanic environments. *Am. J. Sci.*, 280-A: 192–210.
- Olgaard, D.L., 1990. The role of second phase in localizing deformation. In: R.J. Knipe and E.H. Rutter (Editors), *Deformation Mechanisms, Rheology and Tectonics*. Geol. Soc. London, Spec. Publ., 54: 175–181.
- OTTER Team, 1984. The geology of the oceanographer transform: the ridge-transform intersection. *Mar. Geophys. Res.*, 6: 109–141.
- OTTER Team, 1985. The geology of the Oceanographer Transform: the ridge-transform domain. *Mar. Geophys. Res.*, 7: 329–358.
- Ozawa, K., 1983. Evaluation of olivine–spinel geothermometry as an indicator of thermal history for peridotites. *Contrib. Mineral. Petrol.*, 82: 52–65.
- Pickering, F.B., 1976. *The Basis of Quantitative Metallography*. Institute of Metallurgical Technicians, London, 55 pp.
- Ranalli, G. and Murphy, D.C., 1987. Rheological stratification of the lithosphere. *Tectonophysics*, 132: 281–295.
- Robinson, P., Spear, F.S., Schumaker, J.C., Laird, J., Klein, C., Evans, B.W. and Doolan, B.W., 1981. Phase relations of metamorphic amphiboles: natural occurrence and theory. In: D. Veblen (Editor), *Amphiboles: Petrology and Experimental Phase Relations*. Reviews in Mineralogy, 9B. Mineralogical Society of America, pp. 1–211.
- Ross, J.V. and Lewis, P.D., 1989. Brittle–ductile transition: semi-brittle behavior. *Tectonophysics*, 167: 75–79.
- Rutter, E.H. and Brodie, K.H., 1988. The role of tectonic grain size reduction in the rheological stratification of the lithosphere. *Geol. Rundsch.*, 77(1): 295–308.
- Sack, R.O. and Ghiorso, M.S., 1991. Chromian spinel as petrogenetic indicators: thermodynamics and petrological applications. *Am. Mineral.*, 76: 827–847.
- Shaw, P.R. and Lin, J., 1993. Causes and consequences of variations in faulting style at the Mid-Atlantic Ridge. *J. Geophys. Res.*, 98, B12: 21,839–21,851.
- Silantyev, S., Dick, H., Bazylev, B., Dmitriev, L.V., Xia, C., Bougault, H., Rona, P.A. and Blusztajn, J.S., 1995. Mantle peridotites, tectonites and hydrothermal activity at the 15°20' Fracture Zone. Submitted for publication.
- Skolotnev, S.G., Tsukanov, N.V., Peyve, A.A. and Raznitsin, Y.A., 1989. 15°20' Fracture Zone bedrocks: general characteristics. In: Y.M. Pushcharovsky (Editor), *Structure of the Cape Verde Fracture Zone, Central Atlantic*. Acad. Sci. USSR, Order of the Red Banner of Labour Geol. Inst., Trans., 439: 40–60.
- Tucholke, B.E. and Lin, J., 1994. A geological model for the structure of ridge segments in slow-spreading oceanic crust. *J. Geophys. Res.*, 99(B6): 11,937–11,958.

- Tullis, J. and Yund, R.A., 1985. Dynamic recrystallization of feldspar: a mechanism for ductile shear zone formation. *Geology*, 13: 238–241.
- Tullis, J., Dell'Angelo, L. and Yund, R.A., 1990. Ductile shear zones from brittle precursors in feldspathic rocks: the role of dynamic recrystallization. In: A.G. Duba, W.B. Durham, J.W. Handin and H.F. Wang (Editors), *The Brittle–Ductile Transition in Rocks*. Am. Geophys. Union, Geophys. Monogr., 56: 67–82.
- van der Wal, D., Chopra, P., Drury, M. and Fitz Gerald, J., 1993. Relationships between dynamically recrystallized grain size and deformation conditions in experimentally deformed olivine rocks. *Geophys. Res. Lett.*, 20(14): 1479–1482.

Chapter 6

CONCLUSIONS

The ocean crust at slow-spreading ridges is formed by magmatic accretion, and during its transport from the ridge axis to the ridge flank it is extended by faulting and its topographic features are degraded by sedimentation and mass wasting. In this Thesis, I have extracted structural information about the ocean crust, considered the effects of seafloor aging, and thereby derived new insights into the volcanic development and tectonic dismemberment of ocean crust at slow-spreading ridges.

A large portion of this Thesis (Chapters 2 to 4) is based on geological and geophysical data acquired over the crest and western flank of the Mid-Atlantic Ridge (MAR) between 25°25' and 27°10'N (Tucholke et al., 1992). This dataset is ideal for studying the spatial and temporal characteristics of crustal structure because it extends from zero-age crust at the ridge axis to ~29 Ma crust on the ridge flank, and it encompasses all or part of nine spreading segments that are developed between non-transform discontinuities.

In Chapter 2, detailed sediment thickness of the MAR flank was mapped, the factors affecting local and regional distribution of sediments were documented, and the impact of sediment cover on the characterization of basement structures studied in Chapters 3 and 4 was assessed. It is observed that sediment accumulations on the MAR flank are regionally thin (< 50 m), but they locally accumulate within crustal depressions to form thick sediment ponds. Sediment ponds are best developed in ridge-parallel valleys between abyssal hills (thicknesses of 100's of meters) and in the valleys of non-transform discontinuities (thicknesses up to ~800 m). The ridge-parallel valleys also serve as passageways for downslope transport of sediment towards the deeper and larger ponds along discontinuities. Average sediment cover on the MAR flank increases with crustal age

up to ~17 m.y. off-axis and then decreases on older crust to the edge of the study area at ~29 m.y. This long-term change in sediment accumulation is attributed to depression of the calcite compensation depth to depths below ridge-crest level at ca. 17 Ma. Still, even on the oldest crust studied, high-standing features such as ridges and seamounts, and steep-sloped basement structures such as fault scarps, have been largely kept free of sediment by gravity-driven sediment redistribution and by the activity of bottom currents. However, accumulation of sediments at the base of these structures does affect measurements of their physical dimensions, and burial reduces their regional abundance. These effects are considered in the evaluations of the structural record of faulting (Chapter 3) and the production and degradation of seamounts (Chapter 4).

Chapter 3 examines the role of faulting in the formation and evolution of ocean crust at the Mid-Atlantic Ridge. Cross-isochron variations in fault patterns reveal that the creation of rift-valley and abyssal-hill topography is controlled by faulting on both inward-facing and outward-facing faults. Uplift of crust to the crest of the rift mountains is accomplished by slip on inward-facing faults largely at the base of the rift-valley wall. Reduction of the gross topographic relief of the rift valley is accomplished by development of outward-facing faults in the upper rift-valley walls. At the crest of the rift mountains and onto the MAR flank, 40% of the observed faults are outward-facing. The inward- and outward-facing faults typically occur in pairs to create horsts and grabens, and these features form most of the abyssal hills on the ridge flank. There is virtually no active faulting on the ridge flank beyond the crest of the rift mountains. Temporal fluctuations in brittle strain measured from faults on the ridge flank probably is related to cyclicity in magmatism versus tectonic extension at the ridge axis.

Within individual spreading segments, along-isochron variations in faulting are related to tectonic setting. Inside corners of segments are characterized by relatively large brittle strain accommodated along irregular, widely spaced, large-offset faults. In

comparison, faults at segment centers and outside corners are long, linear, relatively closely spaced, and have smaller offsets, resulting in lower brittle strains. Differences in brittle strain between inside corners, segment centers, and outside corners appear to be enhanced with increasing magnitude of offset between segments. Fault patterns also were correlated to regional variations in residual mantle Bouguer anomaly (RMBA) and apparent crustal thickness. We find that brittle strain is enhanced in areas of high RMBA (thin crust) and decreased in areas of low RMBA (thicker crust), consistent with the idea that decreasing magma budget results in increasing brittle strain.

Chapter 4 documents the existence of abundant seamounts on the flank of the Mid-Atlantic Ridge. Analysis of backscatter intensity and seamount/fault relations on the ridge flank indicates that the seamounts were formed on the inner rift-valley floor and not off-axis. The occurrence of large numbers of off-axis seamounts shows that large sections of ocean crust are carried intact through the rift-valley wall and onto the ridge flank. However, faulting in the rift-valley walls does cause changes in seamount population abundance and morphology during transport off-axis. These changes are consistent with fault patterns deduced in Chapter 3. Variations in seamount population beyond the ridge crest, where faulting is no longer active, are attributed to temporal variations in axial seamount production and to crustal aging effects. We also found that the expected population density of off-axis seamounts has a positive correlation to crustal thickness (as inferred from gravity data), suggesting that seamount production is increased with increased magma supply at the rift axis. However, we found no variations in expected seamount population density or characteristic height along-isochrons within segments. This suggests either that seamount production is uniform along the ridge axis, or that along-axis variations in seamount-forming volcanism exist but cannot be detected in our morphological studies.

The results of Chapter 5 have strong implications for the structural development of slow-spreading ridges. Detailed study of the microstructure and geothermometry of abyssal peridotites indicates that fine-grained mylonites, which are associated with shear zones in the mantle, may form at temperatures significantly cooler ($\sim 600^{\circ}\text{C}$) than coarse-grained tectonites ($\sim 755^{\circ}\text{C}$) whose structures reflect mantle upwelling. The microstructural data, combined with flow laws for olivine, suggest that deformation in some fine-grained mylonites occurs by diffusion creep, representing a transition in deformation mechanism from dislocation creep in the more coarse-grained tectonites. Reduction in grain size by cataclasis, or possibly dynamic recrystallization during uplift (and/or cooling) is attributed to this transition in deformation mechanism. Strain localization in the upper mantle therefore can result in localized zones of weakness. Establishment of a localized reduction in the strength of the oceanic lithosphere promotes the existence of long-lived faults. The inference that long-lived, weak faults exist in the upper mantle is consistent with tectonic models that attribute the emplacement of ultramafic rocks at the seafloor to normal extension along detachment faults. In addition, the long-lived faults may contribute to the relatively wide fault spacing observed at the inside corners of ridge segments, where ultramafic rocks are most commonly exposed.

APPENDIX

Table of Individual Seamount Data

Seamount (#)	LAT (deg)	LON (deg)	Depth (m)	Height (m)	D-top (m)	D1 (m)	Orient1 (deg)	D2 (m)	Orient2 (deg)	Mean D (m)
1	26.966077	-45.225170	3534	230	0	1300	85	1800	174	3766.2
2	26.936628	-45.181180	3298	160	55	1600	128	1150	28	3458.2
3	26.924112	-45.139399	3176	150	0	1250	115	950	17	3327.6
4	26.919142	-45.130196	3220	100	153	850	142	800	60	3321.7
5	26.978593	-45.177867	3147	160	128	1100	126	650	34	3311.1
6	26.965525	-45.125963	3200	70	0	1150	18	600	111	3274.6
7	27.005834	-45.127251	3203	120	18	1350	169	800	86	3323.8
8	26.954336	-45.062281	3541	80	57	750	161	550	80	3617.3
9	26.955875	-45.040156	3141	170	0	1200	149	1100	66	3307.1
10	26.930672	-44.983785	2655	100	0	900	9	650	97	2754.3
11	26.945647	-44.951665	2486	110	0	950	16	600	107	2593.7
12	26.954297	-44.872887	3056	90	99	950	7	700	84	3141.8
13	26.988164	-44.907859	2865	130	0	1150	23	850	109	2997.6
14	27.031906	-44.960810	2671	130	59	1250	0	650	92	2799.7
15	26.939941	-44.816766	2670	170	0	1200	30	750	118	2837.9
16	26.951905	-44.814557	2788	170	192	1450	4	1000	88	2962.0
17	26.973808	-44.711116	2677	80	41	1200	17	650	103	2759.7
18	27.018697	-48.815839	4710	110	258	1100	39	750	132	4819.7
19	26.983086	-48.714247	3988	120	176	1300	25	700	119	4106.6
20	26.965717	-48.645618	4264	180	421	1550	50	1500	130	4438.9
21	26.938170	-48.665063	4388	130	157	1100	30	850	125	4515.9
22	26.928987	-48.450998	4772	130	621	2150	173	1350	81	4902.5
23	26.988223	-48.472063	4782	120	545	1850	170	1100	79	4903.9
24	27.088565	-48.536765	3981	140	0	1150	23	650	112	4117.1
25	27.071834	-48.498050	4156	170	76	1550	30	950	111	4323.0
26	27.087009	-48.482486	4216	70	76	700	38	450	128	4283.9
27	27.095958	-48.438670	4437	100	0	800	109	550	21	4537.4
28	27.094791	-48.342953	4568	70	170	750	99	600	15	4635.7
29	27.021252	-48.354237	4780	90	43	1500	15	800	99	4869.0
30	26.991307	-48.400120	4622	120	0	1200	20	900	111	4738.3
31	26.978316	-48.319160	4554	100	223	900	54	550	150	4651.3
32	26.931508	-48.167196	4171	150	102	1700	12	1100	102	4316.2
33	27.067554	-48.202616	3692	90	476	1250	86	950	179	3784.2
34	27.056854	-48.038557	4182	140	0	1350	26	700	116	4323.4
35	27.107047	-48.146919	3974	110	76	1450	28	750	115	4087.8
36	27.028450	-47.952914	4394	70	167	950	81	600	8	4461.9
37	26.966831	-47.962045	4607	80	147	1300	15	1000	114	4686.7
38	26.967157	-47.775463	4361	110	353	1200	50	800	133	4471.3
39	26.993624	-47.766101	4508	200	755	1350	33	950	119	4704.0
40	27.136424	-47.770359	3793	110	537	1150	138	950	53	3906.8
41	26.941354	-47.732844	4426	90	126	1000	110	650	7	4520.4
42	26.952925	-47.732655	4384	140	0	1250	129	950	36	4527.3
43	26.960323	-47.650706	4253	100	233	1100	35	700	131	4351.1
44	26.990485	-47.738535	4467	70	152	1400	27	800	121	4539.4
45	27.026307	-47.723064	4283	140	124	1150	56	800	148	4420.3
46	27.077141	-47.751350	4780	110	304	800	90	750	0	4886.2
47	27.103377	-47.651323	4339	130	447	1650	37	1050	128	4467.1
48	27.115471	-47.641689	4395	80	239	1300	28	750	117	4475.8
49	27.133919	-47.502890	4566	80	397	1000	34	800	117	4642.7
50	27.092924	-47.510884	4511	120	0	850	57	650	48	4630.5
51	27.055414	-47.489976	4232	100	23	1000	22	600	110	4331.5
52	26.986256	-47.572712	4078	110	59	1000	122	850	28	4189.9
53	26.946477	-47.524465	3862	90	0	550	173	500	74	3951.5
54	26.934714	-47.417399	4216	120	0	950	119	800	28	4331.1
55	26.993141	-47.434092	4121	170	0	1300	86	1150	175	4293.7
56	27.000349	-47.407155	4243	80	19	800	0	450	70	4322.0
57	27.097023	-47.371463	3753	140	0	950	26	1000	110	3894.3
58	27.127974	-47.402824	3902	120	20	1150	22	750	106	4024.1
59	27.140507	-47.390399	3874	100	241	1650	35	850	120	3976.2
60	27.162468	-47.437187	3845	160	153	950	88	700	3	4004.1
61	27.163996	-47.417517	3888	80	67	850	18	700	101	3963.5
62	26.983014	-47.196553	3672	80	0	700	19	450	97	3747.5

Seamount (#)	LAT (deg)	LON (deg)	Depth (m)	Height (m)	D-top (m)	D1 (m)	Orient1 (deg)	D2 (m)	Orient2 (deg)	Mean D (m)
63	27.073868	-47.301296	3757	110	30	850	55	600	141	3870.2
64	27.127848	-47.310326	3751	120	0	600	53	550	143	3874.8
65	27.157932	-47.298692	3755	130	21	1250	10	650	95	3888.5
66	27.182610	-47.211194	4030	110	166	750	34	550	125	4138.2
67	27.168555	-47.117043	3867	140	198	1150	33	1300	120	4007.6
68	27.137890	-47.192435	3813	100	76	1000	42	600	129	3913.5
69	27.128515	-47.197317	3837	100	0	600	53	450	143	3940.8
70	27.148633	-47.145949	3991	120	146	800	140	750	58	4106.7
71	27.131640	-47.140676	4000	100	189	1050	87	650	174	4103.4
72	27.144531	-47.097511	4115	120	153	1000	10	750	90	4236.3
73	27.133203	-47.104152	4165	110	0	1150	116	850	29	4275.2
74	27.102965	-47.111383	4192	130	22	1050	4	800	90	4326.3
75	27.097948	-47.088507	4057	160	46	1650	43	1550	133	4217.8
76	27.068851	-47.193458	3765	120	120	800	55	650	152	3882.7
77	27.036743	-47.176602	3851	190	49	1450	10	850	98	4038.9
78	27.066041	-47.138474	4079	110	0	1150	18	650	99	4190.0
79	27.004026	-47.191653	3739	130	39	1100	23	750	115	3865.1
80	27.005784	-47.109035	4326	100	44	1300	18	750	95	4428.2
81	26.995823	-47.100636	4319	100	163	1450	14	850	106	4414.8
82	26.975510	-47.103761	4299	140	262	1300	11	1050	93	4438.9
83	26.949338	-47.112160	4290	130	65	1450	10	1100	91	4420.2
84	26.934689	-47.078761	4415	130	29	1100	55	750	139	4542.7
85	26.934299	-47.115480	4255	120	180	1300	176	900	89	4379.5
86	26.927486	-47.022381	3906	260	110	1650	10	1750	100	4168.8
87	26.939929	-47.016438	3968	130	155	1450	16	900	102	4100.7
88	26.996386	-47.008452	3840	100	181	1200	23	1100	97	3940.4
89	27.004000	-47.023867	3878	100	222	800	68	550	142	3977.0
90	27.011986	-46.929152	3725	120	219	1300	6	1000	92	3841.8
91	26.916714	-46.906123	4252	70	113	700	16	500	96	4322.6
92	27.028917	-47.037044	3818	140	60	1500	135	1450	44	3958.7
93	27.068450	-46.989886	3700	100	223	1250	19	750	102	3795.3
94	27.018060	-47.038890	3930	100	20	800	30	550	120	4025.0
95	26.916603	-46.905496	4252	80	85	850	24	600	104	4330.2
96	26.946429	-46.921967	3984	190	37	1150	23	850	108	4171.6
97	26.971129	-46.920110	3971	70	147	550	2	450	97	4037.2
98	26.979114	-46.890396	3844	110	174	900	5	650	90	3957.4
99	26.966857	-46.866996	4020	240	0	1300	1	1050	95	4256.2
100	26.970572	-46.845267	4223	80	42	650	61	450	156	4139.3
101	27.015700	-46.818710	3698	90	0	900	129	650	40	3789.2
102	27.023098	-46.848385	3906	80	20	550	0	400	90	3984.2
103	27.070858	-46.838553	3844	90	188	950	4	700	93	3933.5
104	27.087513	-46.698206	3575	70	205	750	0	500	90	3646.0
105	27.033733	-46.657269	3437	100	22	1450	4	800	94	3535.4
106	26.974924	-46.731223	3844	130	22	850	63	550	151	3971.6
107	26.915353	-46.776341	3922	300	22	2100	147	1500	60	4217.0
108	26.924142	-46.685324	3886	140	0	1400	27	1000	111	4030.5
109	26.918869	-46.642159	3826	150	19	1100	81	800	160	3973.3
110	27.002464	-46.627119	3692	30	48	1250	56	750	148	3772.0
111	26.920614	-46.587338	3777	170	18	1450	19	950	98	3947.6
112	26.931757	-46.582324	3823	70	334	850	98	650	4	3889.8
113	26.988586	-46.505467	3822	80	0	800	111	600	24	3897.6
114	27.006229	-46.504910	3821	90	228	900	36	650	135	3910.9
115	27.119621	-46.413302	3816	110	30	750	38	500	132	3925.6
116	27.120825	-46.381997	3872	120	0	850	143	850	48	3993.6
117	27.123634	-46.319110	4045	110	109	650	57	600	51	4158.3
118	27.119420	-46.261316	3757	200	185	1450	73	1600	71	3954.3
119	27.107580	-46.285598	3920	90	0	950	163	600	76	4005.9
120	27.089119	-46.300648	3938	150	0	1850	61	1150	162	4084.1
121	27.076878	-46.257504	3991	120	178	1000	21	800	113	4106.7
122	27.063633	-46.297236	3901	110	0	1100	155	650	72	4012.4
123	27.063232	-46.255497	4040	100	67	1350	22	900	120	4136.4
124	27.037546	-46.253089	3970	150	20	2000	39	1450	125	4121.6

Seamount (#)	LAT (deg)	LON (deg)	Depth (m)	Height (m)	D-top (m)	D1 (m)	Orient1 (deg)	D2 (m)	Orient2 (deg)	Mean D (m)
125	27.029921	-46.294628	3997	120	318	1750	93	900	1	4120.1
126	27.039753	-46.322521	4061	130	30	850	6	850	98	4190.6
127	27.031526	-46.334762	4127	170	293	1700	5	1600	91	4298.3
128	26.969846	-46.338411	4088	110	0	800	8	550	98	4198.2
129	26.959104	-46.341145	4148	110	22	1150	40	650	124	4259.9
130	26.944846	-46.345442	4195	70	152	1700	32	1000	136	4268.6
131	26.945627	-46.250714	3720	120	22	1100	130	650	37	3842.8
132	26.962815	-46.248565	3677	130	0	1000	19	650	112	3807.1
133	26.983386	-46.136852	3840	160	41	1050	97	700	5	4000.0
134	27.035539	-46.186575	3804	190	139	500	106	700	104	3992.3
135	27.026509	-46.133196	3908	100	40	1000	155	950	69	4006.1
136	27.039753	-46.111323	3830	160	22	1300	90	850	0	3985.0
137	27.065841	-46.192194	3838	70	0	850	102	600	178	3906.2
138	27.072062	-46.173933	3459	448	22	2400	69	1800	152	3906.9
139	27.085306	-46.197411	3759	220	0	1100	63	700	153	3979.2
140	27.093333	-46.111123	3490	90	0	700	171	600	74	3580.8
141	27.118015	-46.140621	3738	110	0	1250	2	850	94	3851.9
142	27.127447	-46.169117	4053	100	119	950	177	850	91	4156.7
143	26.936842	-46.059835	3304	80	0	950	22	500	118	3384.9
144	26.929699	-45.988971	3869	70	262	1050	133	600	41	3934.6
145	26.936654	-45.972806	3806	90	273	950	38	650	145	3893.0
146	27.009962	-45.959460	3916	160	21	900	176	650	88	4079.8
147	27.021665	-46.073086	4078	90	0	950	11	550	101	4164.1
148	27.137640	-46.089538	3386	70	350	950	27	550	124	3460.0
149	27.119766	-46.042011	3276	160	182	2250	58	1600	142	3439.4
150	27.135812	-46.016826	3340	110	283	900	56	850	147	3449.5
151	27.053959	-45.964424	3737	110	20	950	14	650	99	3842.9
152	27.148498	-45.949772	3364	140	156	1150	166	850	77	3499.9
153	27.113673	-45.915539	3395	130	182	1150	61	650	150	3520.9
154	27.055381	-45.841811	3287	170	90	1600	8	900	91	3453.5
155	27.007188	-45.871063	3229	120	0	950	33	550	124	3352.7
156	26.996289	-45.865419	3206	120	230	1300	4	750	96	3324.6
157	26.968845	-45.808002	3238	140	62	1650	78	1050	163	3376.5
158	26.997744	-45.768480	3462	130	0	1050	7	1000	90	3588.6
159	27.091128	-45.725688	3615	70	0	800	19	650	108	3686.5
160	27.119563	-45.705784	3452	160	20	1550	32	1150	121	3608.2
161	27.143010	-45.762116	3695	100	21	700	7	500	99	3790.7
162	27.134873	-45.729001	3381	160	0	1750	16	1350	103	3536.9
163	27.148309	-45.702508	3406	100	232	1300	39	1000	124	3503.6
164	27.145659	-45.680747	3583	80	73	600	90	400	6	3665.4
165	26.947487	-45.584023	3221	130	0	1250	163	700	67	3349.6
166	26.953745	-45.668138	2959	140	0	1250	14	950	99	3095.8
167	26.981722	-45.661695	2974	90	37	1050	20	550	107	3064.6
168	26.997183	-45.661327	2997	70	27	650	6	400	95	3070.6
169	27.063926	-45.397714	3508	110	153	1250	120	800	38	3615.0
170	27.082621	-45.396521	3499	130	436	1100	15	750	108	3626.5
171	26.930072	-45.452994	4029	110	0	900	129	700	37	3916.1
172	26.942263	-45.411986	3245	110	0	650	11	550	99	3353.5
173	26.926377	-45.405151	3229	150	288	1250	145	950	52	3374.6
174	26.937255	-45.368244	2829	260	235	1650	33	1650	122	3089.3
175	26.924774	-45.327450	3056	110	223	1500	165	1150	85	3163.3
176	26.924961	-45.318881	3059	140	0	950	2	700	82	3198.7
177	26.923284	-45.281627	3369	170	0	1200	78	750	172	3534.6
178	27.022542	-45.361540	3102	150	166	1450	171	1000	87	3250.4
179	26.678965	-45.211518	2261	90	245	1100	171	900	153	2350.5
180	26.746281	-45.175842	2418	100	372	1350	12	750	104	2514.3
181	26.749977	-45.161585	2535	100	184	1050	10	750	104	2635.1
182	26.730088	-45.151377	2458	130	418	1500	65	800	146	2592.9
183	26.691542	-45.198547	2338	80	291	950	6	600	98	2414.1
184	26.688902	-45.127264	2523	100	346	1100	176	700	91	2619.3
185	26.844721	-45.239769	3481	80	214	1100	0	800	94	3563.5
186	26.900120	-45.147146	3234	70	198	1200	25	650	104	3306.6

Seamount (#)	LAT (deg)	LON (deg)	Depth (m)	Height (m)	D-top (m)	D1 (m)	Orient1 (deg)	D2 (m)	Orient2 (deg)	Mean D (m)
187	26.885265	-45.144175	3115	190	571	1700	99	1050	9	3300.3
188	26.866217	-45.142777	3292	100	221	1050	167	700	93	3395.1
189	26.894178	-45.123729	3166	130	371	2650	180	2050	91	3291.7
190	26.893654	-45.096162	3318	120	350	1550	6	900	103	3433.3
191	26.911829	-45.027832	3276	80	0	600	166	400	88	3353.6
192	26.895751	-45.037968	3300	80	451	1300	0	750	89	3383.0
193	26.884741	-44.974181	2644	180	400	1650	5	1100	90	2820.9
194	26.770218	-45.058504	2708	110	411	1200	147	650	57	2813.2
195	26.774442	-45.003590	3117	100	17	900	120	550	27	3219.5
196	26.752969	-44.994262	2972	150	105	950	16	600	111	3119.3
197	26.770218	-44.987573	3188	90	550	1200	11	750	95	3275.6
198	26.770570	-44.976661	3229	110	157	650	97	700	6	3341.3
199	26.737128	-45.085257	2848	90	0	500	168	350	75	2936.7
200	26.717592	-45.057272	2508	100	159	650	0	650	104	2603.7
201	26.610949	-45.041147	2482	80	229	1100	23	600	107	2561.6
202	26.607305	-45.027440	2217	100	194	950	33	550	119	2321.7
203	26.589157	-44.978579	2621	90	615	1350	11	700	97	2715.1
204	26.664043	-44.967874	2858	150	222	950	0	800	101	3003.0
205	26.611469	-44.856788	2926	170	17	450	5	300	97	3092.3
206	26.596200	-44.853317	2940	70	17	300	17	250	107	3007.9
207	26.687318	-44.885837	2383	130	107	600	56	750	60	2510.2
208	26.720936	-44.967680	3110	110	142	500	56	750	55	3220.7
209	26.733960	-44.949786	3187	90	0	1200	159	650	65	3279.2
210	26.736248	-44.891645	2844	80	648	1300	25	800	118	2928.2
211	26.855556	-44.962451	2728	110	187	750	137	450	40	2838.0
212	26.824624	-44.948470	2958	110	130	1100	175	600	82	3063.4
213	26.824274	-44.948645	2954	110	17	1000	170	600	79	3067.4
214	26.823226	-44.871402	2599	70	0	950	11	550	103	2670.3
215	26.872857	-44.865110	2418	140	255	750	57	550	147	2556.8
216	26.823488	-45.243636	3415	120	400	2000	178	1450	83	3531.0
217	26.738888	-44.835925	2573	120	458	1150	8	800	96	2696.1
218	26.604250	-48.601612	4438	170	0	1450	9	800	105	4611.8
219	26.668755	-48.613029	4031	110	375	1800	119	1400	26	4139.8
220	26.694927	-48.598202	4077	80	23	800	27	450	127	4152.9
221	26.737075	-48.615883	4182	70	0	450	90	400	0	4253.3
222	26.804308	-48.654743	4115	150	0	1100	26	750	119	4266.6
223	26.836416	-48.625639	3925	130	140	900	29	600	120	4057.5
224	26.839864	-48.599587	4174	160	99	550	94	650	2	4335.2
225	26.859978	-48.581006	4425	70	71	850	34	450	123	4496.5
226	26.607331	-48.556181	4708	120	258	1500	50	900	147	4828.2
227	26.672378	-48.455877	4675	80	0	600	22	550	108	4751.8
228	26.707192	-48.551649	4011	100	23	800	27	600	116	4114.0
229	26.718194	-48.479326	4030	110	0	550	9	600	98	4143.1
230	26.716564	-48.464658	4020	100	23	900	4	550	96	4124.6
231	26.762810	-48.512737	4148	120	20	1150	0	750	90	4267.2
232	26.805796	-48.540851	4386	100	91	1050	138	700	40	4485.5
233	26.821039	-48.479164	4180	100	0	700	175	850	99	4283.3
234	26.844215	-48.394783	4684	210	0	1500	23	1000	105	4889.8
235	26.805544	-48.323404	4313	120	0	900	50	750	135	4432.7
236	26.787868	-48.367581	5004	150	176	1300	167	1050	78	5154.2
237	26.779719	-48.396917	4525	110	0	1000	13	600	96	4630.7
238	26.629918	-48.340664	4288	100	406	1450	35	800	130	4384.4
239	26.608627	-48.293976	4109	90	93	600	68	500	162	4193.7
240	26.764215	-48.290711	4086	100	0	1000	119	750	28	4190.5
241	26.699861	-48.226562	3932	100	41	1200	14	950	100	4034.2
242	26.771206	-48.238282	4256	70	20	1150	174	700	82	4331.2
243	26.798345	-48.274468	4306	90	0	750	168	500	81	4392.1
244	26.795467	-48.190582	4281	110	141	1100	0	650	95	4394.0
245	26.821475	-48.186944	4234	130	121	1250	35	750	132	4365.6
246	26.832585	-48.225829	4394	90	0	650	27	450	120	4488.1
247	26.840056	-48.251115	4600	120	0	500	54	600	57	4718.6
248	26.860361	-48.267780	4555	160	393	1950	32	1450	117	4710.9

Seamount (#)	LAT (deg)	LON (deg)	Depth (m)	Height (m)	D-top (m)	D1 (m)	Orient1 (deg)	D2 (m)	Orient2 (deg)	Mean D (m)
249	26.740000	-47.840000	3955	80	0	1500	55	1000	145	4030.0
250	26.601298	-48.141272	3944	110	43	500	23	500	127	4056.1
251	26.645605	-48.091309	3452	290	0	1650	166	1400	81	3741.1
252	26.679166	-48.126943	4213	70	94	900	85	650	0	4286.4
253	26.684256	-48.081316	3698	140	0	1050	40	750	134	3836.0
254	26.713712	-48.147540	4015	80	45	950	24	800	122	4098.2
255	26.735103	-48.120851	4187	70	228	950	162	550	68	4252.9
256	26.800703	-48.177283	4335	130	182	1450	14	750	108	4469.5
257	26.812687	-48.130151	4356	90	494	1600	15	850	107	4442.8
258	26.831668	-48.145905	4475	100	0	800	30	650	136	4569.9
259	26.862986	-48.175705	4453	80	0	850	129	800	27	4536.1
260	26.879119	-48.135846	4270	160	21	850	17	650	113	4427.8
261	26.829016	-48.019226	4491	90	44	1350	20	850	114	4580.5
262	26.856144	-47.937458	4526	90	161	500	15	500	90	4615.2
263	26.906936	-48.005181	4600	100	275	1150	122	800	39	4699.8
264	26.905204	-47.968626	4315	140	367	2100	39	1550	129	4452.7
265	26.892891	-47.953812	4344	100	172	900	19	900	122	4448.2
266	26.813432	-47.888782	3606	130	94	1050	53	700	154	3733.2
267	26.773200	-47.985474	4362	120	40	600	171	450	80	4485.5
268	26.717582	-47.939228	4452	80	160	1050	81	600	176	4528.0
269	26.715341	-47.978344	4468	90	0	650	12	400	99	4556.3
270	26.701896	-47.982011	4448	70	0	550	5	350	99	4516.4
271	26.710045	-47.929449	4494	70	20	400	167	300	78	4565.1
272	26.634918	-47.913024	4249	100	0	550	4	800	104	4354.4
273	26.619911	-47.902827	4142	100	552	1200	41	800	136	4244.9
274	26.600479	-47.886666	4264	80	150	550	45	500	146	4345.6
275	26.588743	-47.886859	4255	100	214	1200	12	750	114	4350.8
276	26.622037	-47.862927	4331	70	147	750	8	450	103	4400.1
277	26.656541	-47.869903	4222	110	247	1000	38	750	137	4331.6
278	26.601864	-47.832194	3933	190	0	1850	68	1500	169	4123.0
279	26.615816	-47.772992	4718	140	590	1550	23	1350	118	4862.8
280	26.673698	-47.771672	3922	180	213	1050	4	950	88	4101.1
281	26.811548	-47.803114	4043	90	43	550	45	550	132	4130.8
282	26.608430	-47.742698	4762	150	21	1650	43	1050	138	4908.9
283	26.597050	-47.731878	4673	150	0	1250	46	750	136	4824.6
284	26.606378	-47.702029	4516	90	0	1200	76	650	173	4605.1
285	26.642196	-47.637295	3376	150	130	1650	29	900	121	3523.7
286	26.710707	-47.722439	4446	90	224	1000	25	550	114	4534.7
287	26.710102	-47.703692	4529	120	198	1100	1	600	90	4648.7
288	26.745378	-47.710747	4134	90	232	1050	16	550	96	4228.0
289	26.740137	-47.630317	4133	120	403	1350	44	850	129	4250.4
290	26.804441	-47.689581	3852	130	168	1100	177	650	83	3984.9
291	26.783678	-47.675269	3741	260	255	2150	9	1250	94	4002.1
292	26.790128	-47.654708	3871	200	120	1300	17	950	104	4072.2
293	26.838976	-47.663788	3985	150	0	800	6	550	94	4134.7
294	26.896632	-47.732901	4461	80	0	1100	38	650	113	4539.5
295	26.876596	-47.718333	4518	130	0	1050	36	600	148	4649.1
296	26.911183	-47.557913	4077	70	0	550	2	400	90	4147.6
297	26.890333	-47.479774	3909	110	161	850	78	550	167	4015.8
298	26.823691	-47.615592	3955	100	178	600	103	400	21	4052.1
299	26.805958	-47.608967	4092	70	442	1150	44	650	135	4166.0
300	26.798554	-47.597860	4086	90	283	800	22	600	102	4171.9
301	26.819404	-47.479579	3859	150	650	1550	24	1100	121	4006.7
302	26.775912	-47.558165	3714	100	226	1000	34	700	114	3816.5
303	26.679092	-47.497701	4146	90	145	750	15	450	102	4231.0
304	26.629598	-47.583440	3742	80	19	900	36	600	123	3823.8
305	26.604071	-47.552457	3765	120	0	1350	102	750	10	3882.0
306	26.607968	-47.516798	3901	110	0	750	21	800	107	4006.9
307	26.729611	-47.366896	3809	100	242	1250	95	700	6	3910.4
308	26.766207	-47.347688	3738	160	0	900	23	500	111	3896.2
309	26.813680	-47.466536	3921	130	266	1150	59	950	157	4053.1
310	26.837603	-47.380073	4386	100	0	600	139	600	50	4483.3

Seamount (#)	LAT (deg)	LON (deg)	Depth (m)	Height (m)	D-top (m)	D1 (m)	Orient1 (deg)	D2 (m)	Orient2 (deg)	Mean D (m)
311	26.852861	-47.442613	4147	80	225	850	23	750	125	4229.9
312	26.883566	-47.438657	4275	80	0	900	4	600	92	4357.9
313	26.865482	-47.331849	4129	80	0	950	126	700	29	4213.5
314	26.593621	-47.285159	3593	120	180	1700	23	1200	100	3710.6
315	26.649977	-47.203322	3804	170	155	1650	47	900	148	3969.4
316	26.766276	-47.346760	3739	130	0	850	25	450	125	3871.5
317	26.799436	-47.279234	3826	180	260	1000	89	750	0	4009.1
318	26.811932	-47.273837	3855	70	19	750	175	500	68	3928.7
319	26.841229	-47.307830	3757	140	461	1300	15	750	107	3896.7
320	26.865268	-47.331118	4127	100	140	1000	127	800	31	4225.2
321	26.870715	-47.295059	3793	110	46	1250	33	800	124	3898.3
322	26.880105	-47.261442	3982	90	0	650	108	700	16	4071.7
323	26.819256	-47.202846	3892	90	171	1100	9	650	93	3981.5
324	26.877956	-47.089703	4384	70	172	650	92	500	167	4457.6
325	26.775816	-47.109504	3876	110	658	1600	73	1300	154	3983.9
326	26.680470	-47.159092	4112	70	0	900	13	500	108	4180.2
327	26.729857	-47.072212	3742	140	0	1550	55	900	146	3877.7
328	26.647310	-47.186751	3841	100	220	1600	146	1000	49	3937.7
329	26.670178	-47.069333	3844	90	229	1200	41	700	126	3933.3
330	26.717963	-47.035689	3505	180	474	2950	169	1750	91	3681.5
331	26.877476	-47.021921	4261	110	0	900	61	600	146	4373.7
332	26.881420	-46.987177	4286	110	202	750	24	500	113	4395.9
333	26.741110	-46.704170	3810	90	0	1050	77	700	167	3903.8
334	26.736110	-46.685280	3878	70	0	1150	16	700	106	3952.5
335	26.585995	-46.898266	3319	130	466	1250	7	1100	92	3445.8
336	26.590645	-46.869437	3561	110	19	1200	44	900	122	3675.8
337	26.613894	-46.922445	3355	100	359	1300	36	1300	125	3453.0
338	26.623380	-46.904590	3398	110	145	1200	16	850	108	3509.8
339	26.748590	-46.829088	3248	130	0	1300	129	900	37	3375.4
340	26.763462	-46.822254	3234	150	0	1400	141	900	41	3385.7
341	26.781148	-46.863052	3635	100	137	650	136	550	50	3737.8
342	26.846706	-46.849710	3760	70	21	800	87	550	0	3827.7
343	26.863932	-46.894836	4317	130	0	1100	41	850	129	4447.0
344	26.880222	-46.847838	3862	100	242	1150	36	600	123	3956.7
345	26.906022	-46.857013	4174	130	0	1150	71	900	157	4305.0
346	26.905629	-46.697184	4067	120	21	850	95	600	0	4190.9
347	26.844902	-46.724857	4281	220	0	1050	8	1100	105	4496.7
348	26.796020	-46.762506	4108	130	166	900	167	1150	84	4237.9
349	26.786574	-46.759291	3942	250	176	1550	21	1000	113	4193.1
350	26.670178	-46.683732	3686	150	263	1300	176	1000	88	3833.6
351	26.614256	-46.648871	3803	110	175	1650	27	850	130	3910.1
352	26.584469	-46.655290	3516	110	0	950	31	600	132	3629.1
353	26.615986	-46.648756	3470	100	21	750	10	650	104	3565.7
354	26.659091	-46.572872	3451	160	145	1100	51	950	146	3605.7
355	26.700558	-46.603463	4373	100	628	1350	174	700	80	4470.4
356	26.809258	-46.529893	4396	100	0	800	91	450	0	4494.7
357	26.904189	-46.528395	4193	90	0	650	98	850	3	4284.2
358	26.623582	-46.449366	3413	90	107	700	44	500	140	3499.9
359	26.715843	-46.484040	3407	100	405	2200	174	1650	78	3509.4
360	26.780588	-46.376339	3370	120	416	2400	67	1600	167	3492.6
361	26.874508	-46.408818	4440	80	0	600	94	650	4	4520.4
362	26.908728	-46.384457	4291	100	0	800	175	850	93	4393.5
363	26.891521	-46.383877	4264	110	22	600	39	650	45	4369.9
364	26.883241	-46.340724	4070	150	519	1900	160	1800	80	4224.0
365	26.864184	-46.242885	3259	200	466	1500	5	1900	98	3464.0
366	26.728709	-46.328101	3596	110	0	850	11	550	107	3703.2
367	26.700071	-46.315027	3577	100	0	1350	8	750	96	3677.5
368	26.689073	-46.272279	3876	120	343	900	93	700	2	3998.9
369	26.667987	-46.246225	3799	100	0	550	0	650	88	3893.7
370	26.655806	-46.258406	3780	100	0	1250	15	700	106	3876.3
371	26.622211	-46.268622	3887	100	212	1300	170	850	78	3990.5
372	26.599028	-46.322060	3678	70	29	1100	17	600	117	3750.9

Seamount (#)	LAT (deg)	LON (deg)	Depth (m)	Height (m)	D-top (m)	D1 (m)	Orient1 (deg)	D2 (m)	Orient2 (deg)	Mean D (m)
311	26.852861	-47.442613	4147	80	225	850	23	750	125	4229.9
312	26.883566	-47.438657	4275	80	0	900	4	600	92	4357.9
313	26.865482	-47.331849	4129	80	0	950	126	700	29	4213.5
314	26.593621	-47.285159	3593	120	180	1700	23	1200	100	3710.6
315	26.649977	-47.203322	3804	170	155	1650	47	900	148	3969.4
316	26.766276	-47.346760	3739	130	0	850	25	450	125	3871.5
317	26.799436	-47.279234	3826	180	260	1000	89	750	0	4009.1
318	26.811932	-47.273837	3855	70	19	750	175	500	68	3928.7
319	26.841229	-47.307830	3757	140	461	1300	15	750	107	3896.7
320	26.865268	-47.331118	4127	100	140	1000	127	800	31	4225.2
321	26.870715	-47.295059	3793	110	46	1250	33	800	124	3898.3
322	26.880105	-47.261442	3982	90	0	650	108	700	16	4071.7
323	26.819256	-47.202846	3892	90	171	1100	9	650	93	3981.5
324	26.877956	-47.089703	4384	70	172	650	92	500	167	4457.6
325	26.775816	-47.109504	3876	110	658	1600	73	1300	154	3983.9
326	26.680470	-47.159092	4112	70	0	900	13	500	108	4180.2
327	26.729857	-47.072212	3742	140	0	1550	55	900	146	3877.7
328	26.647310	-47.186751	3841	100	220	1600	146	1000	49	3937.7
329	26.670178	-47.069333	3844	90	229	1200	41	700	126	3933.3
330	26.717963	-47.035689	3505	180	474	2950	169	1750	91	3681.5
331	26.877476	-47.021921	4261	110	0	900	61	600	146	4373.7
332	26.881420	-46.987177	4286	110	202	750	24	500	113	4395.9
333	26.741110	-46.704170	3810	90	0	1050	77	700	167	3903.8
334	26.736110	-46.685280	3878	70	0	1150	16	700	106	3952.5
335	26.585995	-46.898266	3319	130	466	1250	7	1100	92	3445.8
336	26.590645	-46.869437	3561	110	19	1200	44	900	122	3675.8
337	26.613894	-46.922445	3355	100	359	1300	36	1300	125	3453.0
338	26.623380	-46.904590	3398	110	145	1200	16	850	108	3509.8
339	26.748590	-46.829088	3248	130	0	1300	129	900	37	3375.4
340	26.763462	-46.822254	3234	150	0	1400	141	900	41	3385.7
341	26.781148	-46.863052	3635	100	137	650	136	550	50	3737.8
342	26.846706	-46.849710	3760	70	21	800	87	550	0	3827.7
343	26.863932	-46.894836	4317	130	0	1100	41	850	129	4447.0
344	26.880222	-46.847838	3862	100	242	1150	36	600	123	3956.7
345	26.906062	-46.857013	4174	130	0	1150	71	900	157	4305.0
346	26.905629	-46.697184	4067	120	21	850	95	600	0	4190.9
347	26.844902	-46.724857	4281	220	0	1050	8	1100	105	4496.7
348	26.796020	-46.762506	4108	130	166	900	167	1150	84	4237.9
349	26.786574	-46.759291	3942	250	176	1550	21	1000	113	4193.1
350	26.670178	-46.683732	3686	150	263	1300	176	1000	88	3833.6
351	26.614256	-46.704871	3803	110	175	1650	27	850	130	3910.1
352	26.584469	-46.655290	3516	110	0	950	31	600	132	3629.1
353	26.615986	-46.648756	3470	100	21	750	10	650	104	3565.7
354	26.659091	-46.572872	3451	160	145	1100	51	950	146	3605.7
355	26.700558	-46.603463	4373	100	628	1350	174	700	80	4470.4
356	26.809258	-46.529893	4396	100	0	800	91	450	0	4494.7
357	26.904189	-46.528395	4193	90	0	650	98	850	3	4284.2
358	26.623582	-46.449366	3413	90	107	700	44	500	140	3499.9
359	26.715843	-46.484040	3407	100	405	2200	174	1650	78	3509.4
360	26.780588	-46.376339	3370	120	416	2400	67	1600	167	3492.6
361	26.874508	-46.408818	4440	80	0	600	94	650	4	4520.4
362	26.908728	-46.384457	4291	100	0	800	175	850	93	4393.5
363	26.891521	-46.383877	4264	110	22	600	39	650	45	4369.9
364	26.883241	-46.340724	4070	150	519	1900	160	1800	80	4224.0
365	26.864184	-46.242885	3259	200	466	1500	5	1900	98	3464.0
366	26.728709	-46.328101	3596	110	0	850	11	550	107	3703.2
367	26.700071	-46.315027	3577	100	0	1350	8	750	96	3677.5
368	26.689073	-46.272279	3876	120	343	900	93	700	2	3998.9
369	26.667987	-46.246225	3799	100	0	550	0	650	88	3893.7
370	26.655806	-46.258406	3780	100	0	1250	15	700	106	3876.3
371	26.622211	-46.268622	3887	100	212	1300	170	850	78	3990.5
372	26.599028	-46.322060	3678	70	29	1100	17	600	117	3750.9

Seamount (#)	LAT (deg)	LON (deg)	Depth (m)	Height (m)	D-top (m)	D1 (m)	Orient1 (deg)	D2 (m)	Orient2 (deg)	Mean D (m)
373	26.609946	-46.178179	3767	150	21	800	16	950	101	3920.7
374	26.637985	-46.191815	3583	160	149	800	11	900	103	3739.9
375	26.609178	-46.083499	3661	120	328	1650	12	850	109	3780.8
376	26.662184	-46.183749	3548	140	21	850	25	750	107	3684.7
377	26.697996	-46.124016	3848	130	0	700	17	600	112	3975.5
378	26.723106	-46.195194	3471	90	0	600	152	500	57	3560.8
379	26.791171	-46.145183	3242	70	255	950	175	550	90	3312.5
380	26.806839	-46.216844	3695	170	216	1600	6	1250	90	3866.8
381	26.856914	-46.192097	3847	70	19	800	177	450	72	3914.2
382	26.875861	-46.154589	3668	120	151	800	55	1050	64	3788.9
383	26.860587	-46.102581	3870	100	0	900	1	650	95	3972.8
384	26.586324	-46.199113	3639	100	0	1250	4	850	96	3739.2
385	26.614266	-45.971177	3299	130	21	850	88	650	2	3427.2
386	26.697141	-46.072644	4038	110	283	950	20	750	116	4148.7
387	26.752810	-46.027626	4208	80	0	750	178	700	88	4291.9
388	26.768285	-46.046919	4201	140	49	1250	42	1150	123	4336.6
389	26.795216	-46.088521	3999	130	0	1000	18	700	98	4125.1
390	26.779339	-45.963917	3633	130	531	1550	69	800	169	3767.5
391	26.766678	-45.954070	3644	100	360	900	87	850	169	3748.5
392	26.842399	-46.061091	3690	120	73	800	164	550	82	3806.2
393	26.881159	-46.066708	3275	100	73	750	0	650	90	3370.8
394	26.883593	-46.024766	3756	100	63	950	90	600	0	3851.3
395	26.877788	-46.025140	3732	80	0	650	176	650	87	3812.0
396	26.886027	-46.012221	3686	180	196	1550	32	1000	117	3867.7
397	26.893142	-45.982449	3709	110	241	1700	24	950	112	3822.4
398	26.878533	-45.903313	3346	130	114	800	28	900	102	3476.5
399	26.844518	-45.933291	3140	100	160	1950	73	1250	169	3243.7
400	26.887565	-45.847390	3831	110	43	700	95	500	2	3943.6
401	26.842596	-45.847967	3614	140	0	800	35	450	124	3753.7
402	26.821457	-45.842202	3471	110	199	1150	90	950	9	3583.1
403	26.782956	-45.877038	3987	80	78	1050	27	600	113	4063.4
404	26.773109	-45.827196	3568	120	0	700	6	450	101	3690.5
405	26.634818	-45.877561	3986	100	252	1500	119	1150	38	4085.1
406	26.610220	-45.852195	3515	80	86	700	175	500	86	3597.2
407	26.653267	-45.821063	3419	120	0	950	5	800	98	3537.2
408	26.603479	-45.784534	3396	80	205	1600	83	1100	175	3479.8
409	26.693523	-45.696692	3609	110	20	950	17	550	113	3714.4
410	26.727689	-45.724225	3567	80	315	950	45	500	144	3642.7
411	26.726081	-45.793762	3813	140	0	1500	19	1300	106	3951.6
412	26.792000	-45.722617	3215	70	310	750	75	850	161	3289.3
413	26.872920	-45.791829	3333	150	373	1150	1	750	90	3480.3
414	26.590583	-45.650996	3306	120	45	850	123	750	32	3422.8
415	26.621922	-45.627074	3039	130	0	1250	27	800	113	3164.3
416	26.632307	-45.551231	3060	90	37	1050	19	650	112	3148.1
417	26.770618	-45.538707	3594	130	156	1600	101	1000	8	3720.1
418	26.806284	-45.550328	3679	100	46	1300	7	700	100	3774.2
419	26.821721	-45.604263	3330	200	347	1400	172	1050	85	3527.0
420	26.860924	-45.624984	3488	100	246	1200	27	650	116	3587.5
421	26.815561	-45.549192	3630	100	166	700	23	400	120	3726.1
422	26.832175	-45.503075	3225	140	197	1000	46	600	140	3369.6
423	26.807347	-45.506995	3365	160	83	1000	11	750	101	3523.2
424	26.905541	-45.394053	3091	160	73	1550	55	1050	148	3249.0
425	26.793861	-45.435475	2560	120	161	1200	169	800	78	2676.3
426	26.762402	-45.458919	2776	140	0	1350	13	900	91	2919.6
427	26.644360	-45.504681	3088	120	155	950	156	750	67	3205.9
428	26.679593	-45.306955	2521	80	21	750	28	600	123	2601.7
429	26.760399	-45.314997	2757	90	0	1000	167	650	77	2845.7
430	26.770217	-45.387131	2610	90	20	750	8	500	97	2695.5
431	26.806083	-45.317401	2946	160	0	1000	42	750	120	3106.0
432	26.810520	-45.385230	2539	170	145	1250	16	650	101	2704.8
433	26.870818	-45.313544	3280	70	0	650	163	550	69	3346.2
434	26.865031	-45.304770	3159	140	334	1250	49	850	137	3297.5

Seamount (#)	LAT (deg)	LON (deg)	Depth (m)	Height (m)	D-top (m)	D1 (m)	Orient1 (deg)	D2 (m)	Orient2 (deg)	Mean D (m)
435	26.850843	-45.302343	3158	80	83	850	22	500	111	3235.2
436	26.829002	-45.263327	3651	90	111	1350	84	1100	178	3737.1
437	26.704778	-45.473670	2841	200	0	600	70	750	63	3043.1
438	26.672110	-45.487035	3126	110	0	650	30	550	116	3232.3
439	26.150000	-44.920000	2390	170	600	1650	26	1600	116	2560.0
440	26.308313	-45.229300	3248	130	0	1300	154	1150	59	3378.9
441	26.366988	-45.224707	3365	160	851	1600	89	1500	169	3528.9
442	26.367831	-45.244914	3105	130	0	1000	48	650	154	3232.2
443	26.363404	-45.136533	2922	70	0	500	178	450	93	2992.3
444	26.492530	-45.244179	3720	80	0	500	170	400	87	3798.9
445	26.505361	-45.192009	3322	70	0	550	165	350	87	3393.7
446	26.512048	-45.195316	3329	100	317	1000	147	600	59	3431.8
447	26.537892	-45.139656	3309	100	259	800	86	700	0	3405.2
448	26.522892	-45.101975	2867	150	474	1400	47	950	138	3019.2
449	26.548193	-44.991825	2903	80	344	1100	4	750	94	2981.6
450	26.565542	-44.990586	2727	130	146	950	3	700	87	2860.0
451	26.441416	-45.081929	3379	140	0	750	176	700	83	3519.4
452	26.449849	-45.038530	3397	90	141	700	4	550	94	3484.6
453	26.439940	-45.024064	3139	80	23	650	22	400	121	3223.5
454	26.398193	-45.049483	3034	70	62	750	41	550	118	3104.7
455	26.411898	-45.009392	3005	90	21	600	94	550	0	3096.7
456	26.441205	-45.081929	3376	150	0	700	88	800	7	3524.7
457	26.408313	-44.994925	3098	80	0	750	93	550	0	3176.4
458	26.388494	-44.994305	3119	110	330	1100	30	800	126	3226.0
459	26.370572	-45.037084	2760	90	322	800	178	600	92	2845.0
460	26.330181	-45.085029	3254	190	0	1700	157	1150	69	3443.5
461	26.338675	-45.050517	2761	130	20	1250	14	700	96	2887.3
462	26.284277	-45.029851	2573	80	0	1300	9	750	97	2648.2
463	26.255000	-44.923605	2174	80	40	950	169	750	90	2256.3
464	26.451325	-44.948404	3226	80	0	600	40	450	125	3306.1
465	26.357029	-44.932733	2974	100	0	1150	27	600	121	3069.4
466	26.360922	-48.743981	4970	100	0	1350	124	1150	30	5067.3
467	26.271116	-48.792234	4389	70	181	600	124	400	27	4461.8
468	26.266592	-48.645901	4316	110	132	750	104	600	6	4421.5
469	26.271887	-48.577590	4015	90	92	850	59	500	122	4101.1
470	26.299776	-48.608127	3966	90	147	1050	163	850	68	4053.8
471	26.356325	-48.669024	4488	80	131	1050	67	650	161	4568.8
472	26.250000	-48.360000	4235	170	0	1000	50	900	95	4407.5
473	26.245830	-48.194440	3875	170	0	1300	91	850	1	4042.5
474	26.288065	-48.572011	3937	140	71	1000	35	700	122	4077.7
475	26.289519	-48.585824	4145	80	0	550	2	400	95	4224.5
476	26.339680	-48.463692	4596	150	597	1400	39	750	128	4742.9
477	26.429875	-48.558457	3791	170	168	1550	11	950	96	5964.5
478	26.422979	-48.479928	5053	90	87	800	87	500	0	5139.1
479	26.509428	-48.522395	3798	70	322	900	55	500	144	3870.1
480	26.557455	-48.423476	3821	170	351	1450	66	750	157	3988.1
481	26.573884	-48.366458	4311	70	0	650	44	450	135	4377.9
482	26.524597	-48.374575	4042	120	179	1050	89	600	0	4163.5
483	26.560161	-48.315817	3989	140	0	1200	49	650	144	4130.6
484	26.490965	-48.335146	4337	180	0	1550	23	1300	129	4516.3
485	26.441422	-48.388685	4353	80	229	750	52	550	151	4436.1
486	26.411270	-48.418644	4435	100	386	2150	30	1200	122	4538.4
487	26.384403	-48.440292	4319	320	263	2550	34	2100	125	4638.4
488	26.409337	-48.359499	4066	140	304	1150	49	650	147	4209.6
489	26.377638	-48.297262	4402	110	29	750	80	550	167	4508.8
490	26.297585	-48.331666	4316	130	0	850	89	650	4	4441.9
491	26.259895	-48.356213	4281	100	0	900	169	550	77	4381.8
492	26.361221	-48.278726	4158	80	193	750	80	400	166	4235.9
493	26.356836	-48.286400	4265	70	18	550	88	450	0	4334.2
494	26.344961	-48.275072	4245	130	187	1550	80	800	171	4373.3
495	26.453433	-48.298709	4714	110	0	1200	150	1350	67	4819.7
496	26.397122	-48.257720	4223	70	140	750	52	500	147	4291.3

Seamount (#)	LAT (deg)	LON (deg)	Depth (m)	Height (m)	D-top (m)	D1 (m)	Orient1 (deg)	D2 (m)	Orient2 (deg)	Mean D (m)
497	26.401336	-48.228416	4167	110	0	1150	52	950	151	4273.0
498	26.431215	-48.240674	4327	110	0	850	21	500	119	4433.3
499	26.556327	-48.209115	3976	90	0	600	159	450	68	4066.9
500	26.577430	-48.375349	4317	90	179	700	96	600	14	4408.6
501	26.584581	-48.305573	4082	70	0	900	42	550	129	4150.7
502	26.239778	-48.277837	4494	100	350	950	58	750	141	4593.5
503	26.247220	-48.166667	4150	90	0	700	76	600	166	4236.2
504	26.248610	-47.977780	3750	100	0	700	0	600	90	3852.5
505	26.250000	-47.955550	3840	70	0	950	23	650	113	3907.5
506	26.350500	-48.166884	4480	140	186	900	9	700	96	4617.6
507	26.341574	-48.103673	4469	120	215	1550	86	1450	19	4593.3
508	26.264882	-48.047566	3999	100	0	600	114	650	18	4096.2
509	26.384098	-48.116048	4530	80	0	950	5	900	91	4611.0
510	26.397888	-48.063376	4417	120	19	700	141	550	49	4534.8
511	26.417999	-48.055906	4451	100	19	1000	144	700	61	4555.8
512	26.449220	-48.102832	4503	120	267	1150	24	700	99	4620.8
513	26.477889	-48.157047	3836	80	226	1050	30	600	118	3921.0
514	26.527620	-48.117517	3777	90	0	600	143	500	43	3869.3
515	26.528349	-48.141017	3722	140	0	650	122	600	35	3864.5
516	26.571340	-48.037729	4627	90	152	1400	174	850	72	4712.6
517	26.497872	-47.947792	4124	80	0	700	52	450	135	4206.2
518	26.477530	-47.972008	4120	110	29	850	14	700	106	4225.5
519	26.465713	-47.969490	4148	110	86	850	173	500	79	4258.2
520	26.436060	-47.966196	3981	110	19	1150	19	900	114	4092.5
521	26.425211	-47.969684	3999	100	0	1200	37	850	127	4096.5
522	26.400414	-48.002812	4014	90	0	900	11	550	100	4105.3
523	26.317869	-48.015294	3609	100	0	650	0	500	88	3711.3
524	26.326364	-47.917220	3760	70	0	1050	42	1050	122	3834.8
525	26.282346	-47.942897	3755	110	0	1050	36	550	121	3865.9
526	26.275205	-47.778828	4267	90	271	1050	91	650	7	4353.7
527	26.342181	-47.863871	4031	90	20	800	161	500	67	4119.8
528	26.351488	-47.856206	3990	120	0	900	38	650	131	4106.8
529	26.370367	-47.780651	4215	140	0	950	31	600	111	4352.2
530	26.414745	-47.813694	3998	120	0	1300	87	750	177	4122.8
531	26.451054	-47.794099	4022	110	0	650	6	600	94	4134.4
532	26.449325	-47.830600	4145	80	201	1150	14	700	101	4224.4
533	26.470650	-47.863067	4005	120	247	1250	177	850	91	4121.5
534	26.499529	-47.814415	4316	100	184	1050	13	700	97	4412.3
535	26.527633	-47.838686	4266	140	348	1600	176	1400	89	4406.7
536	26.562855	-47.873908	4338	110	20	650	164	550	64	4448.6
537	26.520151	-47.807297	4457	80	419	1000	7	550	98	4535.8
538	26.579917	-47.803116	4482	170	0	850	53	550	138	4657.1
539	26.577672	-47.816214	4544	70	28	850	77	550	153	4619.1
540	26.272590	-47.751968	4112	160	211	1150	68	1000	148	4272.6
541	26.285298	-47.731532	3921	70	259	650	112	600	20	3992.8
542	26.284954	-47.718137	3809	130	103	750	97	700	3	3935.5
543	26.324968	-47.737371	4128	100	206	1150	143	1000	49	4226.8
544	26.376302	-47.695297	3912	70	17	650	64	450	164	3983.5
545	26.435549	-47.723804	4337	250	0	1600	131	1550	48	4590.2
546	26.444136	-47.702510	4361	110	270	1050	179	1150	90	4467.3
547	26.463713	-47.701308	4491	70	67	1150	176	650	90	4557.3
548	26.457187	-47.732047	4551	100	232	1200	31	650	118	4648.5
549	26.448429	-47.767081	4320	90	175	700	6	500	92	4405.5
550	26.452035	-47.759524	4324	80	150	650	85	500	0	4404.2
551	26.423872	-47.663698	3850	120	0	950	18	650	95	3975.0
552	26.471023	-47.728895	4573	100	156	1050	60	650	147	4670.3
553	26.491215	-47.682381	4572	90	426	1300	174	1000	78	4659.2
554	26.498968	-47.651192	4366	110	237	700	8	700	87	4473.5
555	26.526732	-47.767656	4367	100	54	800	30	500	126	4466.2
556	26.543859	-47.631721	4533	110	224	1500	29	900	122	4645.5
557	26.558402	-47.607186	4556	110	0	1050	87	750	6	4666.9
558	26.540954	-47.576317	4540	90	0	1050	26	700	106	4626.1

Seamount (#)	LAT (deg)	LON (deg)	Depth (m)	Height (m)	D-top (m)	D1 (m)	Orient1 (deg)	D2 (m)	Orient2 (deg)	Mean D (m)
559	26.537311	-47.536245	4535	90	242	1000	59	600	142	4626.9
560	26.542488	-47.532794	4514	80	207	750	38	450	114	4589.3
561	26.470397	-47.618115	4486	70	171	550	21	350	114	4558.0
562	26.489953	-47.514963	4261	140	0	850	63	650	153	4397.1
563	26.498198	-47.505952	4289	120	246	1400	80	800	3	4411.8
564	26.412923	-47.583603	3993	130	0	800	2	650	97	4121.6
565	26.410622	-47.476425	3972	120	0	900	27	600	122	4095.8
566	26.395858	-47.482177	3993	90	0	800	69	500	151	4079.1
567	26.377260	-47.492147	4017	80	191	1050	39	850	126	4101.8
568	26.362114	-47.490421	4011	80	209	800	95	650	14	4093.5
569	26.374768	-47.506335	4127	70	234	750	0	400	85	4194.5
570	26.364031	-47.538354	4157	70	196	1550	6	800	97	4229.7
571	26.274186	-47.538929	4102	90	21	900	7	500	90	4194.8
572	26.300837	-47.506527	3886	70	0	650	7	500	97	3955.6
573	26.296619	-47.479492	4099	70	0	950	8	650	95	4171.2
574	26.279363	-47.480259	4071	100	196	800	2	550	90	4173.0
575	26.349834	-47.381547	4217	110	0	850	12	500	107	4322.7
576	26.338235	-47.326994	3949	90	387	1450	12	800	94	4040.8
577	26.301081	-47.371216	3930	90	170	650	88	450	2	4019.3
578	26.365902	-47.435956	4108	110	86	700	122	750	23	4221.2
579	26.492865	-47.355810	4213	150	0	850	30	550	118	4366.3
580	26.231301	-47.640833	3614	70	0	800	29	600	130	3683.4
581	26.150000	-47.195830	3910	70	0	600	93	400	3	3980.0
582	26.265422	-47.316723	3707	230	175	1450	46	1300	45	3937.4
583	26.326145	-47.300598	3889	80	446	1700	72	900	163	3970.4
584	26.314137	-47.229069	4121	80	0	900	27	500	114	4196.3
585	26.328375	-47.220492	4121	100	0	1300	46	950	137	4220.8
586	26.391784	-47.226153	4072	80	19	550	27	400	112	4155.5
587	26.433295	-47.233529	4405	90	235	1200	29	650	125	4491.2
588	26.520791	-47.291507	4029	100	120	1100	70	800	158	4129.6
589	26.556813	-47.332504	3760	90	148	1000	47	750	134	3849.8
590	26.500458	-47.134678	4349	100	194	1050	161	650	75	4453.2
591	26.528036	-47.164164	4371	70	135	600	31	400	121	4442.6
592	26.449466	-47.088887	4352	70	93	1000	169	850	77	4421.1
593	26.449292	-47.088887	4354	70	52	1050	165	850	72	4422.0
594	26.406277	-47.171969	4413	140	116	750	97	550	96	4554.1
595	26.393788	-47.154451	4440	80	140	750	28	400	113	4522.8
596	26.405410	-47.125138	4176	210	0	1000	50	850	138	4386.4
597	26.367597	-47.091315	4345	80	181	800	13	700	104	4426.1
598	26.436328	-46.961748	4557	80	180	850	91	500	174	4641.6
599	26.494277	-46.948059	4296	90	0	650	50	450	140	4388.0
600	26.340026	-47.202515	4089	150	499	1750	9	1100	93	4237.6
601	26.468922	-47.087242	4291	100	673	1200	170	1550	72	4396.0
602	26.381271	-47.199941	4326	100	168	1250	17	700	118	4427.7
603	26.359020	-47.053610	4202	120	0	1050	7	950	90	4319.6
604	26.319745	-46.971402	4230	120	0	1400	48	1350	127	4353.6
605	26.322345	-46.927946	3936	110	0	1350	93	850	176	4049.8
606	26.449932	-47.042414	4377	110	0	950	34	550	116	4483.9
607	26.443956	-47.025233	4500	90	378	1200	126	1200	44	4589.1
608	26.415196	-47.025233	4449	120	0	1150	177	1000	85	4570.2
609	26.307741	-47.197567	4104	70	0	750	172	500	77	4171.0
610	26.241000	-46.754000	4255	80	0	800	25	550	115	4338.8
611	26.288876	-46.885248	4309	90	0	650	137	550	45	4395.6
612	26.410510	-46.802379	3184	110	218	1000	93	650	173	3289.5
613	26.428207	-46.851896	3820	90	237	800	55	500	152	3911.6
614	26.437226	-46.858532	4044	90	141	600	127	450	40	4137.3
615	26.439438	-46.908560	4298	70	17	850	112	450	31	4371.3
616	26.491381	-46.908900	3879	70	117	550	97	350	0	3951.8
617	26.508397	-46.854619	4060	100	34	600	77	450	168	4154.9
618	26.531879	-46.841006	3934	90	0	1100	0	650	87	4024.3
619	26.561828	-46.864998	3729	140	0	900	108	500	22	3867.1
620	26.477088	-46.820076	4148	160	183	1550	102	800	31	4309.3

Seamount (#)	LAT (deg)	LON (deg)	Depth (m)	Height (m)	D-top (m)	D1 (m)	Orient1 (deg)	D2 (m)	Orient2 (deg)	Mean D (m)
621	26.459517	-46.801699	3676	110	34	650	15	450	106	3788.4
622	26.507703	-46.704885	3871	90	0	900	87	800	171	3962.6
623	26.431633	-46.658945	3873	80	0	1250	100	700	3	3953.8
624	26.400490	-46.744460	3618	110	0	800	52	650	155	3724.6
625	26.399629	-46.717102	3750	90	17	750	67	450	160	3842.4
626	26.406340	-46.709359	3719	160	0	950	95	550	176	3883.9
627	26.398081	-46.694390	3866	70	19	850	112	550	27	3934.0
628	26.350128	-46.701788	3867	120	311	1200	24	650	111	3982.8
629	26.293692	-46.639502	3678	170	298	1500	54	900	162	3844.1
630	26.305900	-46.622683	3725	80	17	1150	57	700	151	3801.1
631	26.439921	-46.569125	3181	120	0	1200	22	650	112	3299.1
632	26.442659	-46.539352	3472	80	202	800	14	750	103	3552.8
633	26.512073	-46.549961	3827	90	117	850	79	600	166	3919.2
634	26.466218	-46.793680	3655	100	145	2350	57	1200	144	3758.2
635	26.500072	-46.784496	4062	80	0	350	0	250	98	4140.4
636	26.267145	-46.143530	3958	220	328	1450	24	950	107	4174.1
637	26.265414	-46.099738	4218	90	17	950	7	650	96	4303.4
638	26.329804	-46.082429	3047	110	17	750	91	500	173	3157.5
639	26.333785	-46.181609	2785	150	228	1150	37	850	140	2934.3
640	26.390369	-46.078102	2984	120	576	1250	8	650	90	3103.3
641	26.408024	-46.113931	3176	80	0	1000	94	850	6	3252.5
642	26.415986	-46.161531	2680	100	237	1400	79	1050	172	2778.6
643	26.414255	-46.185244	2777	110	0	900	93	600	4	2882.2
644	26.562127	-46.180571	3705	230	0	1450	30	1200	124	3938.2
645	26.570609	-46.179532	3838	110	278	750	179	800	86	3950.7
646	26.461332	-46.490738	3387	110	129	1050	156	900	57	3494.1
647	26.487128	-46.490050	3477	80	0	550	103	450	12	3553.2
648	26.496767	-46.493320	3508	100	0	400	90	350	0	3609.8
649	26.576806	-46.410354	3606	110	220	800	90	800	8	3716.6
650	26.503421	-46.333514	3534	90	26	750	9	550	101	3621.3
651	26.559118	-46.246662	3785	90	178	1200	173	650	81	3871.3
652	26.573390	-46.329337	3613	80	104	950	28	700	107	3690.9
653	26.574782	-46.339432	3618	90	17	750	102	600	7	3707.9
654	26.386146	-46.360840	3285	120	68	1150	151	600	56	3405.5
655	26.457334	-46.281298	3309	120	0	900	12	650	106	3432.3
656	26.269461	-46.369891	3509	110	175	1250	29	850	121	3620.3
657	26.469047	-46.158660	3469	110	296	1350	33	750	123	3580.8
658	26.270864	-46.005251	3639	80	161	950	20	600	116	3714.3
659	26.332374	-46.075670	3098	70	242	750	103	450	13	3168.4
660	26.352934	-46.017073	3298	70	0	650	168	400	80	3366.0
661	26.372363	-45.998226	2866	90	179	800	144	550	45	2956.0
662	26.381786	-45.989317	2859	70	88	650	70	450	164	2927.2
663	26.439323	-46.035064	3293	120	133	800	144	550	51	3412.7
664	26.418591	-45.981607	3328	90	0	550	172	400	85	3415.3
665	26.462282	-45.959505	3847	100	51	650	114	600	25	3746.4
666	26.527905	-46.018101	3442	120	514	1000	143	1050	53	3559.2
667	26.575194	-45.982292	3470	90	134	750	145	600	40	3562.0
668	26.536608	-45.869508	3694	110	557	1250	16	650	96	3804.9
669	26.546657	-45.863964	3701	90	169	1050	162	550	55	3791.0
670	26.572298	-45.829661	3316	160	17	1250	174	650	87	3476.5
671	26.384716	-45.811816	3657	100	35	900	96	650	14	3761.1
672	26.360981	-45.908143	2669	80	40	800	177	500	92	2752.9
673	26.344120	-45.821345	3450	110	245	1150	99	850	175	3556.5
674	26.252644	-45.887006	2651	160	232	600	23	400	106	2813.1
675	26.305824	-45.714236	3304	140	34	800	92	550	8	3443.9
676	26.417615	-45.695973	3372	230	17	1300	18	850	107	3599.2
677	26.433293	-45.693216	3487	190	115	1350	3	800	94	3674.3
678	26.415203	-45.742319	3720	70	126	650	177	650	95	3794.0
679	26.466201	-45.749039	3885	100	19	450	125	600	124	3981.7
680	26.518105	-45.752657	3679	100	115	750	30	750	117	3779.8
681	26.554631	-45.686669	3423	80	109	900	178	550	90	3504.5
682	26.251390	-45.363890	2395	90	0	500	14	350	104	2480.0

Seamount (#)	LAT (deg)	LON (deg)	Depth (m)	Height (m)	D-top (m)	D1 (m)	Orient1 (deg)	D2 (m)	Orient2 (deg)	Mean D (m)
683	26.430368	-45.275600	3649	90	448	1250	120	850	42	3737.8
684	26.408324	-45.300650	3590	130	50	600	131	500	36	3716.5
685	26.465772	-45.358599	3121	160	707	1550	169	1100	164	3280.9
686	26.505412	-45.363299	3389	110	795	1750	23	1100	110	3497.0
687	26.506075	-45.385508	3427	70	277	900	31	700	117	3497.8
688	26.497954	-45.332470	3333	100	276	1200	176	650	96	3432.7
689	26.526628	-45.286890	3299	100	459	1400	76	900	165	3403.1
690	26.505247	-45.283078	3389	130	0	1350	17	850	103	3519.3
691	26.485192	-45.296669	3577	100	169	900	59	500	146	3672.7
692	26.285022	-45.595945	3469	130	202	1400	147	750	61	3603.7
693	26.310673	-45.645161	3802	80	0	1000	120	550	40	3884.3
694	26.366158	-45.603502	3453	90	50	800	46	500	137	3546.1
695	26.421824	-45.559447	3763	80	0	750	71	550	155	3841.7
696	26.562601	-45.654009	3311	120	513	1850	54	1300	131	3432.3
697	26.573004	-45.654378	3313	80	0	600	80	350	146	3394.7
698	26.476323	-45.483226	3724	120	246	950	160	750	70	3842.7
699	26.523318	-45.419631	3770	110	0	1000	171	550	78	3875.2
700	26.481525	-45.417235	3407	70	443	1150	160	600	70	3478.2
701	26.475426	-45.394931	3425	90	97	700	142	650	30	3512.4
702	26.448401	-45.429770	3391	100	44	1000	115	750	21	3493.8
703	26.439611	-45.503687	3572	70	18	600	19	500	116	3642.9
704	26.365740	-45.429954	3424	80	403	1500	83	900	159	3343.1
705	26.274439	-45.532627	3272	80	145	750	175	400	92	3349.2
706	26.329327	-45.418525	2920	70	178	950	175	500	98	2986.4
707	26.340807	-45.455576	3431	90	55	750	0	550	90	3521.8
708	26.317309	-45.397696	3511	80	76	650	115	500	22	3585.8
709	26.323946	-45.280000	3035	100	300	1100	6	600	80	3133.6
710	26.263677	-45.311152	2840	140	20	500	5	400	95	2975.3
711	26.257517	-45.321290	2846	100	18	300	173	250	78	2942.8
712	26.237850	-44.938196	2279	90	553	1500	132	800	37	2365.3
713	26.114797	-45.049174	2716	270	196	2450	152	1750	71	2989.7
714	26.098538	-45.224555	2938	110	404	1100	125	700	35	3044.5
715	26.162448	-45.196772	2561	100	197	750	106	800	13	2661.3
716	26.196602	-45.105456	3080	250	0	950	77	650	162	3326.7
717	26.097385	-45.102817	3007	190	189	1200	43	1050	136	3197.4
718	26.017813	-45.222863	3272	200	140	950	88	900	90	3474.3
719	26.031104	-45.258272	3499	110	390	1350	166	850	75	3612.0
720	25.944038	-45.262695	3237	140	259	1200	170	1150	92	3376.0
721	25.974999	-45.233125	3260	90	17	800	40	550	124	3350.1
722	26.180741	-48.599965	4582	90	0	1250	108	700	21	4673.3
723	25.927074	-48.876145	4291	200	42	1300	29	1100	123	4490.3
724	26.025478	-48.876840	4013	100	0	800	27	500	117	4116.0
725	26.075371	-48.853998	3905	120	0	1250	178	650	83	4025.9
726	26.188497	-48.719560	4477	140	0	1400	16	1000	102	4616.8
727	26.154335	-48.722547	4475	100	0	500	35	450	111	4572.9
728	26.046718	-48.850151	3952	70	271	900	176	500	81	4020.0
729	26.135482	-48.827108	4011	80	0	750	114	450	30	4086.5
730	26.134480	-48.765795	4334	90	0	950	8	600	94	4424.4
731	26.014044	-48.734651	5066	70	0	550	0	400	90	5132.0
732	25.957485	-48.756162	4693	90	0	950	45	700	150	4778.4
733	26.044113	-48.614058	4077	110	275	1500	51	1050	146	4187.5
734	26.091000	-48.675773	3958	70	0	650	28	350	128	4027.5
735	26.138653	-48.671160	4009	100	188	1000	45	550	132	4107.9
736	25.959722	-48.822220	4900	90	30	750	36	600	126	4985.0
737	25.914671	-48.524181	4759	90	0	800	67	550	158	4847.9
738	26.085507	-48.512566	3492	70	206	1000	3	850	89	3566.1
739	26.130858	-48.567550	4082	70	315	900	11	500	94	4148.0
740	26.215739	-48.401967	4412	140	0	1800	27	1500	107	4552.1
741	26.203632	-48.377754	4425	140	0	1000	24	650	116	4566.0
742	26.228999	-48.316450	4659	80	43	1200	30	750	120	4733.9
743	26.172692	-48.391782	4388	100	149	1150	12	1050	96	4488.8
744	26.169810	-48.316066	4454	80	248	1450	67	950	161	4531.0

Seamount (#)	LAT (deg)	LON (deg)	Depth (m)	Height (m)	D-top (m)	D1 (m)	Orient1 (deg)	D2 (m)	Orient2 (deg)	Mean D (m)
745	26.135603	-48.394473	4296	90	107	950	21	600	110	4387.3
746	26.101560	-48.375631	4239	80	70	1550	20	1050	112	4319.5
747	26.041961	-48.309610	4043	80	49	800	22	450	103	4121.7
748	26.025506	-48.319443	3886	230	147	2150	9	1250	101	4111.2
749	25.967221	-48.441555	4727	80	21	400	90	300	13	4809.7
750	25.961552	-48.367376	4640	70	0	700	43	500	133	4715.2
751	25.968278	-48.322216	3844	260	185	2350	178	2050	101	4105.4
752	25.913700	-48.373141	4677	100	47	1750	140	1050	50	4775.1
753	25.927630	-48.296424	4072	130	0	1950	60	1000	157	4197.6
754	25.973989	-48.270463	4154	160	0	1200	72	1400	157	4314.4
755	26.071764	-48.177355	3736	80	175	1100	20	600	110	3811.6
756	26.119453	-48.234060	3997	80	0	1000	6	1050	110	4075.9
757	26.131876	-48.237266	3977	90	49	950	92	550	2	4065.1
758	26.194658	-48.274282	4319	150	118	1400	5	1250	86	4466.6
759	26.013286	-48.074095	4054	110	21	650	165	550	79	4160.8
760	26.036141	-48.135108	4040	120	136	1200	70	850	163	4161.4
761	26.039753	-48.087349	4032	140	0	1100	129	850	40	4173.4
762	26.038148	-48.057649	4188	70	92	700	167	400	85	4257.8
763	26.024703	-48.048820	4167	90	158	800	19	500	111	4260.1
764	26.035740	-48.033368	4229	80	0	650	15	450	100	4311.1
765	26.067847	-48.114239	3994	70	0	700	2	450	82	4060.2
766	26.081092	-48.066278	4078	100	30	1250	8	650	97	4179.3
767	26.191910	-47.913938	3755	80	47	700	74	500	162	3838.9
768	26.183262	-47.906059	3818	90	0	550	0	300	90	3905.5
769	26.200942	-47.881653	3718	110	0	650	51	550	137	3831.1
770	26.138101	-48.008872	3957	130	21	1050	177	750	80	4087.6
771	26.083500	-47.992153	4451	120	202	2200	11	1500	112	4567.9
772	26.038549	-48.002789	4096	110	22	550	74	550	148	4207.3
773	26.056409	-47.932955	4463	160	0	1050	44	950	141	4625.7
774	25.999506	-47.973127	4410	70	175	600	168	400	77	4477.6
775	25.983555	-47.946607	4435	80	129	1100	2	600	98	4518.4
776	25.941662	-47.961981	4282	100	21	700	12	500	99	4384.2
777	25.921483	-47.894721	4000	70	0	850	164	550	71	4075.5
778	25.939743	-47.852009	4030	70	259	1050	37	550	139	4095.3
779	25.984129	-47.848295	4054	120	0	1200	24	750	109	4176.6
780	26.014400	-47.876152	4210	100	155	850	0	750	91	4305.1
781	26.014772	-47.839752	4220	120	45	1100	16	650	96	4340.2
782	25.989515	-47.763609	3757	190	136	1050	32	950	118	3943.5
783	26.022496	-47.793999	4019	100	30	900	76	550	162	4119.2
784	26.056209	-47.853799	4214	80	179	1000	27	550	107	4294.6
785	26.070456	-47.839150	4317	80	22	550	173	450	90	4397.2
786	26.080490	-47.821090	4294	70	108	1000	14	850	98	4364.0
787	26.165036	-47.782182	4222	150	314	1300	177	1250	91	4370.8
788	26.230473	-47.831914	3779	90	21	650	90	650	4	3871.9
789	26.215142	-47.776386	4196	80	0	850	73	600	160	4279.3
790	26.231301	-47.640833	3614	70	0	800	29	600	130	3683.4
791	25.980850	-47.751292	3997	100	45	850	31	850	122	4100.0
792	26.043111	-47.748301	3846	110	157	1250	86	900	3	3957.7
793	26.054933	-47.743292	3830	110	270	1200	25	900	121	3936.2
794	26.075571	-47.662742	3901	70	293	800	2	550	94	3975.5
795	26.084788	-47.674164	3868	100	60	1250	73	950	172	3970.8
796	26.109033	-47.678772	3863	80	22	1000	132	750	44	3940.0
797	26.155828	-47.665820	3738	100	46	950	3	600	90	3841.9
798	26.172069	-47.721265	3691	80	218	1150	18	700	129	3776.3
799	26.217806	-47.732465	3568	90	222	1050	17	650	119	3654.0
800	26.202804	-47.582621	4204	80	248	1400	6	850	94	4281.5
801	26.185884	-47.635205	4050	100	0	700	2	450	90	4155.3
802	26.047119	-47.600734	4008	160	0	1000	84	650	0	4165.5
803	26.087393	-47.450546	3604	90	90	1050	18	700	102	3695.5
804	26.040907	-47.347756	3609	120	22	1050	5	550	92	3729.7
805	26.069360	-47.383021	3732	80	60	800	83	650	170	3810.1
806	26.105226	-47.382219	3632	110	351	1700	5	1050	102	3744.6

Seamount (#)	LAT (deg)	LON (deg)	Depth (m)	Height (m)	D-top (m)	D1 (m)	Orient1 (deg)	D2 (m)	Orient2 (deg)	Mean D (m)
807	25.959525	-47.288456	3918	120	293	1300	91	800	0	4033.6
808	25.934306	-47.240799	3934	100	0	1000	120	800	25	4037.4
809	26.024477	-47.286824	3995	100	0	650	6	400	93	4092.0
810	26.055734	-47.332509	3578	110	223	1200	9	900	105	3685.5
811	26.073768	-47.310869	3407	170	0	1850	11	1250	98	3580.1
812	26.084989	-47.303054	3420	90	167	1200	40	800	125	3512.2
813	26.122458	-47.322290	3606	110	180	1250	18	850	99	3713.8
814	26.156575	-47.294731	3571	120	195	1750	39	900	131	3689.7
815	26.175990	-47.309105	3675	110	545	1250	84	800	173	3786.9
816	26.168522	-47.312279	3636	100	0	650	74	400	162	3736.3
817	26.184950	-47.309852	3704	100	213	1200	92	800	179	3799.0
818	26.174683	-47.296411	3649	70	173	750	142	650	45	3720.6
819	26.205501	-47.198255	3799	70	103	1700	9	900	88	3865.1
820	26.131876	-47.066522	4001	70	210	1000	100	850	11	4074.9
821	26.121256	-47.116815	3857	110	559	1250	145	900	39	3963.7
822	26.111638	-47.141861	4139	80	70	1200	156	650	57	4219.4
823	26.106228	-47.124229	3833	120	466	1200	1	1050	96	3957.3
824	26.099616	-47.112207	3937	70	0	800	0	600	92	4004.0
825	26.054733	-47.136451	3869	80	229	950	5	800	90	3952.3
826	26.007971	-47.063617	3780	130	173	1100	151	700	59	3905.9
827	25.970796	-47.152413	3814	110	172	1450	176	850	87	3923.6
828	25.948645	-47.179572	3719	140	331	1450	10	1200	93	3860.3
829	25.979181	-46.994131	4037	70	0	1050	83	650	2	4104.9
830	26.032291	-47.011310	3857	140	112	1100	112	850	22	4001.5
831	26.113842	-47.001693	3814	110	0	1000	5	700	95	3921.9
832	26.112239	-46.969834	3708	210	22	1550	108	950	23	3917.2
833	26.164415	-47.008974	3906	150	21	850	165	700	82	4052.6
834	26.166842	-46.979852	3770	80	0	550	0	400	90	3852.7
835	26.179723	-46.952223	3507	120	21	800	40	650	123	3625.2
836	25.967930	-46.851396	3274	80	194	1200	24	650	103	3352.9
837	25.988480	-46.812579	3412	70	0	650	9	450	92	3481.0
838	26.051655	-46.886759	3336	130	66	400	43	650	44	3462.0
839	26.075916	-46.883264	3231	80	0	800	178	550	94	3311.8
840	26.215646	-46.823428	4050	220	0	2200	4	1400	85	4265.5
841	26.196108	-46.847181	4187	80	0	550	94	350	0	4264.9
842	26.197640	-46.805997	4150	80	29	700	150	450	70	4227.3
843	26.186530	-46.781861	4036	70	0	800	165	550	70	4109.6
844	26.171347	-46.761370	3977	200	0	1500	155	950	58	4176.7
845	26.230729	-46.677198	4275	100	0	950	88	750	175	4372.4
846	26.212472	-46.686615	4294	90	115	1200	44	700	131	4386.0
847	26.213817	-46.642991	4341	100	0	750	81	650	171	4436.5
848	26.135987	-46.753491	3834	100	0	1150	143	650	49	3936.1
849	26.126866	-46.664555	4163	70	0	850	2	450	92	4229.6
850	26.110035	-46.657943	4107	120	20	750	14	600	117	4226.8
851	26.102822	-46.674574	4076	140	20	1250	68	750	150	4219.8
852	26.084588	-46.679583	4076	80	0	650	2	500	90	4152.7
853	26.039304	-46.662952	4016	140	0	1050	73	750	164	4157.1
854	25.968677	-46.772477	3336	70	144	850	40	650	139	3409.0
855	25.928372	-46.619192	3536	80	321	1000	116	750	24	3618.4
856	26.168522	-46.618097	4150	100	0	800	23	550	120	4249.2
857	26.245300	-46.431725	3667	130	0	1600	71	900	152	3796.9
858	26.243403	-46.356983	3699	100	0	850	44	700	137	3801.0
859	26.244195	-46.209993	4236	130	0	1100	58	650	134	4361.7
860	25.934631	-46.478119	3854	70	38	800	14	600	107	3923.8
861	25.924736	-46.461946	3739	100	74	850	128	700	33	3836.5
862	25.928161	-46.445772	3862	200	0	1500	175	850	84	4063.2
863	25.952136	-46.421036	3994	90	0	750	108	700	18	4081.5
864	25.948902	-46.394206	3936	70	38	500	33	500	125	4002.3
865	26.017212	-46.505710	3809	90	127	1050	15	550	106	3897.3
866	26.021843	-46.490740	3892	80	94	850	66	600	162	3970.9
867	26.055973	-46.423714	3776	100	116	1300	7	700	92	3871.9
868	26.220818	-46.421857	3794	80	0	500	74	450	161	3873.0

Seamount (#)	LAT (deg)	LON (deg)	Depth (m)	Height (m)	D-top (m)	D1 (m)	Orient1 (deg)	D2 (m)	Orient2 (deg)	Mean D (m)
869	26.154436	-46.228956	4117	80	160	700	88	600	176	4196.4
870	26.102028	-46.288224	3533	100	0	850	174	800	96	3628.5
871	26.078178	-46.273421	3566	110	31	550	118	450	25	3671.6
872	26.072215	-46.304673	3433	120	23	850	172	500	85	3549.9
873	26.033768	-46.325850	3223	80	0	950	89	1100	165	3300.7
874	26.017525	-46.263758	3009	100	326	1450	1	800	87	3111.3
875	25.963569	-46.329462	3545	110	94	750	173	600	83	3651.8
876	25.970295	-46.269888	2832	160	0	1350	146	700	58	2987.1
877	25.923214	-46.120739	3113	210	0	1250	166	1100	73	3321.5
878	25.976683	-46.131776	3540	90	335	1000	141	650	49	3634.4
879	25.985626	-46.185625	3254	140	0	750	105	500	17	3392.8
880	25.972116	-46.110274	3471	150	21	800	9	600	101	3625.8
881	25.997994	-46.142812	3595	170	0	800	106	650	19	3760.8
882	26.183333	-46.263889	4000	150	580	1500	44	1400	134	4147.5
883	26.168056	-46.275000	3830	190	220	1100	3	1000	93	4020.0
884	25.947760	-46.091799	3368	130	0	1100	0	700	92	3499.9
885	25.973067	-45.981247	4007	110	0	850	170	650	80	4119.5
886	26.010552	-46.095034	3851	160	19	800	168	500	83	4014.1
887	26.019305	-46.075054	3910	160	38	1300	157	900	74	4074.2
888	26.002560	-46.022918	3745	100	0	850	3	550	92	3842.5
889	26.013787	-45.958794	3989	80	186	1050	38	800	130	4069.5
890	26.029655	-46.014405	3870	160	0	1300	3	800	87	4027.4
891	26.102850	-46.084105	4001	150	0	1600	46	1100	141	4152.4
892	26.095449	-46.020984	3812	240	172	1750	38	1450	119	4048.3
893	26.151475	-46.040743	4258	130	0	1600	105	1300	19	4387.8
894	26.166799	-45.991513	4496	90	0	1250	30	700	126	4406.7
895	26.195945	-45.861227	2904	120	132	1600	17	950	105	3022.9
896	26.115392	-45.820319	3708	90	0	850	35	650	127	3617.7
897	26.036440	-45.877477	3933	70	0	1000	121	600	27	4001.2
898	26.010534	-45.872542	3993	70	62	600	178	900	101	4063.5
899	25.928402	-45.926373	3242	100	0	850	28	650	125	3341.4
900	25.979156	-45.784462	3772	100	0	700	51	450	141	3874.4
901	25.925117	-45.794928	3463	70	0	600	4	450	95	3535.1
902	25.985055	-45.756872	3892	140	93	800	33	750	125	4032.5
903	25.981439	-45.760297	3855	110	0	550	28	650	118	3967.4
904	25.999135	-45.752305	3934	190	0	1000	29	750	119	4122.8
905	26.003131	-45.686468	4164	90	0	950	94	800	2	4253.8
906	26.027805	-45.791328	3842	90	0	750	80	550	0	3936.3
907	26.148027	-45.688668	3152	140	150	900	63	650	162	3293.5
908	26.216604	-45.758777	3256	90	0	1000	49	600	146	3341.1
909	26.241269	-45.673476	3534	130	0	1050	64	900	151	3663.4
910	26.239764	-45.571908	2641	140	220	1600	17	950	112	2777.2
911	26.243714	-45.255515	2999	100	0	800	23	800	120	3101.7
912	26.238636	-45.390563	2859	110	21	1200	133	850	43	2970.0
913	25.932306	-45.623559	3240	110	42	1100	38	850	131	3347.4
914	25.923630	-45.541963	3383	190	222	1250	57	1050	154	3569.9
915	25.950582	-45.642758	3680	90	278	950	87	700	178	3770.6
916	25.969597	-45.610821	3456	70	209	850	17	550	117	3528.5
917	25.955013	-45.591068	3497	130	226	850	76	650	160	3624.8
918	25.970889	-45.547501	3429	90	0	550	51	400	137	3523.9
919	25.984920	-45.568915	3535	220	138	1200	128	700	54	3750.5
920	26.019257	-45.660112	4132	100	198	850	173	450	85	4232.3
921	26.109187	-45.640915	2706	130	309	1250	32	850	127	2832.9
922	26.108409	-45.570684	2691	110	73	1000	68	800	150	2796.0
923	26.215093	-45.643336	3022	160	189	1200	44	800	130	3186.7
924	26.161623	-45.617961	2631	100	205	1000	35	550	122	2730.7
925	26.186817	-45.476163	3075	130	108	1150	5	600	95	3204.0
926	26.017361	-45.445210	3287	110	188	850	44	550	121	3397.7
927	25.982182	-45.445224	3450	150	60	850	135	950	53	3599.8
928	25.966094	-45.430582	3453	90	405	1050	37	600	135	3544.7
929	25.941328	-45.455528	3319	80	0	700	82	500	165	3402.9
930	25.971878	-45.496924	3634	110	0	600	44	700	136	3748.9

Seamount (#)	LAT (deg)	LON (deg)	Depth (m)	Height (m)	D-top (m)	D1 (m)	Orient1 (deg)	D2 (m)	Orient2 (deg)	Mean D (m)
931	25.968598	-45.374051	3196	160	150	850	56	800	179	3353.6
932	25.926647	-45.283307	3111	110	362	1550	87	950	2	3219.4
933	25.972919	-45.267103	3210	120	97	1800	62	1050	163	3334.2
934	26.139510	-45.312381	2572	80	0	400	0	350	87	2656.8
935	26.180473	-45.297880	2956	70	162	850	90	500	2	3026.3
936	26.212736	-45.343375	2322	90	198	700	62	450	160	2408.7
937	25.898820	-48.749056	4434	70	182	750	6	450	97	4502.8
938	25.594107	-48.887456	3976	100	0	700	20	600	101	4071.8
939	25.620624	-48.935670	3723	140	21	1500	48	1600	129	3864.6
940	25.718721	-48.950377	4275	100	224	2950	135	2300	42	4370.4
941	25.850283	-48.785458	4317	100	86	1750	24	1100	103	4418.9
942	25.836095	-48.763243	4295	90	187	950	13	550	94	4385.6
943	25.732948	-48.765995	4014	100	0	950	25	650	120	4110.6
944	25.772621	-48.710292	3966	70	49	650	163	550	80	4040.8
945	25.684785	-48.800110	4102	80	21	650	34	450	118	4181.1
946	25.590769	-48.709246	4733	70	19	600	166	500	82	4802.7
947	25.649367	-48.704004	4038	170	0	1800	3	1300	89	4202.9
948	25.697883	-48.603038	4076	100	20	800	35	550	124	4179.3
949	25.844123	-48.709057	4074	120	21	850	66	500	150	4192.4
950	25.862231	-48.681801	4206	90	182	1050	4	800	93	4291.4
951	25.589918	-48.584203	3714	70	106	600	10	350	93	3779.1
952	25.613070	-48.530322	3474	100	0	850	21	450	100	3569.3
953	25.599449	-48.504002	3544	100	0	650	158	500	59	3646.7
954	25.600738	-48.476761	3819	70	0	900	123	650	28	3893.8
955	25.750831	-48.558686	3837	210	163	2050	29	1750	122	4047.7
956	25.743075	-48.544367	3879	130	340	2050	29	1300	106	4009.5
957	25.800353	-48.494646	4228	100	30	850	78	550	159	4324.0
958	25.879330	-48.466456	4263	190	19	800	57	500	152	4452.2
959	25.800580	-48.452559	4402	120	0	800	145	600	50	4527.4
960	25.825241	-48.447334	4376	100	396	2050	32	1200	119	4479.0
961	25.824857	-48.407984	4781	80	19	550	57	500	150	4864.6
962	25.727562	-48.396814	3998	120	0	800	13	650	104	4119.7
963	25.652187	-48.398962	3542	70	43	1050	23	550	104	3613.3
964	25.613412	-48.397234	3452	70	207	1050	15	550	103	3519.4
965	25.615908	-48.389364	3394	90	29	1100	164	600	69	3485.1
966	25.589610	-48.307785	4173	120	150	1450	3*	950	119	4292.3
967	25.595584	-48.293260	4196	70	45	800	79	750	2	4267.1
968	25.587302	-48.290684	4104	210	0	1400	2	1050	102	4312.2
969	25.634973	-48.275775	3558	70	208	950	9	650	85	3623.5
970	25.765747	-48.228957	4542	210	491	2200	45	1800	142	4752.5
971	25.787028	-48.296378	4534	190	0	1500	15	1200	107	4727.7
972	25.786033	-48.245464	4557	170	122	1100	88	700	2	4725.2
973	25.779868	-48.252624	4532	90	91	550	40	400	129	4625.8
974	25.820407	-48.234021	4800	90	331	1200	106	700	33	4889.5
975	25.855242	-48.231612	4818	80	28	600	172	350	87	4896.3
976	25.812500	-48.447222	4410	80	30	750	3	450	93	4492.0
977	25.725000	-48.226389	4350	70	160	800	29	500	119	4415.0
978	25.587486	-48.082345	4434	90	18	850	52	650	130	4521.0
979	25.649698	-48.175663	3977	130	90	1350	150	1000	50	4120.0
980	25.713441	-48.086778	3998	150	0	1600	79	1150	171	4152.6
981	25.850980	-48.145588	3613	90	194	1050	80	850	176	3704.6
982	25.862839	-48.139288	3631	90	90	850	26	650	118	3722.3
983	25.868398	-48.075176	3934	100	19	750	178	650	87	4030.1
984	25.827544	-48.015625	4512	90	176	900	71	550	148	4419.9
985	25.866703	-47.944411	4478	70	0	900	129	600	25	4545.3
986	25.645852	-47.887977	3941	120	154	1800	67	950	159	4065.0
987	25.604007	-47.917345	4129	110	21	650	139	700	45	4239.3
988	25.573129	-47.817675	4535	120	69	1050	60	750	144	4655.9
989	25.618039	-47.843075	4234	110	20	800	72	500	164	4345.7
990	25.771913	-47.751480	3373	110	0	2100	47	1550	135	3486.9
991	25.574821	-47.869006	4141	140	65	1150	35	900	40	4279.1
992	25.591325	-47.669699	4576	80	85	1150	5	850	91	4654.6

Seamount (#)	LAT (deg)	LON (deg)	Depth (m)	Height (m)	D-top (m)	D1 (m)	Orient1 (deg)	D2 (m)	Orient2 (deg)	Mean D (m)
993	25.608015	-47.695104	4478	170	309	2300	42	1600	135	4643.2
994	25.623035	-47.633354	4593	70	0	600	16	400	120	4668.4
995	25.632121	-47.682495	4395	120	0	650	167	750	60	4516.9
996	25.712310	-47.717444	2819	90	349	1350	30	850	105	2906.1
997	25.722529	-47.670757	3279	110	0	850	171	600	84	3386.6
998	25.772020	-47.750705	3372	120	45	2000	77	1400	164	3496.3
999	25.874739	-47.695876	3860	100	56	1100	42	850	129	3958.3
1000	25.753786	-47.526797	3280	100	0	1000	168	750	71	3382.9
1001	25.735753	-47.479309	3653	90	283	1050	43	550	130	3738.4
1002	25.647840	-47.548935	3274	70	0	500	92	450	0	3344.9
1003	25.606334	-47.566973	4488	120	134	800	86	650	170	4612.5
1004	25.623790	-47.495791	4685	70	22	600	90	400	3	4614.5
1005	25.579956	-47.538074	4550	90	89	650	4	550	84	4642.9
1006	25.715716	-47.361581	3521	140	0	950	146	700	65	3660.5
1007	25.741965	-47.391236	3626	70	212	950	71	550	149	3696.7
1008	25.825641	-47.380624	3932	90	56	900	11	600	103	4019.7
1009	25.656784	-47.336669	3434	90	0	600	65	450	167	3520.0
1010	25.661606	-47.276402	3442	90	0	450	158	400	72	3533.8
1011	25.845243	-47.324226	3836	70	0	1900	58	1050	153	3911.1
1012	25.865933	-47.083549	3758	160	0	1100	53	950	139	3918.3
1013	25.690269	-47.140259	3700	90	20	800	11	550	96	3786.3
1014	25.580014	-46.963163	4179	100	21	1000	176	800	81	4282.0
1015	25.659751	-46.973176	3321	160	0	1100	35	650	118	3483.8
1016	25.688123	-47.018979	3239	100	0	950	69	750	159	3343.1
1017	25.734751	-46.994880	3447	140	0	1350	30	700	126	3590.8
1018	25.783241	-46.998086	3693	110	0	950	11	600	82	3805.6
1019	25.883085	-46.934608	3715	100	78	750	102	550	17	3819.5
1020	25.816527	-46.930681	3976	80	0	600	12	400	99	4051.7
1021	25.583537	-46.861224	4227	150	222	1500	1	1850	87	4376.4
1022	25.729341	-46.864420	3448	110	110	700	171	850	69	3562.4
1023	25.722128	-46.869429	3355	160	121	950	5	850	35	3519.2
1024	25.749378	-46.891670	3881	80	22	500	128	550	30	3965.8
1025	25.861484	-46.922894	3835	110	21	1150	5	750	89	3941.0
1026	25.860924	-46.885745	3813	90	19	600	67	350	166	3906.1
1027	25.835094	-46.704280	3577	70	187	1250	157	900	75	3643.9
1028	25.786447	-46.768348	3406	80	212	650	97	550	2	3485.5
1029	25.667430	-46.778759	3491	70	45	500	62	400	155	3556.9
1030	25.656956	-46.691091	2914	110	284	1650	33	1300	135	3024.3
1031	25.646677	-46.678872	3043	80	257	1100	9	900	108	3119.2
1032	25.574913	-46.731822	4286	190	0	1550	71	800	160	4471.3
1033	25.578210	-46.714366	4353	100	107	750	48	550	138	4452.8
1034	25.575301	-46.635232	4416	80	108	700	14	500	101	4492.0
1035	25.722128	-46.580691	3490	110	45	1000	29	650	117	3599.9
1036	25.803679	-46.577886	3136	220	0	1550	179	1050	88	3355.2
1037	25.901807	-46.540437	3274	70	85	1200	171	1250	88	3343.9
1038	25.580675	-46.456212	3987	110	0	800	24	550	99	4098.2
1039	25.590983	-46.453820	3951	140	215	1450	157	1550	61	4094.5
1040	25.596320	-46.420505	4112	90	252	1000	49	750	150	4201.9
1041	25.613438	-46.419032	4147	120	0	950	135	600	48	4263.3
1042	25.844310	-46.398685	3918	90	300	1550	175	850	88	4008.1
1043	25.884333	-46.398500	3941	90	271	1050	123	650	49	4027.2
1044	25.890633	-46.405726	3857	150	0	850	80	500	170	4007.4
1045	25.861328	-46.298039	3071	90	314	1400	28	950	104	3163.6
1046	25.836566	-46.281531	3192	110	175	1050	39	950	106	3304.9
1047	25.762366	-46.255757	2536	100	89	950	19	650	103	2631.9
1048	25.690769	-46.319002	2535	100	0	700	80	600	174	2633.2
1049	25.683808	-46.225328	3628	80	160	1200	164	900	70	3710.5
1050	25.656026	-46.251203	3826	100	0	500	74	400	162	3926.6
1051	25.596905	-46.307061	4292	100	196	1150	140	700	53	4393.0
1052	25.579053	-46.331439	4319	100	0	1200	56	750	144	4415.6
1053	25.655587	-46.122519	3442	140	148	1400	1	800	90	3585.5
1054	25.671785	-46.172952	3254	110	143	1000	127	650	37	3363.4

Seamount (#)	LAT (deg)	LON (deg)	Depth (m)	Height (m)	D-top (m)	D1 (m)	Orient1 (deg)	D2 (m)	Orient2 (deg)	Mean D (m)
1055	25.742478	-46.111368	2918	90	77	800	43	450	133	3007.1
1056	25.768134	-46.129864	2899	100	137	900	173	650	74	3001.0
1057	25.775294	-46.106396	2869	130	140	1100	49	600	131	2995.5
1058	25.785039	-46.169044	2608	170	66	1400	19	850	115	2775.0
1059	25.875233	-45.743883	3135	130	330	1100	61	750	148	3267.0
1060	25.844338	-45.738033	2920	110	454	1150	6	700	91	3028.8
1061	25.830079	-45.685566	3034	190	122	1800	29	1600	118	3221.4
1062	25.822949	-45.707321	3093	90	345	1050	65	700	156	3184.8
1063	25.699014	-45.684652	2103	140	301	1000	178	650	88	2244.1
1064	25.696089	-45.692147	2170	80	517	1450	1	900	95	2252.3
1065	25.698649	-45.792876	2329	100	144	1350	20	700	106	2424.7
1066	25.683719	-45.726333	2201	80	301	900	139	650	145	2277.5
1067	25.603533	-45.681197	3821	100	28	1450	142	850	61	3919.2
1068	25.604270	-45.703491	3755	110	0	1500	101	1050	3	3861.5
1069	25.581792	-45.727259	3573	120	188	800	126	650	27	3691.5
1070	25.572387	-45.774961	3689	160	294	1000	102	700	10	3845.7
1071	25.576124	-45.845776	3845	80	379	1850	53	1050	148	3925.0
1072	25.586418	-45.885850	3790	120	522	1050	49	900	131	3908.6
1073	25.599102	-45.856806	3977	80	28	1200	42	650	126	4057.6
1074	25.607374	-45.896696	3856	80	0	1200	155	950	67	3938.0
1075	25.673736	-45.847430	2574	110	64	750	161	550	73	2680.2
1076	25.773030	-45.815996	2712	100	18	750	177	550	88	2814.4
1077	25.787736	-45.839526	2788	110	83	1250	51	1100	141	2902.5
1078	25.743801	-45.905152	2454	90	18	850	179	700	85	2543.8
1079	25.872739	-45.894674	3083	80	64	900	177	500	88	3160.2
1080	25.849944	-45.829783	3097	90	0	1200	16	650	104	3192.5
1081	25.879540	-45.825923	3217	90	128	1650	158	950	63	3308.7
1082	25.912997	-45.827026	3329	100	101	750	130	600	23	3424.7
1083	25.836893	-45.872431	2879	70	45	600	178	650	72	2953.3
1084	25.857113	-45.938057	3058	90	0	800	155	850	169	3148.5
1085	25.857702	-46.034008	3436	70	298	1100	85	600	159	3506.6
1086	25.811889	-46.090910	2839	100	186	1400	47	1000	125	2939.4
1087	25.803142	-46.071982	2837	70	132	850	22	950	38	2907.2
1088	25.758357	-46.003912	2773	180	300	1400	170	750	63	2952.5
1089	25.692802	-46.094073	2798	130	20	800	23	500	110	2932.4
1090	25.717228	-46.009121	3225	90	0	350	93	400	0	3317.2
1091	25.651846	-46.079166	3584	70	255	800	69	550	159	3655.0
1092	25.591895	-45.598201	3028	140	194	750	41	550	138	3164.8
1093	25.587030	-45.595421	3056	70	355	1050	34	550	128	3129.7
1094	25.593459	-45.586906	3065	80	195	750	43	550	132	3145.7
1095	25.570174	-45.567791	3241	150	210	600	77	600	76	3390.7
1096	25.730331	-45.609857	1956	80	226	650	5	500	98	2039.6
1097	25.805754	-45.659907	2728	150	196	900	164	750	81	2877.5
1098	25.901666	-45.638904	3166	100	250	750	9	1000	107	3265.1
1099	25.809430	-45.570471	2407	110	232	1050	169	600	87	2513.5
1100	25.817831	-45.593223	2600	90	198	700	177	500	80	2693.8
1101	25.829732	-45.590598	2684	90	235	750	129	750	39	2774.6
1102	25.855265	-45.468388	2872	100	228	800	12	600	107	2976.1
1103	25.848619	-45.428853	2501	190	156	1100	15	800	111	2692.8
1104	25.856458	-45.417606	2604	120	0	900	140	900	62	2720.2
1105	25.881167	-45.445042	2958	110	102	800	125	450	39	3067.4
1106	25.804313	-45.476227	2541	100	275	800	34	1000	13	2645.2
1107	25.747344	-45.478704	1938	140	236	1050	178	900	91	2075.2
1108	25.724174	-45.507365	1820	130	287	1400	19	900	108	1948.4
1109	25.753569	-45.407058	1760	160	775	1750	19	1000	121	1920.5
1110	25.833112	-45.374335	2348	120	340	1250	173	950	88	2471.6
1111	25.820161	-45.331051	2278	130	386	1150	178	750	83	2407.6
1112	25.908262	-45.354908	2795	130	381	1300	21	700	105	2927.5
1113	25.572481	-48.953379	4310	90	0	350	0	300	87	4395.7
1114	25.495477	-48.720507	4027	120	28	1150	38	750	127	4145.1
1115	25.475247	-48.766641	4496	70	277	1050	75	750	175	4561.4
1116	25.424400	-49.018060	4870	110	20	1000	33	750	123	4982.5

Seamount (#)	LAT (deg)	LON (deg)	Depth (m)	Height (m)	D-top (m)	D1 (m)	Orient1 (deg)	D2 (m)	Orient2 (deg)	Mean D (m)
1117	25.420800	-49.009722	4650	80	20	650	16	400	106	4730.0
1118	25.537382	-48.411377	4360	90	48	700	158	500	55	4451.4
1119	25.563967	-48.304249	4347	110	0	1150	151	750	53	4451.9
1120	25.472305	-48.202293	4457	70	225	650	152	700	60	4529.1
1121	25.463930	-48.231897	3920	130	22	900	37	700	136	4050.1
1122	25.439001	-48.220211	4452	90	0	800	73	500	168	4539.7
1123	25.445623	-48.186907	4204	130	0	900	8	650	100	4329.2
1124	25.563617	-48.206490	4453	150	173	1050	58	1100	71	4604.5
1125	25.543513	-48.276482	4432	140	198	1600	54	1100	141	4574.9
1126	25.569211	-48.034463	4273	70	0	550	75	450	160	4340.8
1127	25.428873	-48.149988	4225	90	259	700	142	650	55	4319.7
1128	25.451465	-48.144535	4333	80	269	950	5	900	99	4416.6
1129	25.500616	-48.111672	4409	90	203	1100	168	700	88	4496.6
1130	25.545242	-48.127967	4496	110	0	1100	46	650	127	4607.4
1131	25.554130	-48.086119	4496	80	0	850	65	550	153	4580.6
1132	25.529132	-48.037049	4489	70	208	1050	90	700	170	4555.0
1133	25.482469	-48.029642	4316	200	56	1350	25	1150	117	4511.8
1134	25.495437	-47.991574	4428	140	160	1450	39	950	130	4567.2
1135	25.493625	-47.783326	4272	110	187	1250	18	1050	100	4377.5
1136	25.532716	-47.850153	4368	110	223	1050	9	600	84	4474.1
1137	25.534205	-47.831352	4446	80	0	850	177	650	92	4524.7
1138	25.534950	-47.822789	4397	160	0	1050	6	750	84	4555.4
1139	25.519872	-47.804919	4514	130	0	1550	25	1400	117	4640.3
1140	25.499134	-47.745002	4488	90	0	850	47	650	139	4393.4
1141	25.503764	-47.725744	4235	100	21	850	64	650	155	4335.8
1142	25.548575	-47.707413	4511	90	226	1300	125	1000	41	4601.8
1143	25.522095	-47.655010	4318	170	248	1100	45	750	145	4491.3
1144	25.541518	-47.608947	4507	80	248	1050	50	600	139	4588.6
1145	25.541124	-47.594965	4300	110	0	1050	47	1050	138	4415.3
1146	25.551561	-47.582755	4301	130	388	1650	81	900	171	4429.0
1147	25.529505	-47.543370	4378	110	0	750	165	550	68	4489.9
1148	25.564952	-47.497683	4479	110	0	850	105	550	7	4592.0
1149	25.466883	-47.552232	4139	90	0	1250	165	800	64	4229.3
1150	25.455361	-47.338210	3987	100	0	1050	28	700	116	4083.2
1151	25.490646	-47.412045	4498	140	173	850	53	750	125	4633.6
1152	25.521920	-47.331070	4544	130	104	1150	27	750	123	4674.3
1153	25.565478	-47.455045	4475	210	91	1550	48	1150	143	4681.2
1154	25.462956	-47.296617	4025	100	283	850	56	700	136	4125.8
1155	25.478581	-47.219456	4048	130	125	1050	31	900	122	4180.8
1156	25.538020	-47.278525	4509	120	345	1150	42	900	138	4629.8
1157	25.534687	-47.262600	4445	70	132	650	68	500	147	4516.8
1158	25.534822	-47.068231	3967	130	254	1300	26	800	113	4098.3
1159	25.465878	-46.910225	3901	150	218	1250	115	1000	16	4048.4
1160	25.503491	-46.975850	3930	70	215	1200	157	800	68	3999.9
1161	25.526201	-46.931546	4037	100	41	850	3	750	93	4137.6
1162	25.430821	-46.878175	3938	120	0	1250	125	900	37	4054.6
1163	25.439585	-46.861231	4257	110	29	600	162	450	75	4368.4
1164	25.482839	-46.853895	4307	100	132	1050	58	650	145	4407.9
1165	25.513763	-46.820195	4373	100	314	1000	30	750	119	4474.5
1166	25.572632	-46.743346	4368	120	0	1300	42	900	137	4485.3
1167	25.533641	-46.680724	4149	110	20	500	2	450	93	4260.2
1168	25.557666	-46.646655	4475	100	179	1000	77	550	178	4571.6
1169	25.471967	-46.752996	4062	120	0	500	177	400	85	4177.6
1170	25.276677	-46.550638	3498	170	408	1400	172	1450	95	3664.5
1171	25.526573	-46.620816	3990	140	211	1450	114	1250	25	4128.2
1172	25.558777	-46.593080	4380	90	60	650	155	400	55	4468.5
1173	25.558300	-46.606900	4490	70	300	850	56	600	148	4558.0
1174	25.559125	-46.302798	4011	150	183	1050	35	1250	131	4159.3
1175	25.565338	-46.273615	4195	70	477	1150	51	600	136	4265.1
1176	25.544251	-46.309953	3996	100	92	1150	55	1200	143	4098.1
1177	25.509419	-46.347043	3804	160	0	1300	34	850	132	3967.4
1178	25.494922	-46.301480	3539	70	0	550	34	650	111	3611.2

Seamount (#)	LAT (deg)	LON (deg)	Depth (m)	Height (m)	D-top (m)	D1 (m)	Orient1 (deg)	D2 (m)	Orient2 (deg)	Mean D (m)
1179	25.484943	-46.303928	3515	100	0	1350	16	700	112	3611.5
1180	25.554319	-46.410237	4246	120	0	800	52	650	139	4361.6
1181	25.308037	-46.332734	3050	80	0	900	59	550	152	3127.5
1182	25.299753	-46.292255	3424	140	0	1000	46	750	130	3568.5
1183	25.357545	-46.150742	3225	100	335	1000	58	600	143	3328.4
1184	25.526914	-46.129919	3986	70	0	700	117	550	17	4060.3
1185	25.565712	-46.083824	3890	70	0	750	20	550	111	3957.8
1186	25.370359	-46.040066	3071	120	171	1150	28	650	123	3187.0
1187	25.500146	-46.024582	3828	70	133	450	126	450	38	3902.9
1188	25.497667	-45.947394	3329	140	0	1000	124	800	30	3469.8
1189	25.539355	-45.910287	3567	120	376	1100	21	850	114	3687.3
1190	25.532577	-45.928738	3529	130	588	1350	33	1000	117	3662.9
1191	25.533331	-45.895789	3562	130	0	1000	19	850	117	3691.0
1192	25.527117	-45.898237	3535	120	172	700	30	700	119	3652.0
1193	25.514315	-45.901061	3497	110	303	900	20	850	119	3607.4
1194	25.466680	-45.917441	3351	130	73	950	10	550	96	3477.1
1195	25.471011	-45.860581	3173	150	839	1950	42	1100	118	3327.3
1196	25.471011	-45.839494	3143	140	141	900	32	800	120	3282.2
1197	25.452389	-45.927232	3314	100	66	850	39	700	133	3416.7
1198	25.453519	-45.902002	3280	100	365	1000	60	750	140	3384.2
1199	25.460108	-45.884493	3249	160	477	1550	19	1150	118	3413.3
1200	25.282440	-45.712589	2235	70	81	1100	164	800	74	2305.7
1201	25.315721	-45.714546	2333	100	178	900	142	850	56	2432.2
1202	25.439586	-45.889953	3237	120	431	1350	18	900	106	3357.9
1203	25.446364	-45.866041	3207	100	480	800	21	650	98	3308.5
1204	25.546313	-45.794635	3533	120	0	750	134	850	38	3653.3
1205	25.520685	-45.756192	3369	110	113	800	69	700	141	3482.9
1206	25.509651	-45.751031	3204	260	62	1700	102	1650	16	3466.4
1207	25.555665	-45.628748	3070	100	92	500	59	550	139	3167.1
1208	25.559782	-45.593578	2994	150	504	1950	42	1300	128	3147.7
1209	27.054519	-44.611435	2660	100	116	950	84	1000	175	2758.2
1210	26.997144	-44.574620	2567	210	361	2300	15	1250	104	2781.4
1211	26.923716	-44.629409	2721	120	296	1000	31	950	107	2843.1
1212	26.922586	-44.562759	3241	80	184	1150	39	900	132	3323.8
1213	26.988763	-44.532966	3221	110	175	1350	42	1200	134	3330.4
1214	27.069110	-44.536465	2539	150	302	1400	49	1200	142	2684.5
1215	27.118914	-44.478296	3263	120	274	1750	11	1450	110	3386.5
1216	27.140235	-44.479490	3258	140	342	2700	80	2050	175	3394.6
1217	27.150566	-44.509034	2860	120	328	2150	21	1250	111	2979.8
1218	26.572701	-44.775357	2451	300	965	2400	103	1700	44	2753.0
1219	26.587645	-44.820368	2927	90	611	1550	37	1100	121	3016.1
1220	26.588005	-44.748890	2727	80	454	1350	120	1150	38	2808.5
1221	26.597907	-44.745469	2712	100	180	1050	86	850	8	2809.3
1222	26.635537	-44.758432	2839	90	357	1650	26	950	117	2933.1
1223	26.652281	-44.732146	2708	80	429	1400	166	1000	73	2783.5
1224	26.679288	-44.724584	2664	170	80	1500	106	1650	17	2837.9
1225	26.643999	-44.826670	3002	110	122	700	13	650	98	3109.0
1226	26.657142	-44.816587	2995	70	132	900	21	700	106	3063.4
1227	26.678928	-44.799303	2879	80	175	950	136	750	46	2956.4
1228	26.707594	-44.796492	2767	100	230	1700	15	1000	107	2871.4
1229	26.742029	-44.765754	2686	80	246	950	120	1200	34	2766.1
1230	26.717321	-44.698246	2732	100	155	1800	29	1150	120	2834.5
1231	26.770822	-44.738906	2804	80	153	1150	119	1200	36	2888.8
1232	26.777631	-44.806998	2519	80	266	1050	94	1000	13	2597.2
1233	26.803505	-44.802718	2496	110	156	1600	7	950	94	2608.9
1234	26.802338	-44.787154	2530	70	217	1400	2	850	74	2602.1
1235	26.816397	-44.782452	2509	110	265	1550	31	850	125	2617.3
1236	26.858992	-44.836285	2689	100	185	850	15	900	112	2792.5
1237	26.852648	-44.771033	2435	150	437	2050	11	1050	104	2581.9
1238	26.909535	-44.633739	2656	110	335	1500	54	1200	139	2762.0
1239	26.909911	-44.585540	2723	120	241	1200	121	1050	26	2842.3
1240	26.889201	-44.629786	2660	120	553	2200	8	1150	96	2784.8

Seamount (#)	LAT (deg)	LON (deg)	Depth (m)	Height (m)	D-top (m)	D1 (m)	Orient1 (deg)	D2 (m)	Orient2 (deg)	Mean D (m)
1241	26.883929	-44.593636	2762	80	348	950	16	550	105	2843.9
1242	26.853240	-44.615665	2636	130	475	1500	44	1150	132	2770.0
1243	26.850039	-44.597778	2805	130	119	1750	4	1000	83	2931.0
1244	26.837801	-44.637317	2607	110	140	1850	10	1250	107	2717.7
1245	26.816526	-44.608887	2678	180	302	1600	24	1550	116	2857.3
1246	26.782105	-44.690616	2668	160	369	1950	28	1500	103	2823.8
1247	26.797085	-44.606377	2670	130	173	1250	5	650	102	2797.0
1248	26.785607	-44.609101	2656	110	190	850	37	500	126	2768.0
1249	26.723936	-44.676219	2624	70	230	1000	91	800	12	2693.6
1250	26.725492	-44.664936	2545	80	183	950	24	800	124	2626.9
1251	26.704870	-44.673885	2546	80	522	1400	88	1150	5	2624.2
1252	26.664884	-44.688716	2452	150	0	1100	38	950	123	2606.4
1253	26.905212	-44.547460	3041	200	265	2250	83	1900	173	3236.5
1254	26.338324	-44.866571	2247	110	317	1850	108	1750	25	2352.5
1255	26.342947	-44.757764	3365	160	267	2050	151	1700	65	3521.9
1256	26.367956	-44.727955	3625	90	334	1600	12	900	113	3712.8
1257	26.432469	-44.716679	3241	100	77	1600	28	1400	111	3337.6
1258	26.458349	-44.701336	3199	110	72	1200	159	1300	68	3308.0
1259	26.501916	-44.743424	2802	70	99	1000	26	700	124	2871.6
1260	26.538740	-44.701820	3510	70	290	1100	2	1100	78	3576.4
1261	26.506783	-44.680809	3250	110	177	1600	11	1250	100	3357.7
1262	25.908282	-45.219123	3079	240	75	2700	149	2650	60	3320.2
1263	25.943931	-45.176812	3379	70	147	1400	62	950	147	3444.5
1264	25.936549	-45.143503	3231	70	349	1850	53	1000	145	3304.6
1265	25.954734	-45.167629	3361	100	231	950	130	1050	46	3459.8
1266	25.970218	-45.155926	3347	90	63	1000	39	950	136	3438.9
1267	25.996505	-45.182753	3488	80	207	950	75	750	166	3565.0
1268	26.052963	-45.137312	3336	70	263	1250	175	850	91	3410.3
1269	25.996202	-45.117754	2999	100	238	900	11	1000	104	3095.2
1270	26.052963	-45.104390	3039	100	204	1050	51	950	141	3141.7
1271	26.118525	-44.925338	3017	100	218	1750	37	950	125	3114.5
1272	26.101600	-44.975990	2987	200	159	1550	64	1850	160	3191.2
1273	26.145310	-44.910546	3206	130	362	1100	111	1200	31	3336.0
1274	26.182467	-44.896590	3142	70	108	1100	33	750	122	3211.7
1275	26.201680	-44.912721	2936	90	124	1150	51	700	147	3024.0
1276	26.207480	-44.856714	3358	110	97	1200	19	800	109	3470.4
1277	26.219805	-44.856351	3398	70	93	700	44	500	141	3467.7
1278	26.228868	-44.852545	3376	100	151	1350	40	750	140	3474.3
1279	26.233762	-44.917434	2315	110	170	1200	18	850	111	2426.9
1280	25.677346	-45.216851	3436	240	623	2650	11	1900	104	3675.7
1281	25.679210	-45.239230	3626	70	163	550	49	600	143	3691.3
1282	25.843075	-45.244399	2577	80	164	950	175	800	94	2657.9
1283	25.842702	-45.257673	2522	100	244	1350	62	1300	162	2625.3
1284	25.852984	-45.161575	3137	110	271	1650	21	1200	118	3242.0
1285	25.738650	-45.397503	1829	110	271	1450	15	1050	113	1943.3
1286	25.685673	-45.448474	2522	70	140	1100	166	850	72	2594.7
1287	25.606134	-45.393187	3416	90	318	1000	57	900	155	3509.3
1288	25.593400	-45.388826	3402	80	416	1500	44	900	147	3486.3
1289	25.591543	-45.374526	3384	120	209	1150	110	950	23	3506.0
1290	25.595257	-45.324197	3550	100	236	1750	75	1550	169	3650.2
1291	25.630914	-45.332183	3610	90	227	1150	45	950	129	3704.1
1292	25.643729	-45.267740	3639	110	299	1350	27	800	123	3749.3
1293	25.660072	-45.261797	3675	70	298	1400	88	1200	14	3742.4
1294	25.716376	-45.285481	2522	120	136	900	18	700	105	2645.4
1295	25.775172	-45.305348	2415	80	343	1400	17	750	119	2493.5
1296	25.784604	-45.288692	2253	110	249	1650	178	900	84	2358.4
1297	25.803668	-45.295113	2143	150	189	1700	31	900	115	2292.1
1298	25.807740	-45.279872	2320	80	96	1350	60	850	162	2400.8
1299	25.818397	-45.261736	2420	70	168	750	9	450	95	2489.0
1300	25.283435	-45.559429	2574	170	212	2050	113	1650	30	2742.0
1301	25.402958	-45.568810	2734	80	259	1400	33	750	120	2817.7
1302	25.421490	-45.565607	2799	70	188	1150	42	850	114	2873.0

Seamount (#)	LAT (deg)	LON (deg)	Depth (m)	Height (m)	D-top (m)	D1 (m)	Orien.1 (deg)	D2 (m)	Orient2 (deg)	Mean D (m)
1303	25.545522	-45.427531	3192	130	203	1400	89	1650	171	3325.2
1304	25.529421	-45.396305	3239	80	399	1450	17	1250	112	3322.5
1305	25.513564	-45.469247	3014	120	219	1550	37	800	126	3135.1
1306	25.498195	-45.401916	3172	160	219	2000	20	1850	108	3335.6
1307	25.480874	-45.488276	2851	110	263	1400	24	850	107	2956.6
1308	25.473556	-45.419968	3331	90	154	1100	40	900	135	3419.6
1309	25.456129	-45.423628	3349	110	596	2200	117	2150	33	3456.7
1310	25.412217	-45.473150	3018	130	170	1550	18	1050	111	3144.8
1311	25.399531	-45.502913	2601	431	860	3550	37	2700	111	3032.0
1312	25.376600	-45.441436	3498	210	449	2600	114	2300	33	3706.7
1313	25.358059	-45.516818	3013	80	203	950	24	750	109	3092.2
1314	25.340072	-45.446803	3517	170	271	1600	37	1300	126	3682.5
1315	25.291525	-45.477542	3266	100	136	1350	20	800	103	3365.3

Depth=water depth to summit; D-top=diameter of seamount top; D1=diameter of seamount base along long-axis; Orient1=trend of D1; D2=diameter of seamount base along short-axis; Orient2=trend of D2; Mean D=mean water depth of seamount base.

DOCUMENT LIBRARY

Distribution List for Technical Report Exchange – February 1996

University of California, San Diego
SIO Library 0175C
9500 Gilman Drive
La Jolla, CA 92093-0175

Hancock Library of Biology & Oceanography
Alan Hancock Laboratory
University of Southern California
University Park
Los Angeles, CA 90089-0371

Gifts & Exchanges
Library
Bedford Institute of Oceanography
P.O. Box 1006
Dartmouth, NS, B2Y 4A2, CANADA

Commander
International Ice Patrol
1082 Shennecossett Road
Groton, CT 06340-6095

NOAA/EDIS Miami Library Center
4301 Rickenbacker Causeway
Miami, FL 33149

Research Library
U.S. Army Corps of Engineers
Waterways Experiment Station
3909 Halls Ferry Road
Vicksburg, MS 39180-6199

Institute of Geophysics
University of Hawaii
Library Room 252
2525 Correa Road
Honolulu, HI 96822

Marine Resources Information Center
Building E38-320
MIT
Cambridge, MA 02139

Library
Lamont-Doherty Geological Observatory
Columbia University
Palisades, NY 10964

Library
Serials Department
Oregon State University
Corvallis, OR 97331

Pell Marine Science Library
University of Rhode Island
Narragansett Bay Campus
Narragansett, RI 02882

Working Collection
Texas A&M University
Dept. of Oceanography
College Station, TX 77843

Fisheries-Oceanography Library
151 Oceanography Teaching Bldg.
University of Washington
Seattle, WA 98195

Library
R.S.M.A.S.
University of Miami
4600 Rickenbacker Causeway
Miami, FL 33149

Maury Oceanographic Library
Naval Oceanographic Office
Building 1003 South
1002 Balch Blvd.
Stennis Space Center, MS, 39522-5001

Library
Institute of Ocean Sciences
P.O. Box 6000
Sidney, B.C. V8L 4B2
CANADA

National Oceanographic Library
Southampton Oceanography Centre
European Way
Southampton SO14 3ZH
UK

The Librarian
CSIRO Marine Laboratories
G.P.O. Box 1538
Hobart, Tasmania
AUSTRALIA 7001

Library
Proudman Oceanographic Laboratory
Bidston Observatory
Birkenhead
Merseyside L43 7 RA
UNITED KINGDOM

IFREMER
Centre de Brest
Service Documentation - Publications
BP 70 29280 PLOUZANE
FRANCE

REPORT DOCUMENTATION PAGE	1. REPORT NO. MIT/WHOI 97-09	2.	3. Recipient's Accession No.
4. Title and Subtitle The Geological Record of Oceanic Crustal Accretion and Tectonism at Slow-Spreading Ridges			5. Report Date December 1996
7. Author(s) Gary Edward Jaroslow			6.
9. Performing Organization Name and Address MIT/WHOI Joint Program in Oceanography/Applied Ocean Science & Engineering			8. Performing Organization Rept. No.
12. Sponsoring Organization Name and Address Office of Naval Research			10. Project/Task/Work Unit No. MIT/WHOI 97-09
			11. Contract(C) or Grant(G) No. (C) N00014-93-1-1153 (G) N00014-90-J-1621
15. Supplementary Notes This thesis should be cited as: Gary Edward Jaroslow, 1996. The Geological Record of Oceanic Crustal Accretion and Tectonism at Slow-Spreading Ridges. Ph.D. Thesis. MIT/WHOI, 97-09.			13. Type of Report & Period Covered Ph.D. Thesis
			14.
16. Abstract (Limit: 200 words) The objective of this Thesis was to interpret the structural development of slow-spreading ridge segments by: 1) delineating the nature, magnitude, and relative importance of primary tectonic and volcanic processes that control crustal morphology, 2) investigating the spatial and temporal variability of these processes, and 3) examining how rheological variations in the lithosphere control its structural configuration. To that end, this Thesis provides detailed documentation of faults and volcanoes (seamounts) at the Mid-Atlantic Ridge from 25°25'N to 27°10'N and extending from zero-age crust at the ridge axis to ~29 Ma crust on the ridge flank. This information was used to analyze the evolution of ocean crust from initial formation in the rift valley to degradation by aging processes on the ridge flank. Accumulation of sediments affects the seafloor morphological expression of ocean crustal structure, and sediment thicknesses were also mapped to facilitate study of the morphological record of crustal accretion and tectonism. In addition, deformation conditions in the lithosphere were analyzed by study of microstructure and geothermometry of abyssal peridotite mylonites recovered from fault zones at slow-spreading ridges.			
17. Document Analysis			
a. Descriptors mid-Atlantic Ridge mid-ocean ridges tectonics			
b. Identifiers/Open-Ended Terms			
c. COSATI Field/Group			
18. Availability Statement Approved for publication; distribution unlimited.	19. Security Class (This Report) UNCLASSIFIED	21. No. of Pages 214	
	20. Security Class (This Page)	22. Price	

49°00'

48°45'

27°
15'

SEDIMENT T
Western Mid-Atlantic Ridge

Gary E. Jaroslow and

Contours in
C. I. = 50 m (Thickness)

Universal Transverse M
Scale 1:2

Map 1

27°
00'



①

48°30'

SEDIMENT THICKNESS
Mid-Atlantic Ridge Flank, 25°20'N to 27°15'N

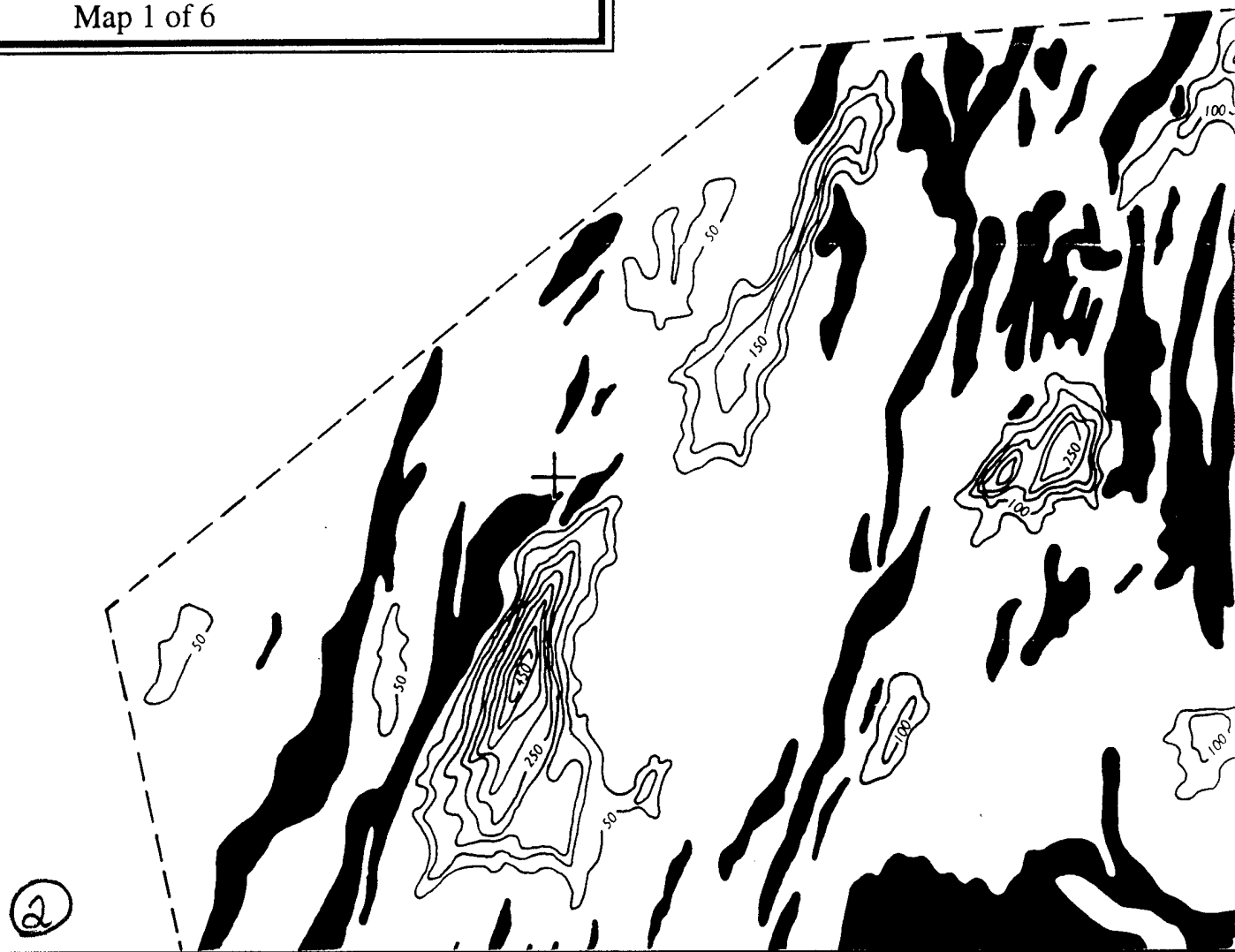
Gary E. Jaroslow and Brian E. Tucholke

Contours in meters

C. I. = 50 m (Thicknesses <10 m are Black)

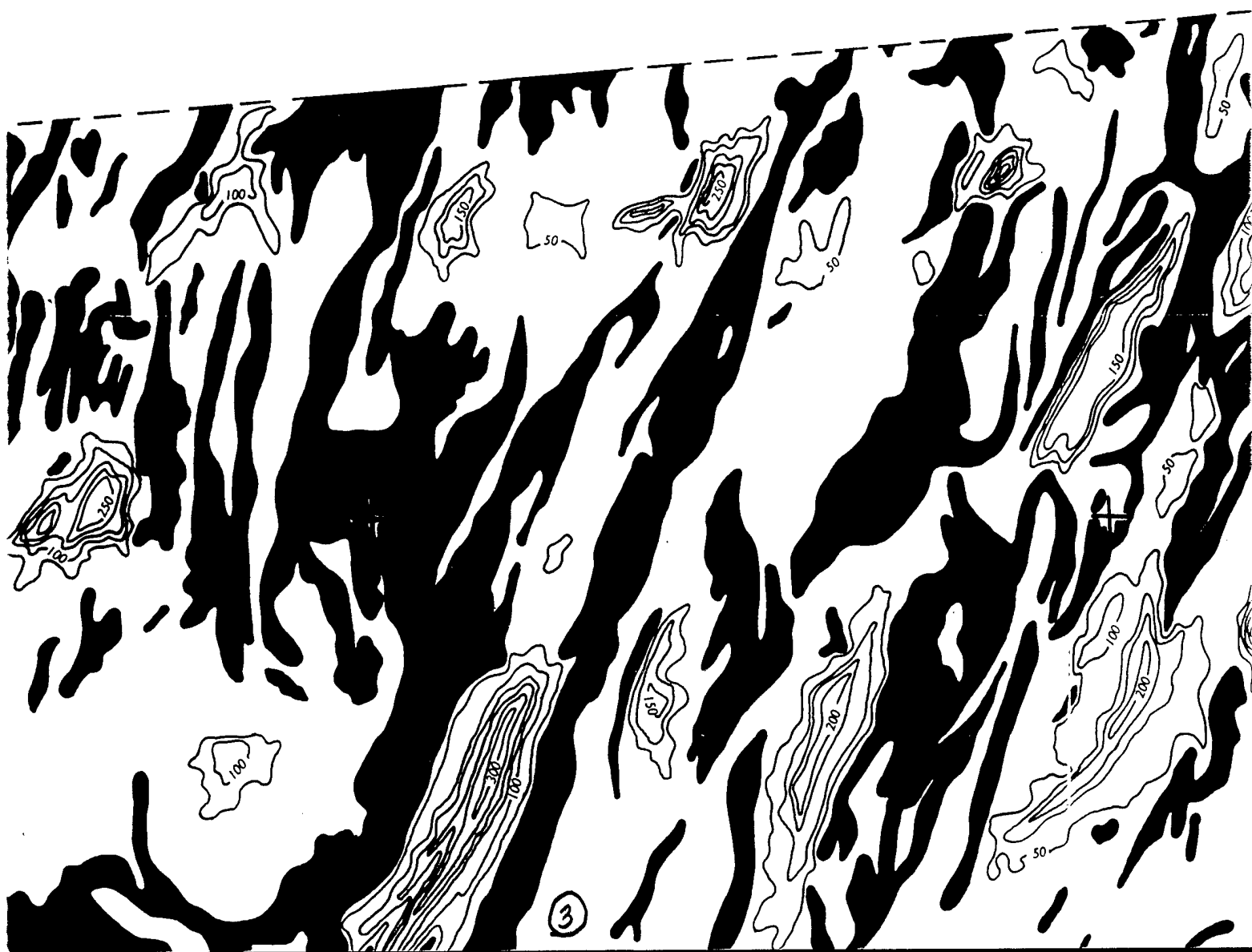
Universal Transverse Mercator Projection
Scale 1:200,000

Map 1 of 6



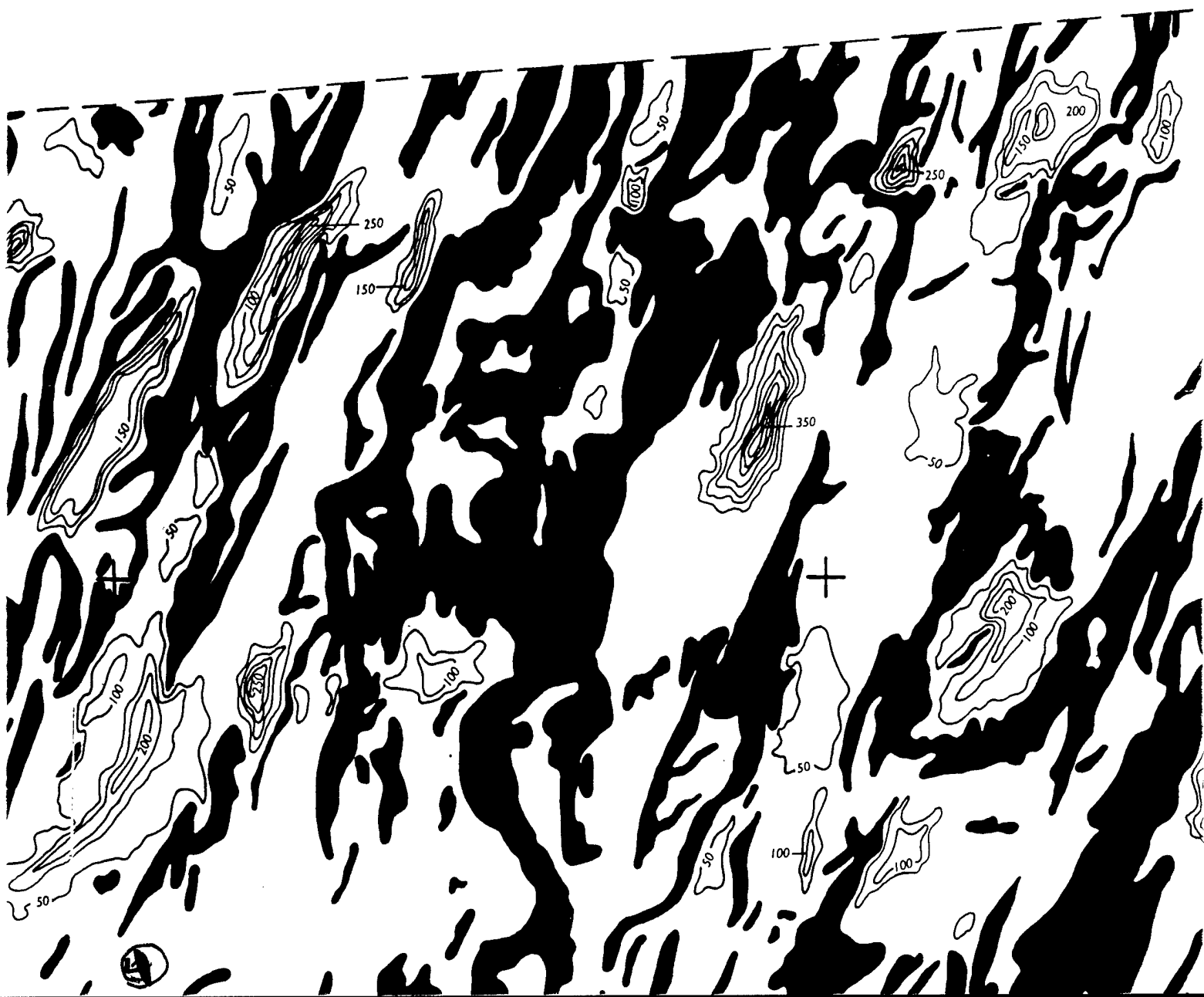
48°15'

48°00'



43°00'

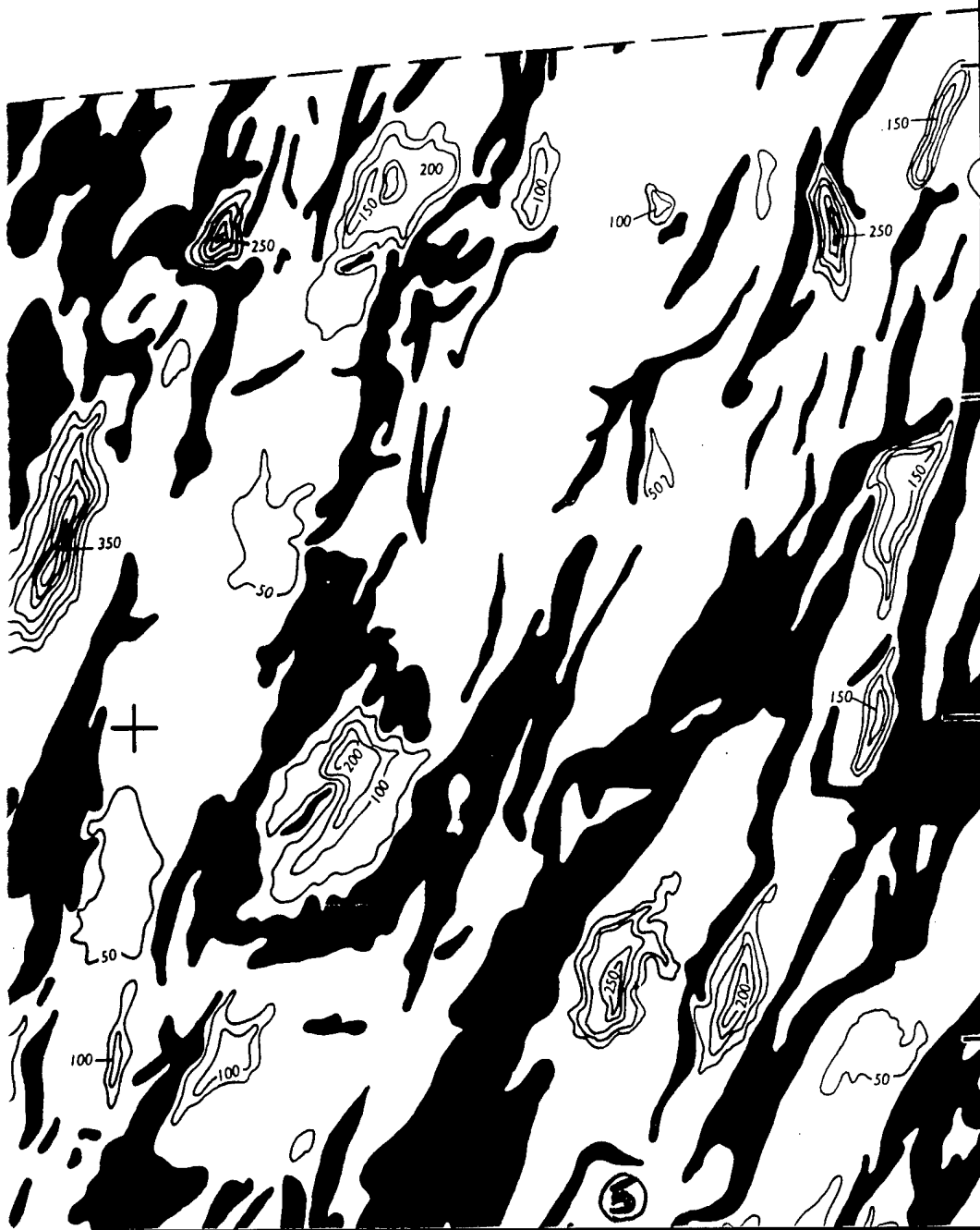
47°45'



47°45'

47°30'

27°
15'



27°
00'

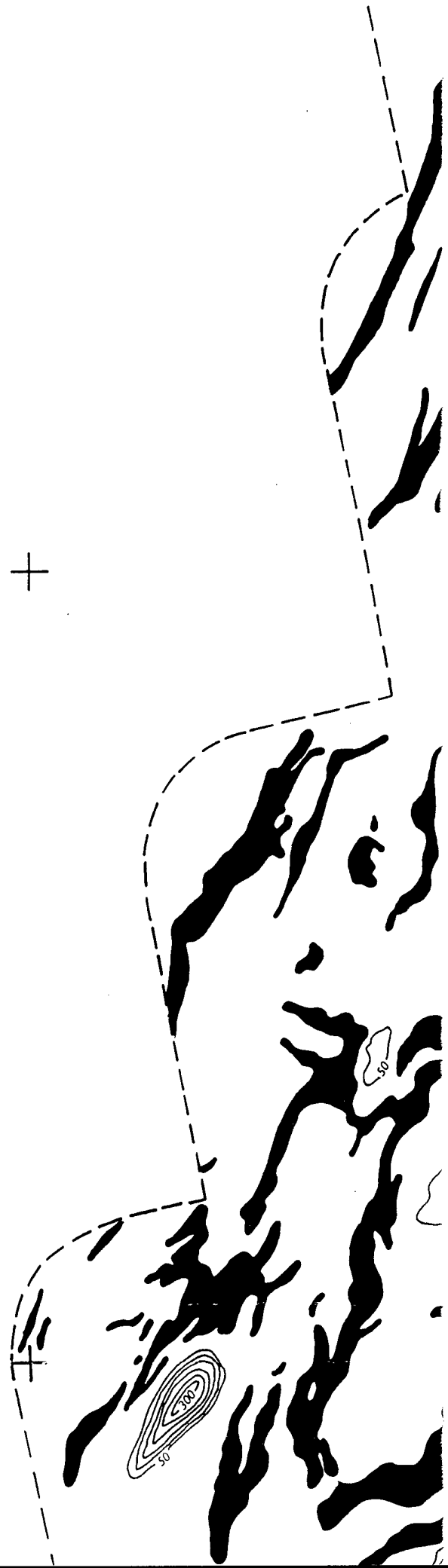
⑤

26°
45'

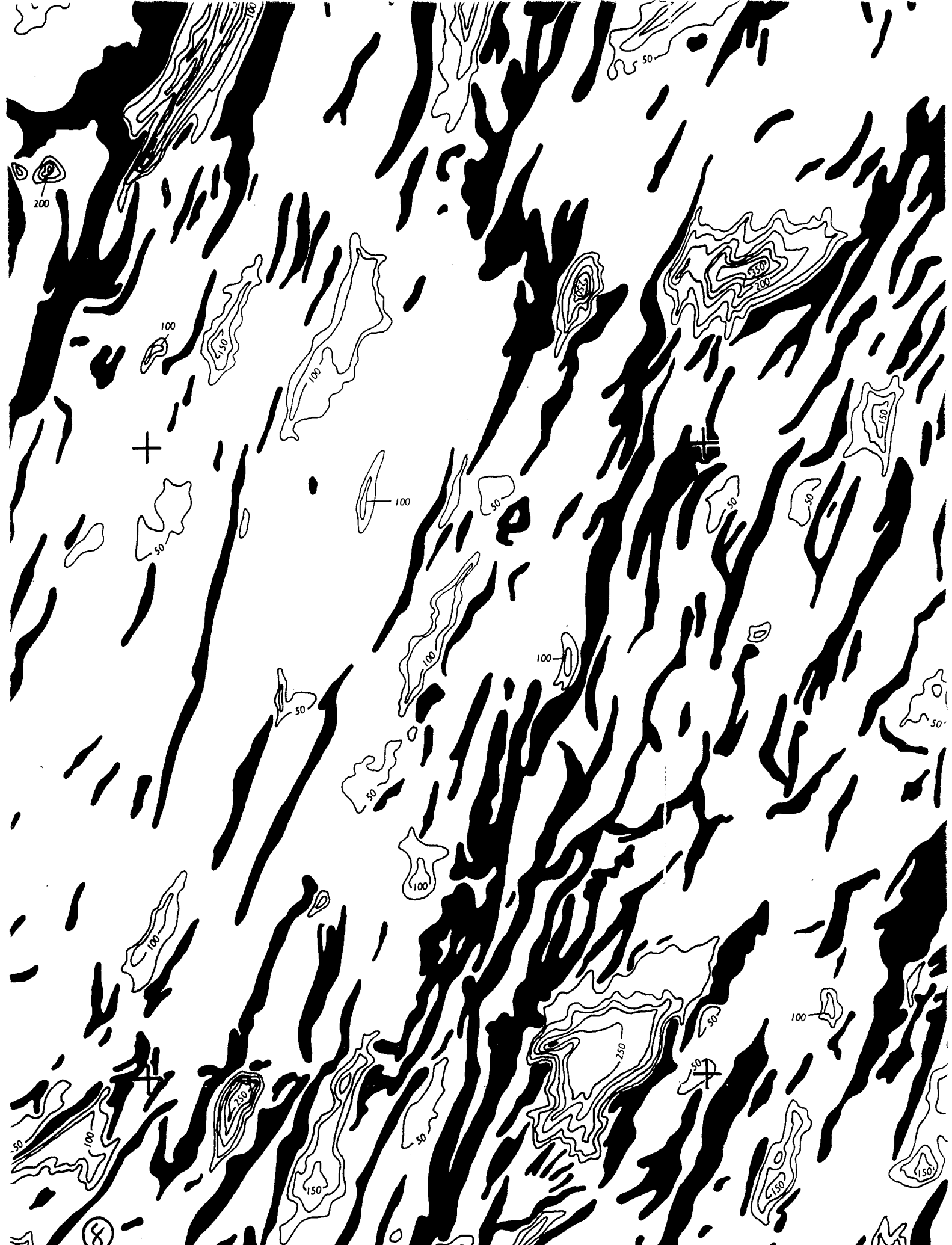
26°
30'



(6)











26°
45'

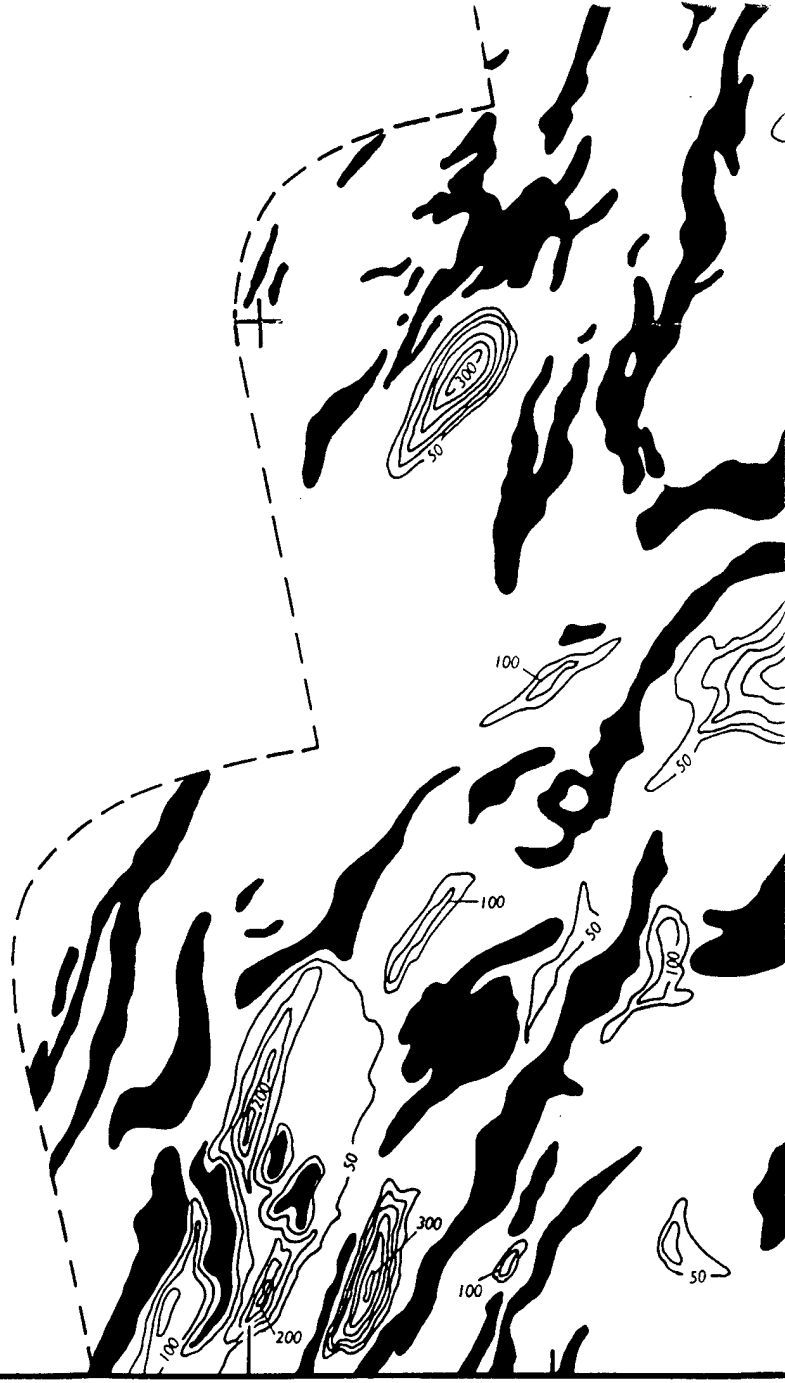
26°
30'

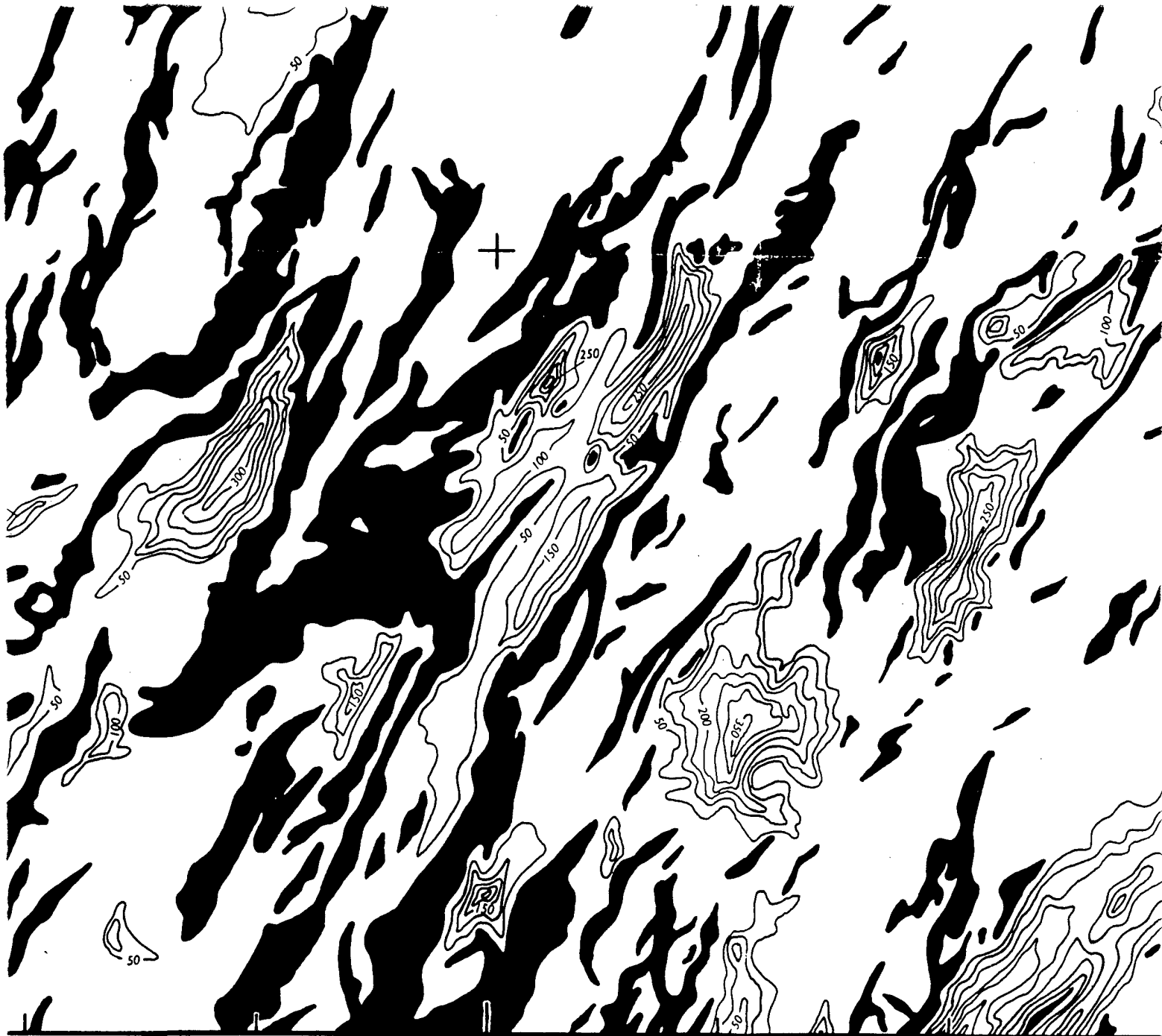
26°
30'

26°
15'

49°00'

48°45'

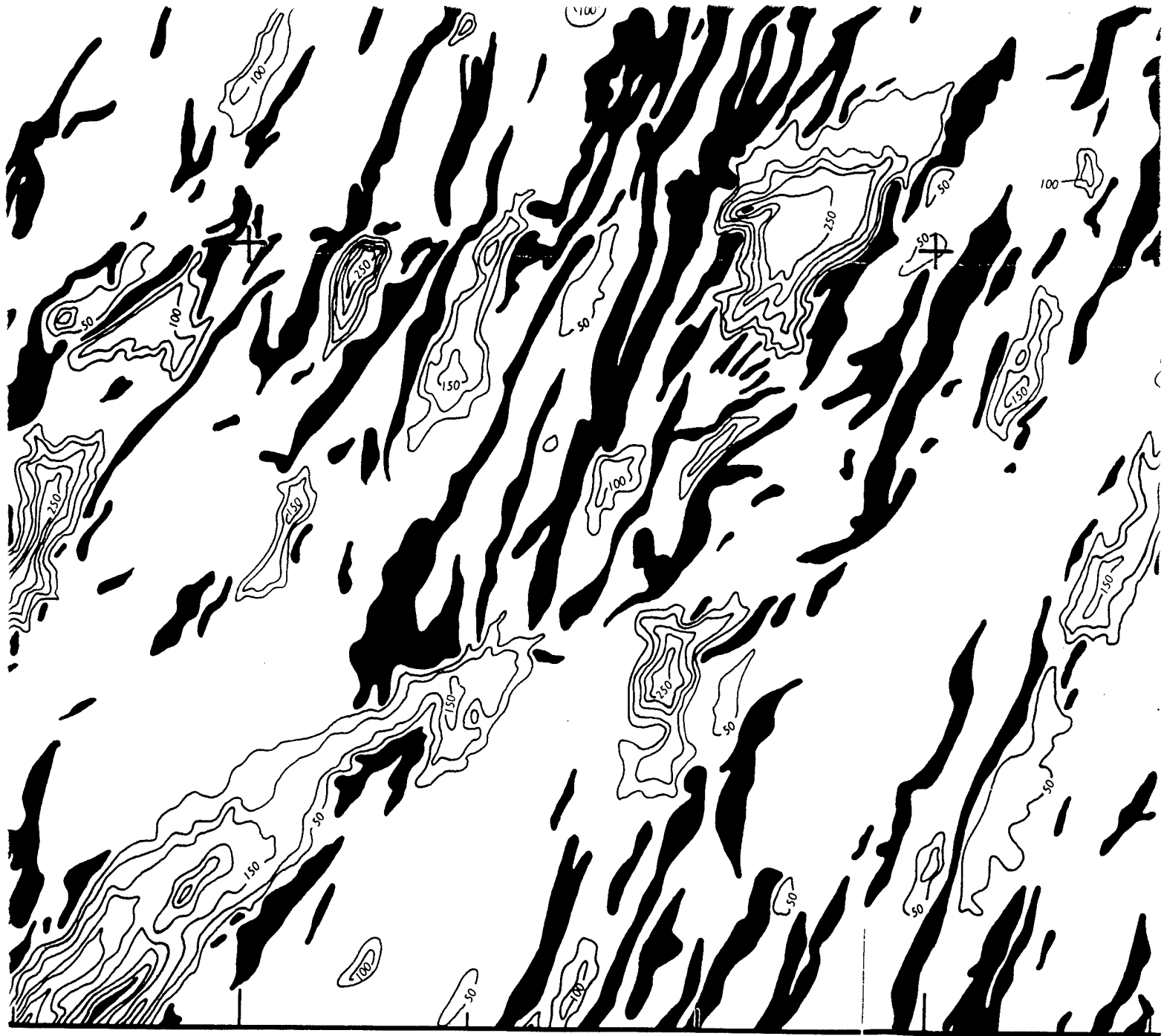




48°30'

48

12a



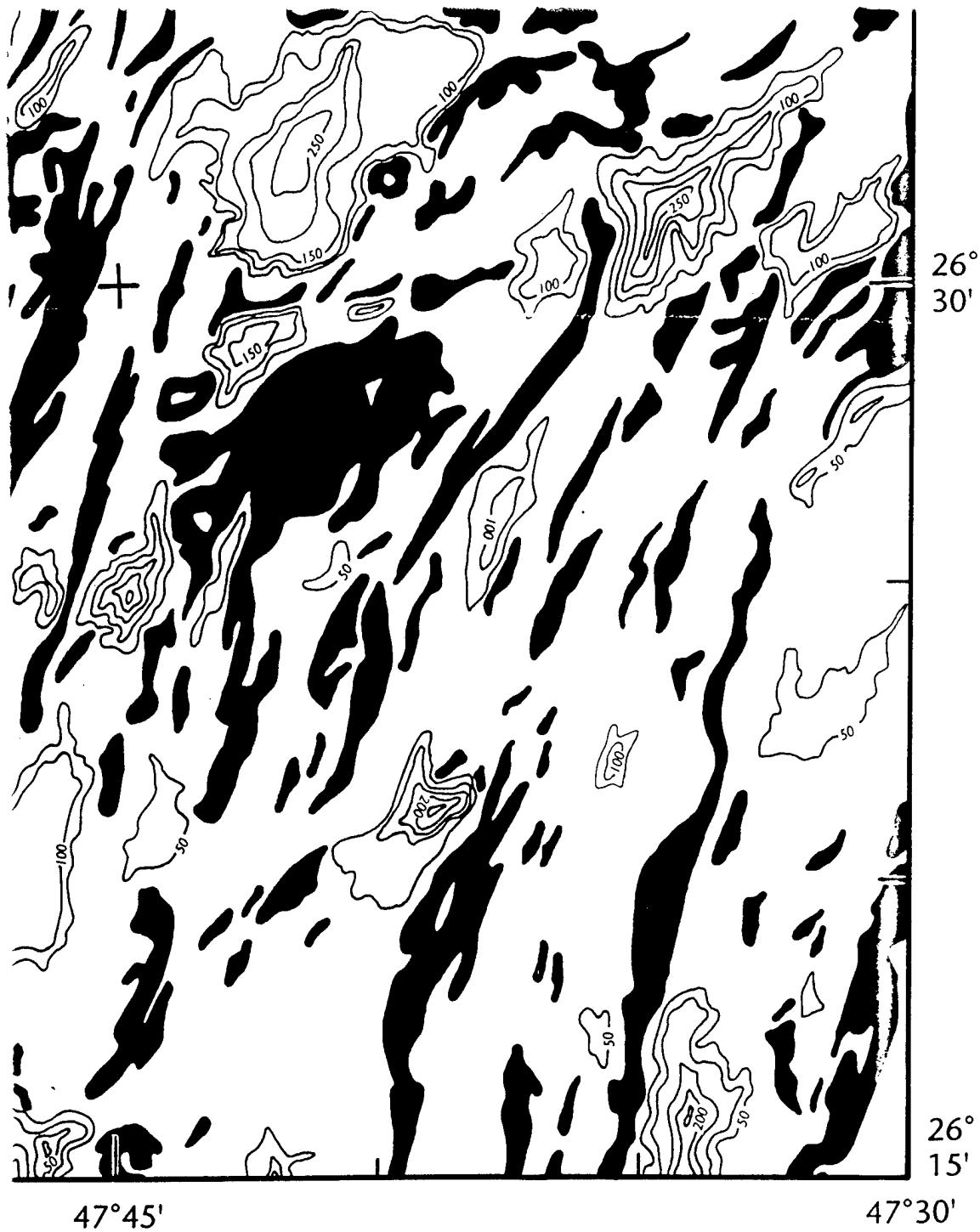
48°15'

48°00'



00'

47°45'



15

47°30'

27°
15'

27°
00'



47°00'

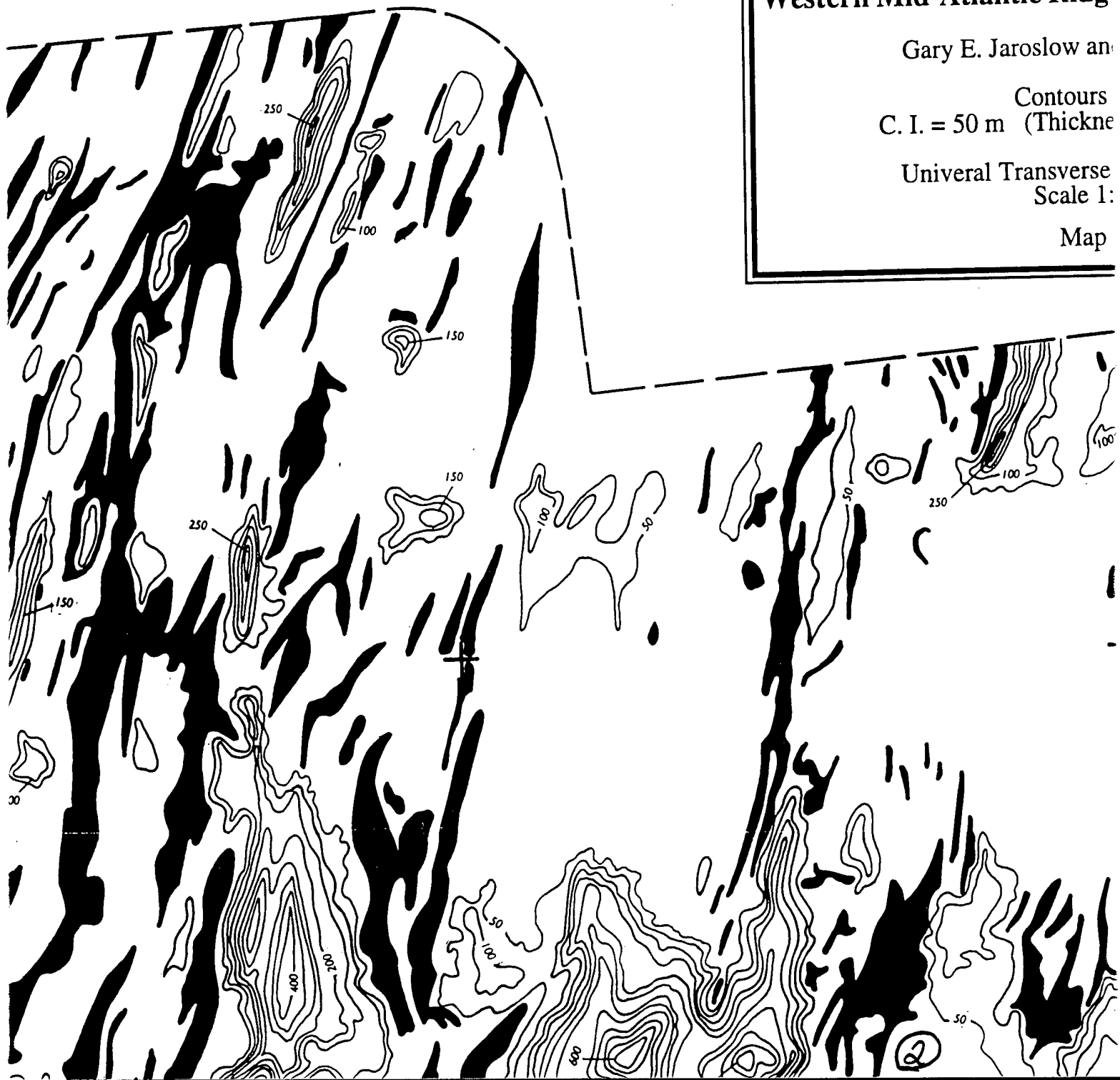
SEDIMENT
Western Mid-Atlantic Ridge

Gary E. Jaroslow and

Contours
C. I. = 50 m (Thickne

Univeral Transverse
Scale 1:

Map



46°30'

SEDIMENT THICKNESS

on Mid-Atlantic Ridge Flank, 25°20'N to 27°15'N

Gary E. Jaroslow and Brian E. Tucholke

Contours in meters

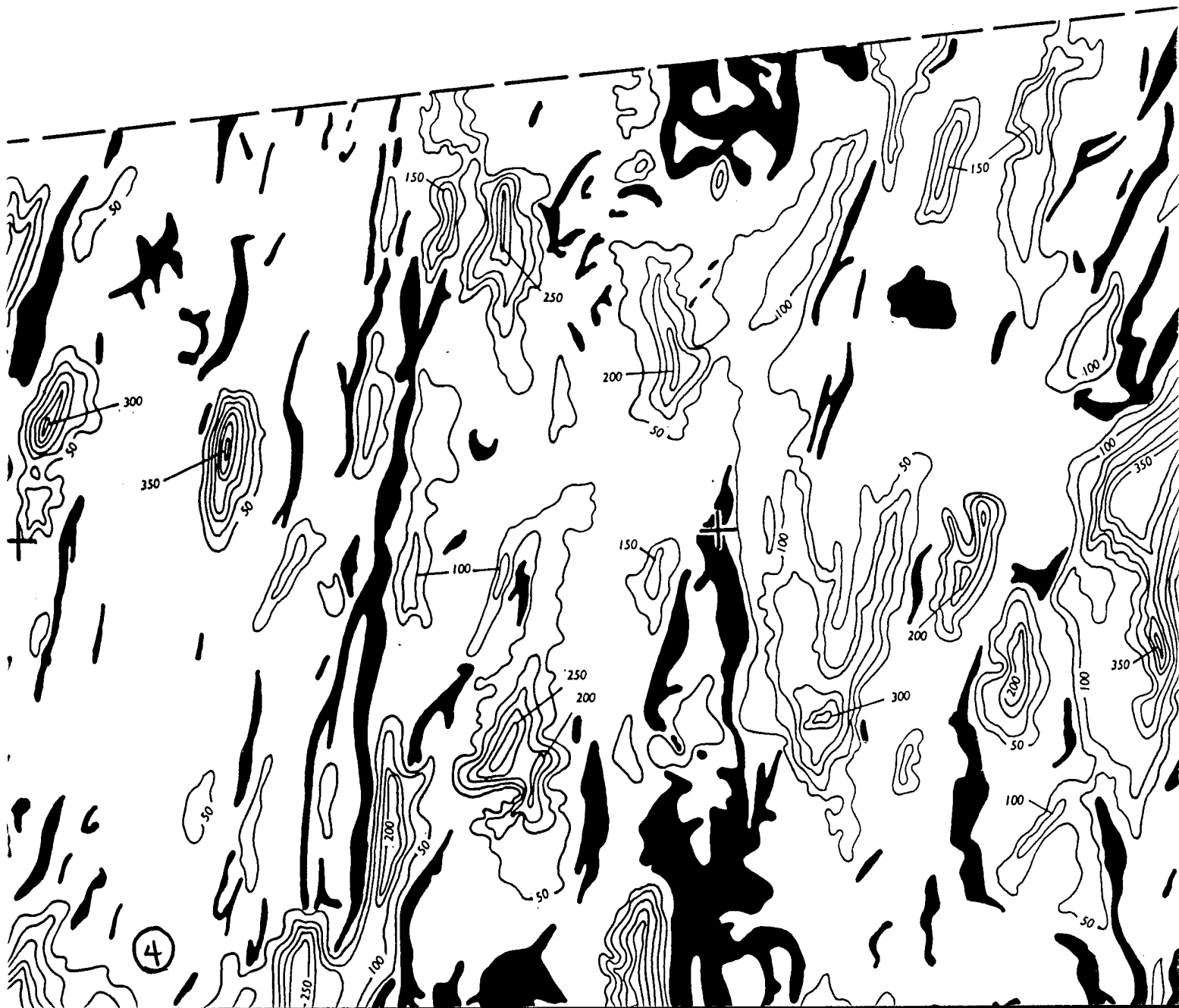
C. I. = 50 m (Thicknesses <10 m are Black)

Universal Transverse Mercator Projection
Scale 1:200,000

Map 2 of 6

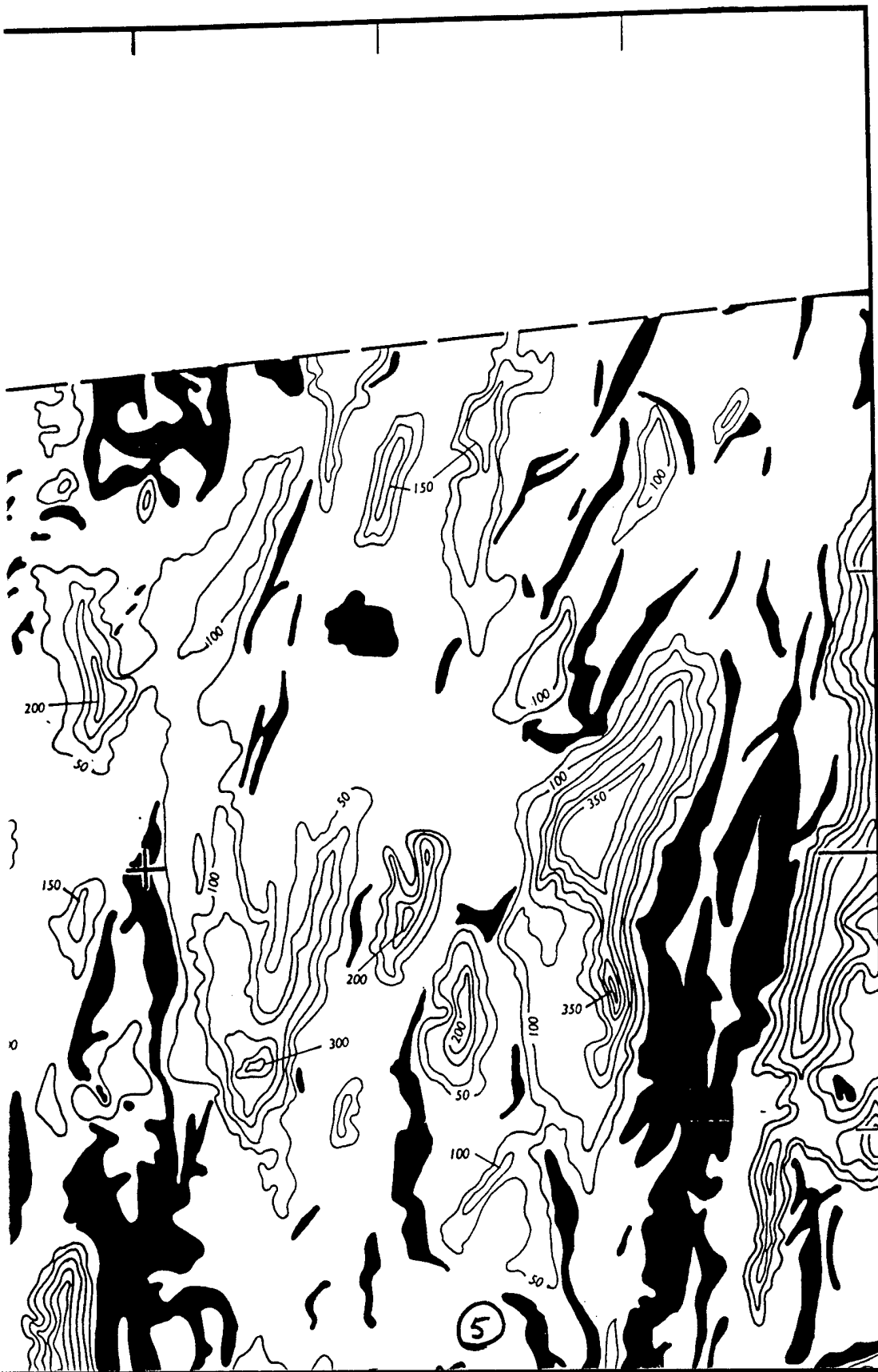


30'



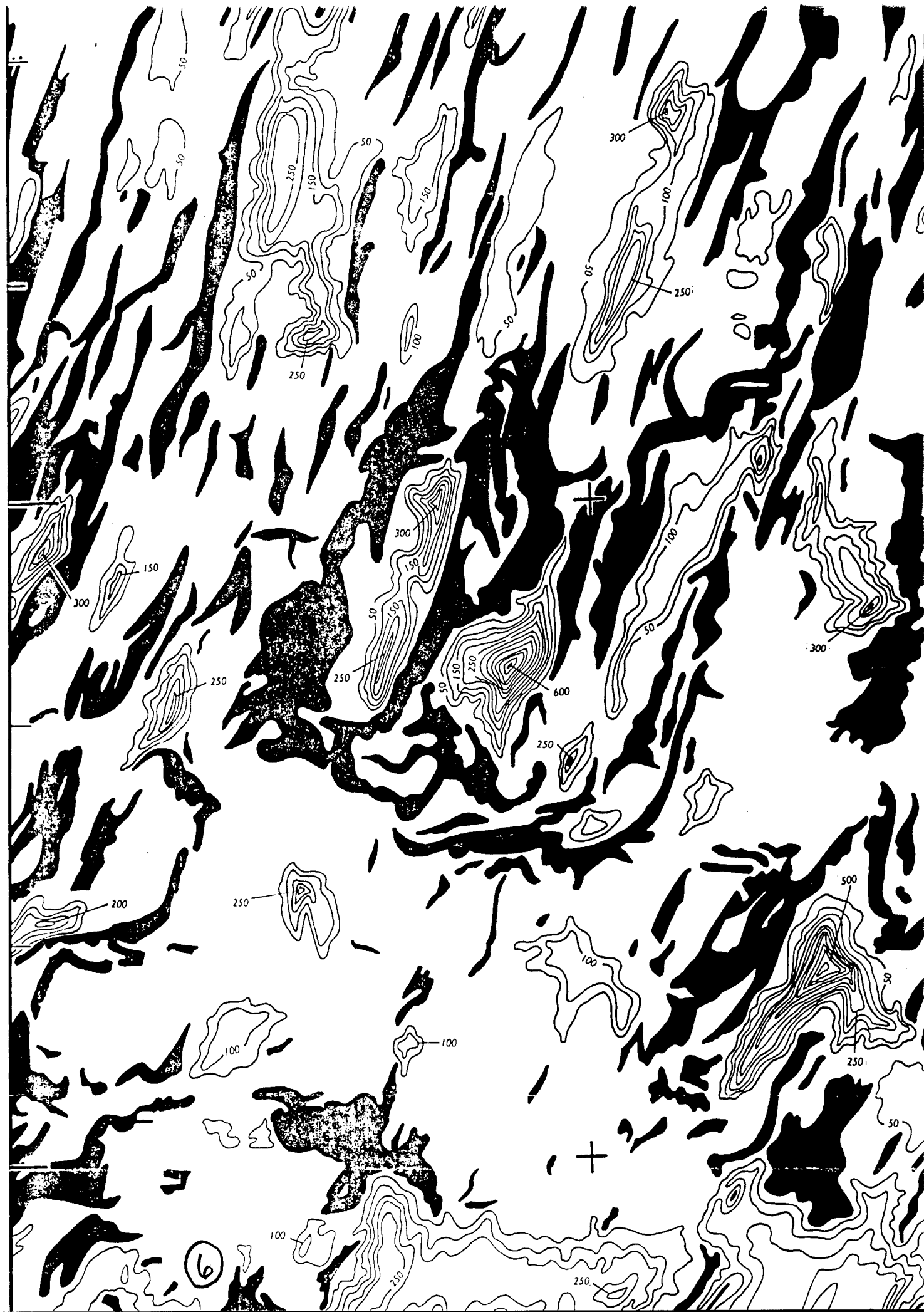
27°
15'

27°
00'



26°
45'

26°
30'





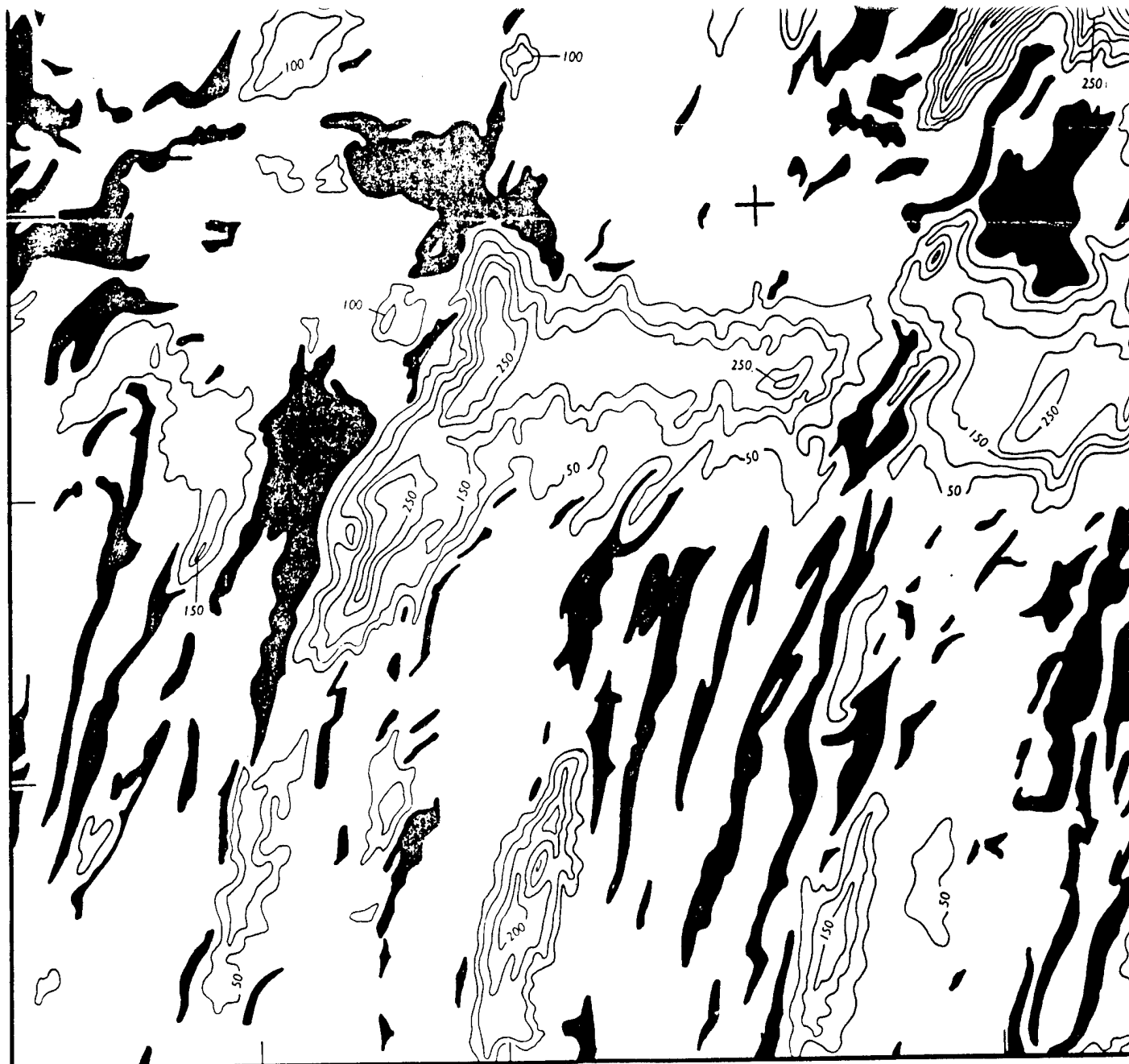




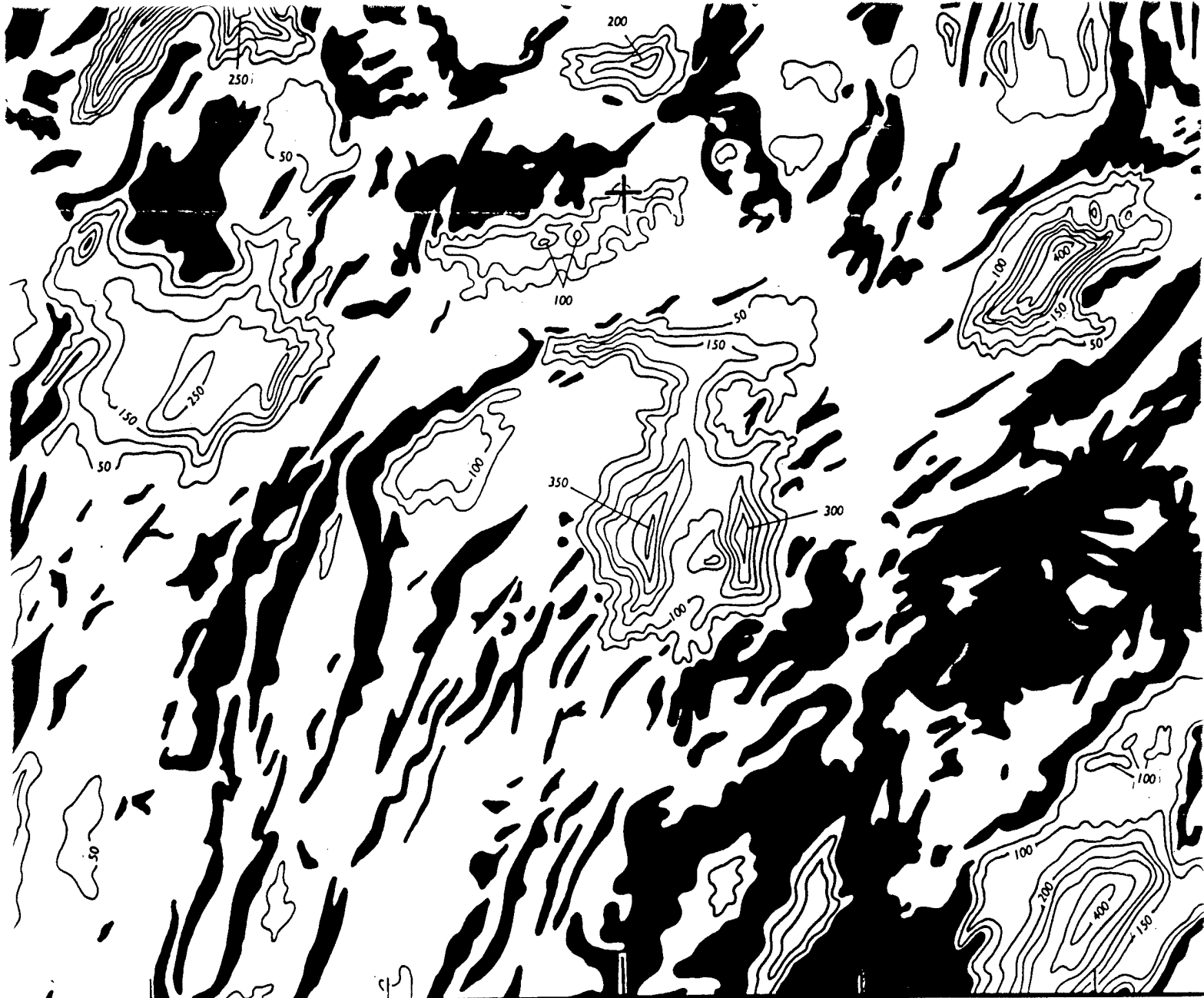
26°
30'

26°
15'

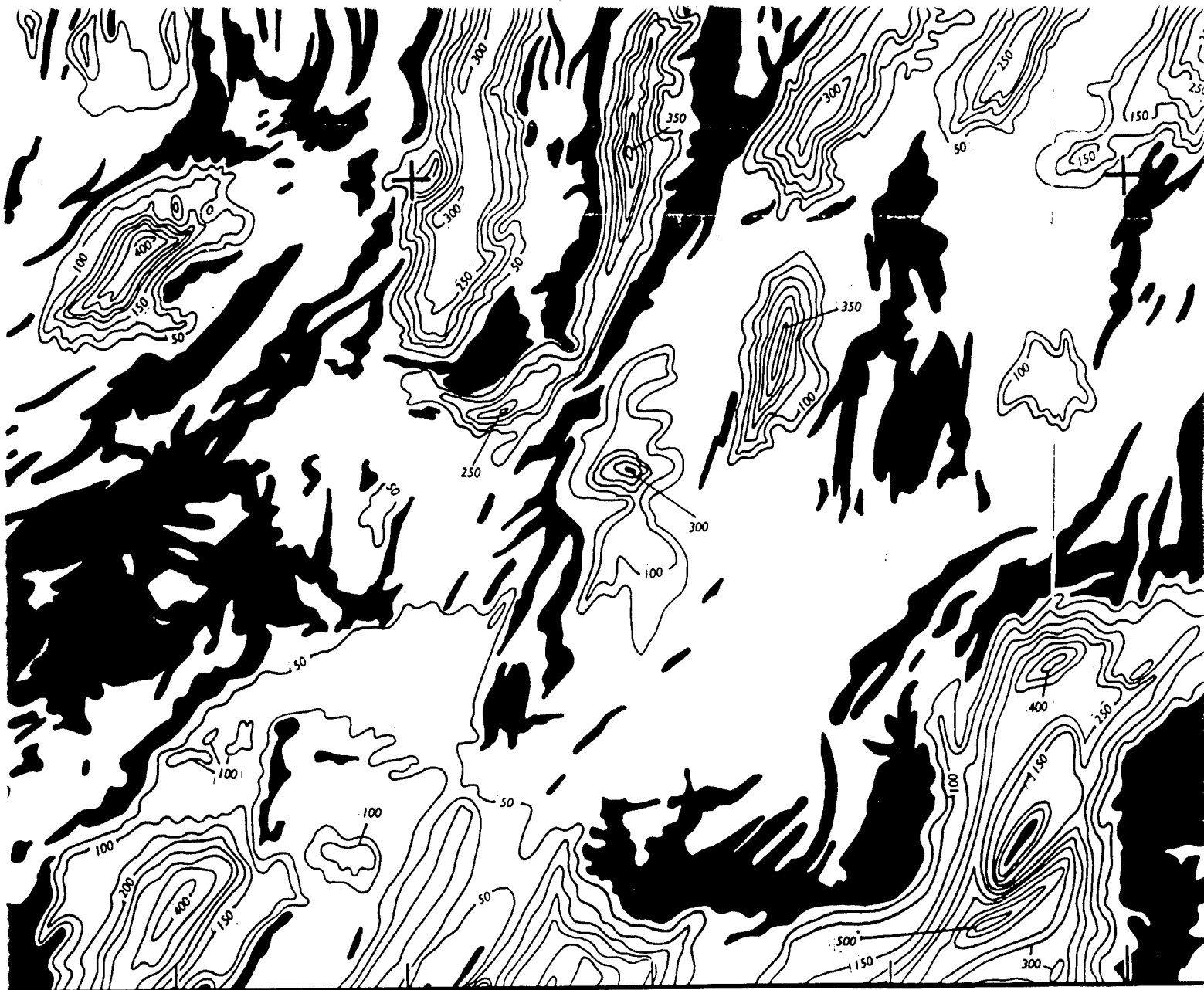
47°30'



(11)

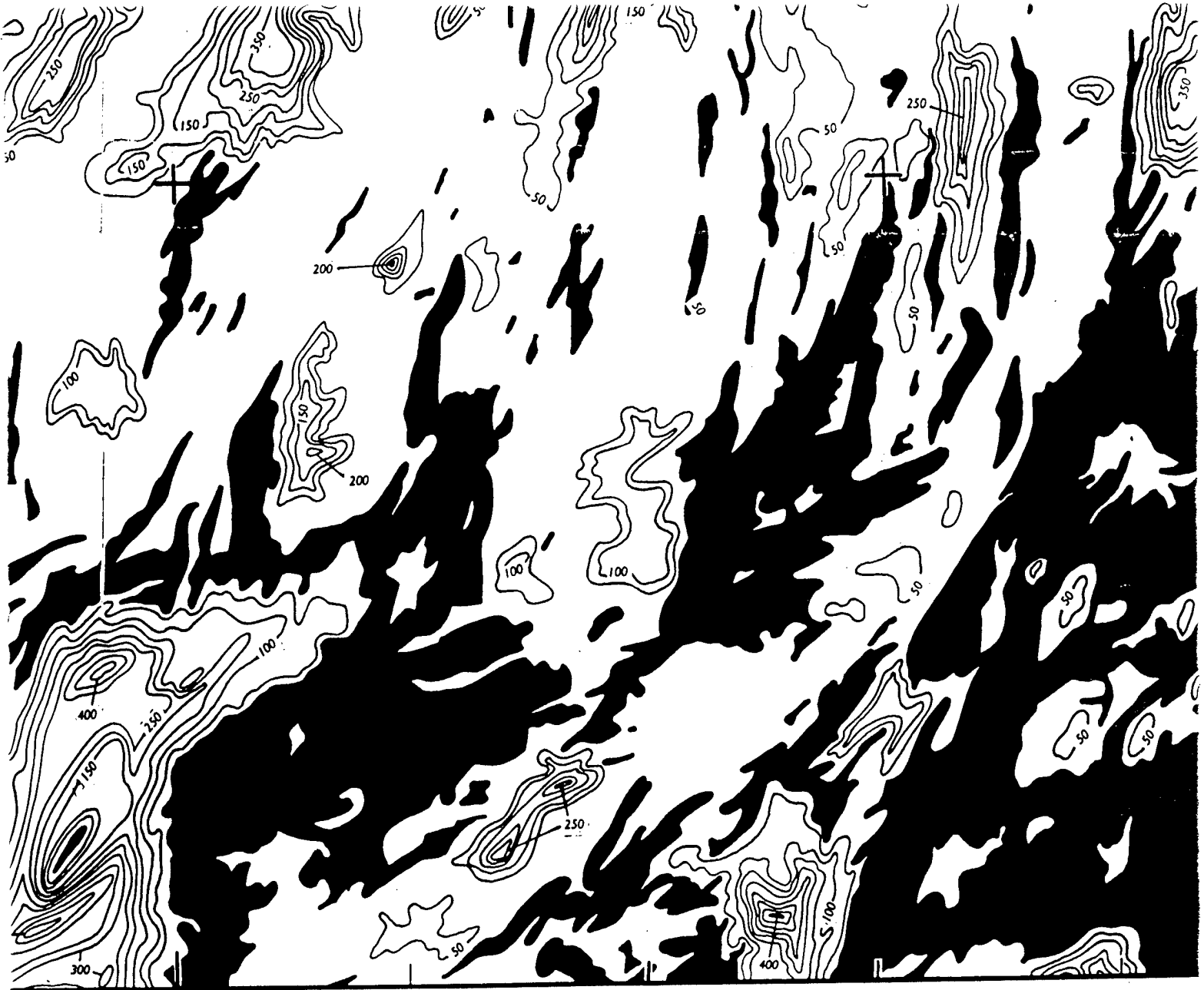


47°00'



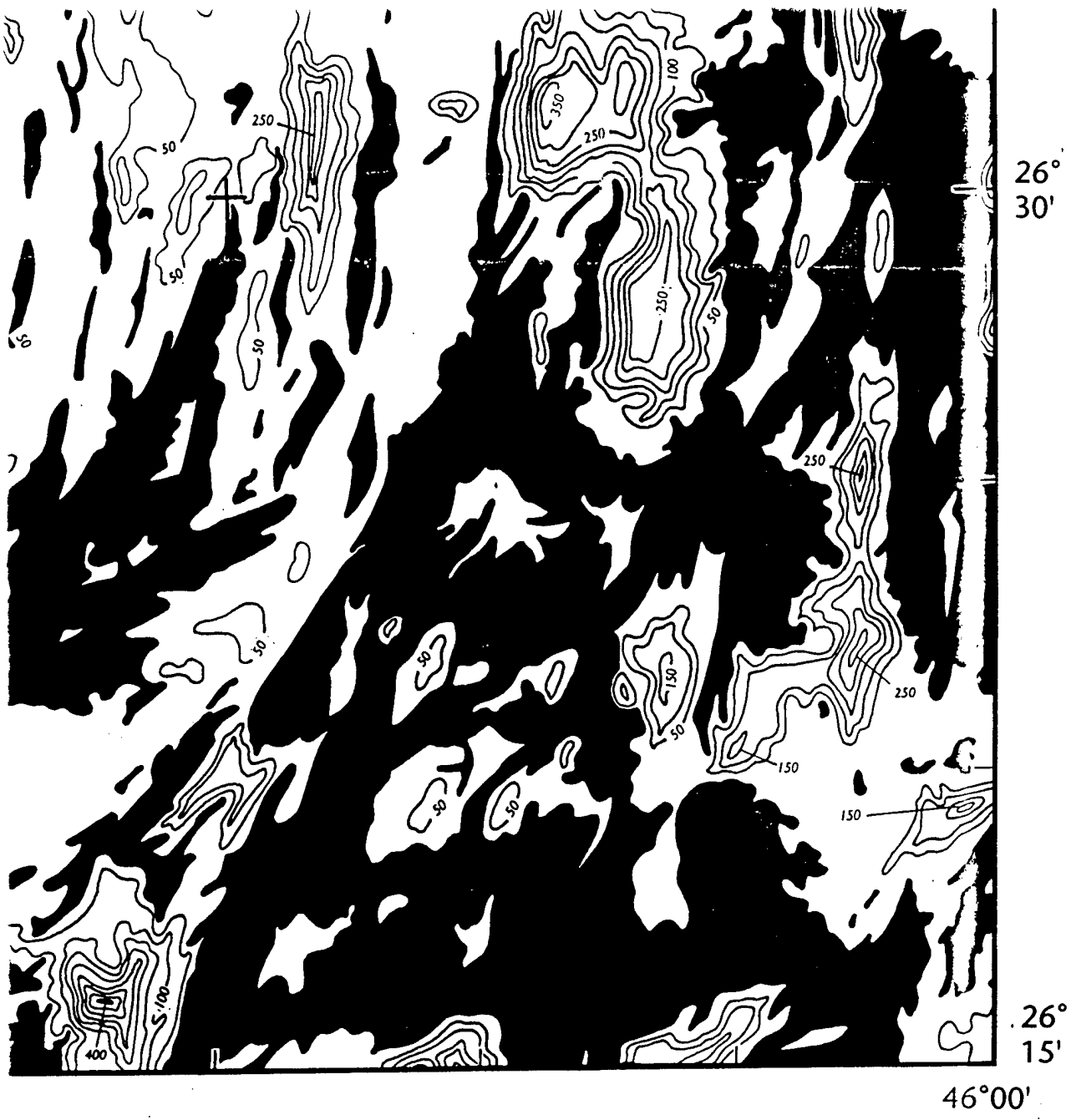
46°30'

13



46°30'

14



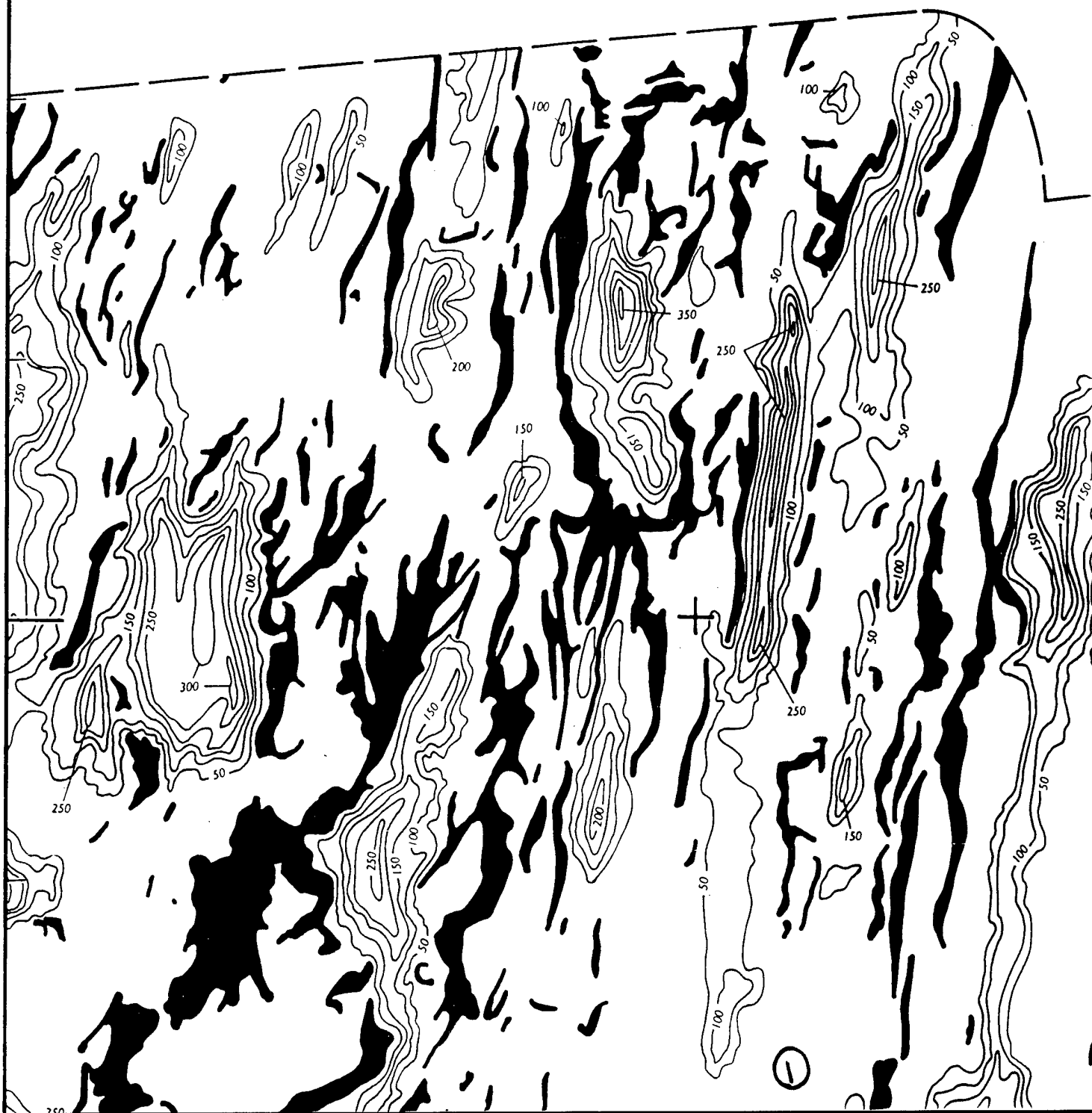
(15)

46°00'

45°45'

27°
15'

27°
00'



45°30'



45°15'

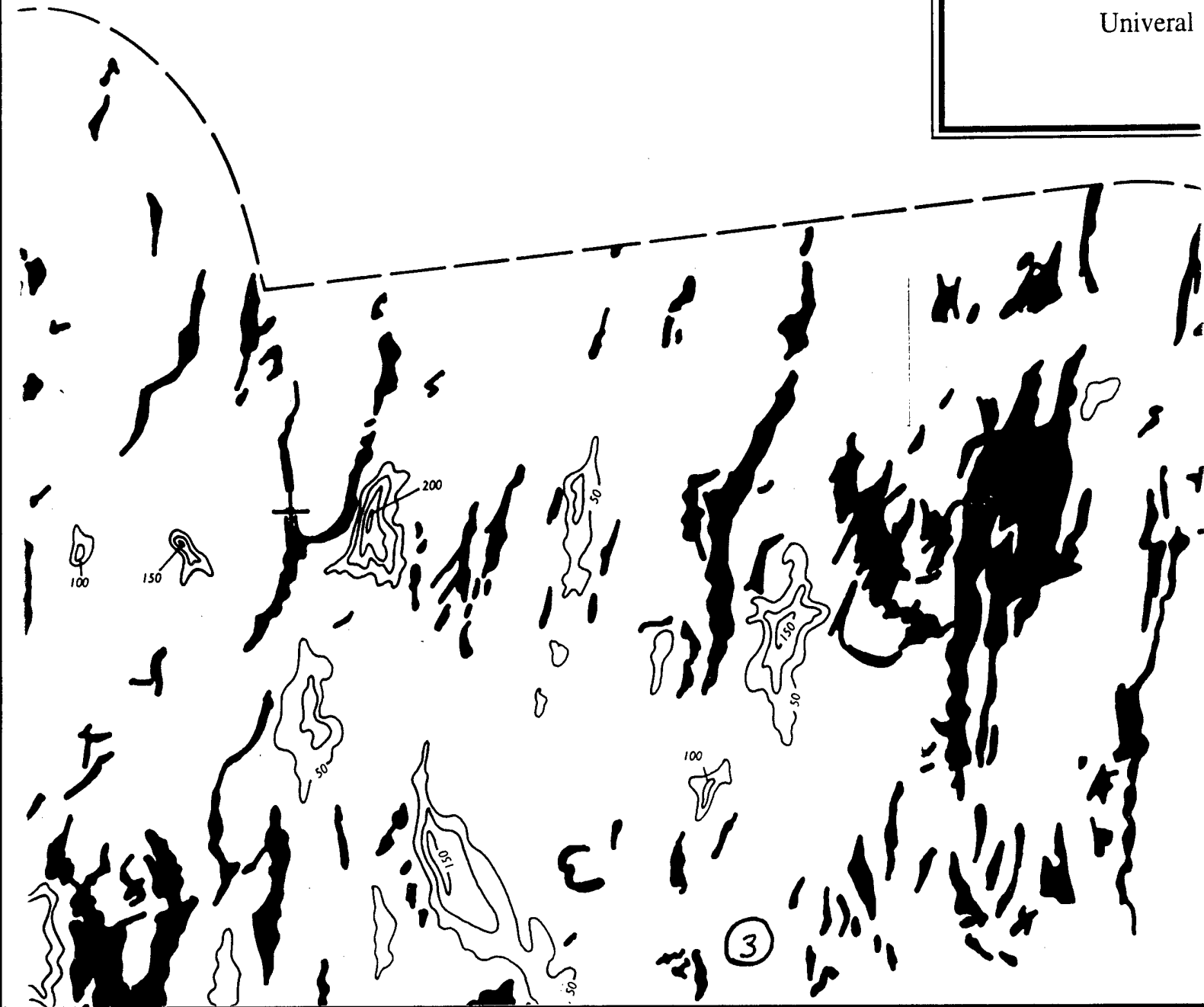
45°00'

SEI
Western Mid-Atla

Gary E. .

C. I. = 50 r

Univeral



45°00'

44°45'

SEDIMENT THICKNESS

Western Mid-Atlantic Ridge Flank, 25°20'N to 27°15'N

Gary E. Jaroslow and Brian E. Tucholke

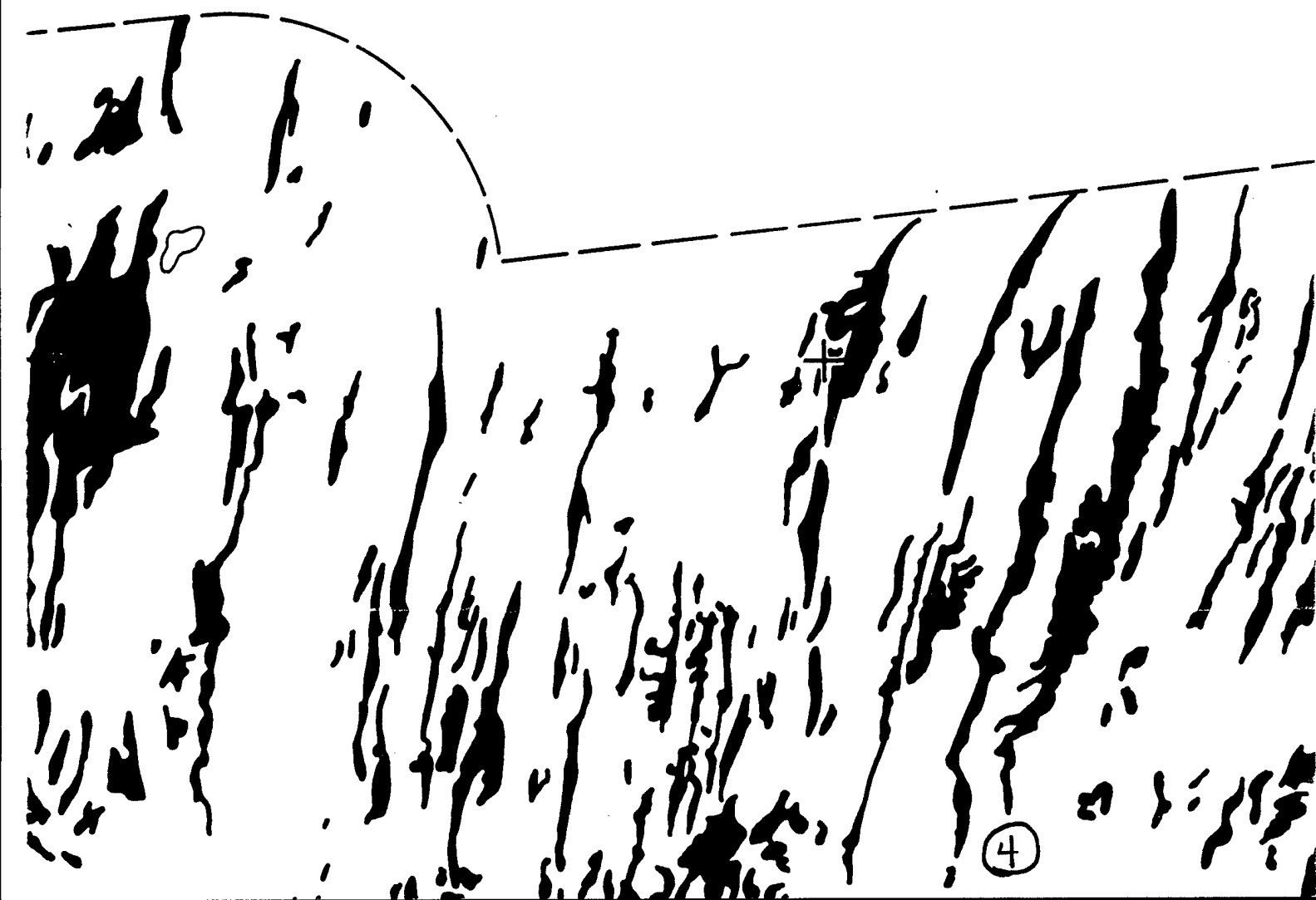
Contours in meters

C. I. = 50 m (Thicknesses <10 m are Black)

Universal Transverse Mercator Projection

Scale 1:200,000

Map 3 of 6



44°45'

44°30'

27°
15'

°15'N

27°
00'

5

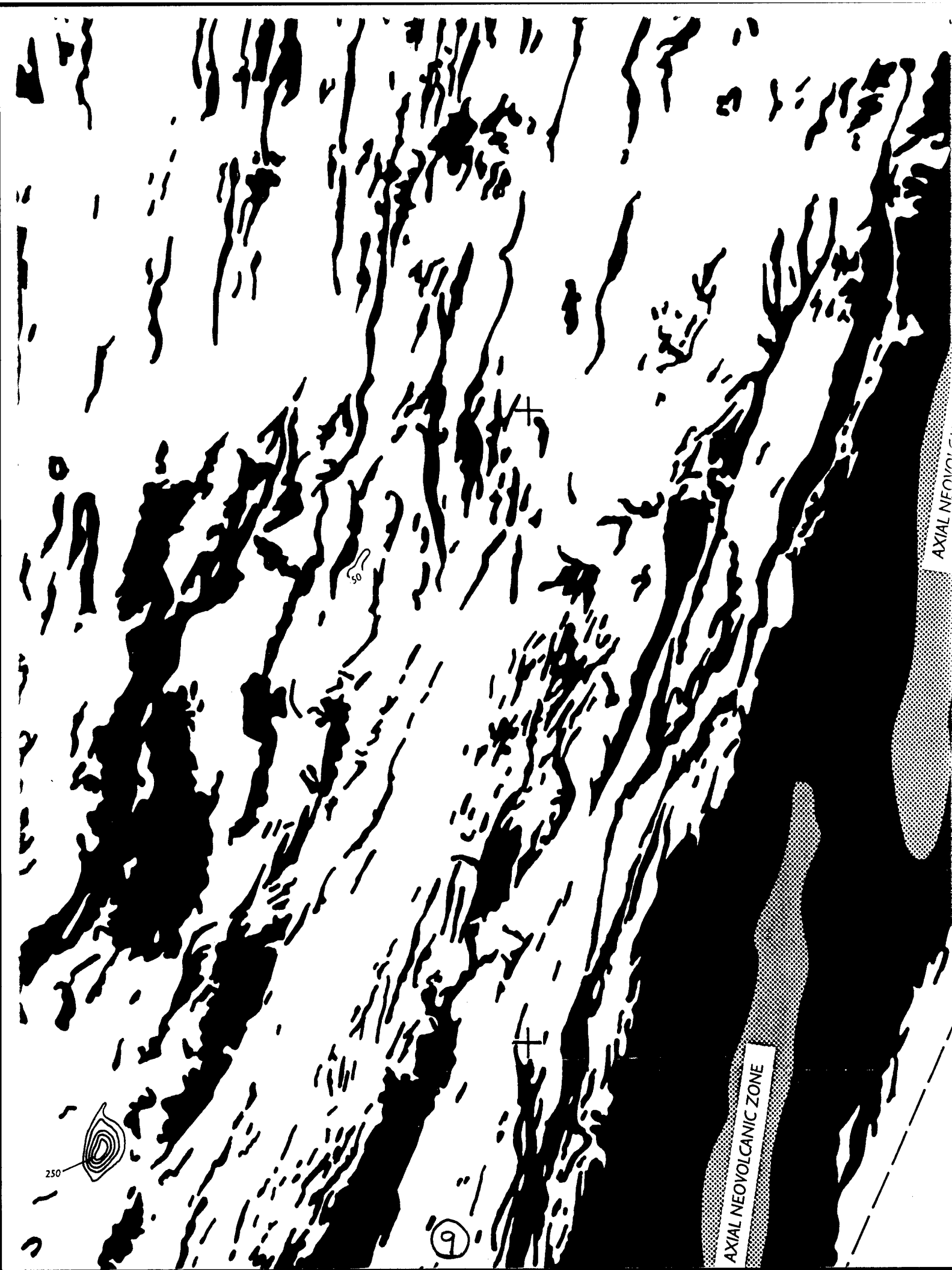
26°
45'

26°
30'







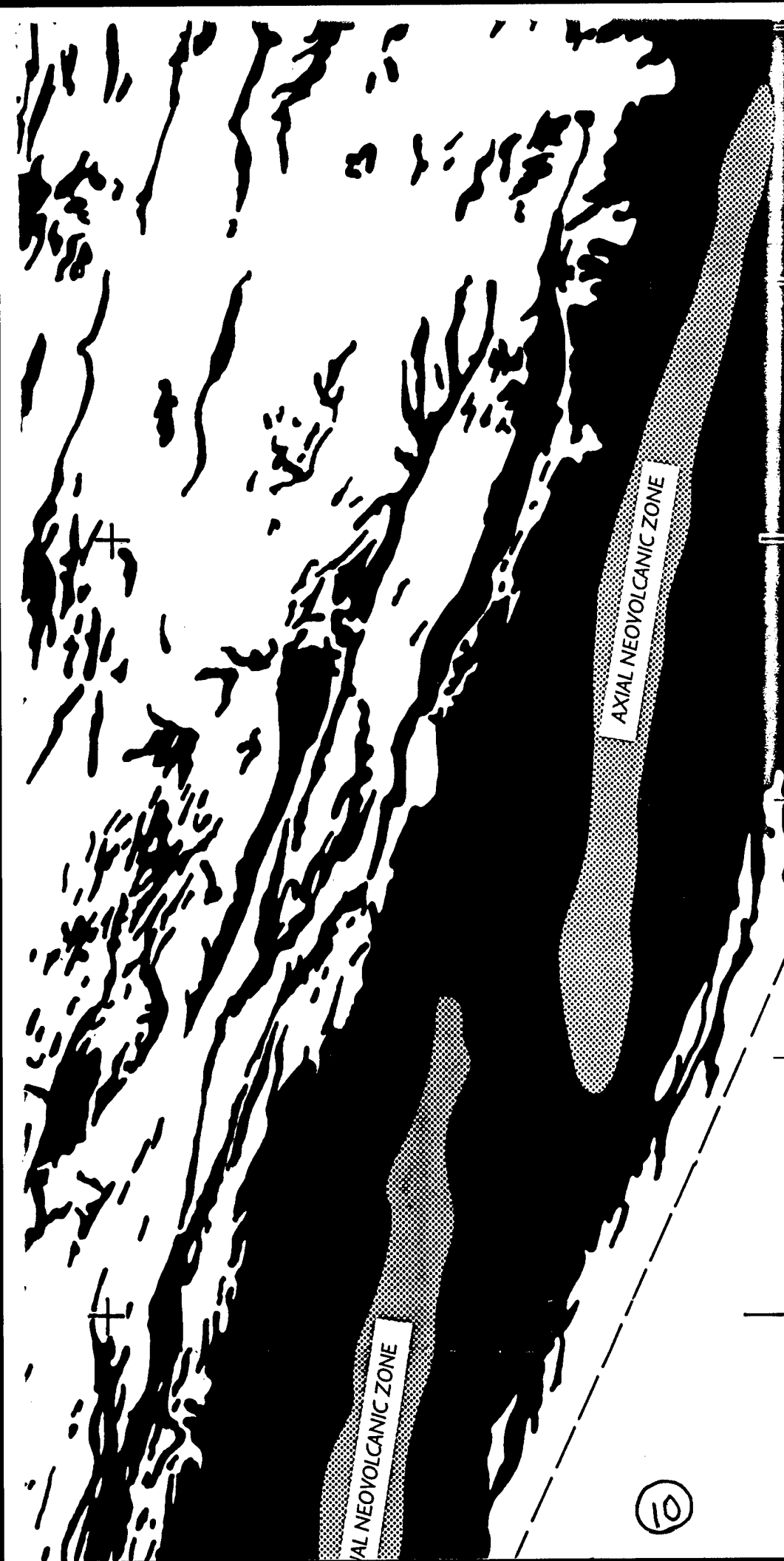


AXIAL NEOVOLCANIC ZONE

AXIAL NEOVOLCANIC ZONE

250

9



AXIAL NEOVOLCANIC ZONE

AXIAL NEOVOLCANIC ZONE

26°
45'

26°
30'

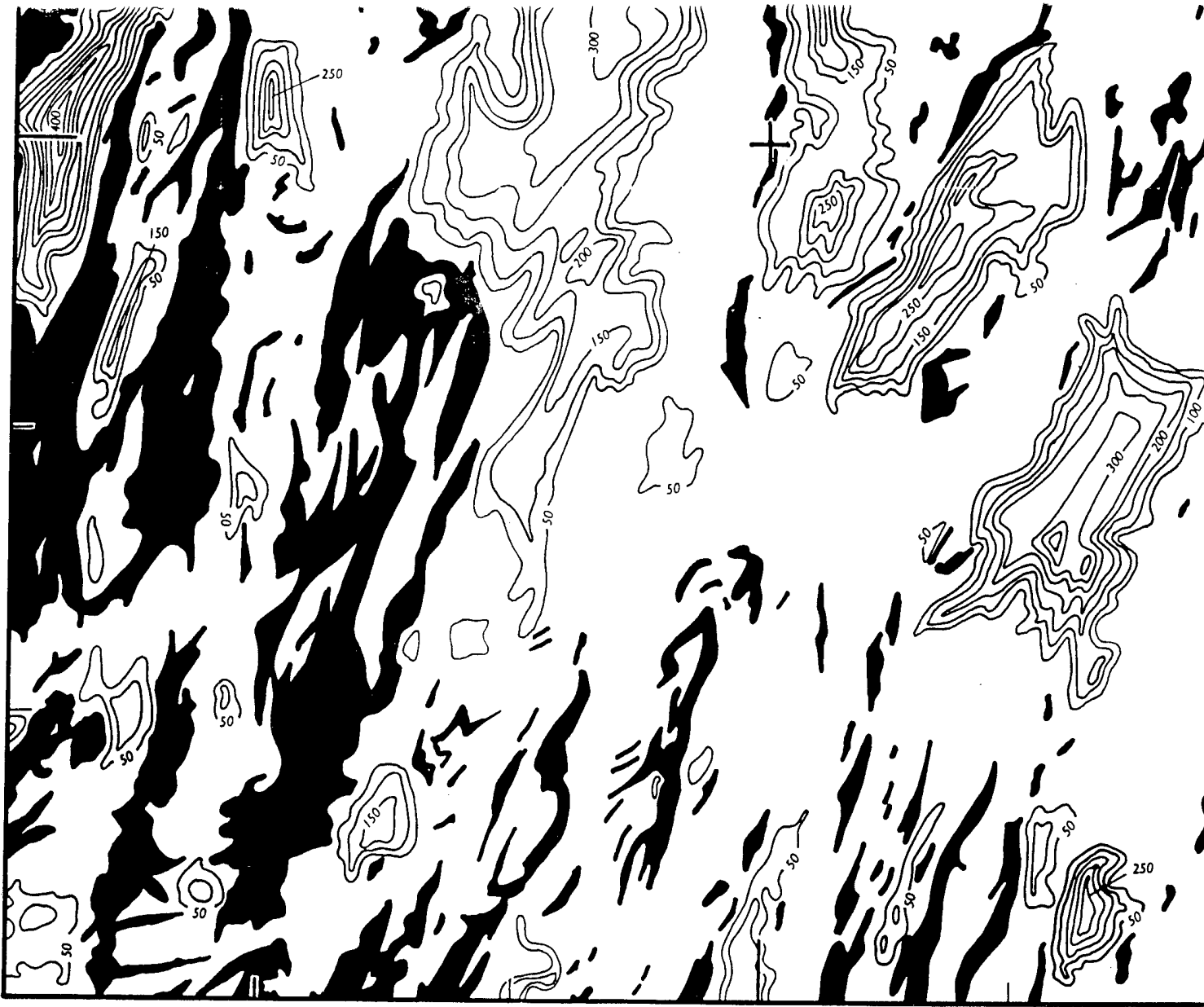
10

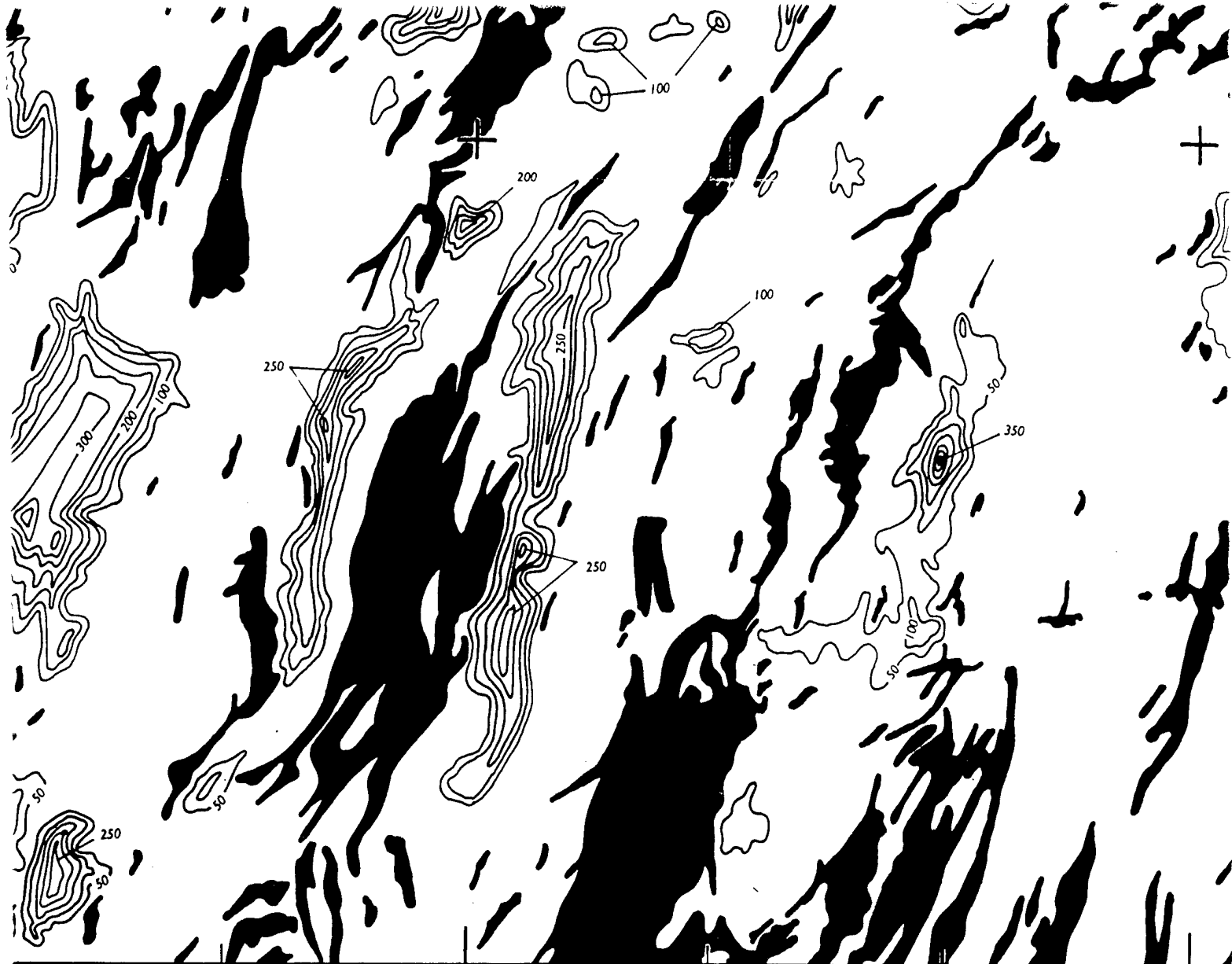
26°
30'

26°
15'

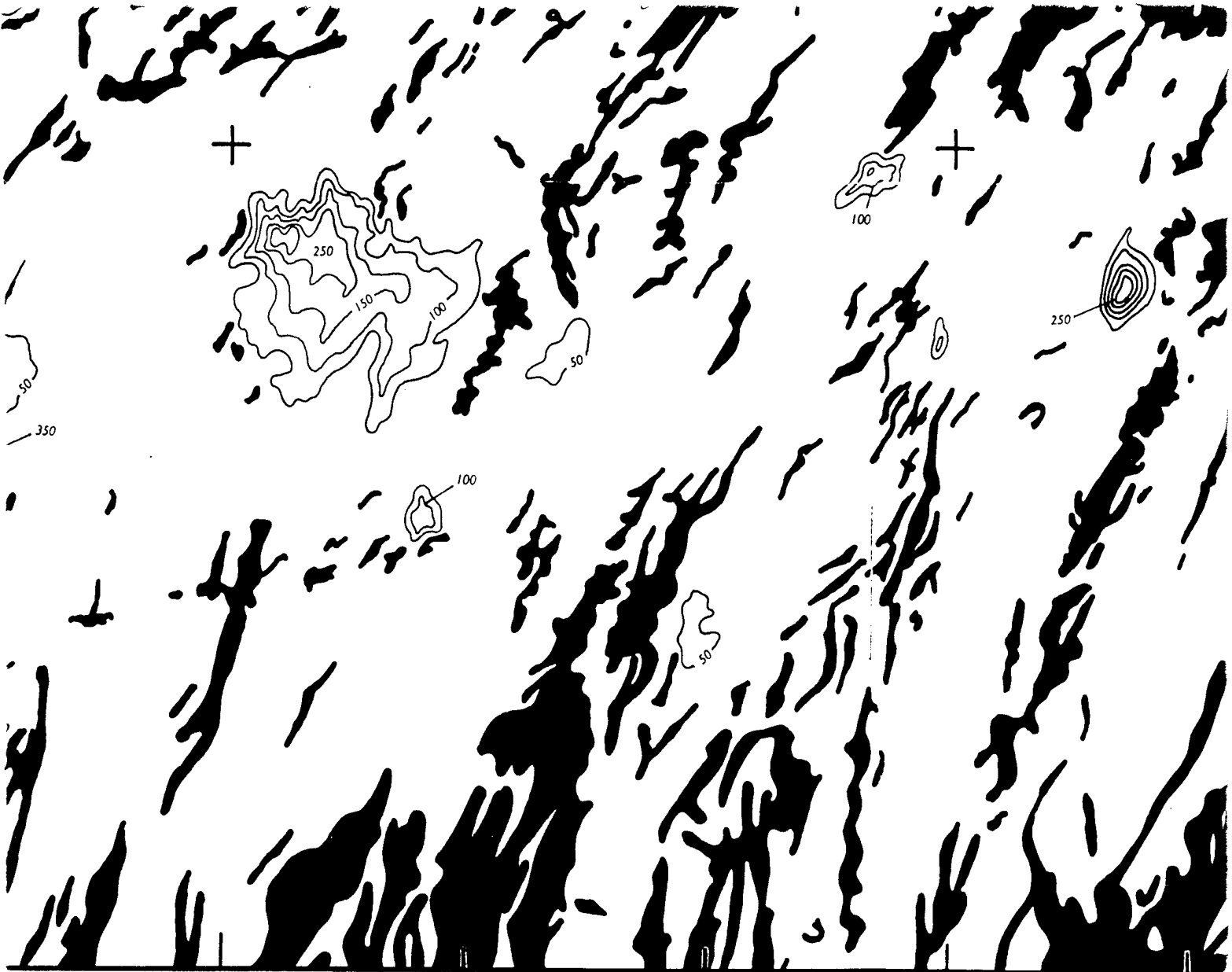
46°00'

45°45'





12



45°15'

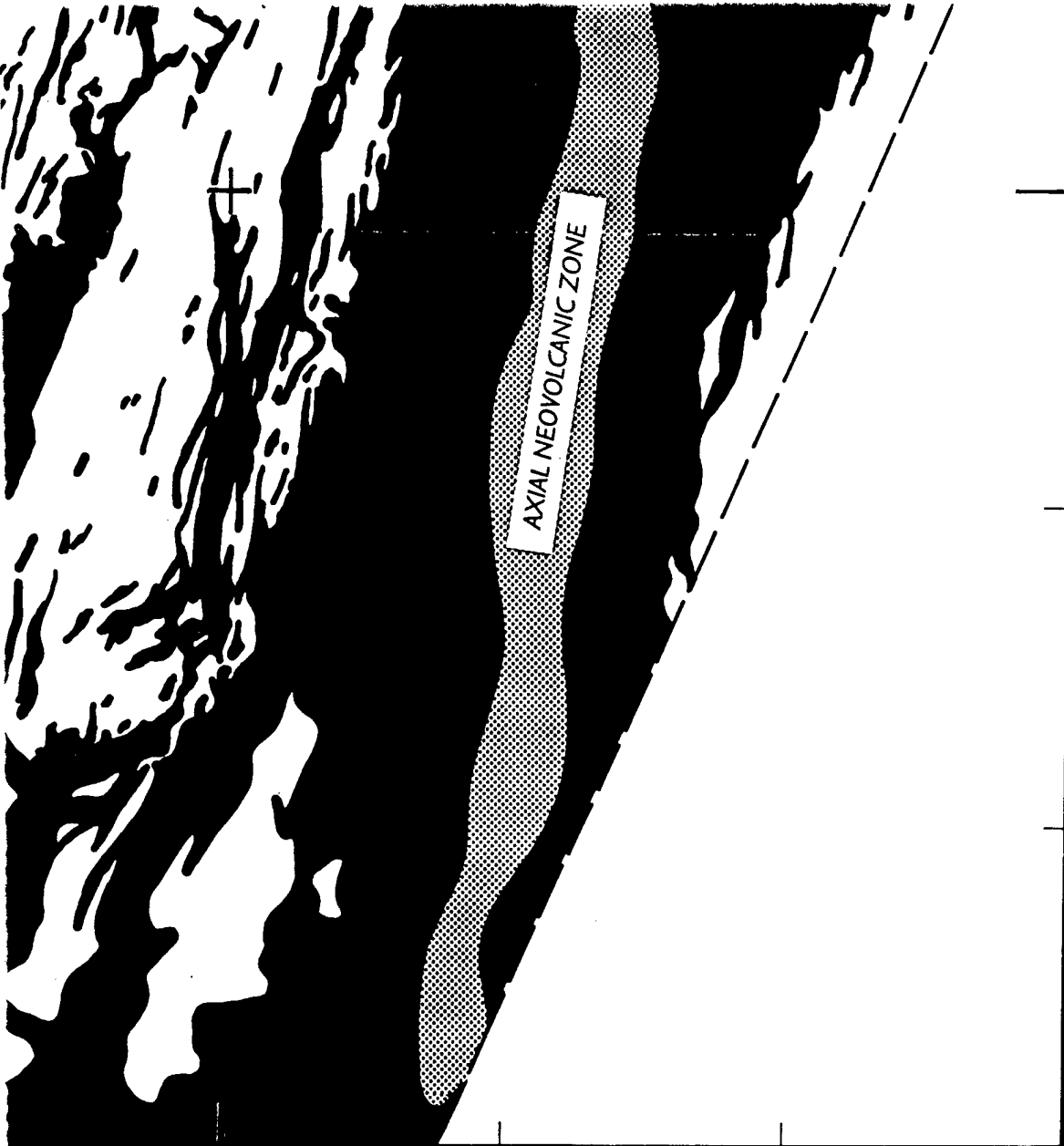
45°00'



45°00'

44°45'

14



26°
30'

26°
15'

44°45'

44°30'

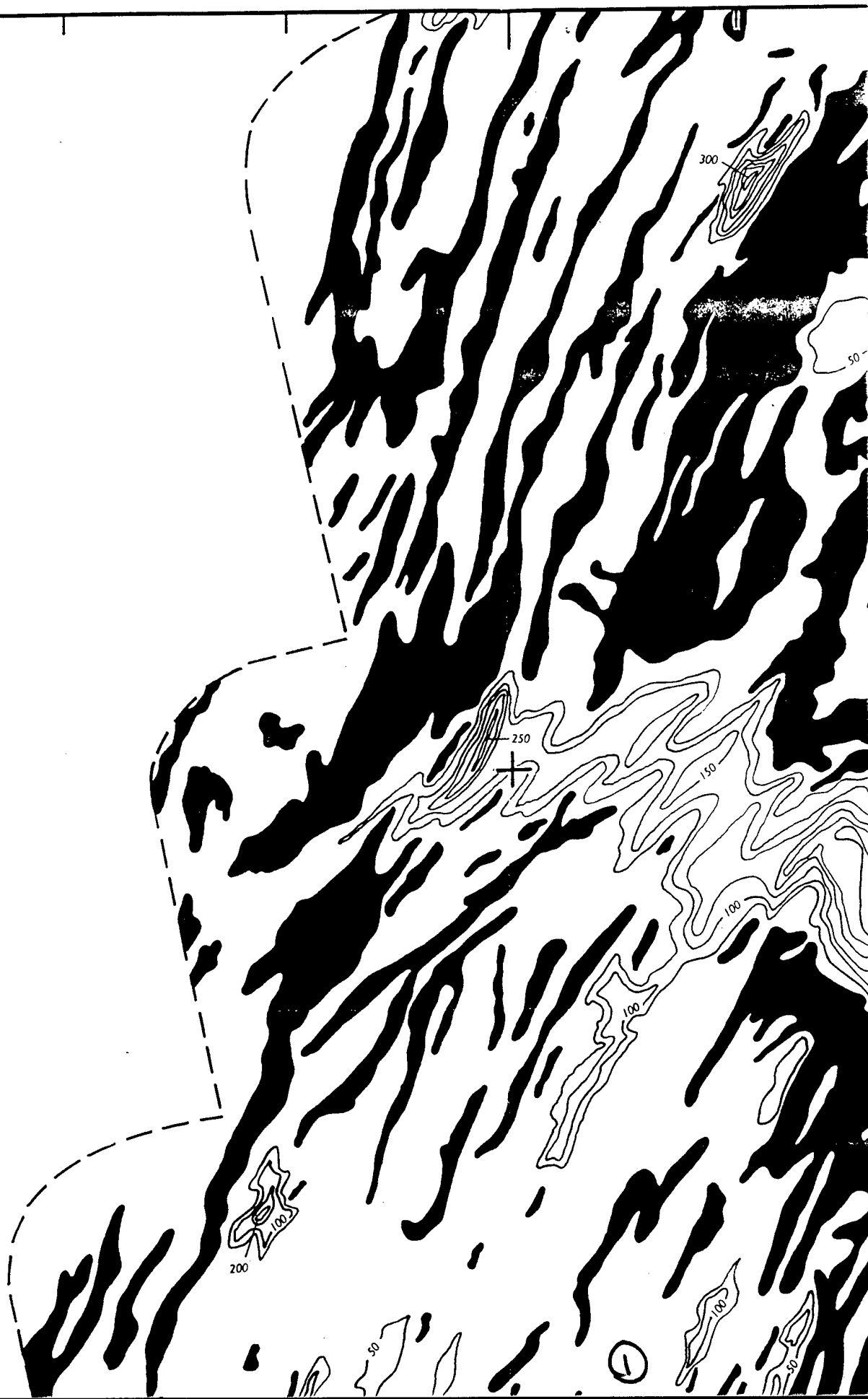
15

49°00'

48°45'

26°
15'

26°
00'

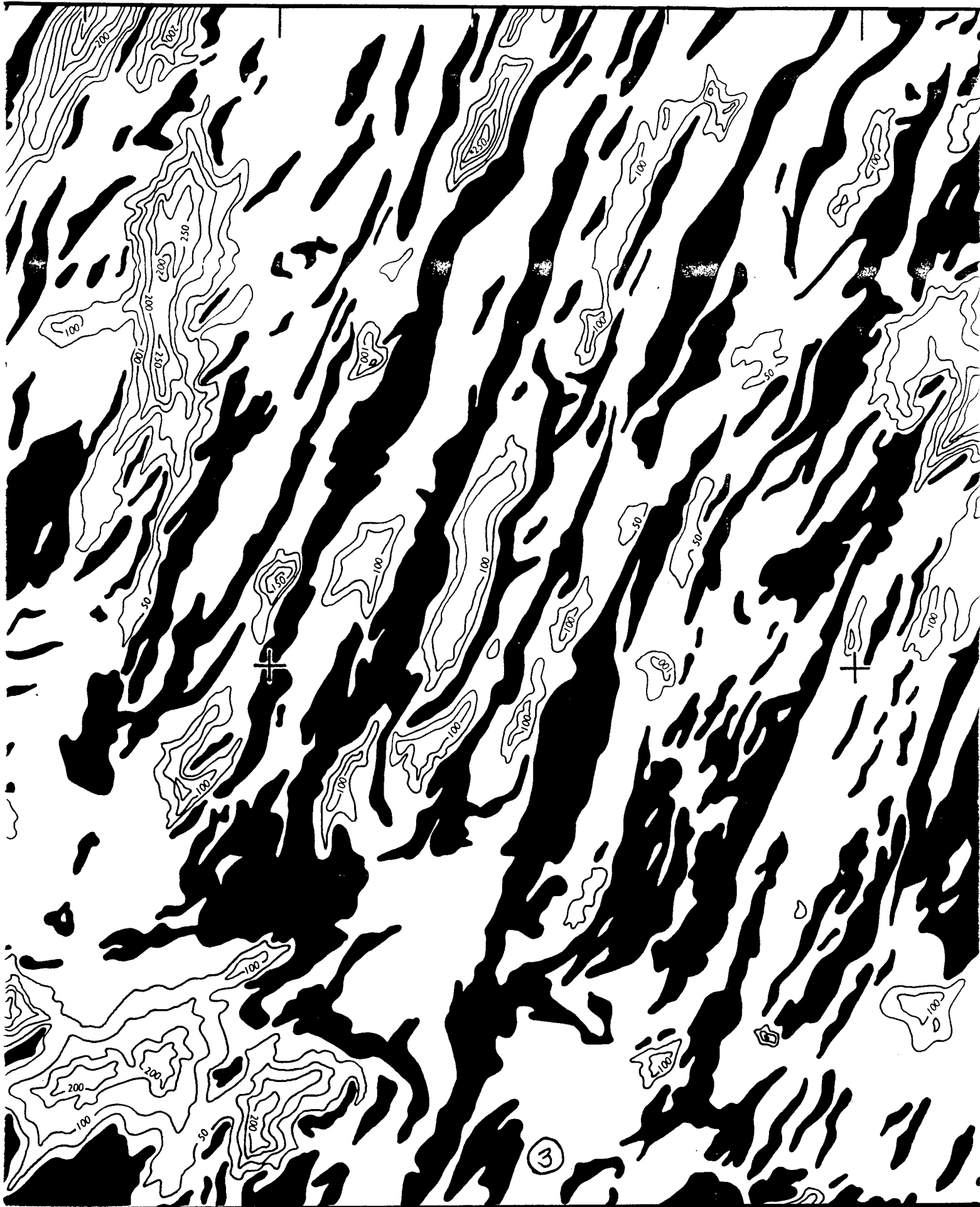


48°30'



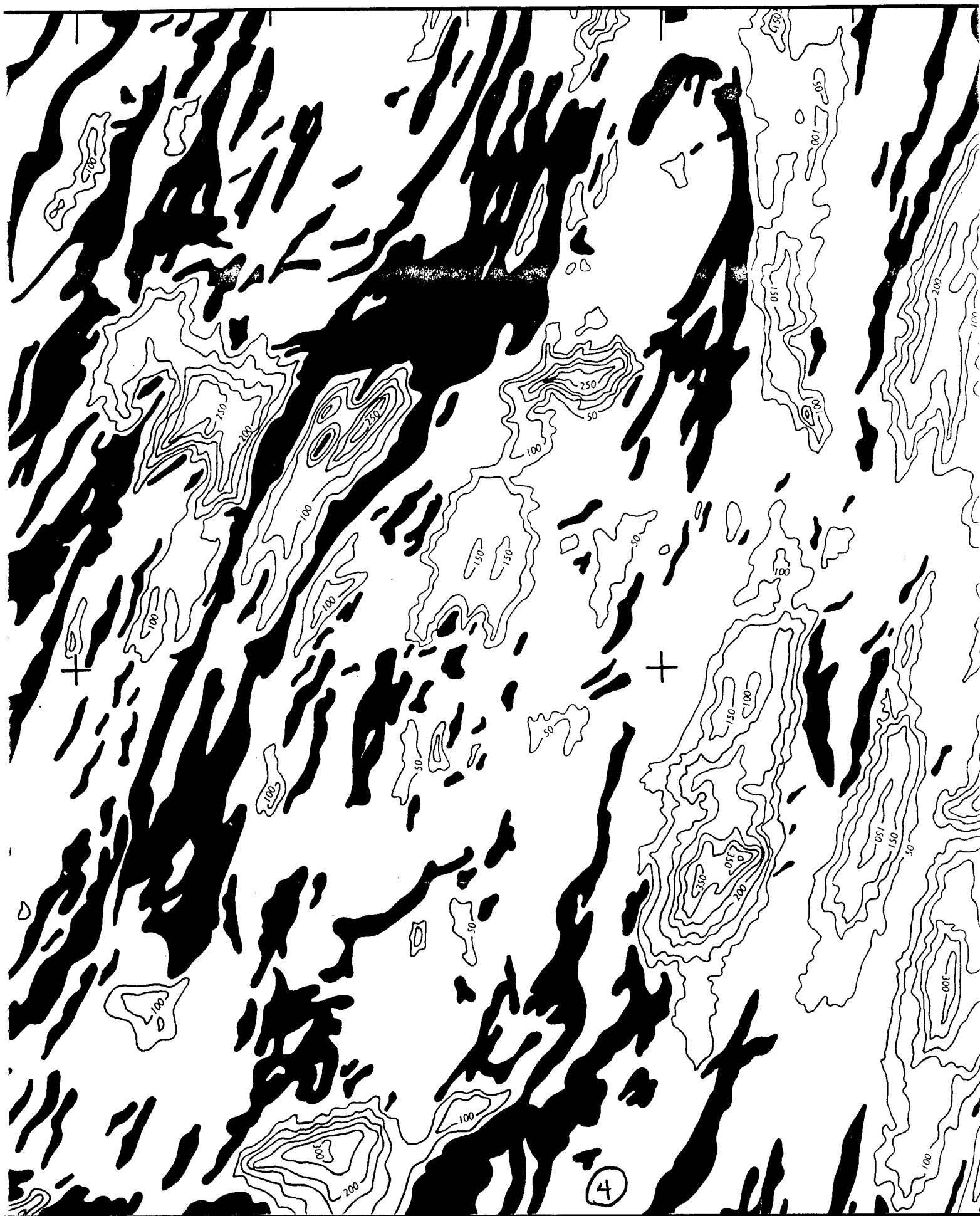
48°15'

48°00'



48°00'

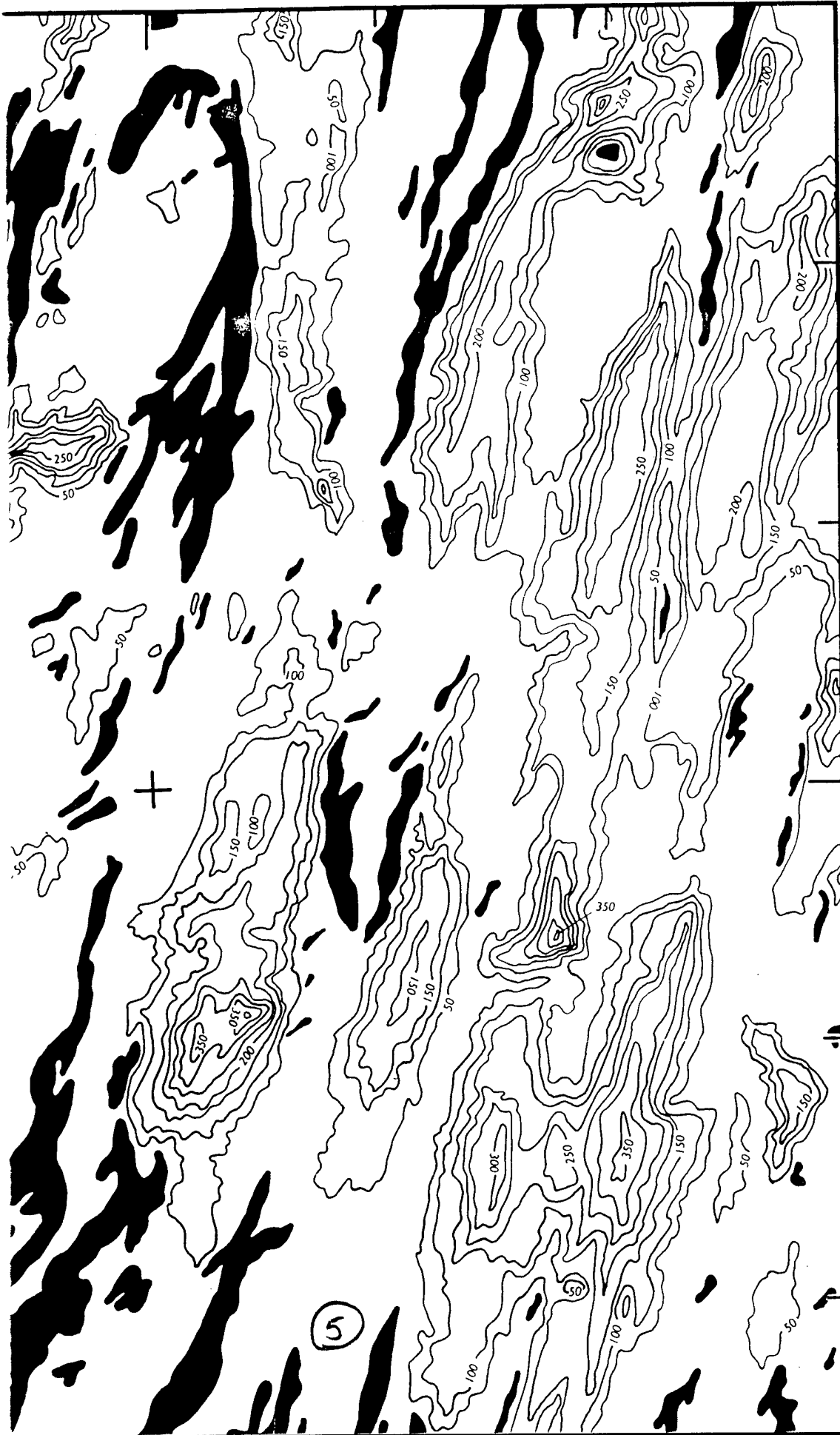
47°45'



47°45'

47°30'

26°
15'

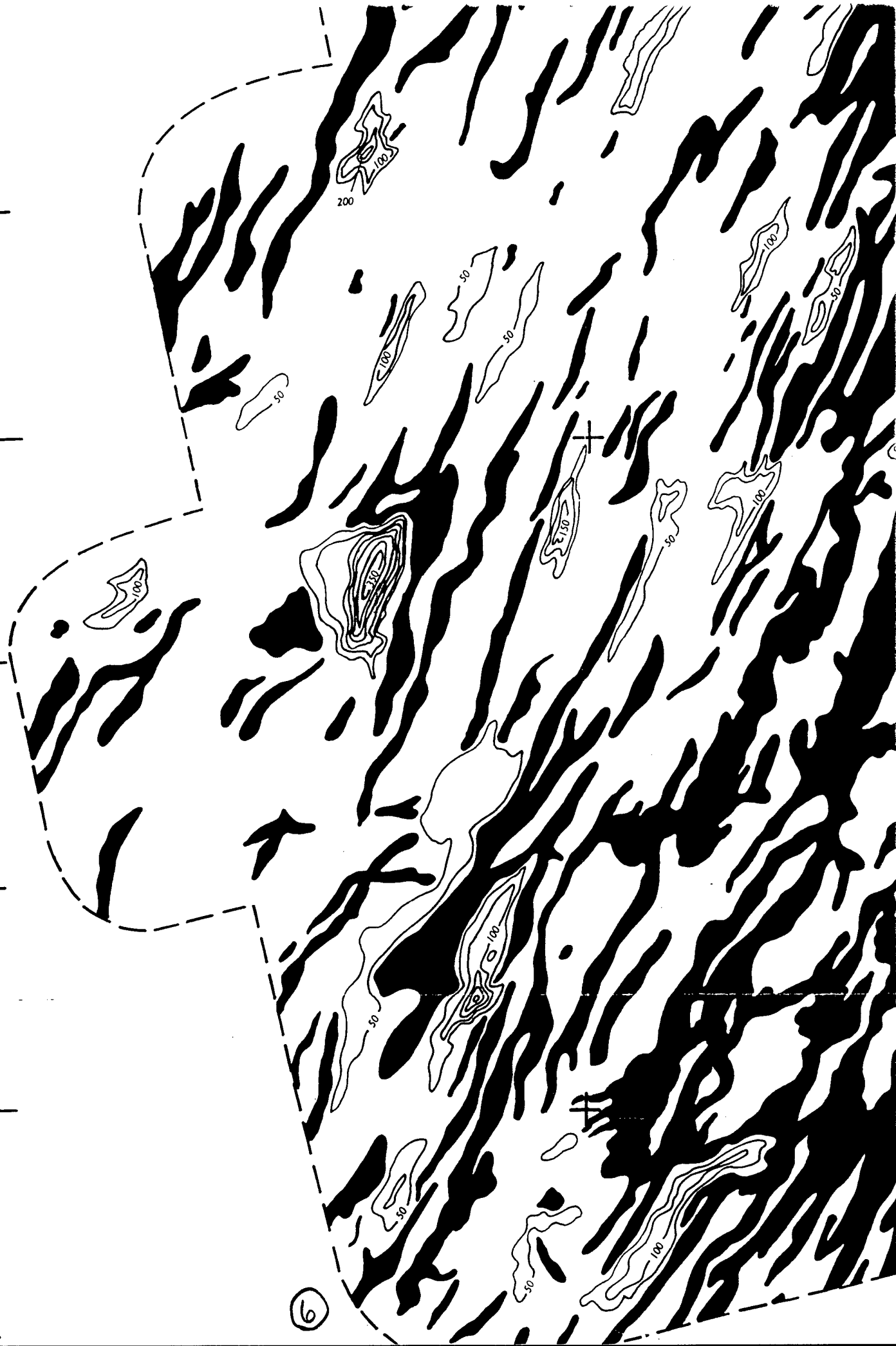


26°
00'

5

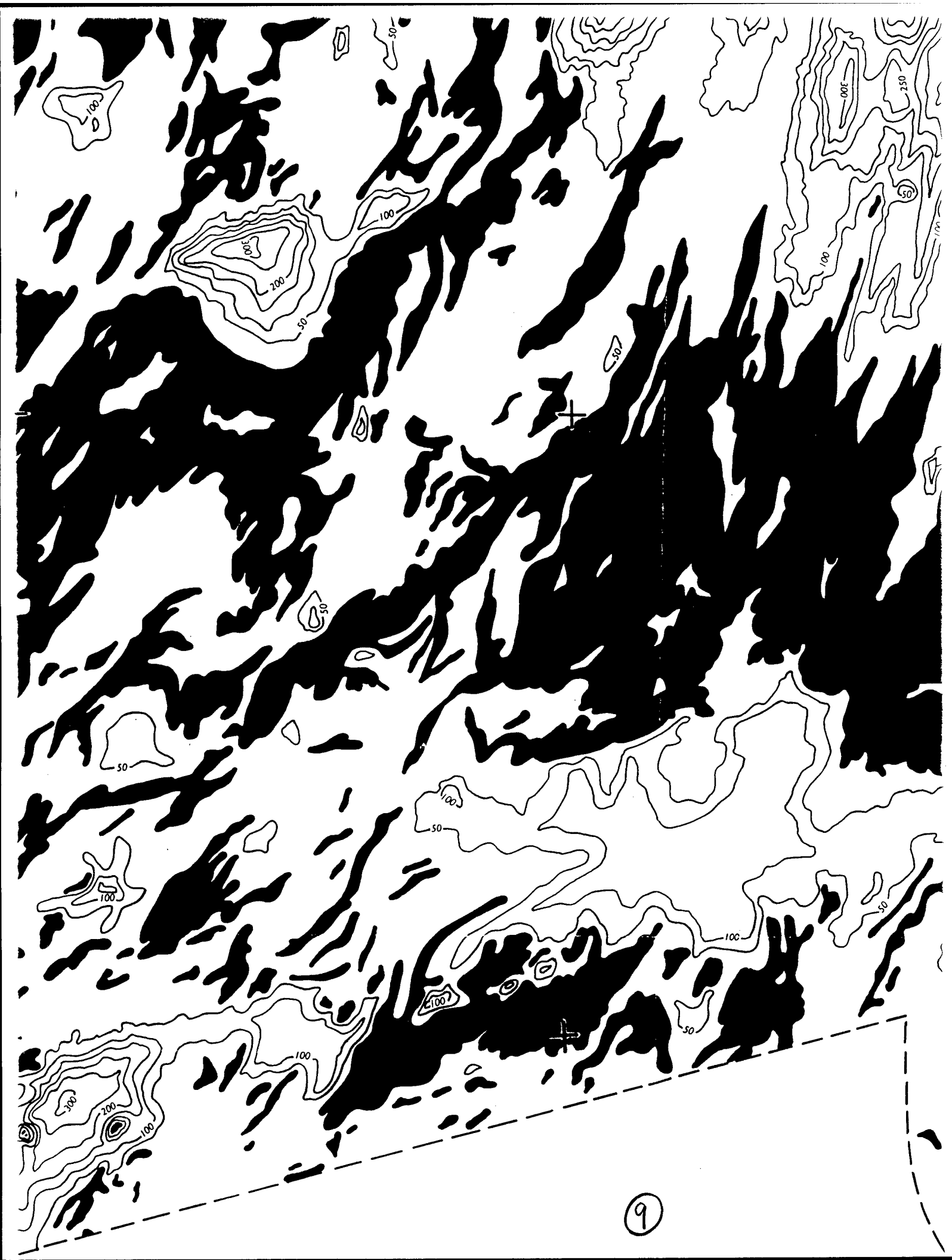
25°
45'

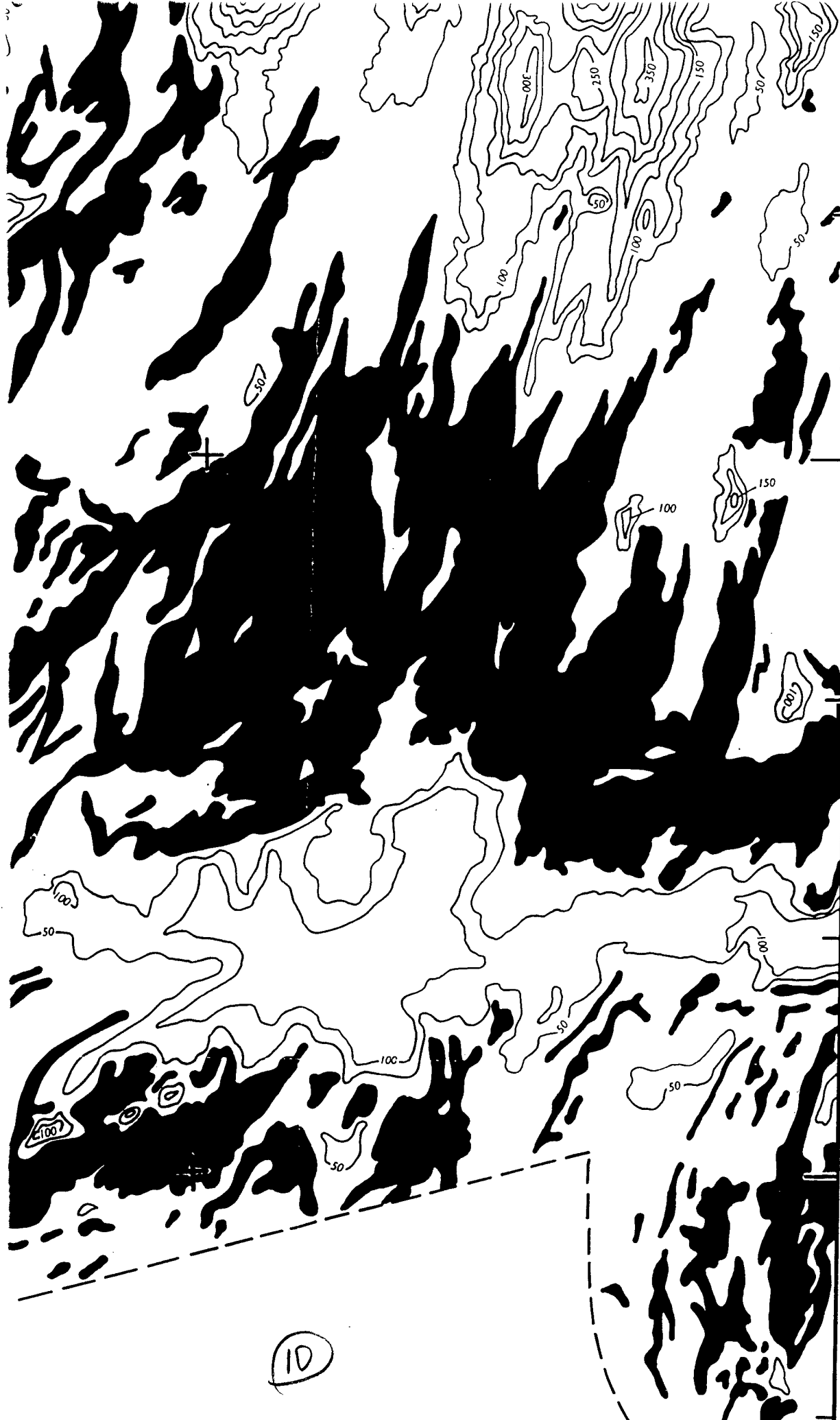
25°
30'









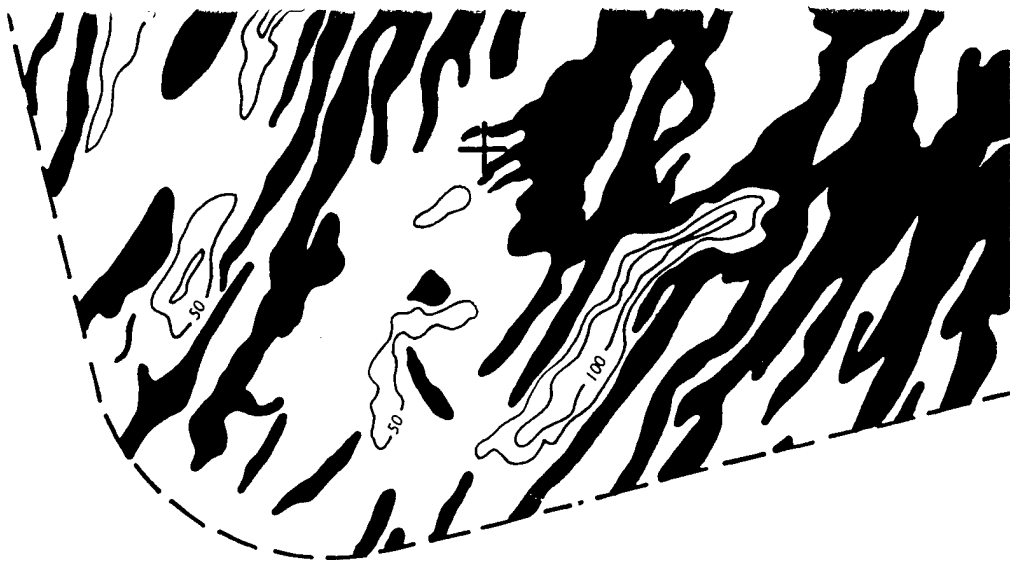


25°
45'

25°
30'

(10)

25°
30'



SEDIMENT THICKNESS
Western Mid-Atlantic Ridge Flank

Gary E. Jaroslow and Brian

Contours in meters
C. I. = 50 m (Thicknesses)

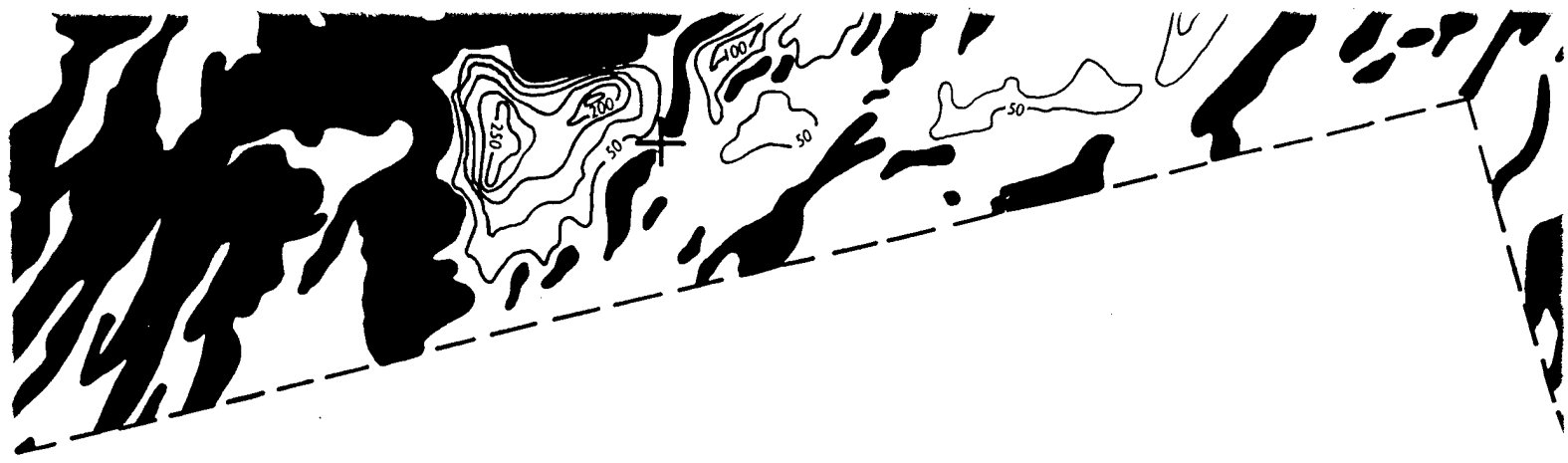
Universal Transverse Mercator
Scale 1:200,000

Map 4 of 6

25°
15'

49°00'

48°45'



SEDIMENT THICKNESS
Atlantic Ridge Flank, 25°20'N to 27°15'N

Gardner and Brian E. Tucholke

Contours in meters
(Thicknesses <10 m are Black)

Transverse Mercator Projection
Scale 1:200,000

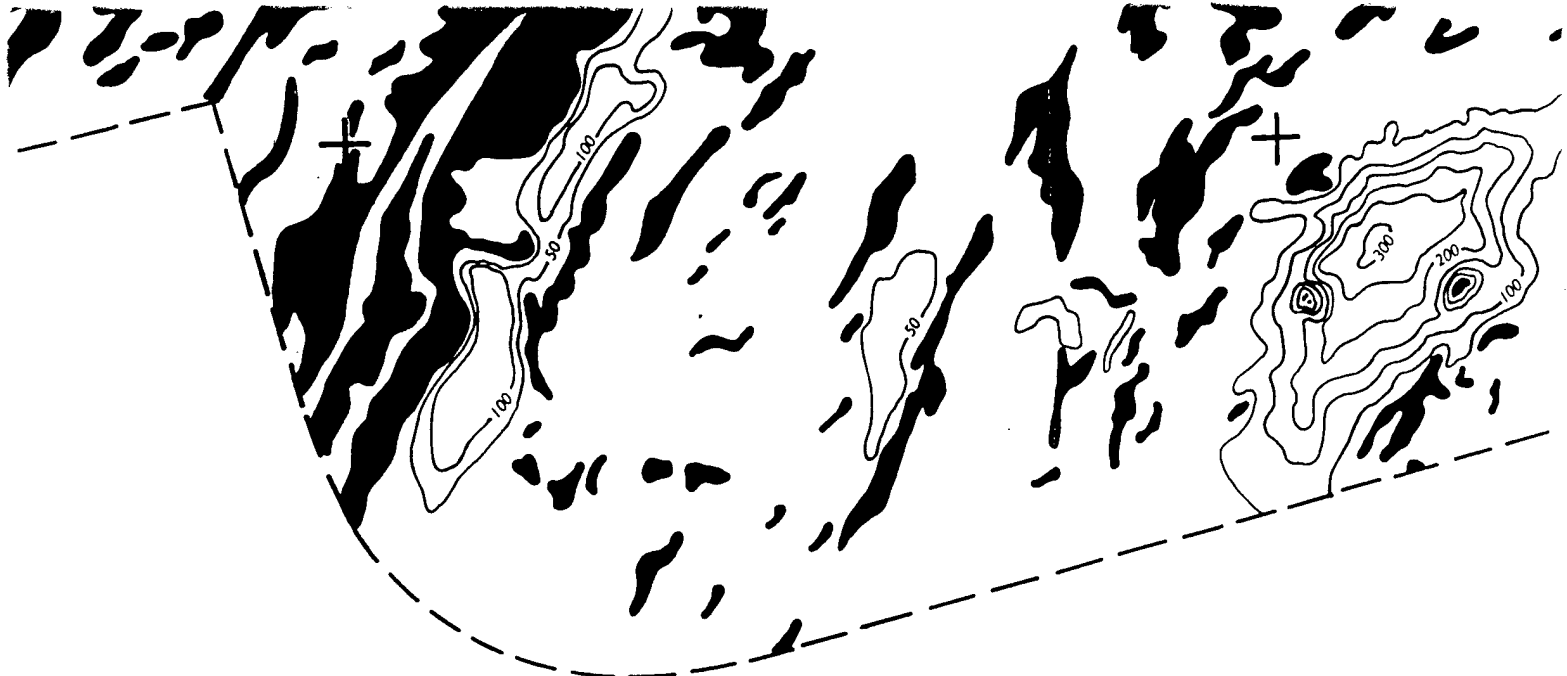
Map 4 of 6



48°30'

4

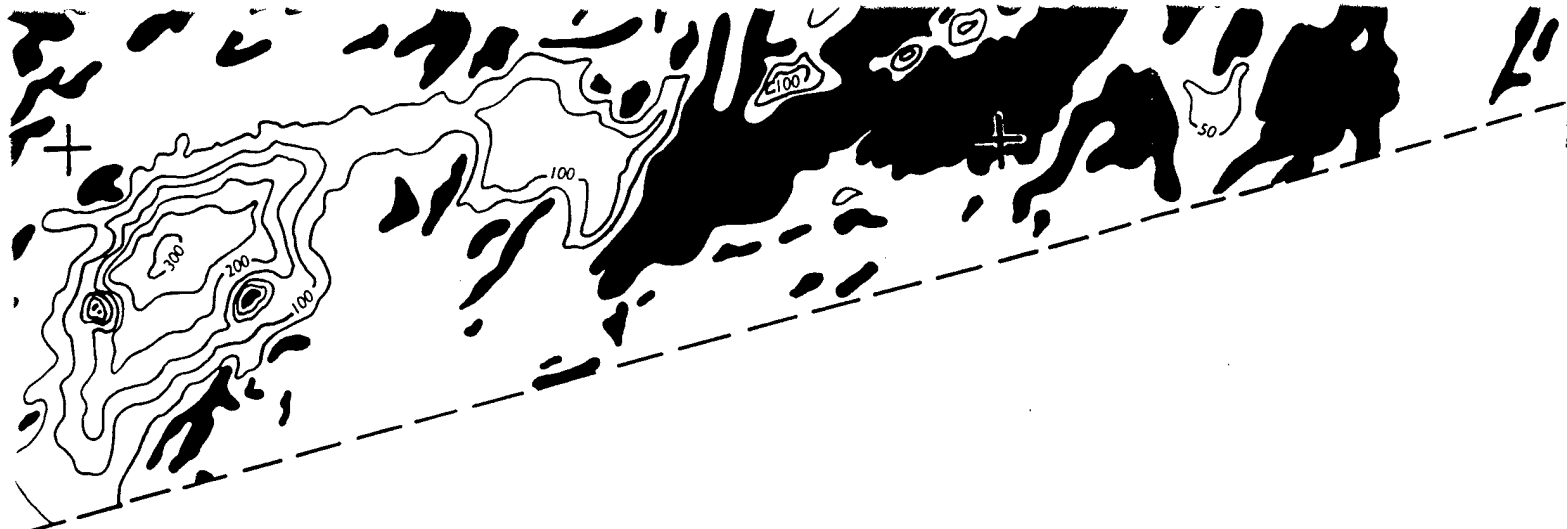
12



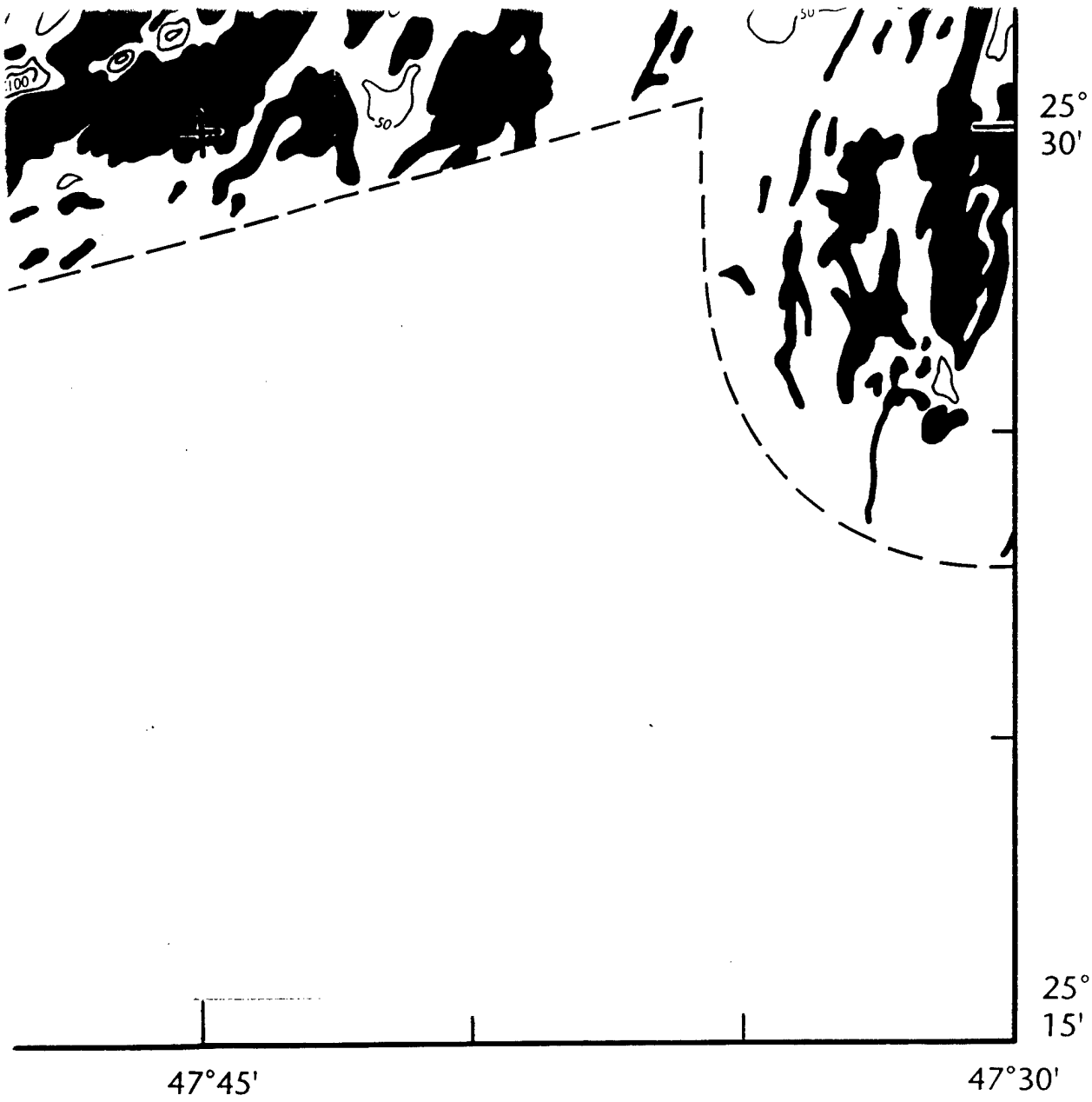
48°15'

48°00'

13



14

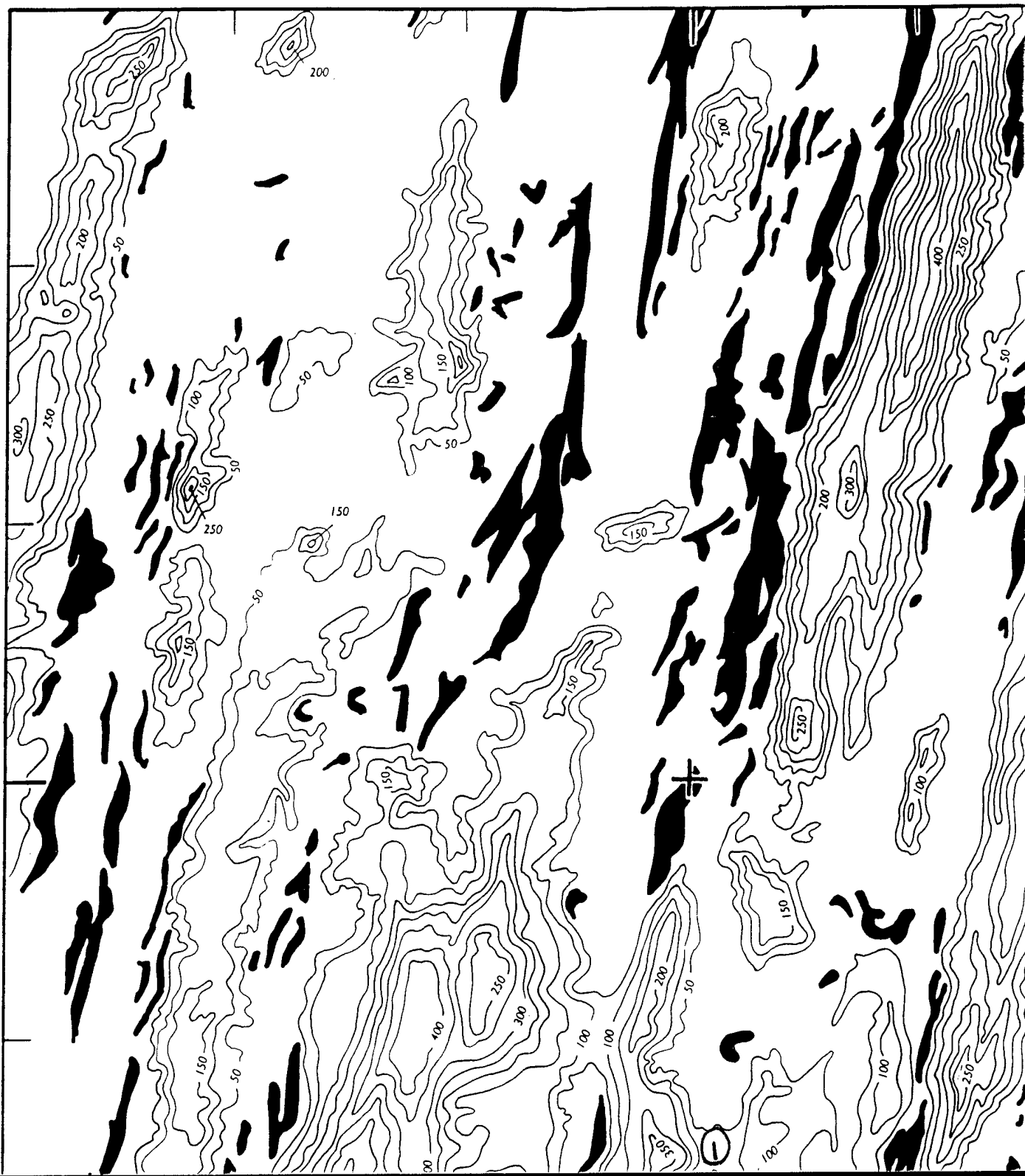


47°30'

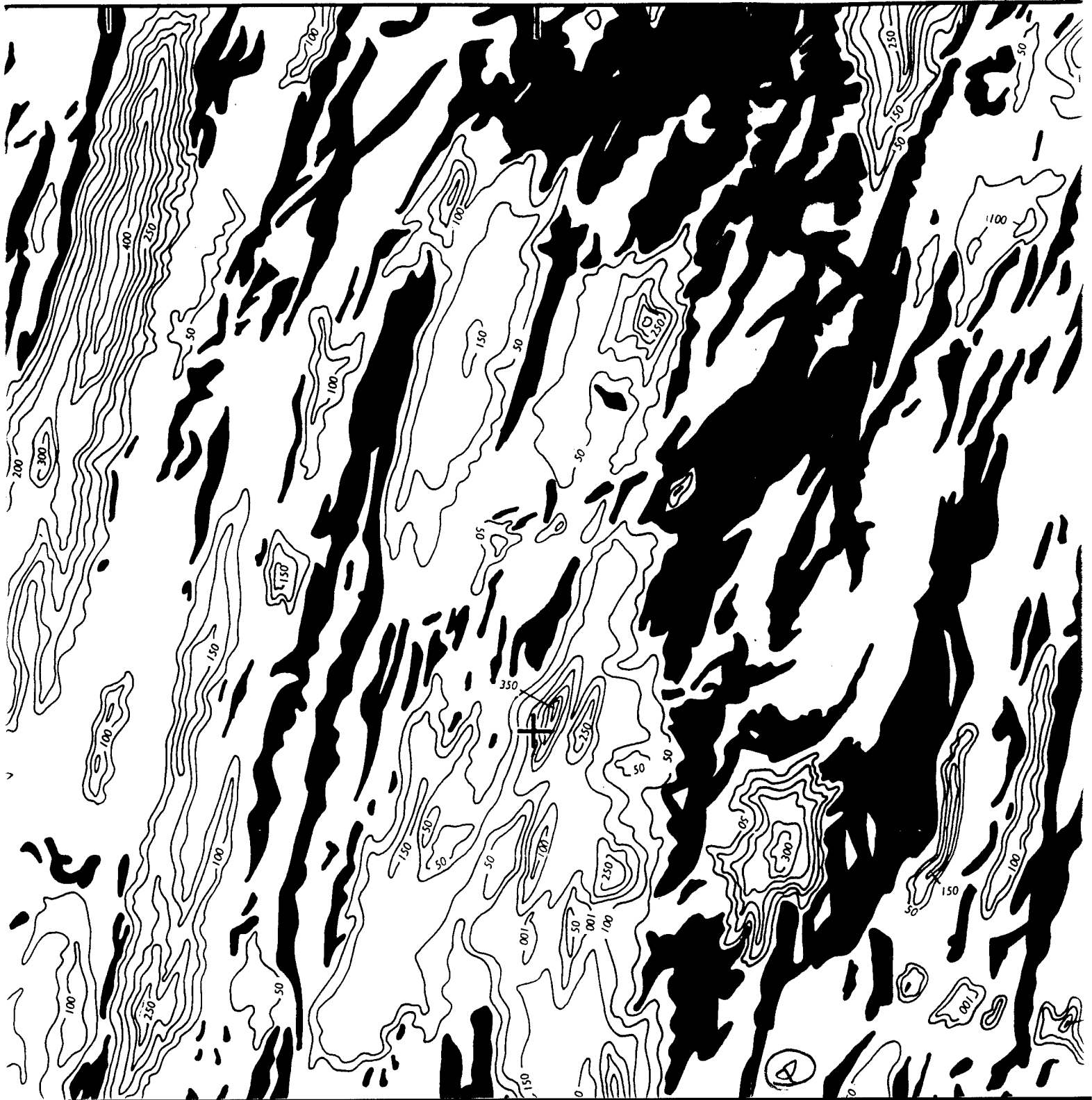
47°15'

26°
15'

26°
00'

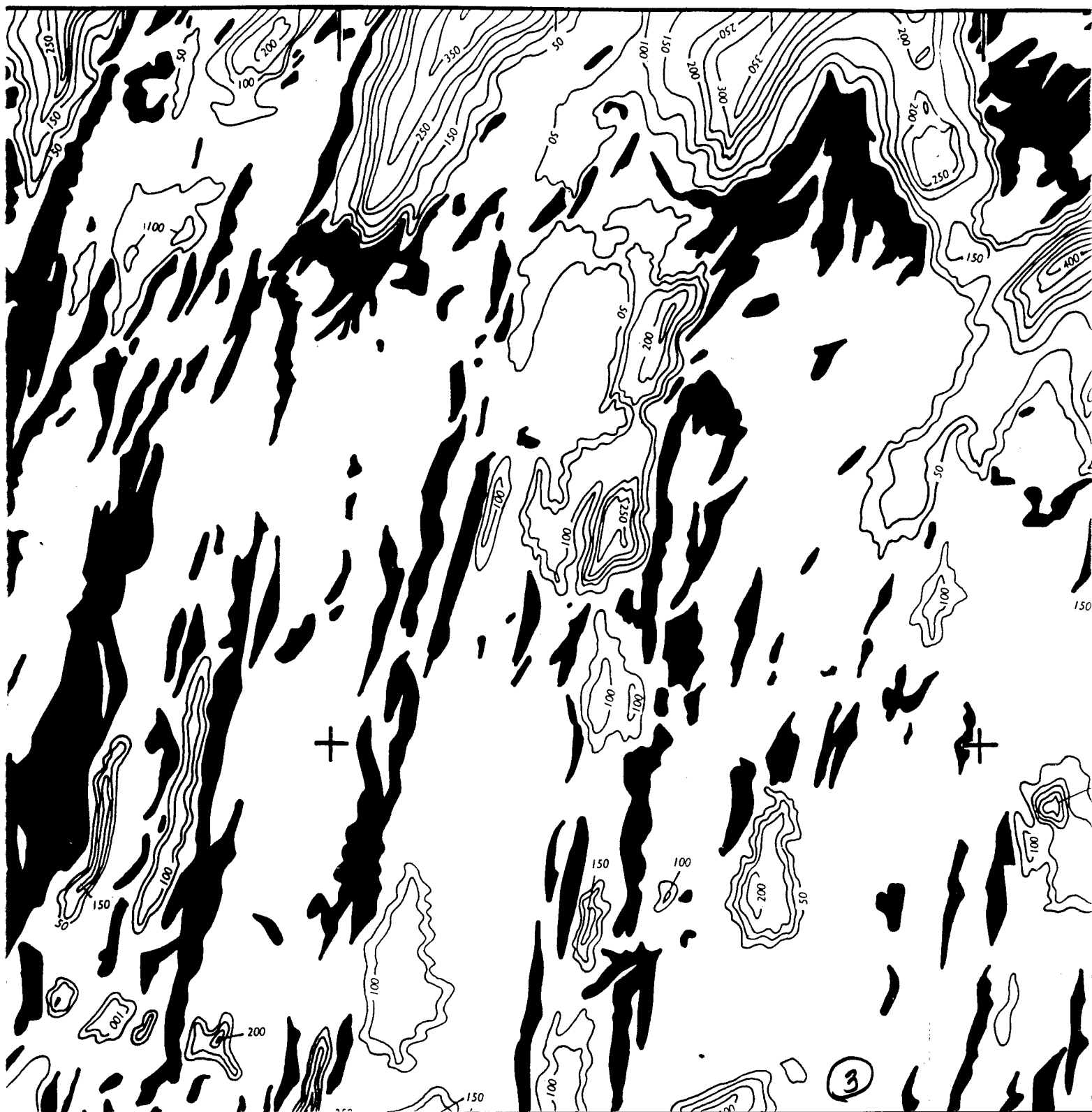


47°00'



46° 45'

46° 30'



46°30'

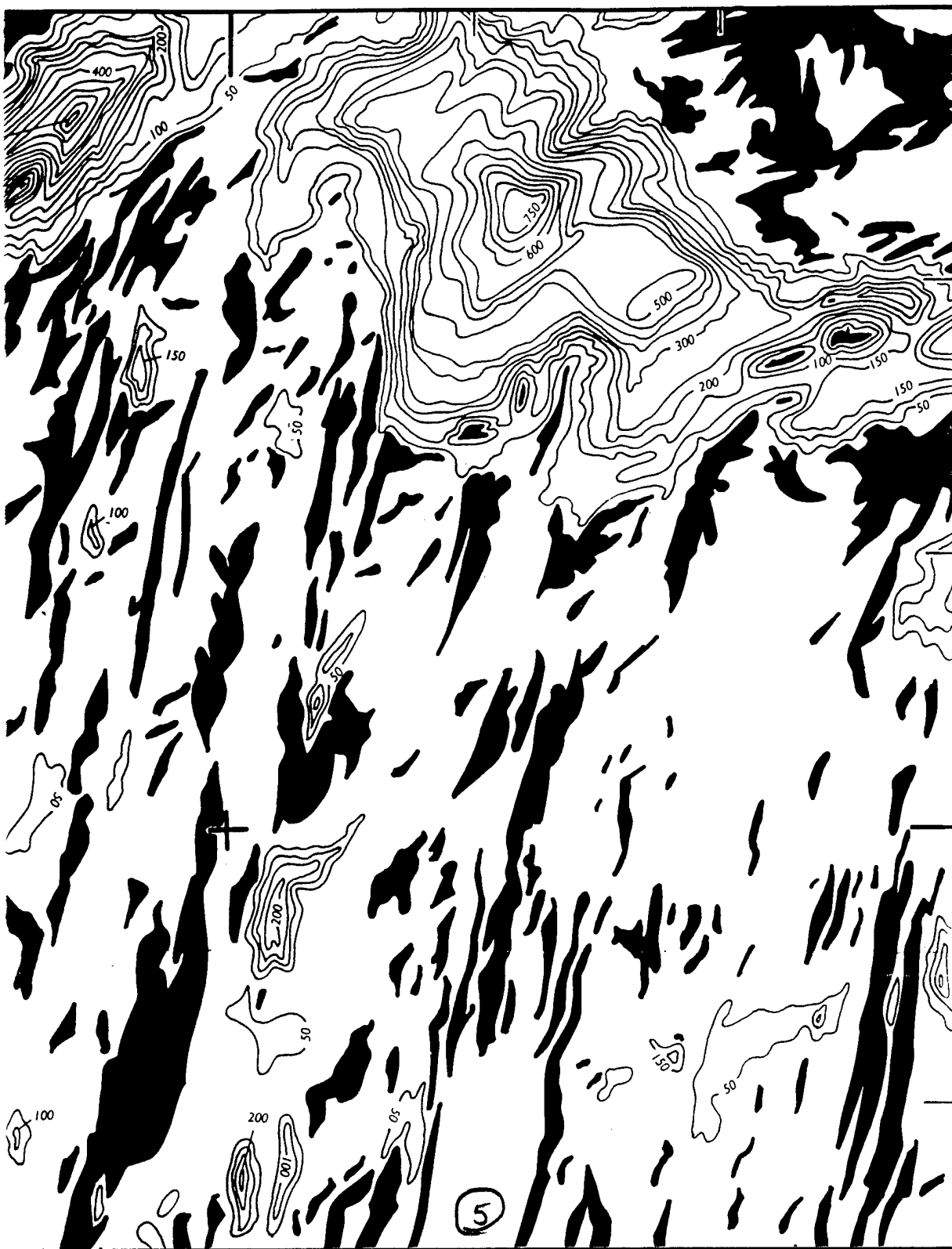
46°15'



46°15'

46°00'

26°
15'

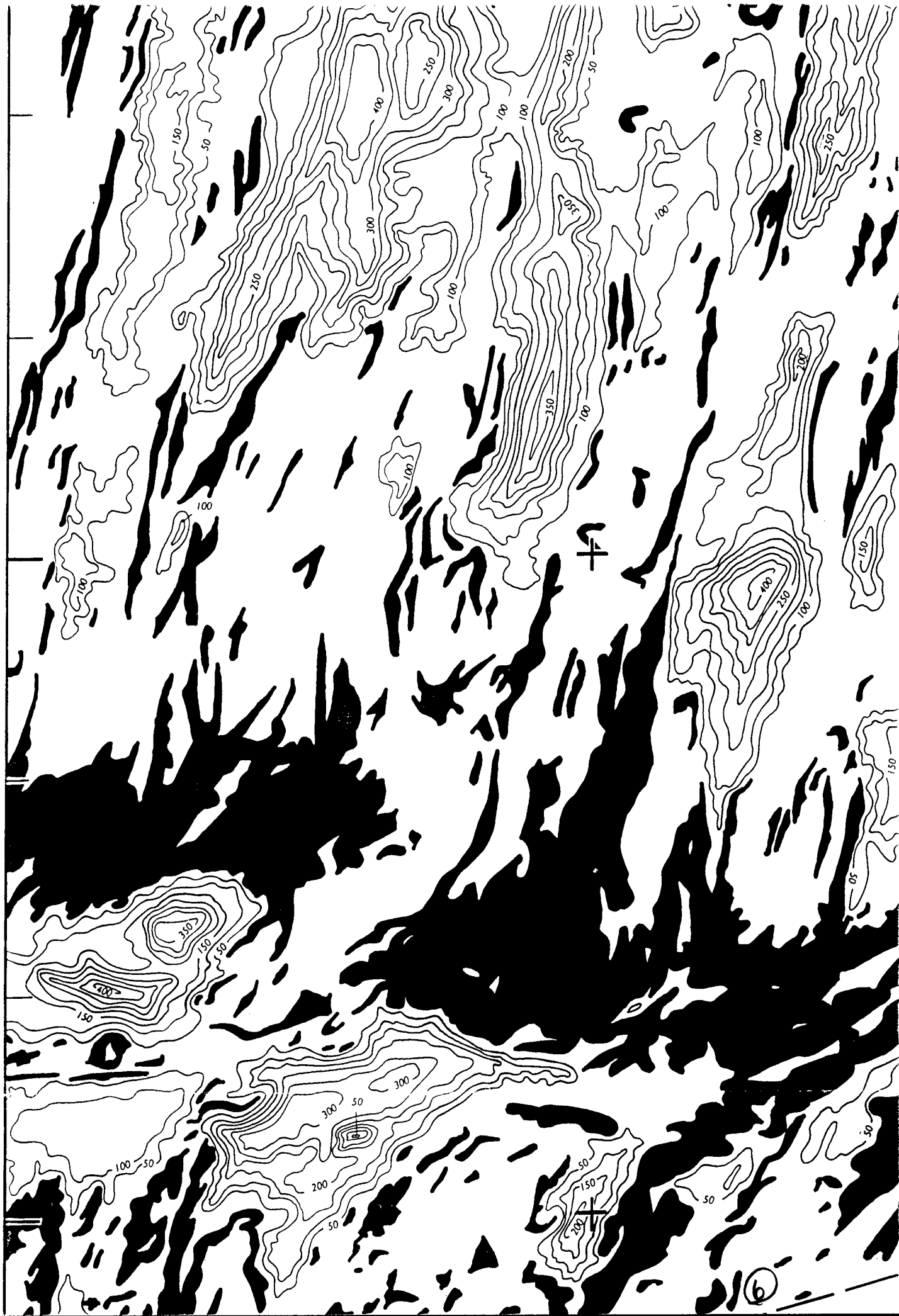


26°
00'

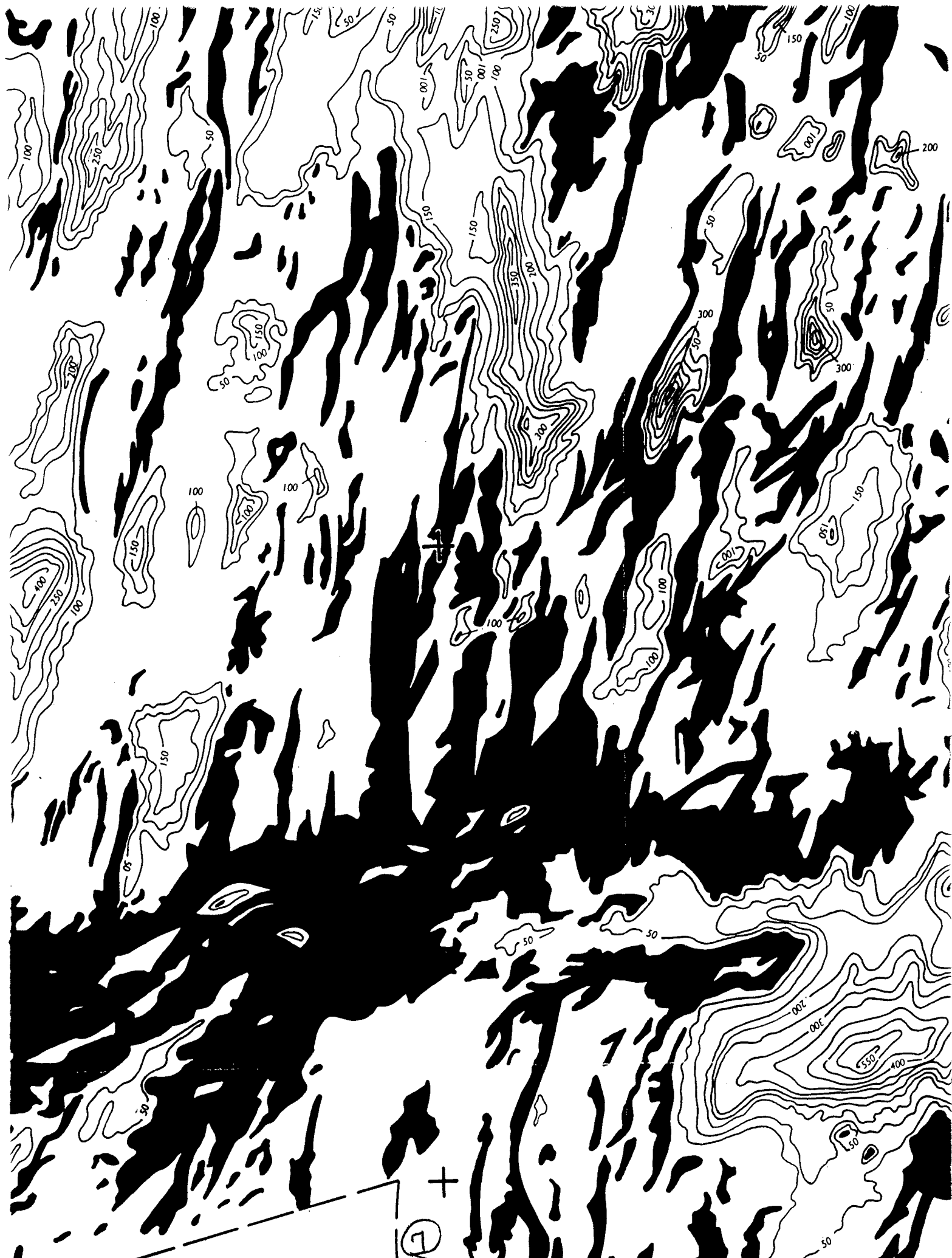
5

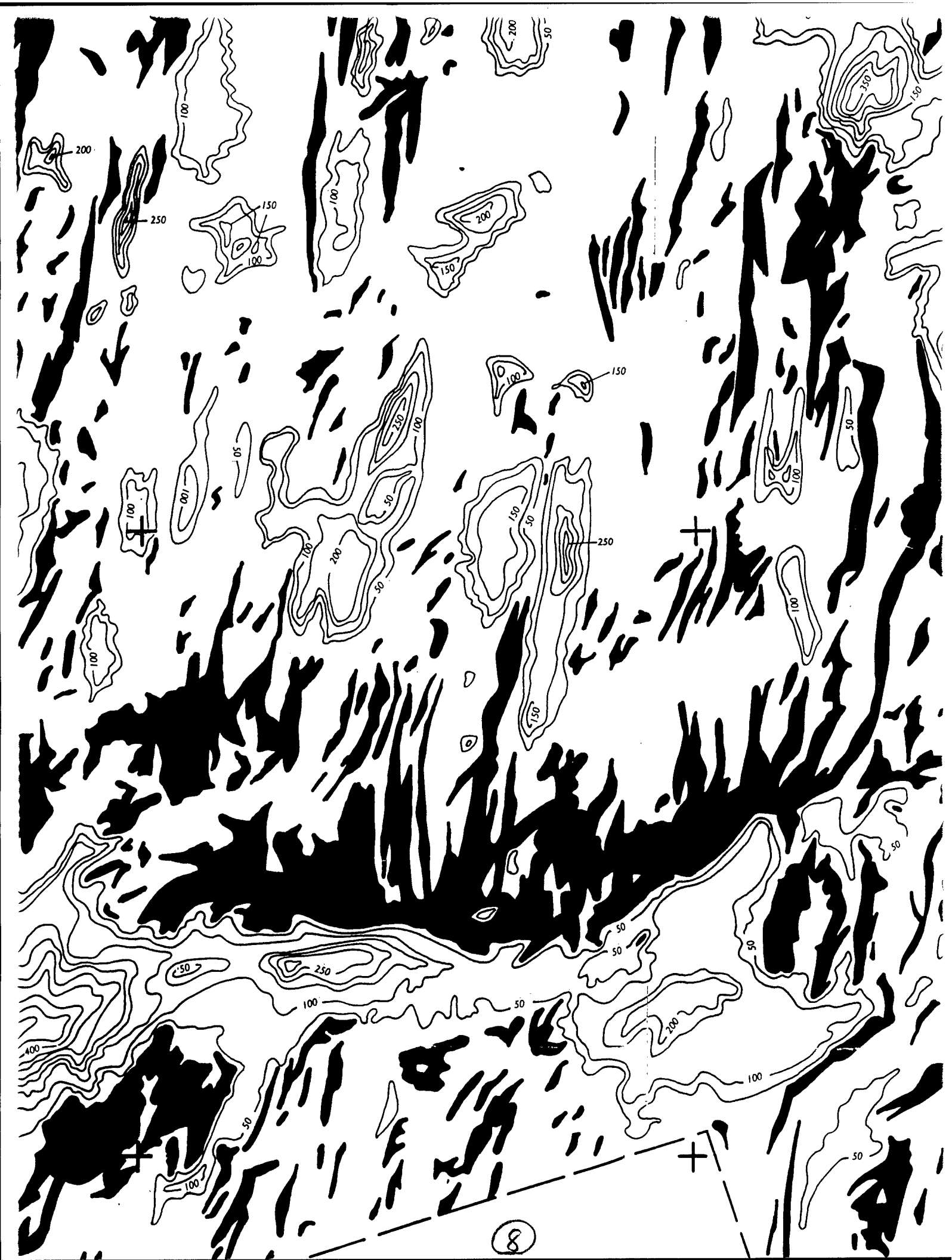
25°
45'

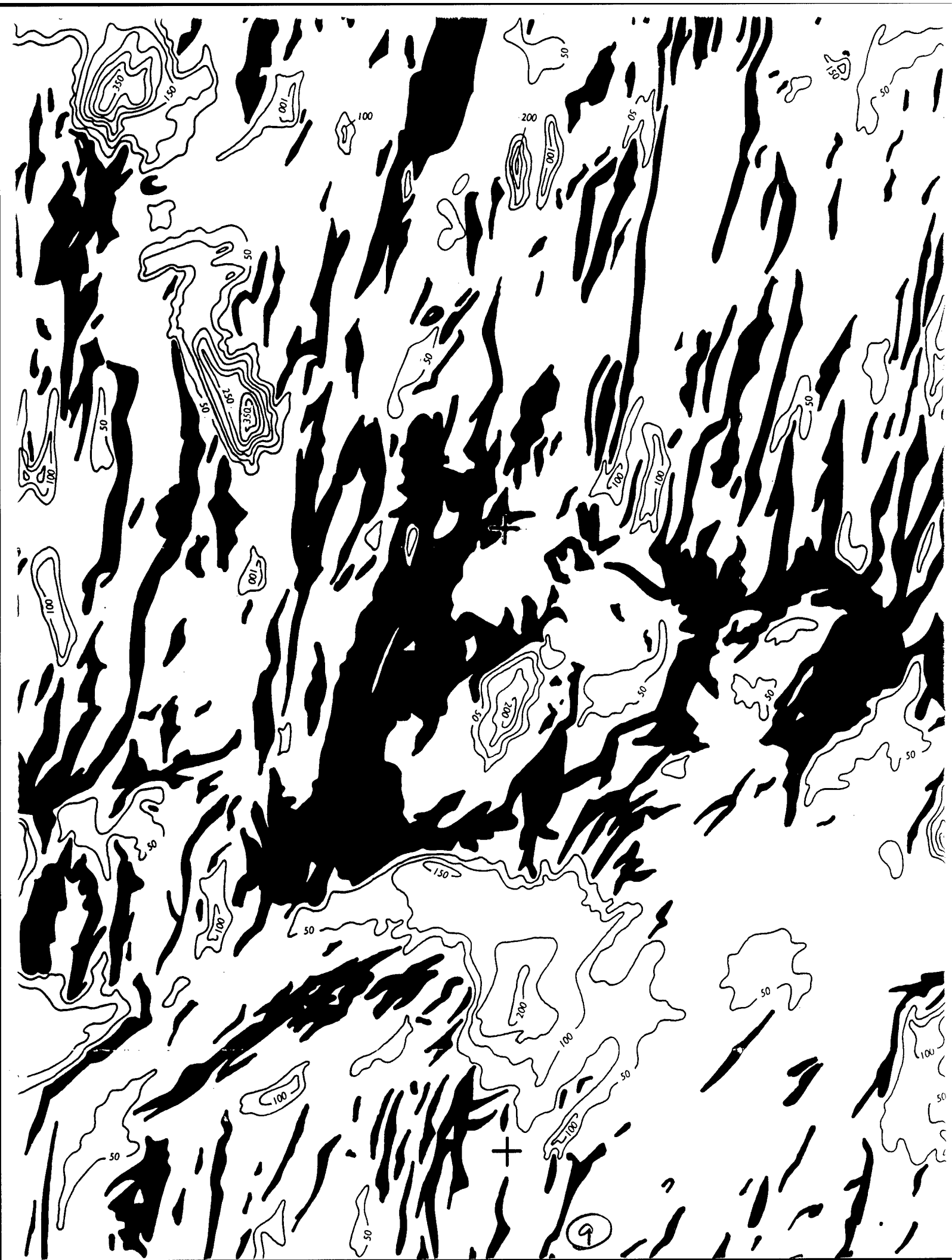
25°
30'



⑥





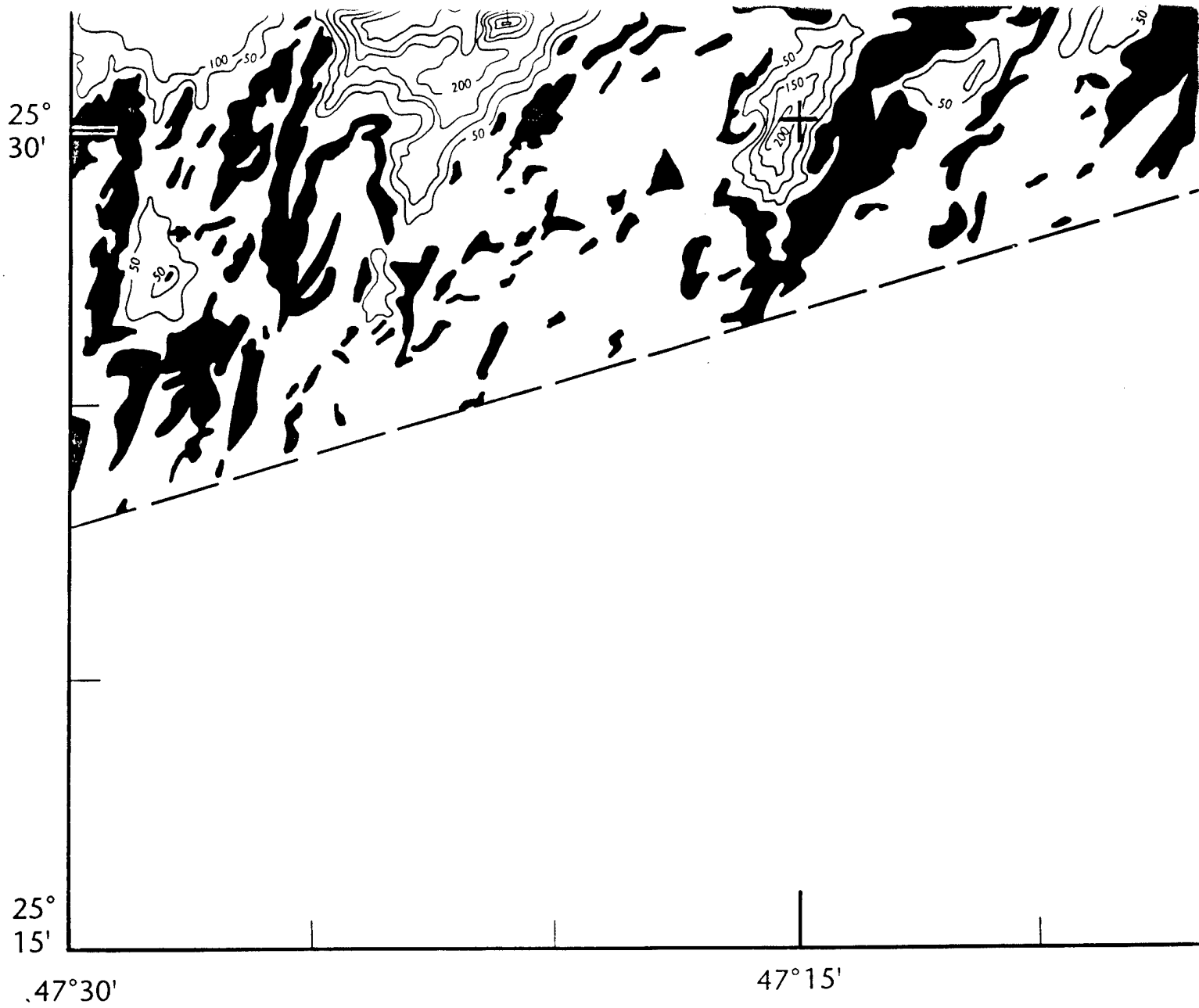




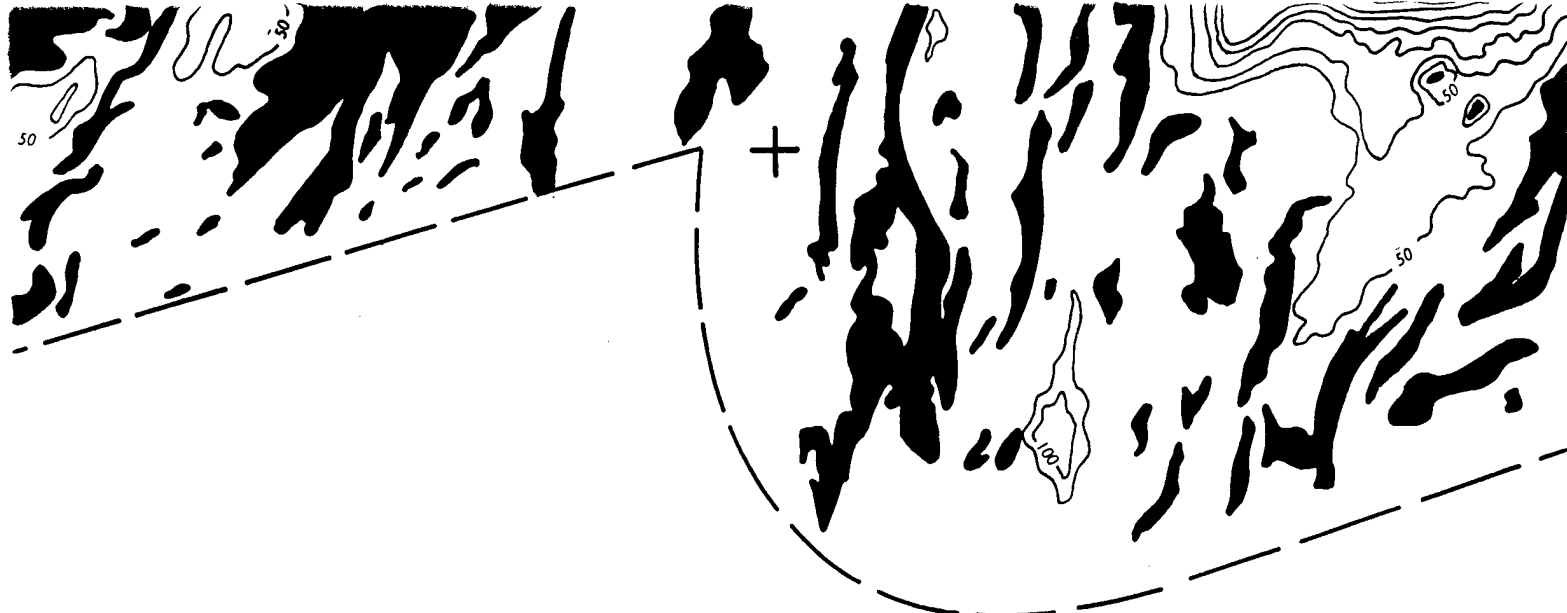
25°
45'

25°
30'

10



(11)



SEDII
Western Mid-Atlant

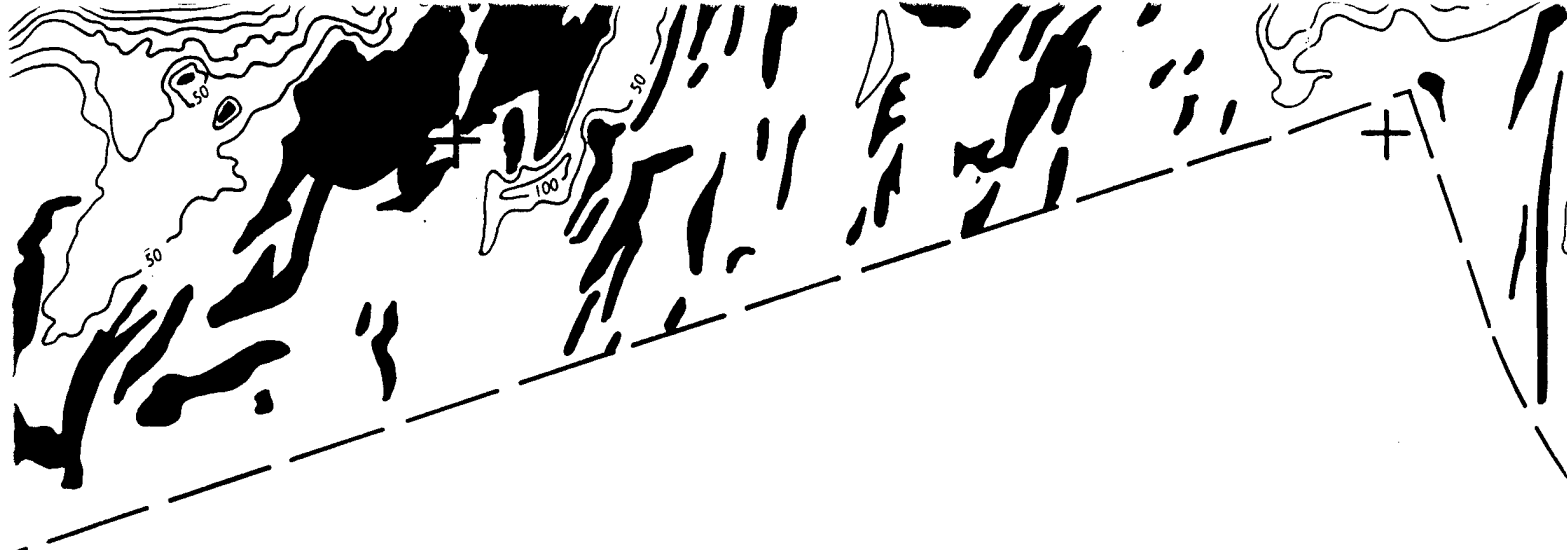
Gary E. Jar

C. I. = 50 m

Univeral Ti

47°00'

(12)



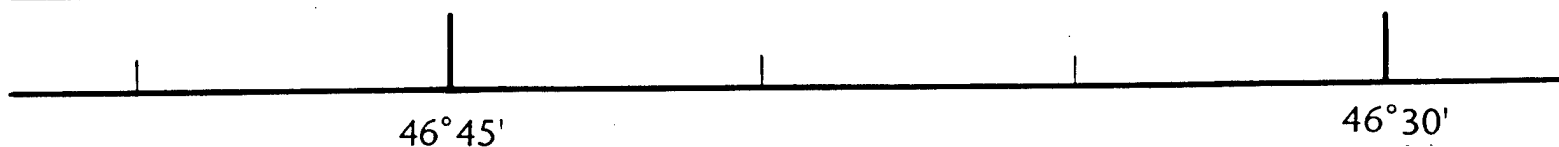
SEDIMENT THICKNESS
western Mid-Atlantic Ridge Flank, 25°20'N to 27°15'N

Gary E. Jaroslow and Brian E. Tucholke

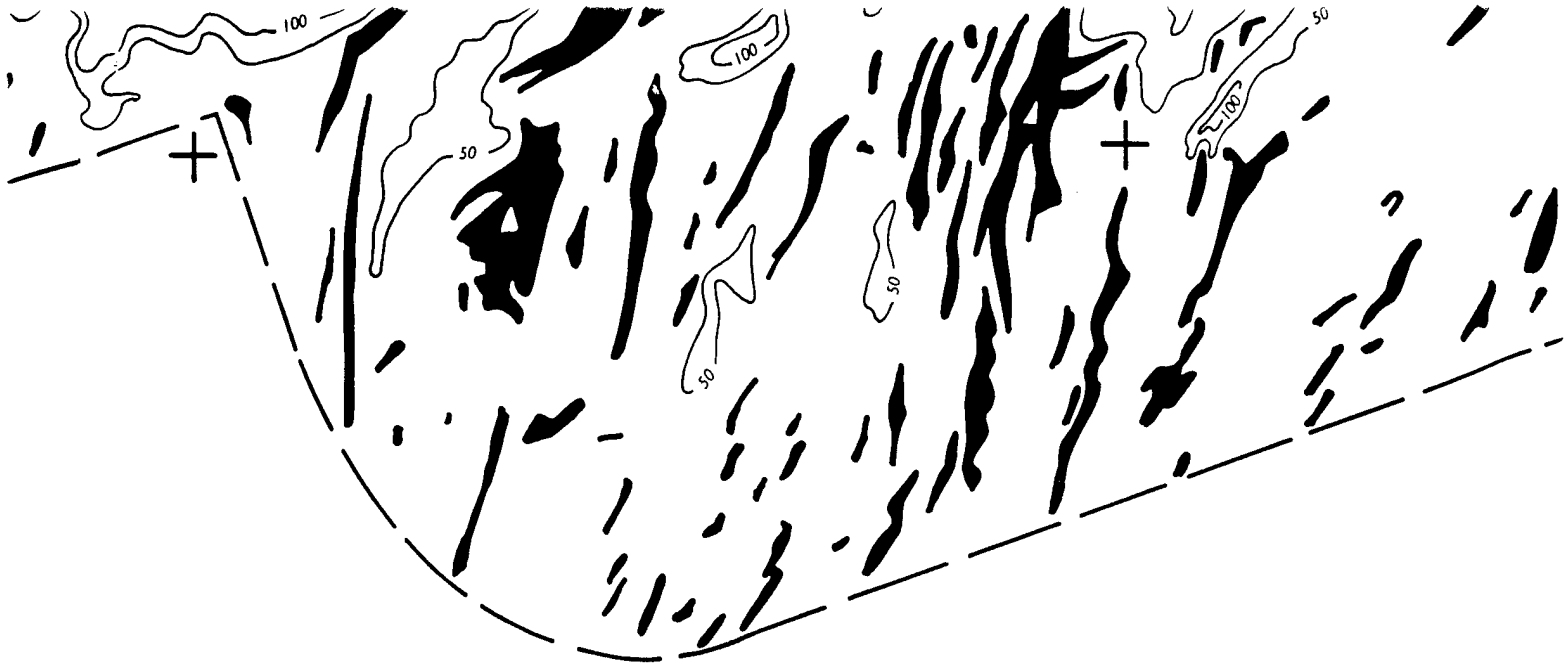
Contours in meters
C. I. = 50 m (Thicknesses <10 m are Black)

Universal Transverse Mercator Projection
Scale 1:200,000

Map 5 of 6



(13)



46°30'

46°15'

14

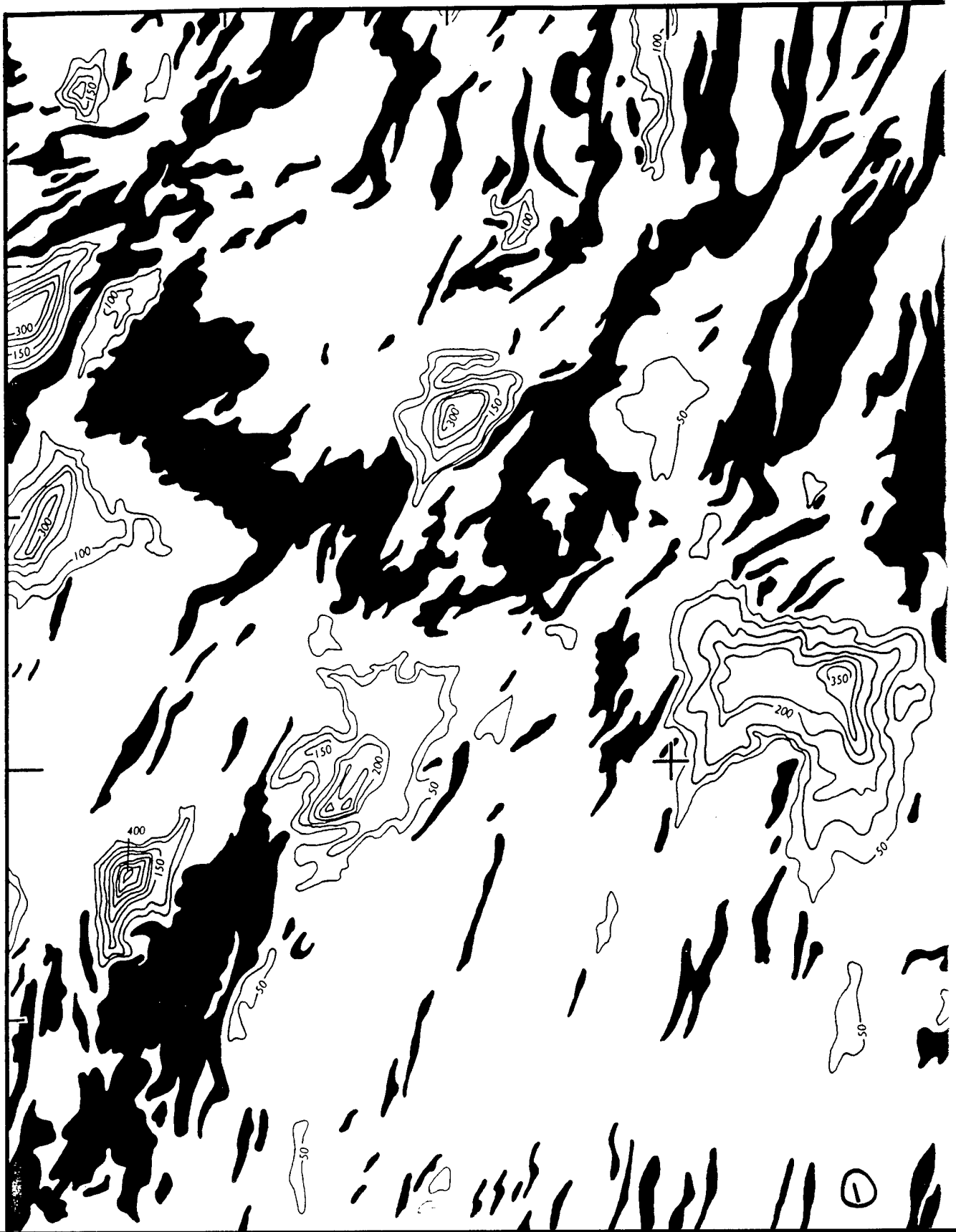
NOTES

46°00'

45°45'

26°
15'

26°
00'



45°30'



45°15'

45°00'



45°00'

44°45'

TAG
HYDROTHERMAL
MOUND

4

44°45'

44°30'

26°
15'

26°
00'

+

5

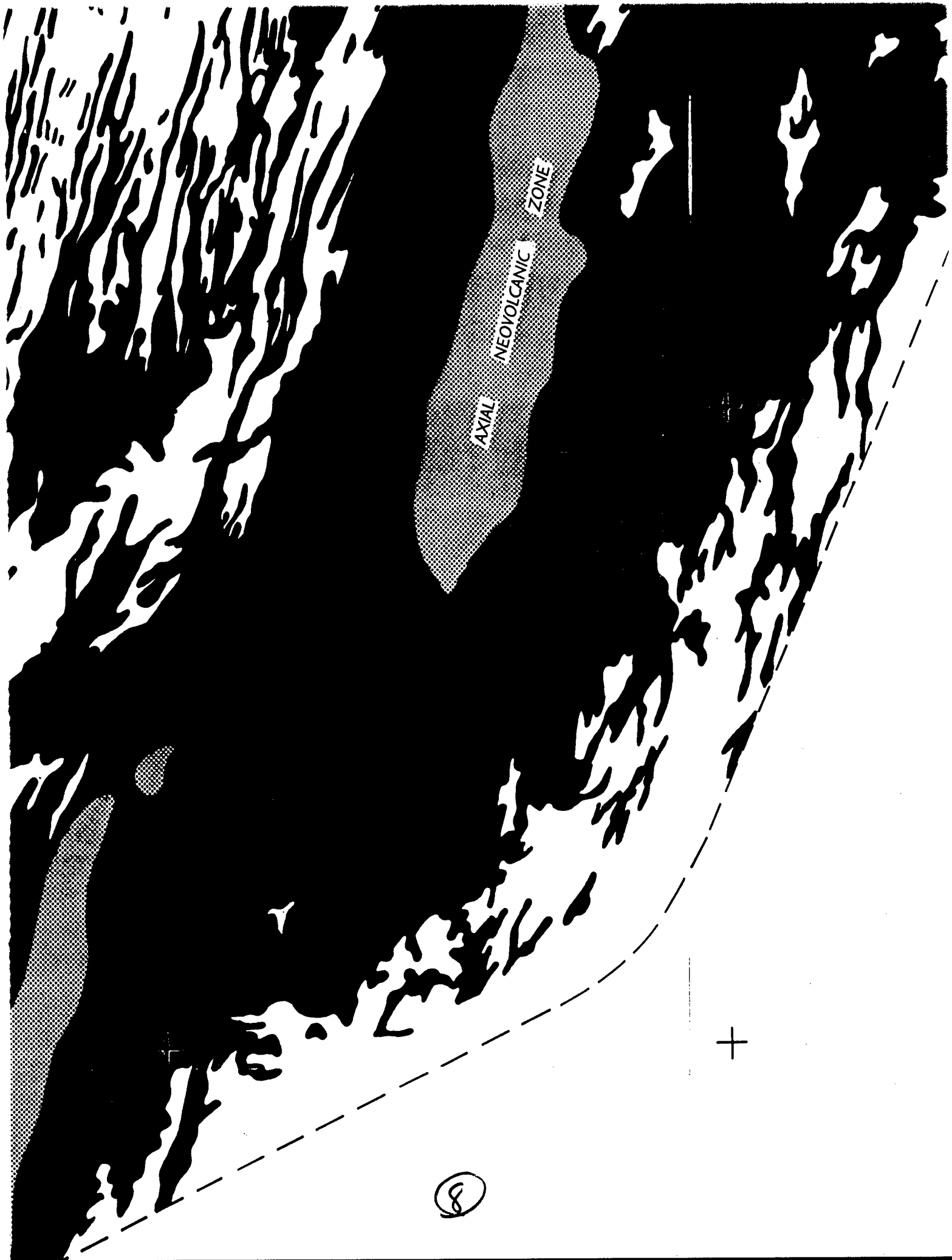
25°
45'

25°
30'

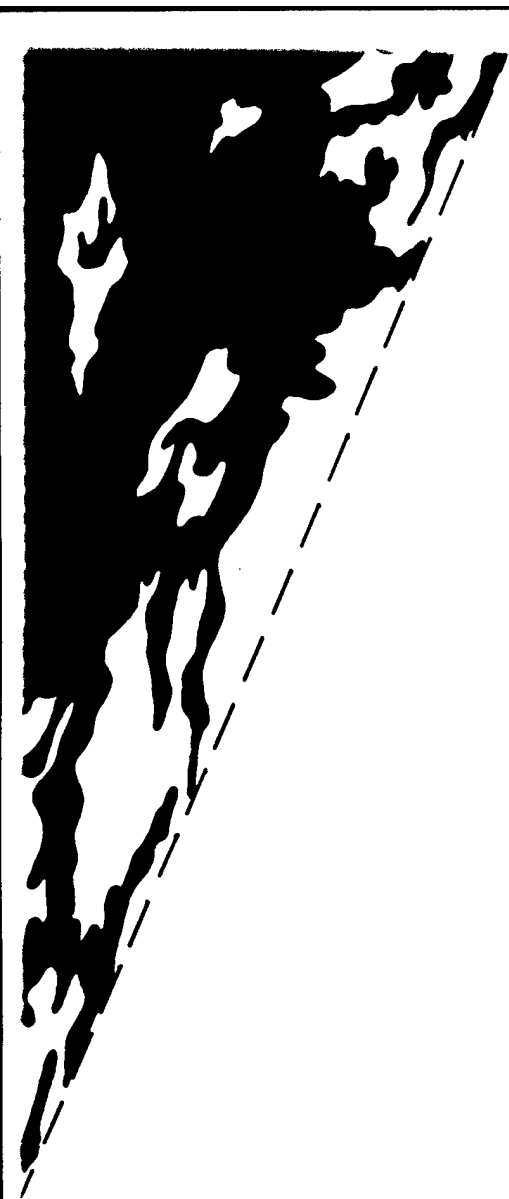


6





8



+

+

9

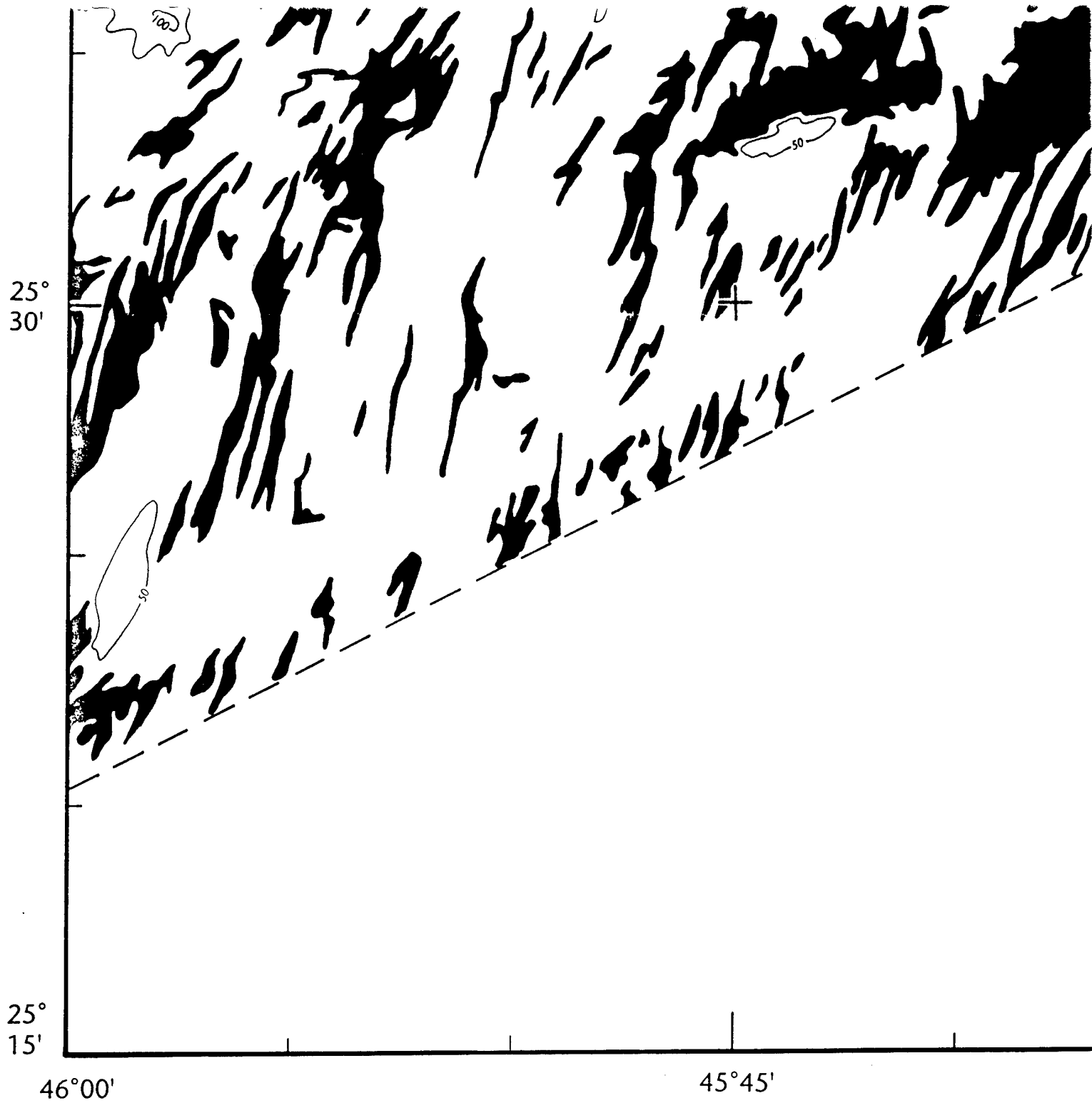
+

25°
45'

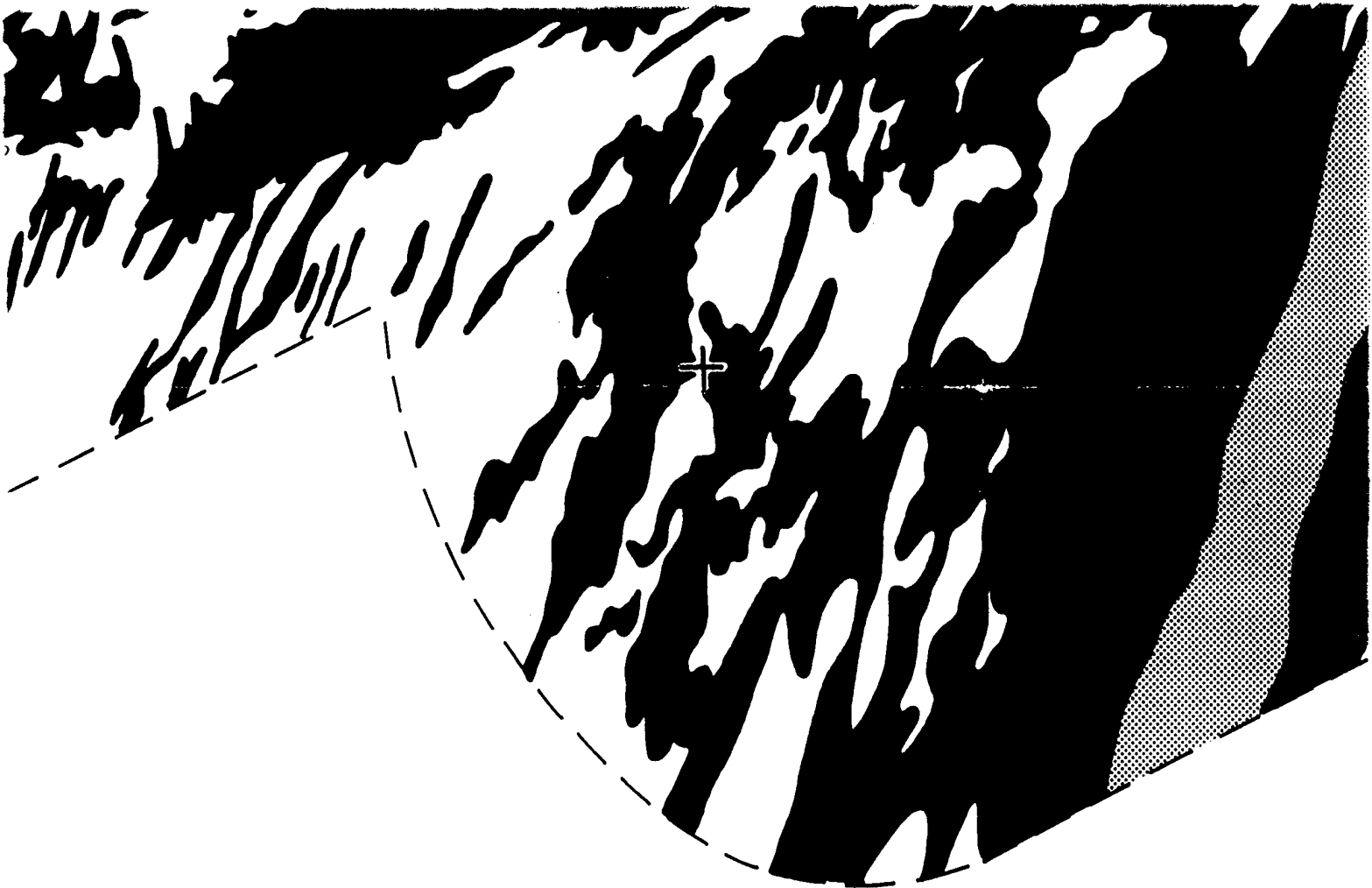
+

(10)

25°
30'

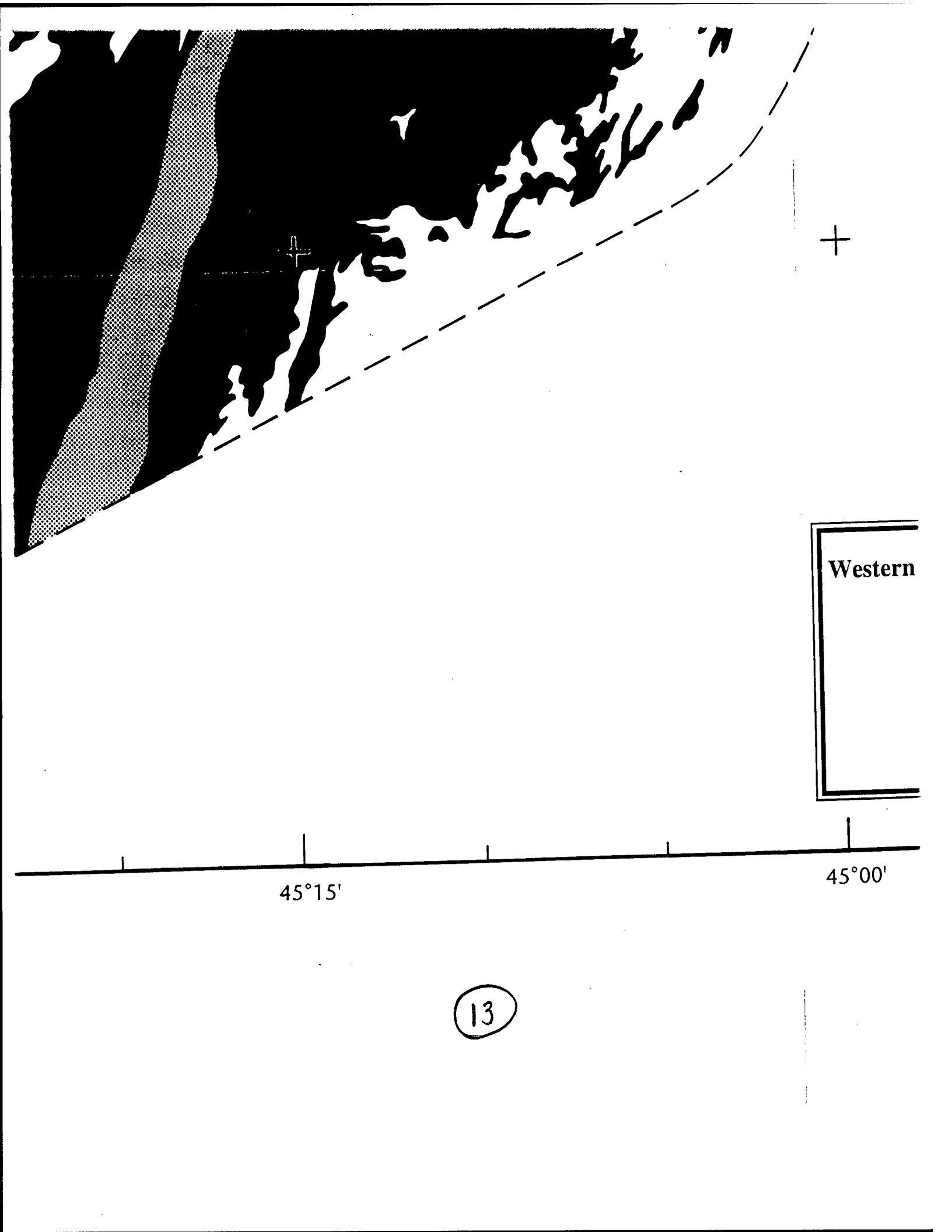


(11)



45°30'

18



Western

45°15'

45°00'

13

SEDIMENT THICKNESS
Western Mid-Atlantic Ridge Flank, 25°20'N to 27°15'N

Gary E. Jaroslow and Brian E. Tucholke

Contours in meters
C. I. = 50 m (Thicknesses <10 m are Black)

Universal Transverse Mercator Projection
Scale 1:200,000

Map 6 of 6

45°00'

44°45'

+

25°
30'

ICKNESS
ank, 25°20'N to 27°15'N

ian E. Tucholke

eters
<10 m are Black)

cator Projection
000

6

25°
15'

44°45'

44°30'

15